UNIVERSITA' DEGLI STUDI DI VERONA
DIPARTIMENTO DI SCIENZE NEUROLOGICHE,
NEUROPSICOLOGICHE, MORFOLOGICHE E MOTORIE

SCUOLA DI DOTTORATO DI RICERCA
IMAGING MULTIMODALE IN BIOMEDICINA

PROBING BRAIN FUNCTION WITH PHARMACOLOGICAL MRI

A Ph.D thesis presented by

Alessandro Gozzi

Course Coordinator: Prof. Andrea Sbarbati

Advisor: Prof. Pasquina Marzola

Years 2008-2011

a Paola, Thomas and Francesca

“I wanted, I always wanted, I wanted to the utmost.”

“Volli, sempre volli, fortissimamente volli.”

V. Alfieri (1749-1803; Italian writer)

Table of contents

Acknowledgements

I have been unusually fortunate as a researcher at GSK to have had the opportunity to train under the direction of my friend and mentor Angelo Bifone. I owe a tremendous debt of gratitude to Angelo, for his contagious and genuine passion for science which provided so much impetus to my research, and for showing me the critical direction that I have needed in my early years in the lab as a junior and untrained scientist - I am truly grateful. I also need to thank my friend and colleague Adam Schwarz for his day-to-data advice and invaluable instruction in the theoretical and practical aspects of MRI image analysis.

The implementation of complex methods such as fMRI is necessarily the result of a multidisciplinary effort. It would not have been possible to complete all of the projects in the last three years without the help and support from many members of the GSK Verona and Harlow communities. In particular I would like to thank Valerio Crestan and Giuliano Turrini for the precious and skilful technical support, Mauro Corsi and Emilio Merlo-Pich, for giving me the chance to pursue my doctorate and for the numerous brainstorming sessions; Charles Large and Hugh Herdon for their expert insight into the pharmacology of the NMDA receptor, Giuseppe Graniti, Marcel Clemens and Federica Agosta, for their invaluable contribution in implementing IDL code for image analysis, and Stefano Lepore for helping me sifting through the huge data backlog of the lab.

I would also like to give my deepest gratitude to Dr. Cornelius Gross at EMBL, for providing experimental animals and guidance in the interpretation of the pharmaco-genetic results. Cornelius is an exceptionally thoughtful scientist and thinker from whom I have learned a lot. I am also indebted to my academic supervisor, Prof. Pasquina Marzola, for the support she has provided throughout the duration of my doctorate, and Prof. Andrea Sbarbati for permitting me to perform extra-mural research. I am also grateful to Prof. Fabio Beltram for giving me the great opportunity to join the extraordinarily-talented research pool at NEST in Pisa.

Lastly, I am immensely grateful to my loving wife Paola, who supported me with unwavering trust and confidence, and never failed to remind me to pause, enjoy the moment and enrich my life with a healthy level of distractions. Paola, I owe you a big one!

Summary

The development of functional Magnetic Resonance Imaging (fMRI) has heralded a revolution in neuroscience, providing clinicians with a method to non-invasively investigate the spatio-temporal patterns of neuro-functional activity. Although primarily developed for human investigations, there exists significant scope for the application of fMRI in pre-clinical species as a translational and investigational platform across different areas of neuroscience and psychiatry research. However, the realization of this potential is hampered by a number of experimental constraints which make the application of fMRI methods to animal models less than straightforward. As a result, most fMRI research in laboratory species has been reduced to the employment of basic somato-sensory stimulation paradigms, thus greatly limiting the translational potential of the technique.

An interesting approach to overcome some of these limitations has been dubbed "pharmacological MRI" (phMRI) and relies on the use of fMRI to map patterns of brain activity induced by psychoactive drugs. The approach has demonstrated the ability to elicit reliable fMRI signals even under anaesthesia, and to enable selective stimulation of different neurotransmitter systems. Building upon the homology between brain circuits in humans and laboratory animals, phMRI techniques thus offer the opportunity of significantly expanding the stimulation repertoire available to preclinical fMRI research, by allowing to selectively probe specific aspects of brain function under different preconditioning states.

Within this framework, the research presented herein was aimed to broaden the scope of application of preclinical phMRI both as a translational technique, when applied to clinically-relevant disease models, and more generally as a versatile platform for the pre-clinical investigation of brain activity and its functional topology as a function of behavioural, pharmacological or genetic preconditioning.

In a first group of studies, we developed a phMRI assay to map the circuitry activated by NMDAR antagonists in the rat brain. These psychotogenic compounds are widely exploited to model schizophrenia symptoms and to provide experimental models that may prove useful in the development of novel treatments for the disorder. The results of this research highlighted a conserved cortico-limbo-thalamic circuit that is activated by NMDAR antagonists both in humans and preclinical species, which can be modulated by existing and novel antipsychotic drugs (Section 4.1).

The translational potential of phMRI measurements was further corroborated by a second group of studies, where a multi-parametric phMRI-based approach was applied to investigate multiple facets of brain function in a rodent cocaine self-

administration model, a behavioural paradigm of established construct-validity for research of drug addiction. This line of investigation revealed specific basal and reactive functional alterations in the brain of cocaine-exposed rodents closely related to those observed in analogous neuroimaging studies in humans (Section 4.2).

In a third line of investigation, the combined use of advanced neuro-genetic targeting strategies (i.e. pharmacogenetic silencing) and phMRI has proven successful in establishing direct correlations between cells, circuit and complex behaviours in genetically engineered mouse lines. These studies (Section 4.3) have led to the identification of a novel cell population in the amygdala that controls the behavioural response to fear through the recruitment of cholinergic circuits.

Finally, the phMRI approach has proven a powerful tool to explore functional connectivity in rodents, and to map a variety of different neurotransmitter pathways by performing measures of correlated responses in spatially remote brain areas. This has provided a useful playground to explore novel statistical methods of analysis of functional connectivity represented in terms of complex networks (Section 4.4).

Collectively, the results of this work strongly corroborate the translational use of phMRI approaches, and pave the way to the integrated implementation of phMRI and advance genetic manipulation as a novel powerful platform for basic neurobiological research.

Riassunto

Lo sviluppo di tecniche di risonanza magnetica funzionale (fMRI) ha rivoluzionato le ricerca neuroscientifica clinica, determinando la possibilità di investigare le dinamiche spazio-temporali dell'attività cerebrale in maniera non invasiva e con grande accuratezza. Sebbene la tecnica sia stata originariamente sviluppata in ambito clinico, essa ha il potenziale di poter essere utilizzata in ambito preclinico come efficace strumento investigativo e traslazionale. Tuttavia, l'implementazione preclinica di questi metodi è complicata da una serie di costrizioni sperimentali, *in primis* l'utilizzo di anestetici, che minano fortemente il potenziale traslazionale di queste tecniche.

Il recente sviluppo di tecniche di "MRI farmacologico" (phMRI) offre la possibilità di superare alcune delle limitazioni sperimentali correlate all'implementazione di approcci fMRI classici in animali da laboratorio. La tecnica si basa sull'utilizzo di metodi fMRI per mappare alterazioni di attività cerebrale prodotte dalla somministrazione di sostanze psicoattive. Studi preliminari hanno evidenziato la capacità di generare robusti e specifici segnali phMRI anche in condizioni di anestesia, ed ha dimostrato la possibilità di stimolare selettivamente diversi sistemi di neurotrasmettitori.

Sfruttando la conservazione di circuiti cerebrali tra specie, tecniche phMRI offrono quindi l'opportunità di ampliare in maniera significativa il repertorio di stimolazione neuronale a disposizione in ambito preclinico, consentendo di indagare selettivamente specifici aspetti della funzione cerebrale in diversi stati di pre-condizionamento neuronale.

In tale contesto, le attività di ricerca di questa tesi sono state finalizzate ad ampliare il campo di applicazione di metodi phMRI preclinici in due diversi ambiti sperimentali: a) come modalità di indagine traslazionale, qualora applicata a modelli di malattia clinicamente rilevanti, b) più in generale come piattaforma investigativa per l'indagine della funzione cerebrale e della sua topologia funzionale in contesti sperimentali diversi.

In un primo gruppo di studi, tecniche phMRI sono state impiegate per mappare i circuiti neuronali attivati da antagonisti del recettore del glutammato NMDA nel cervello del ratto (Sezione 4.1). Tali composti, grazie alle loro proprietà psicotogeniche, sono ampiamente sfruttati come modelli sperimentali di schizofrenia in animali ed in volontari allo scopo di valutare e validare nuovi trattamenti per la malattia. I risultati di questa ricerca hanno evidenziato uno specifico circuito cortico-limbo-talamico che risulta essere attivato da antagonisti NMDAR sia nell'uomo che in

specie precliniche, e che è risultato essere modulabile da meccanismi antipsicotici diversi (Sezione 4.2).

Il potenziale traslazionale dei metodi phMRI è stato ulteriormente avvalorato da un secondo gruppo di studi, in cui un approccio multi-parametrico "phMRI-based" è stato impiegato per indagare molteplici aspetti della funzione cerebrale in un modello murino di dipendenza da cocaina. Questa linea di investigazione ha evidenziato multiple alterazioni della funzione cerebrale basale e reattiva nel cervello di roditori esposti alla cocaina strettamente connesse a quelle osservate in analoghi studi di imaging su pazienti cocaina-dipendenti (Sezione 4.2).

In una terza linea d' investigazione, l'uso combinato di avanzate strategie di targeting neuro-genetico (pharmaco-genetic silencing) e phMRI si è dimostrato efficace nello stabilire correlazioni dirette tra cellule, circuito e comportamento in linee di topo geneticamente modificate. Questi studi hanno portato all'identificazione di una nuova e circoscritta popolazione neuroni nell'amigdala, in grado di controllare qualitativamente la risposta comportamentale alla paura attraverso il reclutamento di circuiti colinergici corticali (Sezione 4.3)

Infine, l'approccio phMRI si è dimostrato uno strumento potente e versatile per l'implementazione di misure di connettività funzionale nel cervello di roditori. Questo aspetto ha permesso l'esplorazione di nuovi approcci statistici per l'analisi della topologia funzionale del cervello basati sulla rappresentazione di misure di connettività in termini di reti complesse (Sezione 4.4).

Complessivamente, i risultati di questo lavoro avvalorano il potenziale traslazionale di metodi phMRI nell'ambito di diverse aree delle neuroscienze e della psico-farmacologia. La combinazione di phMRI e tecniche di manipolazione genetica avanzate definisce una nuova, potente piattaforma tecnologica per lo studio delle basi circuitali del comportamento in animali da laboratorio.

LIST OF ABBREVIATIONS

5-HT: 5-hydroxytryptamine

Acb: nucleus accumbens

ANOVA: analysis of variance

AMPA: alpha-amino-3-hydroxy-5-methyl-4-isoxazolepropionic acid

BOLD: blood oxygen level dependent

CBF: cerebral blood flow

CBV: cerebral blood volume

CRF: corticotropine releasing factor

DTI: diffusion tensor imaging

EPI: echo-planar imaging

EEG: electro-encephalogram

FDG: ^{18}F-fluoro-deoxy-glucose

fMRI: functional magnetic resonance imaging

GABA: γ-aminobutyric acid

GlyT-1: glycine transporter type-I

mCPP: 1-(m-chlorophenyl)piperazine

mPFC: medial pre-frontal cortex

MEG: magneto-encephalography

MRI: magnetic resonance imaging

nAChR: nicotinic acetylcholine receptors

NK1: neurokinin 1 (NK1)

NMDAR: N-methyl-D-aspartate receptor

PCP: phencyclidine

PET: positron emitting tomography

phMRI: pharmacological magnetic resonance imaging

rCBV: relative cerebral blood volume

VTA: ventral tegmental area

5-HT: 5-hydroxytryptamine

Acb: nucleus accumbens

BOLD: blood oxygen level dependent

CBF: cerebral blood flow

CBV: cerebral blood volume

CRF: corticotropine releasing factor

EEG: electro-encephalogram

FDG: ^{18}F-fluoro-deoxy-glucose

fMRI: functional magnetic resonance imaging

GABA: γ-aminobutyric acid

GlyT-1: glycine transporter type-I

mCPP: 1-(m-chlorophenyl)piperazine

mPFC: medial pre-frontal cortex

MABP: mean arterial blood pressure

MEG: magneto-encephalography

MRI: magnetic resonance imaging

nAChR: nicotinic acetylcholine receptors

NK1: neurokinin 1 (NK1)

NMDAR: N-methyl-D-aspartate receptor

PCP: phencyclidine,

PET: positron emitting tomography

phMRI: pharmacological magnetic resonance imaging

rCBV: relative cerebral blood volume

RARE: rapid acquisition with relaxation enhancement

SEM: standard error of the mean

TE: echo time

TR: repetition time

VTA: ventral tegmental area

1 - INTRODUCTION

1.1 Background

Since its inception in the 1970s, Magnetic Resonance Imaging (MRI) has rapidly become a widely applied radiological technique owing to its superior soft-tissue contrast, absence of ionizing radiation exposure, and versatility. Multiple combinations of pulse sequences, acquisition parameters and exogenous contrast agents can be used to sensitize image contrast to different tissue characteristics and physiological parameters, thus enabling a variety of clinical applications to musculoskeletal, oncological, cardiovascular and neurological imaging. The discovery by Ogawa and colleagues (Ogawa et al. 1990a) that brain MR Images are sensitive to changes in tissue perfusion and blood oxygenation levels paved the way for the development of non-invasive MR imaging of brain function, dubbed functional MRI (fMRI). Since then, the inherent advantages of fMRI over other functional imaging methods (e.g. water PET, EEG, MEG etc) in terms of spatio-temporal resolution and non-invasiveness have determined the prevalence of this technique in functional neuroimaging. Following the first pioneering studies, fMRI has been extensively applied to study the neuronal circuits engaged by neuropsychological paradigms in the healthy human brain, and has brought about considerable progress in our understanding of the brain functional architecture. Likewise, functional imaging methods have provided novel tools to investigate the neurobiological substrates of psychiatric and neurological illnesses.

Although primarily developed for human investigations, there exists significant scope for the application of fMRI in preclinical species. Animal fMRI studies may be employed to understand and demonstrate the construct-validity of disease models, thus improving their relevance to the human condition and their predictivity. Moreover, the combination of functional MRI with more invasive techniques in preclinical species may be useful to understand the physiological basis of the fMRI responses, and to validate the imaging endpoint for clinical investigation. Last but not least, animal models may provide useful tools to test the effects of putative medicines on the activity of specific brain circuits thought to be implicated in aspects of the human disease prior to proceeding to more complex and expensive clinical trials, thus expediting the drug-discovery process. Hence, the translational potential of a non-invasive imaging technique like fMRI is attractive for both basic and applied brain research.

However, a number of constraints make the application of fMRI methods to animal models, and particularly to rodents, less than straightforward. In particular, the use of anaesthesia to prevent motion artefacts and ensure animal restraint strongly limits the repertoire of stimulation paradigms that can be used under constrained experimental conditions of an fMRI experiment. As a result, most fMRI research in rodents has been reduced to the employment of basic somato-sensory stimulation paradigms, thus greatly limiting the translational potential of the technique. This aspect highlights the need to develop refined fMRI paradigms that could serve as a translation al bridge between clinical and preclinical research.

1.2 The Scope of this Thesis

An interesting approach to broaden the fMRI stimulation repertoire in laboratory animals has been dubbed “pharmacological MRI” (phMRI) and relies on the use of fMRI to map spatio-temporal patterns of brain activity induced by psychoactive drugs (Leslie and James 2000). In this context, acute drug administration serves as a probe to stimulate or inhibit activity in neuronal circuits, or to study the modulatory effects of behavioural pre-conditioning, pharmacological pre-treatment or genetic background on drug-induced patterns of activation. Originally developed to describe psycho-pharmacological action at a systems level, the main merits of phMRI lie in its ability to elicit robust and reliable fMRI signals even under anaesthesia and to enable selective stimulation of different neurotransmitter systems, thus providing a means to study the neurochemical basis of fMRI responses and the corresponding circuitry engaged.

Building upon the homology between brain circuits in humans and laboratory animals and the exquisite spatio-temporal resolution of MRI, in the research that follows we have developed refined phMRI approaches that significantly expand the scope of application of preclinical fMRI both as a translational technique, when applied to clinically-relevant disease models, and more generally as a versatile platform for the pre-clinical investigation of brain activity and its functional topology with respect to different behavioural, pharmacological or genetic preconditioning states.

As a first example of significant-translational value, we have developed a phMRI assay to map the circuitry activated by NMDAR antagonists in the rat (Section 4.1). These compounds (i.e. ketamine and PCP) are widely exploited pre-clinically and more recently in clinical research to model schizophrenia symptoms and to provide experimental models that may prove useful in the development of novel treatments for the human disorder. We have also investigated the neuro-chemical determinants of the functional cascade produced by these drugs by using current and future anti-psychotic mechanisms.

Moreover, in an attempt to further improve the translational scope of phMRI, we have developed a multi-parametric phMRI-based approach to investigate multiple facets of basal and reactive brain function in preclinical models of psychiatric disorders. We have implemented the approach to study brain function in a rat model of cocaine self-administration, a behavioural model of established face- and construct-validity and high translational significance in the research of cocaine-addiction (Section 4.2).

Furthermore, when combined with advanced neuro-genetic targeting strategies (i.e. pharmacogenetic or optogenetic methods), the preclinical implementation of f/phMRI can define a novel investigational platform to establish direct correlations between circuit and behaviour in living animals. By using genetically engineered mouse lines produce by Dr. Gross (EMBL Monetrotondo) and refined phMRI methods, we have provided a first compelling demonstration of the potential of this approach by unravelling the cellular and circuital basis of complex behavioural responses like those elicited by fearful and aversive stimuli (Section 4.3).

Finally, the phMRI approach has proven a powerful tool to explore functional connectivity in rodents, and to map a variety of different neurotransmitter pathways by performing measures of correlated phMRI responses in spatially remote brain areas. This has provided a useful playground to explore novel statistical methods of analysis of functional connectivity represented in terms of complex networks (Section 4.4).

1.3 Main Contributions

The main contributions of this work can be divided in methodological and neurofunctional. Methodological contributions include:

i. Development of high spatial resolution methods to map brain function in the rat and its modulation by pharmacological or behavioural pre-conditioning
ii. Implementation of measures of correlated phMRI responses as an index of functional connectivity in the rat and in transgenic mice
iii. Development of a robust multiparametric phMRI protocol for the assessment of multiple facets of basal and evoked brain function in rodent disease model
iv. Development of high-resolution phMRI protocol to map evoked brain function in transgenic mice
v. Contribution to the implementation of complex networks approaches to describe the functional topology of rat and mouse brain

Neuro-functional contributions include

i. Identification of a phMRI-based translational paradigm to map and investigate the circuitry acutely activated by psychotogenic doses of NMDAr antagonists
ii. Definition of major neuro-chemical determinants of NMDAr antagonist-induced functional response in the rat brain
iii. Identification of the site of action and neural circuitry modulated by current and novel anti-psychotic mechanisms
iv. Identification of altered basal and evoked functional states mimicking clinical neuroimaging findings in a widely-employed rat model of cocaine addiction
v. Identification of the cellular and circuital determinants of passive and active behavioural response to aversive stimuli in the mouse (in collaboration with Dr. C. Gross, EMBL, Monterotondo).

All the methodological and neurofunctional contributions have been published in the form of peer-reviewed manuscripts or conference communications, with the exception of the cocaine work (Appendix 5) which is currently under review (see appendixes and publication list).

The structure of the present thesis comprises a first theoretical introduction to the principles of MRI (Chapter 2), followed by a description of the neurovascular foundations of the haemodynamic response and its measurements in fMRI and phMRI paradigms (Chapter 3). The results of the experimental work are described in the form of a general outline in Chapter 4, followed by the original manuscripts (appendixes 1-7).

2 - BASIC PRINCIPLES OF MAGNETIC RESONANCE IMAGING

2.1 Nuclear Magnetic Resonance (NMR)

The phenomenon of Nuclear Magnetic Resonance was first described by Edward Purcell and Felix Bloch in 1946. The discovery, for which they received the Nobel prize in 1952, led to the rapid diffusion of NMR as a powerful analytical tool for the investigation of molecular structure and chemical composition. Approximately two decades later Paul Lauterbur and Mansfield demonstrated the use of NMR to obtain spatially resolved images of the distribution of proton spins in objects, a discovery that paved the way to the development of MRI. Since then, the technique has been considerably refined and MRI is now routinely employed in numerous areas of science and it has become the most common diagnostic imaging procedure in hospitals. The prevalence of MRI, together with recent breakthroughs in hardware design, have been instrumental in determining the explosion of interest in the development of fMRI methods. As a testimony of the invaluable contribution of MRI as a diagnostic and functional tool in biomedicine, Lauterbur and Mansfield were jointly awarded the 2003 Nobel prize in physiology and medicine.

This chapter briefly describes the theoretical foundations of nuclear magnetic resonance and magnetic resonance imaging. The chapter serves as an outline of the basic principles of NMR and MRI. A more detailed description can be found in specialized texts on the subject (e.g. McRobbie et al. 2007; Gadian 2004; Huettel et al. 2004).

2.2 Quantum Mechanical description of NMR

The quantum mechanical description of atoms and molecules, as originally formulated by Dirac in 1930, accurately describes fundamental properties of atomic nuclei and the way these interact with radiation. Central to the description of NMR phenomena are the concepts of *nuclear spin angular momentum* and *nuclear spin magnetic momentum*.

The *spin angular momentum* of an atom or nucleus is a vector quantity whose total magnitude and orientation relative to some external axis are restricted to discrete values, specified by a quantum number *I*. Expressed in quanto-mechanical terms, this relationship states that the nuclear wave function (ψ) is always found to be an eigenfunction of the operator (*L*) corresponding to the square of the angular momentum

$$L^2\psi = I(I+1)\frac{h^2}{4\pi^2}\psi \qquad (2.1)$$

where *h is* the Planck constant. The quantum number *I*, often called "spin of the nucleus" may only have integral or half-integral values as follows: a) *I* is integral for nuclei with even mass number b) *I* is zero for nuclei with even number of both neutrons and protons c) *I* is half-integral (½) for nuclei with odd mass number (i.e ^{1}H, ^{13}C, and ^{31}P). The latter class of nuclei is of paramount importance for NMR, as these are the nuclei that tend to have the most favourable NMR characteristics. As far as medical applications of NMR are concerned, the proton (^{1}H) is by far the nucleus of most interest, because of its high natural abundance (99.98%) and high concentration (75-90%) as part of water or lipids in most living systems. As a consequence, the vast majority of the radiological and functional applications of MRI are primarily based on the detection of signal from water protons. However additional nuclei may play a role in specific diagnostic or investigational NMR-based techniques. These include ^{13}C, whose low abundance relative to ^{12}C makes it suitable for tracer studies, or the naturally occurring phosphorous nucleus ^{31}P, which is widely used as a non-invasive marker of tissue metabolism in living systems.

Equation 2.1 states that the operation on ψ by the angular momentum operator *L* gives solutions only for certain values of the angular momentum, the magnitude of which is given by

$$|\mathbf{P}| = \hbar\sqrt{I(I+1)} \qquad (2.2)$$

where $\hbar$ is equal to $h/2\pi$. Quantum mechanics also dictates that the orientation of the vector **P** relative to any given direction is also restricted. In the presence of a magnetic field applied along the z axis, it turns out that the possible values of the z-components of the angular momentum are given by

$$P_z = m\hbar \qquad (2.3)$$

where *m* may have any of the 2 *I* + *I* values, *I, I*-1*, I*-2 ... – *I*, and so for a nucleus of spin ½, m can be +½, or -½. Therefore, for such a nucleus

$$P_z = \pm ½\ \hbar \qquad (2.4)$$

This relationship states that the angular momentum vector can rotate about the z-axis, in that its components in the x or y directions are not quantized. Using Dirac's notation, the eigenfunction describing the spin state of the proton nucleus can be written as $|+½\rangle$ or $|-½\rangle$ and since in quantum mechanics every physical observable has an associated operator, two eigenvalue equations can be written to describe the observation of the spin state as

$$I_z|+½\rangle = +½\hbar|+½\rangle \qquad (2.5)$$

$$I_z|-½\rangle = -½\hbar|-½\rangle \qquad (2.6)$$

where I_z is the operator describing measurement of the angular momentum along the z axis.

In order to measure the energy of the spin system, a Hamiltonian operator needs to be built. Since nuclei by virtue of their electrical charge have magnetic properties, the form of the Hamiltonian can be derived from classical electromagnetism for the energy of a magnetic dipole moment placed in a magnetic field.

The magnetic moment $\boldsymbol{\mu}$ of a nucleus is found to be proportional to its angular momentum

$$\boldsymbol{\mu} = \gamma \mathbf{P} \tag{2.7}$$

with the constant of proportionality, γ, being called the gyromagnetic ratio. The gyromagnetic ratio is a property of the particular nucleus which cannot be predicted from classical physics, and has a value of 2.67 x 10^8 rad/T for the proton. It should be noted that, although for most nuclei γ is positive, for some, such as ^{15}N, γ is negative.

If a static magnetic field **B** is applied along the z-axis, the nucleus acquires energy *E* as a result of the interaction between the magnetic field along z (B_z) and the nuclear magnetic moment $\boldsymbol{\mu}$

$$E = -\mu_z B_z \tag{2.8}$$

where μ_z is the component of the magnetic dipole moment of the nucleus along the z-axis. By combining equations 2.4, 2.7 and 2.8 a Hamiltonian (known as Zeeman Hamiltonian) can be defined as

$$H = -\hbar \gamma B_z I_z \tag{2.9}$$

From this relationship the energy of the eigenstate m_I can be derived as follows

$$\begin{aligned} H|m_I\rangle &= -\hbar \gamma B_z I_z |m_I\rangle \\ H|m_I\rangle &= -\hbar \gamma B_z m_I |m_I\rangle \\ E &= -\hbar \gamma B_z m_I \end{aligned} \tag{2.10}$$

So for a proton with m_I=±½, a transition between the two states represents a change in energy

$$\Delta E = \hbar \gamma B_z \tag{2.11}$$

$$\Delta E = \frac{h}{2\pi} \gamma B_z \tag{2.12}$$

This is called the *Zeeman splitting*, and these two states are given a variety of labels, but most commonly referred to as 'spin up', and 'spin down', with the spin-down state having a higher energy than the spin-up state. Transitions between the two

adjacent states can be induced by absorption or emission of a photon of frequency ν_0 such that

$$\Delta \mathrm{E} = \hbar \gamma B_z = h\nu_0 \tag{2.13}$$

$$\nu_0 = \frac{\gamma}{2\pi} B_z \tag{2.14}$$

Expressing the frequency in angular terms gives the *Larmor equation* which underpins the whole of NMR as it expresses the resonance conditions for a nucleus of gyromagnetic ratio γ:

$$\omega = \gamma B_0 \tag{2.15}$$

The characteristic frequency, ω, is often termed as the *Larmor frequency*. The magnetic field, labelled B_0, is still assumed to be applied along the z axis, and is now subscripted with a '0' to distinguish it from the applied radio frequency field which will be introduced later.

This description of the quantum mechanical behaviour of an atomic nucleus leads to the way NMR is performed. Transitions between the two energy states, spin-up and spin-down, can occur by absorption or emission of electromagnetic radiation of frequency given by the Larmor equation. This frequency depends, for a given species of nuclei, purely on the applied magnetic field. It is the strength of the field experienced by the nucleus that enables structure to be determined in spectroscopy experiments, and spatial encoding in imaging experiments. However, in a real system there is not just one nucleus in isolation, but many nuclei all of which could occupy a particular spin state. This means that the theory must be extended to consider an ensemble of spins. To do this, a single eigenstate ψ, which is a linear combination of the possible spin states for a single nucleus is defined

$$\left|\Psi\right\rangle = \sum_{m_I} a_{m_I} \left|m_I\right\rangle \tag{2.16}$$

where a_{m_I} are the coefficients that determine the superposition state. So for the case of a proton with two spin states ± ½:

$$\left|\Psi\right\rangle = a_{+½}\left|+½\right\rangle + a_{-½}\left|-½\right\rangle \tag{2.17}$$

Note that here, to simplify operations, the factor $\hbar$ has been removed from the eigenvalues of the operator I_z, which corresponds to expressing the hamiltonian in frequency units rather than in joules.

When making a measurement on such a system, the expectation value of the operation on this superposition of states is

$$\left\langle I_z \right\rangle = \left\langle \Psi \middle| I_z \middle| \Psi \right\rangle = \frac{1}{2}\hbar\left(a_{+½}a^*_{+½} - a_{-½}a^*_{-½}\right) \tag{2.18}$$

where $a^*_{+½}$ and $a^*_{-½}$ represents the complex conjugate of the coefficients $a_{+½}$ and $a_{-½}$, respectively. In an ensemble of *N* spins, the total z-magnetization is the sum of the z-components of the magnetic moment of each spin (eq. 2.18), multiplied by gamma

$$M_z = \frac{1}{2}\gamma\hbar N\overline{\left(a_{+½}a^*_{+½} - a_{-½}a^*_{-½}\right)} \tag{2.19}$$

where the line indicates an ensamble average. Note that to preserve correct dimensionality here the factor $\hbar$ has been reintroduced. Since the probability of finding a particular spin in the level $|+½\rangle$ is $a_{+½}a^*_{+½}$, by adding up these probabilities for all the spins in the sample it is possible to find the number $n_{+½}$ of spins which, on measurement are in the level +½. This number can be interpreted as the population of the level +½.

$$n_{+½} = N\overline{a_{+½}a^*_{+½}} \tag{2.20}$$

Similar considerations can be done for the level -½

$$n_{-½} = N\overline{a_{-½}a^*_{-½}} \tag{2.21}$$

These relationships allow to express bulk magnetization as a quantity proportional to the population difference between states

$$M_z = \frac{1}{2}\hbar\gamma(n_{+½} - n_{-½}) \tag{2.22}$$

At equilibrium, these populations are predicted by the Boltzmann distribution

$$n_{+½} = \frac{1}{2}Ne^{-\frac{E_{+½}}{K_BT}} \quad \text{and} \quad n_{-½} = \frac{1}{2}Ne^{-\frac{E_{-½}}{K_BT}} \tag{2.23}$$

where $E_{+½}$ and $E_{-½}$ are the energies of the two levels, K_B is the Boltzmann constant and *T* the temperature of the system. As for gamma positive the +½ state has lower energy, the ratio of the populations of the two energy states from Boltzman statistics is

$$\frac{n_{-½}}{n_{+½}} = e^{-\frac{\Delta E}{K_BT}} = e^{-\frac{\gamma\hbar B_0}{K_BT}} \simeq 1 - \frac{\gamma\hbar B_0}{K_BT} \tag{2.24}$$

provided $K_BT >> \gamma\hbar B_0$.

Combining equations 2.22 and 2.24, the bulk magnetisation of the *N* spin ensemble becomes

$$M_z \approx N \frac{\gamma^2 \hbar^2 B_0}{4 K_B T} \tag{2.25}$$

This equation is central to the theory of MRI, as it states that the use of stronger magnetic field strengths results in an increased the magnitude of bulk magnetisation and hence the theoretical MR signal produced by the spin ensemble. Moreover, the possibility to describe the behaviour of all the spins in the system in terms of magnetisation allows a transfer from a quantum mechanical to a classical description of NMR. The advantage of the classical description is that it gives a simple and intuitive picture of NMR experiments and the effect of RF pulses in MRI.

2.3 Classical description of NMR

2.3.1 Spin precession

According to the classical description of NMR, a nuclear spin can be visualised as a small sphere of distributed positive charge that rotates at high speed about its axis. Because of its rotation, it produces a current that in turn generates a small magnetic field. According to this conceptualisation, if nuclei are regarded as tiny rotating bar magnets possessing angular momentum **P**, it is possible to show using classical physics that they will precess about a static magnetic field $\mathbf{B_0}$ with a characteristic angular frequency as a consequence of the torque $\boldsymbol{\tau}$ experienced.

The magnitude of the torque experienced when a nucleus moves at some angle θ to the magnetic field $\mathbf{B_0}$ will be only determined by the component of the magnetic moment vector perpendicular to the static field $\tau = \mu \sin\theta B_0$ or, in vector form

$$\boldsymbol{\tau} = \boldsymbol{\mu} \times \mathbf{B}_0 \qquad (2.26)$$

As the torque defines the change of angular momentum over time, eq. 2.26 can be rewritten as

$$\boldsymbol{\tau} = \frac{d\mathbf{P}}{dt} = \boldsymbol{\mu} \times \mathbf{B}_0$$

or (eq. 2.7)

$$\frac{d\boldsymbol{\mu}}{dt} = \gamma(\boldsymbol{\mu} \times \mathbf{B}_0) \qquad (2.27)$$

These equations state that the exposure to a static magnetic field $\mathbf{B_0}$ induces a torque that changes the angular momentum and magnetic moment of the spin over time. Breaking down the magnetic moment $\boldsymbol{\mu}$ into scalar components along perpendicular dimensions, eq. 2.27 becomes

$$\frac{d\mu_x}{dt} = \gamma\mu_y B_0 \qquad \frac{d\mu_y}{dt} = \gamma\mu_x B_0 \qquad \frac{d\mu_z}{dt} = 0 \qquad (2.28)$$

which has solution

$$\boldsymbol{\mu}(t) = (\mu_x \cos\omega t + \mu_y \sin\omega t)\mathbf{x} + (\mu_y \cos\omega t + \mu_x \sin\omega t)\mathbf{y} + \mu_z\mathbf{z} \qquad (2.29)$$

where **x**, **y** and **z** are unit vectors along three spatial dimensions, and $\omega = \gamma B_0$. This equation specifies that the magnetic moment precesses at an angular velocity ω that is given by the same frequency of an emitted or absorbed electromagnetic pulse during spin state changes derived in the quantum mechanical description (eq. 2.15) thus unifying the classical and quanto-mechanic perspectives of NMR phenomena.

This unification allows to visualize the quantum behaviour of spins using classical mechanics modelling to derive basic equations for MR signal generations.

2.3.2 Measuring the Magnetic Moment of Spins in Bulk Matter

In NMR experiments, spin ensambles containing a large number (typically 10^{18} or more) of nuclei are typically studied. These "nuclear magnets" all precess about the static field $\mathbf{B_0}$. However, as there is no preferred orientation in the plane perpendicular to $\mathbf{B_0}$ (commonly described as *xy*-plane) the net component of magnetic moment in the *xy*-plane is zero. There is however a net magnetisation along the z-axis as a result of the slight prevalence of nuclei oriented with the field, a phenomenon that in classical terms can be described as vector sum of the μ_z components of eq. 2.29, and in quanto-mechanical terms corresponds to bulk magnetisation (M_z) of the *N* spin ensemble specified by eq. 2.25. In other words, while the net magnetisation vector **M** initially points along the main magnetic field, its precession angle is 0° at equilibrium.

In order to measure the magnetisation of a sample exposed to static field $\mathbf{B_0}$, the vector **M** can be tilted towards or into the *xy*-plane (known as the transverse plane) and the corresponding NMR signal recorded using a detector (i.e a coil of wire) sensitive to magnetic fields in the transverse plane. This can be accomplished by means of appropriate radiofrequency (r.f.) pulses applied in the *xy*-plane, which cause the magnetization vector to precess around the main axis of the field, analogously to a single magnetic moment. The process is called *spin excitation*.

Central to the design of effective r.f. excitation pulses is the concept of resonance. The idea is to apply a time-varying small magnetic field along a transversal axis (i.e x-axis) but – crucially – to make this pulse resonant with the Larmor precession frequency. In MR scanners such oscillating magnetic field is commonly generated by feeding some RF power to the coil such to induce an oscillating current and magnetic field ($\mathbf{B_1}$) at the same frequency as the spin precession. This field is called the *radiofrequency field* or *r.f. field.*

Felix Bloch derived a set of differential equation based on the classical model of NMR that describe the changes in magnetisation upon the application of an excitation pulse. In analogy with single spin precession reported above (eq. 2.27), the net magnetisation vector M, when placed in a magnetic field **B** that tips it away from its equilibrium position, will experience a torque and start a precession motion described by

$$\frac{d\mathbf{M}}{dt} = \gamma \mathbf{M} \times \mathbf{B} \; = \gamma[(M_y B_z - M_z B_y)\mathbf{x} + (M_z B_x - M_x B_z)\mathbf{y} + (M_x B_y - M_y B_x)\mathbf{z}] \qquad (2.30)$$

Here the torque on the net magnetisation depends upon the total magnetic field **B** experienced by the spin system, which includes a static field along *z* ($B_z=B_0$) and the field ($\mathbf{B_1}$) rotating in the transverse plane produced by the excitation pulse. If only the

circularly polarised component of $\mathbf{B_1}$ rotating in the same direction as the precessing magnetisation vector is considered

$$\mathbf{B}_1(t) = (B_1 \cos \omega_0 t)\mathbf{x} - (B_1 y \sin \omega_0 t)\mathbf{y} \tag{2.31}$$

equation 2.30 can be broken down as follows

$$\begin{aligned}
\frac{dM_x}{dt} &= \gamma[M_y B_0 + M_z B_1 \sin \omega_0 t] \\
\frac{dM_y}{dt} &= \gamma[M_z B_1 \cos \omega_0 t - M_x B_0] \\
\frac{dM_z}{dt} &= \gamma[-M_x B_1 \sin \omega_0 t - M_y B_1 \cos \omega_0 t]
\end{aligned} \tag{2.32}$$

If a starting condition $\mathbf{M}(0)=M_0\mathbf{k}$ is defined then the solutions for **M** are

$$\begin{aligned}
M_x(t) &= M_0 \sin \omega_1 t \sin \omega_0 t \\
M_y(t) &= M_0 \sin \omega_1 t \cos \omega_0 t \\
M_z(t) &= M_0 \cos \omega_1 t
\end{aligned} \tag{2.32}$$

where $\omega_1 = \gamma B_1$. This implies that by applying an oscillating magnetic field of frequency ω_0, the net magnetisation vector simultaneously precesses about $\mathbf{B_0}$ at ω_0 and $\mathbf{B_1}$ at ω_1, a spiralling motion known as "nutation" (Figure 2.1).

At this point it is convenient to introduce a new frame of reference for viewing the evolution of the magnetisation vector, the so-called "rotating frame", which rotates about the z-axis at frequency ω_0. If in the rotating frame an axis system (x',y',z) is defined, then equation 2.30 can be re-written as

$$\left(\frac{d\mathbf{M}}{dt}\right)_{rot} = \left(\frac{d\mathbf{M}}{dt}\right)_{fixed} - \boldsymbol{\omega} \times \mathbf{M} = \gamma \mathbf{M} \times \mathbf{B} - \boldsymbol{\omega} \times \mathbf{M} = \gamma \mathbf{M} \times \mathbf{B} - \gamma \mathbf{M} \times \frac{\boldsymbol{\omega}}{\gamma} \tag{2.33}$$

where $\boldsymbol{\omega}$ is the rotational frequency of the rotating frame. The equation can thus be re-arranged to the following form:

$$\left(\frac{d\mathbf{M}}{dt}\right)_{rot} = \gamma \mathbf{M} \times \left(\mathbf{B} + \frac{\boldsymbol{\omega}}{\gamma}\right) = \gamma \mathbf{M} \times \mathbf{B}_{eff} \tag{2.34}$$

where $\mathbf{B}_{eff} = \left(B_0 - \frac{\omega}{\gamma}\right)\mathbf{z} + B_1\mathbf{x}'$ (2.35)

and (**x'**, **y'**, **z**) are unit vectors in the (x',y',z) directions. The result of solving these equations is a magnetisation vector which precesses about $\mathbf{B}_{eff}$, which is the effective magnetic field experienced by the spins. Importantly, if the applied $\mathbf{B_1}$ field is in

resonance (i.e. $B_0 = \frac{\omega}{\gamma}$), the magnetisation vector will precess in the rotating frame about the x'-axis at a frequency $\omega_1 = \gamma B_1$.

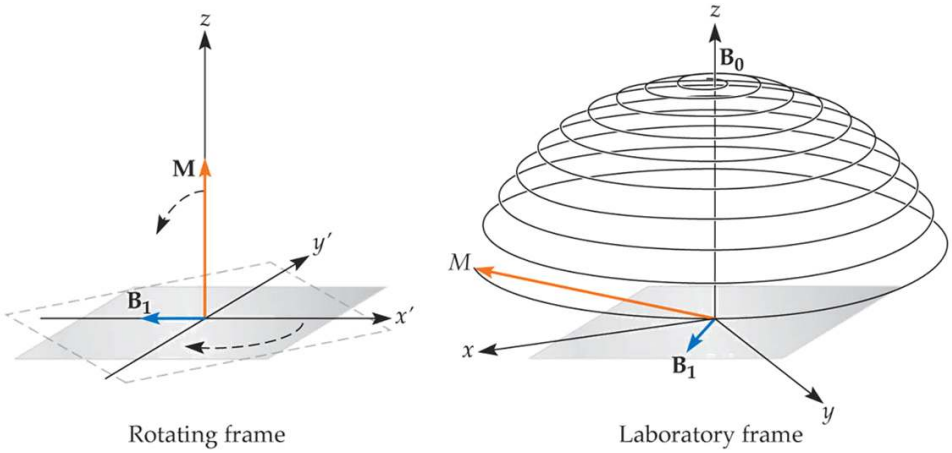

Figure 2.1

Spin nutation. Tipping the longitudinal magnetization into the transverse plane by a simple rotation in the rotating reference frame (A) results in a wobbling motion known as nutation in the laboratory frame (B). The r.f. energy is called B_1 because it behaves like a second magnetic field (adapted from Huettel et al. 2004).

The most common way to carry out an NMR experiment is to apply a short burst of resonant r.f. field. If the duration of this r.f. pulse is *t*, then the magnetisation will rotate by an angle

$$\alpha = \gamma B_1 t_p \qquad (2.36)$$

In a typical NMR experiment, a 90° pulse is applied to tip the magnetisation vector from the longitudinal plane to the transverse plane. The r.f. pulse has also the important effect of bringing all the spins into phase coherence. This means that they all point to the same position on the precession circle. Once in the transverse plane, the magnetisation precesses about the z-axis, and can produce NMR signal in the form of an oscillating current in a receiver coil that is placed in the transverse plane. The signal thus obtained is called Free Induction Decay (FID).

2.3.3 NMR Signal Relaxation

The NMR signal after the application of a resonant r.f. pulse does not last indefinitely but decays over time, generally within a few seconds, a phenomenon called relaxation. Two primary mechanisms contribute to the loss of signal: spin-lattice (or longitudinal) relaxation and spin-spin (or transversal) relaxation (Figure 2.2).

Spin-lattice relaxation involves exchange of energy between the spin system and its surroundings, and the rate at which equilibrium is restored is characterised by the spin-lattice relaxation time, T_1, in a new equation of motion for Mz

$$\frac{dM_z}{dt} = -\left(\frac{M_z - M_o}{T_1}\right) \quad (2.37)$$

The spins however do not only exchange energy with the surrounding lattice, but also among themselves. This is generally a faster process than spin-lattice relaxation, and is characterised by the spin-spin relaxation time, T_2, in the equations describing the evolution of M_x and M_y

$$\frac{dM_x}{dt} = -\frac{M_x}{T_2} \quad (2.38) \qquad \frac{dM_y}{dt} = -\frac{M_y}{T_2} \quad (2.39)$$

These relaxation processes constrain how much NMR signal can be acquired following a single r.f. excitation pulse. Equations 2.36, 2.37 and 2.38, when combined with the earlier equation of motion (eq. 2.30) form what are known as Bloch equations.

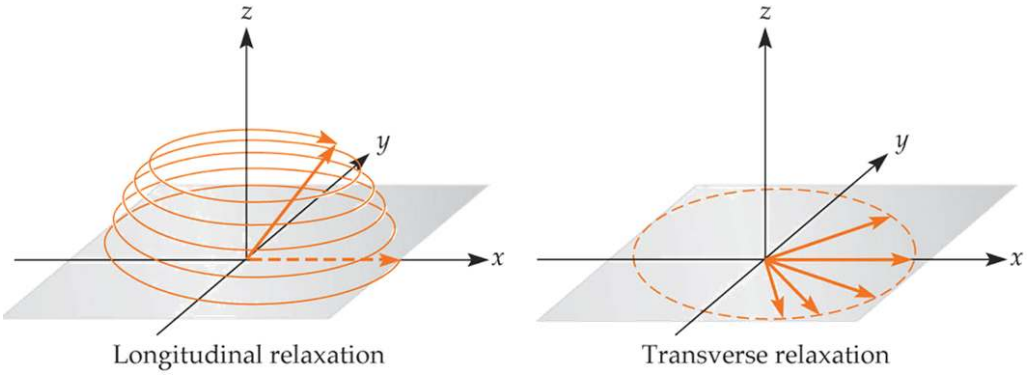

Figure 2.2
Left; longitudinal relaxation refers to the decay of magnetisation along the Z axis; Right; transverse relaxation refers to the decay of magnetisation on the xy plane (adapted from Huettel et al. 2004).

For a magnetic field including both a static ($B_z = B_0$) and a rotating resonant component on the transverse plane ($B_x = B_1 \cos \omega t$ and $B_y = B_1 \sin \omega t$)

$$\frac{dM_x}{dt} = \gamma(M_y B_0 + M_z B_1 \sin \omega t) - \frac{M_x}{T_2} \quad (2.40)$$

$$\frac{dM_y}{dt} = \gamma(M_x B_1 \cos \omega t - M_x B_0) - \frac{M_y}{T_2} \quad (2.41)$$

$$\frac{dM_z}{dt} = \gamma(M_x B_1 \sin \omega t + M_y B_1 \cos \omega t) - \left(\frac{M_z - M_o}{T_1}\right) \quad (2.42)$$

These equations provide the theoretical foundation for all NMR experiments and can be solved with appropriate limiting conditions. For example, immediately after the r.f. pulse is switched off ($B_1 = 0$), the solutions are

$$M_x(t) = \left[M_x(0)\cos\omega_0 t + M_y(0)\sin\omega_0 t \right] e^{-t/T_2} \quad (2.43)$$

$$M_y(t) = \left[M_y(0)\cos\omega_0 t - M_x(0)\sin\omega_0 t \right] e^{-t/T_2} \quad (2.44)$$

$$M_z(t) = M_z(0)e^{-t/T_1} + M_0\left(1 - e^{-t/T_1}\right) \quad (2.44)$$

For a s system at equilibrium, and a r.f. pulse of 90°, $M_x(0)=M_z(0)=0$ and $M_y(0)=M_0$ giving (in complex notation)

$$M_{xy}(t) = M_0 e^{i\omega_0 t} e^{-t/T_2} \quad (2.45)$$

$$M_z(t) = M_0\left(1 - e^{-t/T_1}\right) \quad (2.46)$$

These equations are of utmost importance for MRI: by determining the rate at which longitudinal and transversal magnetisation return at equilibrium state, the relaxation times T_1 and T_2 play a crucial role in defining image contrast, a consequence of the different relaxation rates exhibited by protons in different tissues and molecular milieus.

2.4 Magnetic Resonance Imaging (MRI)

2.4.1 Magnetic Field Gradients

As previously shown (Section 2.2), the Larmor equation is fundamental to the theory of magnetic resonance, as it describes the precession frequency of spins as a function of the local magnetic field strength. Since a measurement of the frequency of precession of magnetisation can give information on the field experienced by a group of spins, by manipulating the spatio-temporal variation of the field in a known way (i.e. via magnetic field gradients), this frequency information can be used to provide spatial information. Such use of spatial magnetic field gradients is necessary for measurement of spatial properties of a sample and lies at the basis of modern MRI techniques, in essence allowing NMR to become MRI.

After the spin excitation, the magnetic field **B** experienced by spins at a given location may be described as a linear combination of the static field $\mathbf{B}_0$ and direction-specific time-varying gradient fields **G** that may be introduced to modulate the field strength across the sample (Figure 2.3):

$$B(t) = B_0 + G_x(t)\,x + G_y(t)\,y + G_z(t)\,z \tag{2.47}$$

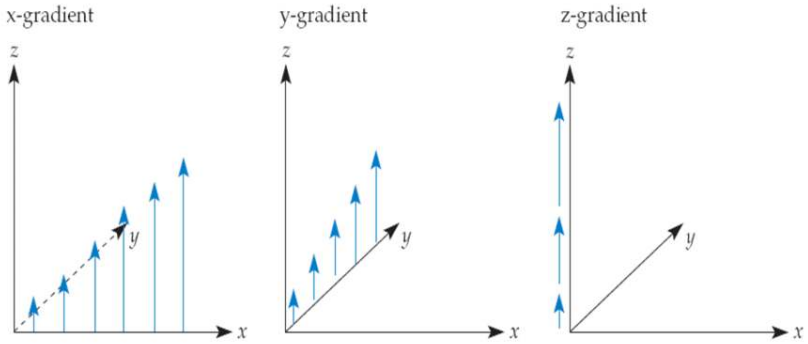

Figure 2.3
Magnetic field gradients change the strength (but not the direction) of the static magnetic field along different three-dimensional pathways in the image space.

Knowing that $\omega_0 = \gamma B_0$, and combining eq. 2.47 and 2.45 we obtain the following relationship that describes the evolution of transverse magnetisation in the presence of magnetic field gradients as a function of location and time:

$$M_{xy}(x,y,z,t) = M_{xy0}(x,y,z)\,e^{-t/T_2}\,e^{i\gamma B_0 t}\,e^{i\gamma\int_0^t (G_x(t)x + G_y(t)y + G_z(t)z)\,dt} \tag{2.48}$$

As the MRI signal ($S(t)$) is detected by using a single antenna (e.g. a volume coil), it reflects the sum of transverse magnetisations of all voxels within the excited sample:

$$S(t) = \iiint M_{xy}(x,y,z,t)\,dxdydz$$

Combining eq. 2.47 and 2.58 results in the following equation, known as MR signal equation as it reveals the relationship between the acquired signal and the properties of the object imaged:

$$S(t) = \iiint M_{xy0}(x,y,z)\, e^{-t/T_2} e^{i\omega_0 t} e^{i\gamma \int_0^t \left(G_x(t)x + G_y(t)y + G_z(t)z\right)dt}\, dxdydz \qquad (2.49)$$

Equation 2.49 can be simplified by removing the term $e^{i\omega_0 t}$ (as modern scanners demodulate the detected signal with the resonance frequency) and by ignoring the term e^{-t/T_2}, which only affects the magnitude but not the spatial location of the signal, giving this simplified version

$$S(t) = \iiint M_{xy0}(x,y,z)\, e^{i\gamma \int_0^t \left(G_x(t)x + G_y(t)y + G_z(t)z\right)dt}\, dxdydz \qquad (2.50)$$

which points out the profound importance of the gradient fields for encoding spatial information within an MR image. Equation 2.50 is in three-dimensional (3-D) form. However, 3-D MR imaging presents additional technical challenges and presents low tolerance to hardware imperfections; as a result, the vast majority of imaging modes relevant to fMRI and phMRI studies use two-dimensional (2-D) imaging sequences.

2.4.2 Slice Selection

In order to reduce the signal equation to two dimensions, variation over one spatial dimension is eliminated by separating the signal-acquisition process into two steps: 1) a particular slice within the total imaging volume is selected using a one-dimensional excitation pulse 2) a two-dimensional encoding scheme is used within the slice to resolve the spatial distribution of the spins.

Slice selection is accomplished by the application of a specially designed r.f excitation pulse in combination with a static magnetic field gradient along the slice selection axis (e.g. G_z). This results in the excitation of only those spins whose Larmor frequency, which is dictated by their position, is the same of the applied r.f. pulse. In order to obtain sharp-edeged pseudo-rectangular slices, sinc-modulated electromagnetic pulses are typically used, coupled to interleaved slice acquisition schemes are used to minimise off-resonance effects across adjacent slices.

For a selective pulse along the *z* direction, the magnetic field gradient introduces a position-dependent spread *f* in the Larmor frequency about the carrier frequency f_0 such that

$$\Delta f(z) = \frac{\gamma}{2\pi} z G_z \qquad (2.51)$$

If an amplitude modulated r.f. 90° pulse of form

$$B_1(t) = A(t)\cos(2\pi f_0 t) \qquad (2.52)$$

is applied, where A is the pulse envelope, and f_0 is the "carrier" frequency, recalling equation 2.36, the resultant flip angle will be (approximately)

$$\alpha(z) = \gamma \int A(t) e^{i2\pi \Delta f(t)} dt \qquad (2.53)$$

The integral is the Fourier transform of $A(t)$, i.e. $\alpha(z)=\gamma A(f)$. So the shape of the r.f pulse's spectrum determines the shape of the slice with regard to the selection direction (here z).

2.4.3 Reciprocal (k) Space

The slices chosen by the selection process are defined by their location, orientation and thickness. For a given location (x,y) within a slice centered at $z=z_0$, the total magnetisation summed along the z-direction for a thickness Δz is given by

$$M(x,y) = \int_{z_0-\frac{\Delta z}{2}}^{z_0+\frac{\Delta z}{2}} M_{xy0}(x,y,z)\, dz \qquad (2.54)$$

Thus, by selecting an imaging slice, and denoting the number of spins at a particular location as the spin density $\rho(x,y)$, eq. 2.50 can be reduced into a 2-D form

$$S(t) = \iint \rho(x,y) e^{i\gamma \int_0^t \left(G_x(\tau)x + G_y(\tau)y\right) d\tau} dxdy \qquad (2.55)$$

stating that the total signal recorded from a slice depends upon the magnetisation (i.e. spin density) at every location, with the phase of individual spins dependent upon the strength and duration (τ) gradient fields at that location.

In order to facilitate a better understanding of the relation between the MR signal and the object to be imaged, a different notation scheme known as *k-space* is introduced. This follows the definition of quantities $k_x(t)$ and $k_y(t)$ such that

$$k_x(t) = \frac{\gamma}{2\pi} \int_0^t G_x(\tau)\, d\tau \qquad (2.56)$$

$$k_y(t) = \frac{\gamma}{2\pi} \int_0^t G_y(\tau)\, d\tau \qquad (2.57)$$

These equations state that changes in *k*-space over time, are given by the time integral of gradient waveforms. By substituting these terms into eq. 2.55 the MR signal equation can be restated using *k*-space coordinates

$$S\left(k_x(t), k_y(t)\right) = \iint \rho(x,y) e^{i2\pi k_x(t)x} e^{i2\pi k_y(t)y} dxdy \qquad (2.58)$$

which highlights an inverse Fourier relationship between MR signal and spin density. Hence, the application of the gradients allows to encode the MR signal in terms of k-space spatial frequencies, and position (x,y) and spatial frequency (k_x,k_y) constitute a Fourier transform pair. The process by which raw MR signal as acquired in *k*-space form is converted via Fourier transforming into spatially informative images is called *image reconstruction*.

The consequences of Fourier MRI relate to the properties of the *k*-space. An important property of k-space is that its central portion, corresponding to the area covering lower spatial frequencies, is the one that determines the overall brightness and contrast of the final image whilst the outer regions (higher spatial frequencies) determine the fine detail.

2.4.4 Spatial Encoding

Once spins are excited within the desired slice, they must be spatially encoded so to resolve the spatial features of the imaged object. To this purpose, magnetic fields gradients that differ across two dimensions are applied to the sample, a process known as *frequency* and *phase encoding*. In k-space terms, this is equivalent to introducing sampling paths whose trajectories are determined by the shape and time of gradient functions. While different paths can be used to cover the k-space, in the majority of imaging sequences k-space is filled one line at a time, following a succession of individual excitation pulses. This process is exemplified in figure 2.4. During each excitation the combination of r.f. pulse and the G_z gradient selects the desired slice. Then the G_y gradient is turned on before the data acquisition period, so to induce a certain amount of phase offset before the activation of the G_x gradient, which changes the frequency of the spins as a function of their position. This corresponds to the movement of the effective location of data acquisition along the *y*- and *x*-directions, respectively. According to this scheme, gradients like G_y are typically referred to as *phase-encoding* gradients, while the G_x gradient is typically denoted as *frequency-encoding* gradient. An implication of this data acquisition scheme is that *k*-space is sampled in a discrete fashion: along the K_y axis, each line represents a separate amplitude of the G_y gradient. While the trajectory along the K_x direction is continuous, the MR signal is sampled digitally with a specific interval. After the *k*-space is filled, a 2-D inverse Fourier transform for conversion of raw data to image space $M(x,y)$. As a consequence of the reciprocal arrangement between the quantities *x* and k_x, the highest spatial frequency ($N\Delta k$) represents the smallest object detectable (i.e. the pixel size) and the largest object (i.e. the field of view, FOV) is determined by the smallest spatial frequency $1/\Delta k$).

It should be noted that different *k*-space collection schemes have been developed and entered clinical routine in MRI, including 3-D (where slice selection is replaced by additional phase encoding along *z* direction), spiral and radial and more. Their theoretical implementation can be easily extrapolated from that of 2-D imaging presented above.

2.4.5 MR Contrast Mechanisms and Pulse Sequences

As derived in previous sections, longitudinal and transverse magnetization decay according to the relaxation time constants T_1 and T_2 as described by equations 2.45 and 2.46. Two important factors that govern the time at which MR images are collected are the *repetition time* (TR) and *echo time* (TE). TR is the time interval between successive excitation pulses; in order to reduce acquisition times, oftentimes consecutive excitations occur at time intervals not long-enough to allow

full recovery of the longitudinal magnetization. TE can be defined as the time interval between excitation and data acquisition of the center of *k*-space. Under such conditions, the transverse magnetization is described as

$$M_{xy}(t) = M_0\left(1 - e^{-TR/T_1}\right)e^{-TE/T_2} \qquad (2.58)$$

illustrating that MR signal depends not only on the original magnetization (i.e. proton density), but also on the T_1 and T_2 relaxation constant of the tissue being imaged. As substantial differences exist between relaxation times of protons of different tissues, by manipulating TR and TE it is possible to alter the contrast (i.e. signal difference between any two types of tissue) and thus the appearance of the MR images, a feature that underscores the high versatility of MRI compared to other imaging modalities.

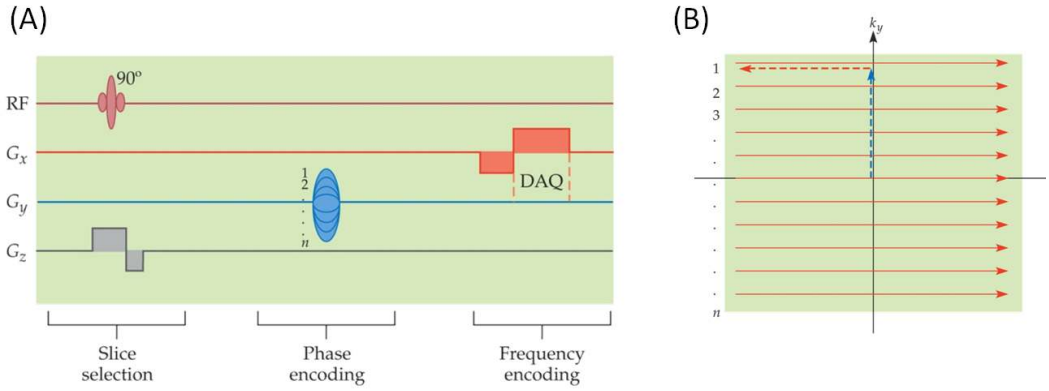

Figure 2.4

A typical two-dimensional pulse sequence. Shown in (A) are lines representing activity of the r.f. field and the three spatial gradients. The pulse sequence begins with a combined slice selection gradient and excitation pulse. The G_y gradient is used for selecting one line of k-space following each excitation pulse, while the G_x gradient is turned on during data acquisition (DAQ). The sequence depicted is a gradient echo sequence where each line of k-space is acquired following a separate excitation (adapted from Huettel et al. 2004).

One of the simplest forms of MR contrast is *proton-density* imaging, where contrast is determined by the sheer number of protons in the voxel. This can be achieved by minimising T_1 and T_2 contrast through the use of long TRs and short TEs. In order to reduce imaging time, small flip angles (<90°) are often used to achieve faster full longitudinal recovery.

A third important form of contrast is T_2 weighting. In *T_2-weighted* images the amount of signal loss depends upon the time between excitation and data acquisition (TE). This can be achieved by employing long TRs (TR>T1), and 'intermediate' T_2 so to maximize difference in transverse magnetization and minimize T_2-mediated signal loss.

Another common form of contrast is T_1 weighting. *T_1-weighted* images can be obtained choosing "intermediate" TRs such to allow longitudinal magnetization to recover, but at the same time maximizing tissue differences in T_1 relaxation rates. For

any two tissues that differ in T_1, there is an optimal TR valued that maximally differentiates between them. To have exclusive T_1-contrast, very short TE must be used ($TE<<T_2$).

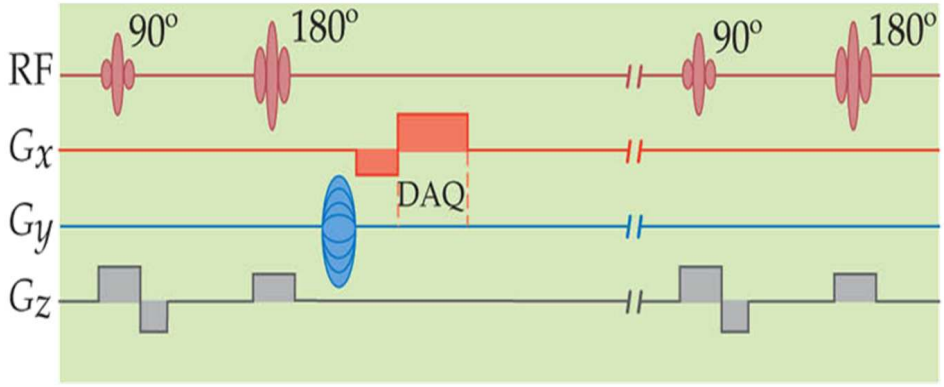

Figure 2.5

A typical two-dimensional spin-echo pulse sequence. In spin-echo imaging, the time between excitation and data acquisition (DAQ) is termed echo time (TE). In spin-echo imaging, a 180° refocusing pulse is used at TE/2 to restore phase coherence (adapted from Huettel et al. 2004).

Unlike proton-density or T_1-weighted images, whose generation can be obtained by employing multiple types of pulse sequences, T_2-weighted images can only be obtained using spin echo-based pulse sequences, because only this kind of sequences allow true spin-spin relaxation that does not depend on the field inhomogeneity. A typical spin-echo pulse sequence diagram is shown in Figure 2.5. Spin-echo sequences use a second 180° electromagnetic pulse, called refocusing pulse, to generate a "signal echo". Because the 180° echo pulse reverses the loss of phase coherence experienced by spins, spin-echo imaging is insensitive to static magnetic field inhomogeneities. This is not case of *gradient-echo* sequences (Figure 2.4). These sequences use only gradients to generate a signal echo in the centre of the *k*-space. In this case, the transverse relaxation is the sum of two independent components: spin-spin interaction (T_2) and changes in spin precession frequency due to local inhomogeneities in the magnetic field (governed by the fictitious constant T_2'). The combined effect of these two factors is described by the time constant T_2^*. Though T_2 and T_2^* are related ($1/T_2^*=1/T_2+1/T_2'$), the former constant is always greater than the latter. Like T_2 contrast, *T_2^*-weighted* images are generated using long TRs and medium TEs, with the necessary requirement of the use of a gradient-echo sequence, as refocusing pulses will eliminate field in homogeneity effects. On the other hand, both gradient- and spin-echo sequences can be used to generate proton density or T1-weighted images, provided TRs and TEs are appropriately chosen.

The discovery that blood-oxygen level dependent (BOLD) contrast could be used as an effective and sensitive marker of neuronal activation has led to a rapid increase the use of T_2^*-based imaging protocols in the field of brain functional MRI (fMRI). A more detailed discussion of the physiological basis of the BOLD effect and its implications for functional neuroimaging will be given in chapter 3.

2.4.6 Fast Spin Echo: the RARE Sequence

The use of fast spin-echo sequences plays a central role in the work presented here, given the numerous advantages of this imaging method over standard T_2*-based functional imaging methods, particularly in small animal research (see sections 3.5 and following).

The Rapid Acquisition with Relaxation Enhancement (RARE) sequence, also known as Fast spin echo (FSE) or turbo spin echo, is a spin-echo sequence originally described by Hennig (Hennig et al. 1986) which has gained wide popularity over the last years given its reduced acquisition time and remarkable experimental versatility. RARE imaging relies on the use of evenly spaced multiple refocusing pulses (commonly 180°) to form an echo train Figure 2.6. The extra echoes are thus used to acquire multiple lines of k-space data through the combined use of different phase encoding for each echo, a strategy called "segmented" imaging. The echo train length (or RARE factor) is the number of echoes in the spin echo train. The total scan time is thus proportional to TR, number of phase encoding steps, and number of signal averages, and is inversely proportional to the RARE factor. As a consequence, a sequence with a RARE factor of 8 (i.e. 8 echoes) will run 8 times faster than the equivalent conventional spin echo. In fast or segmented spin echo sequences like RARE, an *effective echo time* (TE_{eff}) is defined as the echo time that dominates the image contrast. This corresponds to the echo that coincides with the central parts of the k-space (see section 2.4.3). As a consequence, the order in which the phase encoding is applied is an important parameter that can be manipulated to affect contrast (Figure 2.7).

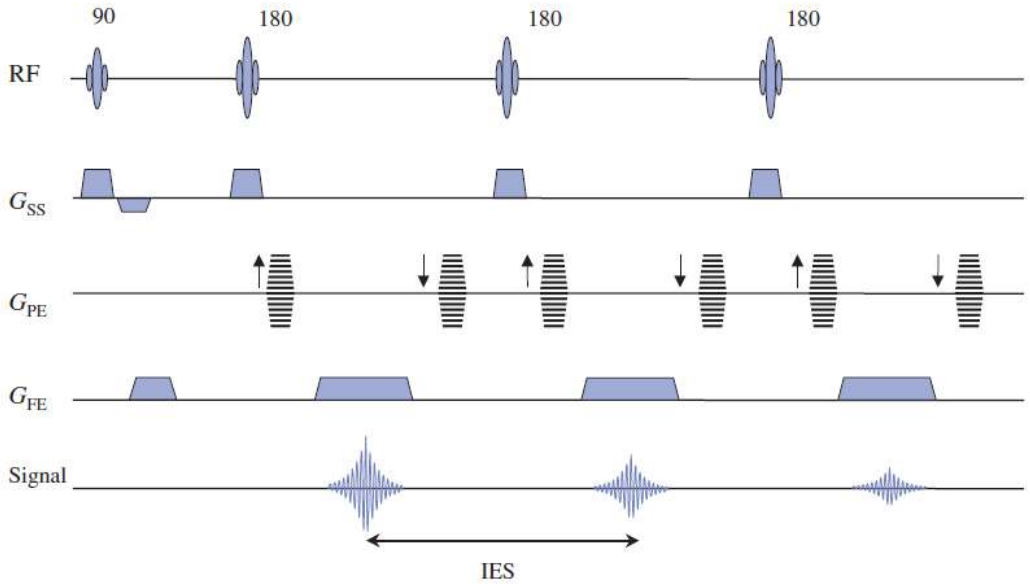

Figure 2.6
Fast spin-echo (RARE) sequence with an echo train length (RARE factor of 3). IES denotes inter echo spacing, i.e. the time between successive echoes (modified from McRobbie et al. 2007).

Although fast and versatile, the RARE sequence involves compromises, including recued slice number (slice interleaving within TR is limited by the long echo train),

complicated contrast behaviour (depending of phase encoding ordering, and relative echo time of low and high spatial frequencies) and higher RF exposure. The latter is measured in terms of the Specific Absorption Ratio (SAR) defined as the total power in watts (W) per kilogram of tissues, and is found to be proportional to the number of r.f. pulses in a given time, the square of B_0 and the square of the flip angle. As deposition of r.f. energy may lead to tissue heating, a careful control of SAR is of pivotal importance in *vivo* imaging. The RARE sequence is characterized by a high SAR per unit time, particularly on high filed scanners like the one used in the present work (4.7 T). One way of reducing this effect is to use smaller flip angles during the refocusing echo train. Since the discovery of the spin-echo effect by Hahn (Hahn 1950), a number of classical studies have shown that in evenly spaced-apart multi-echo sequences like RARE, a number of *coherence pathways* are formed and include contributions from "stimulated echoes", which can coincide with the spin echoes and combine with them to produce larger signals, as well as affect the image contrast by introducing a T_1-weighted component (reviewed by Hennig 1988). Under this conditions, it can be demonstrated that the signal rapidly reaches a pseudo-steady state of amplitude proportional to $sin(\vartheta/2)$ (Hennig 1988) . This phenomenon offers the opportunity of using reduced flip angles (i.e. 90° instead of 180°), producing a significant reduction of SAR (i.e. ¼ with a flip angle of 90°) with a moderate cost in terms of SNR (i.e. ≈30% since sin90°= 0.71).

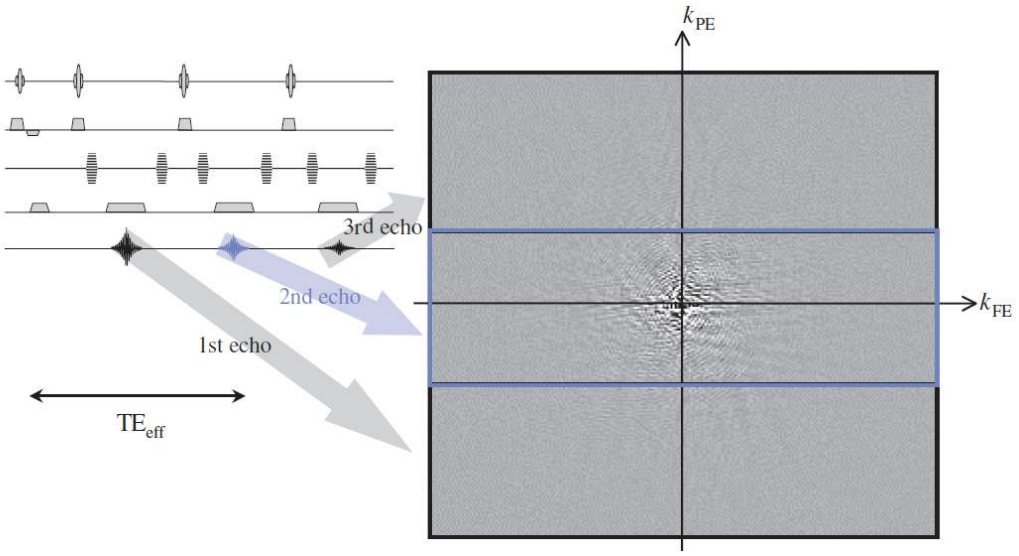

Figure 2.7

Data acquisition (k-space) filling for a three echo RARE sequence. The effective TE (TE_{eff}) is given by the time from the initial excitation to the second echo, which is the one the fill the central line of the k space. Each point k_{PE} and k_{FE} represents a spatial frequency in the image (modified from McRobbie et al. 2007).

Collectively, the possibility of acquiring fast high-resolution T_2-weighted spin echo images with controlled SAR using reduced flip angles make the RARE sequence an ideal tool for functional MRI imaging in small animals, particularly in experimental settings requiring the sequential acquisition of multiple images over long periods of time. These features, together with the reduced susceptibility artefacts exhibited by SE sequences vs. GE, led us to employ a RARE sequence with a 90° flip angle as

sequence of choice for all the functional imaging studies reported in this thesis. The use of fast spin-echo sequences for functional neuroimaging has also important practical and theoretical implications in terms of signal and vascular weighting of the functional signal measured, an aspect that is discussed in greater detail in section 3.5.

3 - FUNCTIONAL MRI OF THE BRAIN

In the previous chapter I have introduced the principles of magnetic resonance imaging and their application to create images of biological tissues reflecting different biophysical properties of proton nuclei. However, for MRI to become fMRI, it is necessary to sensitise images to biophysical processes that can be directly or indirectly related to neuronal activity. This was made possible by the discovery of the Blood Oxygen Level Dependent (BOLD) effect in the early 1990s by Ogawa and co-workers.

This chapter briefly describes the neuro-physiological foundations of the BOLD effect, and introduces to the measurement of individual haemodynamic parameters (i.e. CBV) as an advantageous alternative to BOLD fMRI in small animal functional imaging of the brain.

3.1 From Neuronal to Haemodynamic Activity

The fundamental element of information processing in the human brain is the neuron. Neuronal cells exert their signalling action through changes in cell membrane potential, leading to synaptic release of neurotransmitters. The change in membrane potential is the consequence of the movement of ions across neuronal membranes, a process that take the typical form of a “depolarisation” spread along neuronal axons known as *action potentials*. Action potentials sweep down the axon in a self-propagating manner until they reach the synapse, where they trigger neurotransmitter release.

The generation of action potentials does not in itself require energy, because the ions move along transmembrane concentration gradients. However, the restoration of ion concentration gradients in active neurons *does* require a significant energy supply, an aspect that underlies the large metabolic demand of the brain (Figure 3.1). By comparing the metabolic demand in normal and comates brains, it has been estimated that the restoration of transmembrane ionic gradients in neurons accounts for 75% of the energy expenditure in grey matter (Attwell and Laughlin 2001). As the brain is devoid of significant local energy stores, the primary metabolites (glucose and oxygen) required by active neurons are then directly supplied by the vascular system, and a tight coupling between neuronal activity and vascular delivery of glucose and oxygen ensures the metabolic demand of active neurons are met under a wide range of homeostatic conditions. The presence of tight neuro-metabolic and neurovascular coupling mechanism defines the fundamental physiological relationship underlying all forms of functional neuroimaging: measures of metabolic or vascular correlates of neuronal activity can be used to make inferences about the local functional state of the brain.

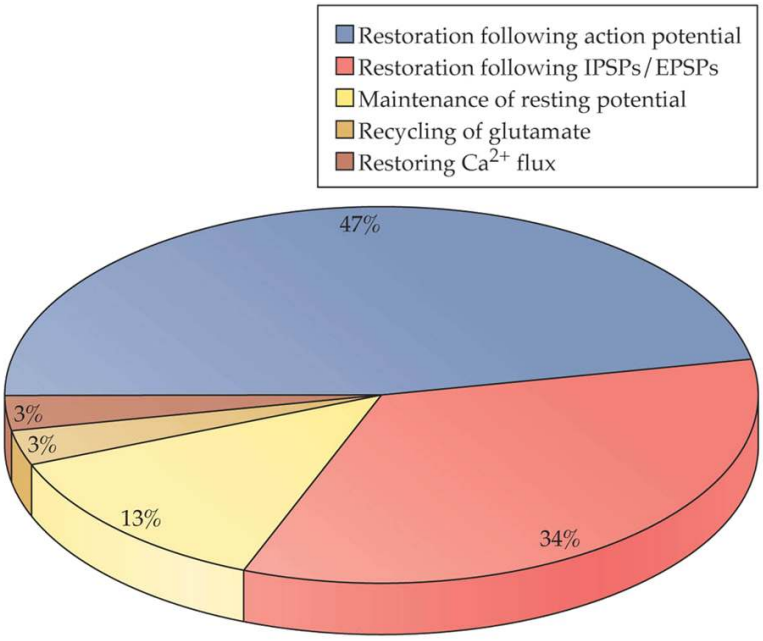

Figure 3.1
The energy budget of the rodent brain (Attwell and Laughlin 2001); the vast majority of the brain's energy requirements are due to the need to restore ion concentration gradients (adapted from Huettel et al. 2004).

An important implication of the presence of neuro-vascular coupling mechanism is the occurrence of local changes in the microvascular system of the brain in response to neuronal activity. This phenomenon, known as *haemodynamic response*, typically presents itself in the form of increased blood flow in areas of elevated neuronal activity. Changes in blood flow accompanying neuronal activity are believed to be initiated when active neurons release substances that diffuse to the nearby blood vessels. These vasoactive substances cause the vessel to dilate, thus reducing the vessel's resistance to flow and producing an increased flow. However, this dilation is not sufficient in and of itself to regulate blood flow but requires the upstream involvement of small arteries (arterioles) on the pial surface of the brain. These vessels, known as *resistance vessels* as they convert the pulsatile ejection of blood from the heart into a steady flow, play a crucial contribution in controlling cerebral microcirculation and blood flow through the capillary bed (Figure 3.2). Animal studies have shown that pial arteries dilate in response to a number of neuronal stimuli, leading to capillary increases of blood flow with a remarkable degree of neuro-vascular selectivity (Ngai et al. 1988; Iadecola et al. 1997; Ngai et al. 1995). Several candidate substances have been indentified that may play a role in the local control of blood flow. These include K^+ ions, adenosine and nitric oxide (Dirnagl et al. 1994; Paulson and Newman 1987). The latter substance is thought to mediate both local and distal vasodilation through a propagated action roughly analogous to a propagated neuronal potential (Iadecola et al. 1997). Mice genetically deficient in an enzyme responsible for the production of nitric oxide showed highly attenuated haemodynamic response, supporting the role of nitric oxide in triggering the blood flow increases through the control of upstream resistance vessels (Yang et al. 2003). However additional components may play a role in the neurovascular cascade, and it should be noted that a generally accepted model that details the specific neuro-

molecular events underlying the haemodynamic response is still lacking. Moreover, many cortical vessels are also surrounded by intertwining neuronal processes, raising the possibility that some aspects of cerebral microcirculation may be partly controlled by neuronal innervations. A few studies have shown that neurotransmitters released by these projections can dilate or constrict the vessel. For example, dopaminergic terminals are found in apposition to small intracortical arterioles and capillaries, whereas noradrenergic terminals are found to innervate large pial surface vessels (Krimer et al. 1998). However, the relation between the putative neurogenic action of dopamine and noradrenaline and local brain function remains unknown.

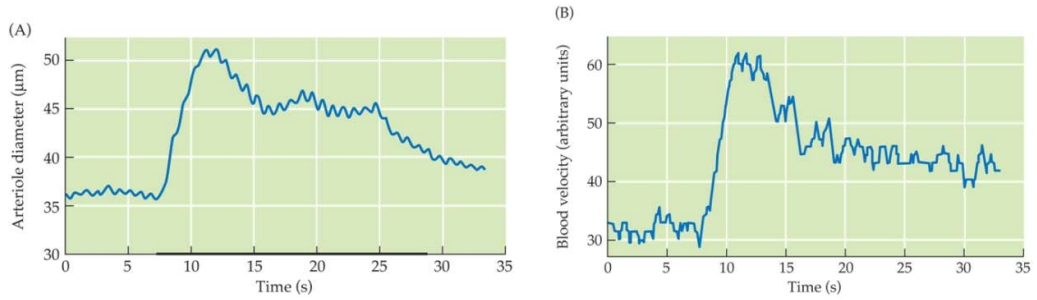

Figure 3.2

The relation between sensory stimulation and local blood flow changes (Ngai et al. 1988). Upon peripheral stimulation of sciatic nerve of the rat (solid line), an increased arteriole diameter and increased blood flow were recorded in the somatosensory cortex (adapted from Huettel et al. 2004).

The major and most likely effect of increased blood flow upon capillaries is the regularisation of flow. Studies of capillaries during baseline conditions have shown a remarkable heterogeneity of flow velocities through individual capillaries. Upon neuronal stimulation, the distribution of flow velocities has been shown to increase and become more uniform. This process is accompanied by capillary distension, a process whereby individual capillaries distend slightly and thus decrease their resistance to flow, leading to increased flow and increased blood volume within the capillary bed (Ngai et al. 1988; Ngai et al. 1995; Hudetz 1997). This capillary distension would increase the surface area of individual capillaries thus maximising the efficiency of the transfer of oxygen and glucose. This phenomenon also provides a neuro-physiological basis for the measurement of capillary cerebral blood volume (CBV) as a correlate of neuronal activity, a strategy that will be covered more in detail in section 3.6. In order to better appreciate the implications of the use of single haemodynamic parameters like cerebral blood volume (CBV) vs. conventional BOLD methods, a brief introduction to the BOLD contrast and its haemodynamic components will be given in the next sections.

3.2 Blood-Oxygen–Level-Dependent (BOLD) contrast

The vast majority of fMRI studies rely on endogenous measure known as blood-oxygenation-level-dependent (BOLD) contrast. Early research on the blood's magnetic properties performed by the Nobel laureate Linus Pauling in 1936 led to the important discovery that haemoglobin (i.e. a blood protein responsible for oxygen

transport and delivery) has magnetic properties that differ depending upon whether or not is bound to oxygen. Oxygenated hemoglobin (Hb) is diamagnetic (i.e. it has no unpaired electrons, and zero magnetic moment) whereas deoxygenated haemoglobin (dHb) is paramagnetic, that is, it has both unpaired electrons and a significant magnetic moment. One crucial consequence of this is that deoxygenated blood has a magnetic susceptibility significantly greater than fully oxygenated blood. This aspect was verified experimentally by Thulborn and colleagues in the 1980, who found that the decay of transverse magnetization depended on the proportion of oxygenated Hb within a test tube of blood (Figure 3.3).
The authors also noted that the magnitude of this effect increased with the square strength of the static magnetic field, a first experimental hint of the race for high fields that characterise modern BOLD fMRI. Importantly, these results provided a theoretical basis for measurement of blood oxygenation changes using MRI *in vivo.*

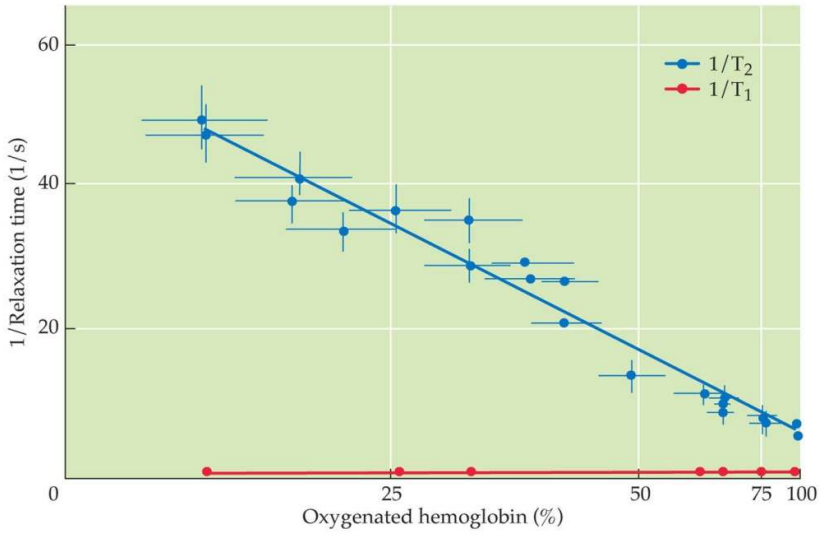

Figure 3.3
Relationship between blood oxygenation and MR relaxation rates (Thulborn et al. 1982). T_1 is not affected by blood oxygenation, while $1/T_2$ decreases with increasing oxygenation(adapted from Huettel et al. 2004).

During the late 1980s, Ogawa and colleagues (1990) investigated the possibility of exploiting the magnetic properties of haemoglobin to study brain physiology using MRI. By manipulating the proportion of oxygen delivered to experimental animals and using GE images, the authors were able to visualize blood vessels in the brain cortex of living rodents, an effect that was present only under hypoxic conditions, according to an increased presence of dHb in the blood. These results demonstrated that the presence of deoxygenated blood decreases the measured MR signal on T_2* images, relative to the presence of oxygenated blood. The authors speculated that this finding, which would come to be called BOLD contrast, could enable measurement of functional changes in the brain.

In subsequent *in vivo* experiments Ogawa and colleagues were able to demonstrate, by performing BOLD measurements at different levels of general anaesthesia, that the metabolic demand for oxygen was a pre-requisite for BOLD contrast (Ogawa et al.

1990a). Moreover they observed that increasing blood velocity through the addiction of the vasodilatory gas carbon dioxide to the breathing mixture significantly reduced bold contrast (Ogawa et al. 1990b). Collectively, the early research by Ogawa provided important evidence that BOLD contrast was dependent upon the total amount of deoxygenated Hb present in a brain region, which in turn depended upon the balance between oxygen consumption (metabolism), and oxygen supply (i.e, blood flow and volume).

The first BOLD fMRI studies in humans were reported in 1992 by three groups. Kwong and colleagues used EPI at 1.5 T, and demonstrated region-specific BOLD-signal increases in the visual cortex upon presentation of visual stimuli (Kwong et al. 1992). These finding were replicated by a similar study published by Ogawa et al, who likewise evaluated changes in fMRI GE signal resulting from long-duration presentation of visual stimuli (Ogawa et al. 1992). The authors also demonstrated that the signal was dependent on T_2*, as by changing T_E they were able to make the stimulus-effect disappeared. Similar effects were reported by Bandettini using a motor task (Bandettini et al. 1992). The publication of these first pioneering studies spurred a great interest in the method, which proved robust and of relatively easy implementation. These factors, in conjunction with increased prevalence of MRI scanners and the development of high-speed pulse sequences, set the stage for the exponential growth of fMRI from the early 1990s up to this date (in 2010, 25227 entries in the pubmed database contained the keyword fMRI).

3.3 Components of the BOLD Haemodynamic Response

The change in MR signal triggered by neuronal activity is known as the haemodynamic response (HDR). Multiple studies have investigated the nature and dynamics of the HDR produced by different evoking stimuli under different experimental conditions. The results of this research have highlighted a complex dynamics between the neural events triggering the HDR and its shape. For instance, cortical neuronal response occur within tens of milliseconds following a sensory stimulus, but the first observable HDR changes do not occur until 1 to 2 seconds later (Logothetis et al. 2001). Thus, the HDR is said to “lag” the neuronal events that initiate it.

The dynamics of the HDR waveform can be better understood when the HDR is compared to the timecourse of its individual constituents. Figure 3.4 reports the shape of the HDR and its individual haemodynamic components (CBV ad CBF) in the rat somatosensory cortex upon forepaw stimulation (Mandeville et al. 1998). The same figure also describes the timecourse of Hb and dHb measured in a analogous sensory stimulation paradigm (Malonek and Grinvald 1996). By comparing the two figures, the overall features of a typical HDR can be inferred. After a short latency, the metabolic demands of increased neuronal activity over baseline levels result in an increased blood flow which in turns determine and increased inflow of oxygenated blood (CBF increase, Figure 3.4). Importantly, the evoked changes in Hb and dHb are quite distinct. The dHb time curve showed a rapid increase, followed by a rapid decline to values that were below the pre-stimulus levels. In contrast, oxygenated-Hb had a slightly delayed onset followed by a slower gradual increase lasting throughout

the stimulation time and that was much greater in amplitude than the dHb changes. These important results, confirmed by subsequent investigators (reviewed by Mangia et al. 2009) suggest that more oxygen is supplied to the stimulated area than extracted, resulting in a *decrease* in the amount of deoxygenated haemoglobin within the voxel, corresponding to an *increased* BOLD response. After reaching its peak, the BOLD signal decreases in amplitude to a below-baseline level, and remains below baseline for an extended interval. This effect, known as *pos-stimulus undershoot*, is thought to arise from a temporary mismatch between CBF and CBV. According to this theory, following cessation of neuronal activity, blood flow decreases more rapidly than blood volume leading to a transient increase in the deoxyHb level. Recent experimental data support this view (Poser et al. 2010). Some researchers also reported the presence of an initial transient decrease in BOLD signal (negative dip) due to initial oxygen extraction before increases in blood flow (Menon et al. 1995). This effect has however not consistently observed, and its nature remains elusive (Uludag 2010). In broader terms, several theories have been invoked to explain the paradoxical mismatch between oxygen consumption and delivery underlying BOLD fMRI, and the interested reader may refer to the recent review by Mangia et al., for an exhaustive discussion of these aspects (Mangia et al. 2009). Once again, it should be noted that a generally accepted model detailing the temporal dynamics underlying the HDR is still lacking, probably because different stimulation paradigms and neuro-anatomical locations may entail complex and varying contributions that need to be better understood (Ekstrom 2010).

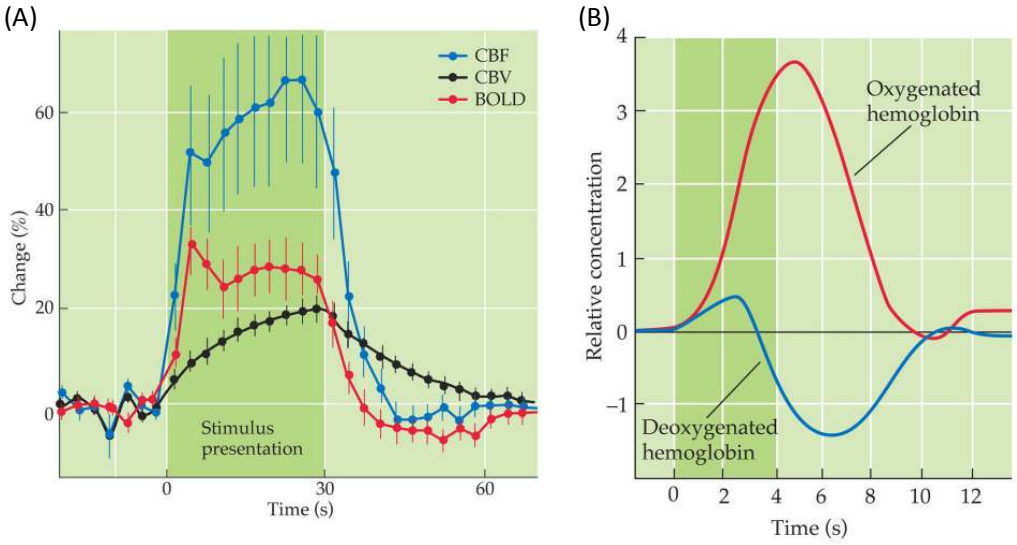

Figure 3.4

(A) Timecourse of the BOLD haemodynamic response and correspondign reclative changes in CBF and CBV following neuronal activty evoked by forepaw stimulation in the rat somatosensory cotrtex (Mandeville et al. 1998). (B) Using a similar paradigm, Malonel et al (1996) measured the time evolution of Hb and dHb following presentation of a short (4s) sensorial stimulus (adapted from Huettel et al. 2004).

3.4 Vascular Components and Spatial Specificity of Conventional BOLD Imaging

Neuronal activity associated with specific stimulation processes unfold in time and in space. While the spatial resolution of an fMRI experiment is primarily given by its voxel size, its ultimate functional resolution depends on the concordance of haemodynamic and neuronal activity. In a seminal study, Logothetis and colleagues investigated the correspondence between BOLD signal and electrophysiological measures in the primary visual cortex of monkeys, and found good spatial (and temporal) correspondence between the measures, particularly between BOLD and local field potentials that reflect summated excitatory and inhibitory post synaptic potentials (Logothetis et al. 2001). These results suggest that the BOLD contrast mechanism reflects primarily the integrative aspects of neuronal processing (i.e. input and neuronal processing in a given area), rather than its signalling counterpart (i.e. the output reflected in action potential firing). They also indicate that the BOLD fMRI signal is well-correlated with neural activity at a coarse spatial resolution. To further examine the spatial extent of BOLD fMRI, Disbrow et al. (2000) measured BOLD fMRI with 9-mm3 resolution and electrophysiolgical activity in anesthetized monkeys. Interestingly, they found that the overlap between fMRI and electrophysiological foci was 55% and the largest mismatch between the two measurements was located at areas close to large vessels. This *large vessel effect* is a well-known artefact in BOLD measurements that may significantly limit the functional resolution of this fMRI technique.

As explained in Section 3.2 the BOLD signal is generated by the presence of paramagnetic deoxygenated haemoglobin (dHb). As a result, the BOLD signal is only produced in capillaries and veins, as dHb is absent in fully oxygenated arterial blood. Because dHb molecules are paramagnetic, they create magnetic field gradients within the vessels that extend into surrounding tissues. On a microscopic scale, the primary mechanism for BOLD signal is thus the dephasing of spins within water molecules as they diffuse through these gradients fields, which can be divided into intravascular (IV) and extravascular (EV) (i.e. parenchymatic) components.

Since exchange of water between these two compartments (average water residence time in capillaries >500 ms) is relatively slow when compared with the imaging time (echo time <100 ms), MRI signals from these can be treated as separate pools. In a typical fMRI experiment using gradient-echo sequences, the BOLD signal reflects both intravascular and extravascular sources. However, because dHb is removed from the brain by the venous system, confounding signal changes unrelated to neuronal activity can arise from draining veins that are distant from neuronal activity, giving rise to *large-vessel effects* (*supra vide*).

Advanced acquisition techniques can be used to exclude components of BOLD signal that are distant from the neuronal activities. These techniques take advantage of different magnetic properties of large- and small-calibre vessels, and the different diffusion properties of EV and IV spins (Figure 3.5). When a blood vessel is considered

as an infinite cylinder, the frequency shift induced by dHb within the vessel (IV) can be approximated by

$$\Delta\omega_{in} = 2\pi\Delta\chi_0(1-Y)\omega_0(\cos^2\theta - 1/3) \quad (3.1)$$

where $\Delta\chi_0$ is the maximum susceptibility difference between fully oxygenated and fully deoxygenated blood, Y is the fraction of oxygenation in venous blood, ω_0 is the applied magnetic field of the magnet, and θ is the angle between the applied magnetic field (B_0) and vessel orientation (Kim and Ugurbil 2003). It should be noted that frequency and magnetic field (B_0) are interchangeable because $\omega_0=\gamma B_0$ where γ is the gyromagnetic ratio. Typically, many vessels with different orientations exist in a given voxel. When components with different frequency shifts are added within a voxel, signal loss will occur for T_2* -weighted MRI.

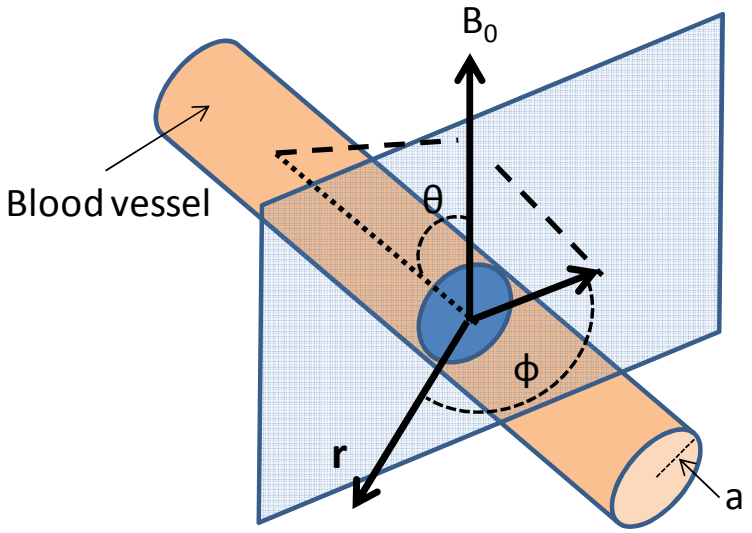

Figure 3.5

Diagram of a blood vessel and the parameters that determine the susceptibility effect induced by dHb in red blood cells at a distance r from the center of a vessel. The vessel with a radius a *is oriented at angle* θ *from the main magnetic field* B_0. Φ *is the angle between r and plane defined by* B_0 *and the vessel axis.*

Importantly, during fMRI measurements, water rapidly exchanges between red blood cells with paramagnetic dHb and plasma (average water residence time in blood cell is 5 ms) and travel through inhomogeneous magnetic fields by exchange and diffusion. Since the diffusion distance of intravascular water is large compared to the spatial extent of the deoxygenated Hb-induced magnetic field (e.g., diffusion distance during 50 ms measurement time is ca. 17 μm), ‘‘dynamic’’ time averaging occurs over the many different fields induced by dHb (i.e. the spins experience a dynamic magnetic field inhomogeneity), resulting in reduction of T_2. It should be noted that at high magnetic fields, venous blood T_2 can be shortened relative to tissue T_2 because the $R_2=1/T_2$ of venous blood is quadratically dependent on magnetic field (Thulborn et al. 1982). Thus, by setting an echo time to be much longer than T_2*/ T_2 of venous blood at sufficiently high fields (i.e. > 7T) the IV effect can be virtually eliminated (Duong et al. 2002).

At any location outside the blood vessel, the frequency shift can be described by

$$\Delta\omega_{out} = 2\pi\Delta\chi_0(1-Y)\omega_0(a/r)^2(\sin^2\theta)(\cos 2\Phi) \quad (3.2)$$

where a is the radius of the blood vessel, r is the distance from the point of interest to the center of the blood vessel, and ϕ is the angle between r and the plane defined by B_0 and the vessel axis (Figure 3.5). At the lumen of vessels (r=a) $\Delta\omega_{out}$ is identical and independent of vessel size. At r=5a, the susceptibility effect is 4% of the maximally available $\Delta\omega_{out}$. Hence, the same frequency shift is observed at 15 µm around a 3 µm-radius capillary and hat 150 µm around a 30 µm-radius venule. The dephasing effect around a larger vessel is therefore more spatially extensive because of a smaller susceptibility gradient. As a result, the EV contribution from large vessels to conventional BOLD signal is significant, regardless of magnetic field strength (Lu and van Zijl 2005). These contributions highlight a major limitation in the spatial specificity of classic gradient echo BOLD measurements, that is, the presence of unspecific functional contributions from large-vessels. This aspect is often non-negligible in preclinical fMRI research, where the small dimensions of the rodent brain imposes the application of high-resolution functional methods to adequately resolve small brain structures.

The use of conventional BOLD schemes in small animals is also limited by the presence of significant susceptibility artefacts at air-tissue interfaces, a contribution that is exacerbated by the use of T_2*-weighted EPI sequences typically employed in BOLD imaging. As a consequence of the particular anatomy of auditory canals in rodent species, these artefacts are particularly severe in ventro-lateral brain regions (i.e. amygdala, hypothalamus, midbrain, ventral hippocampus etc.). Consequently, the implementation of whole-brain multi-slice BOLD acquisition schemes is vexed by the presence of signal dropouts and distortion artefacts that prevents the investigation important limbic and midbrain structures, an effect greatly exacerbated by the use of high magnetic field strengths due to increased T_2* (Huettel et al. 2004).

Taken together, the limitations of conventional BOLD schemes highlight the need to develop more accurate and functionally sensitive fMRI approaches, particularly in experimental applications requiring maximal spatial resolution like the implementation of whole-brain functional neuroimaging in small preclinical species.

3.5 Improving the Spatial Specificity of fMRI: Spin-Echo Imaging

To improve the spatial specificity of fMRI by minimising the extra-vascular effects from large vessels, SE-based fMRI methods can be used (Weisskoff et al. 1994; Ogawa et al. 1993; Boxerman et al. 1995). As water molecules diffuse ≈17 µm during a typical echo time used for fMRI studies (e.g., ≈ 50ms), the extension of this motion covers the entire range of susceptibility around a small capillary (i.e 3-µm radius), but only a limited portion of the static susceptibility effect associated to a 30-µm radius venule. Thus, tissue water spins around capillaries will be ‘‘dynamically’’ averaged

over the many different fields. However, as the magnetic field gradient surrounding large vessels changes more slowly, the static dephasing effect is dominant and can be refocused by a SE 180° r.f. pulse, thus minimising the extra-vascular contribution of large vessels (Figure 3.6). This feature, together with the insensitivity of SE sequences to "through-plane" susceptibility gradients (i.e. at air-tissue interface), make SE fMRI an attractive alternative to gradient-echo BOLD, particularly in preclinical paradigms requiring high-resolution whole-brain coverage with high spatial specificity. It should however be noted that spins within intravascular diffusing water molecules will also experience dynamic magnetic field inhomogeneities, and for this reason, SE sequences are still sensitive to the intravascular BOLD signal in small as well as in large vessels. Thus, while SE pulse sequences can eliminate the extravascular large-vessel component of the BOLD signal, their use is not in and of itself sufficient to eliminate the intravascular large-vessel BOLD signal, especially at low magnetic fields (i.e < 5 Tesla).

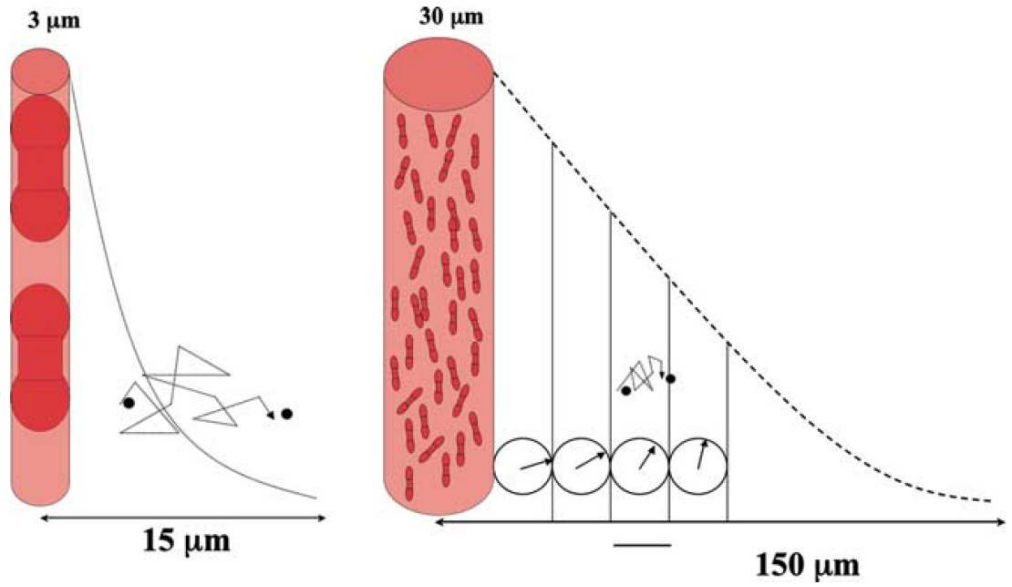

Figure 3.6

Extravascular dephasing effects from a 3 μm-radius capillary and a 30-μm-radius venule. Magnitude of dephasing effect (dashed decay lines from vessels) is shown as a function of distance. Displacement of a water molecule due to diffusion is indicated. Spin-echo cannot refocus dephasing effects around a small vessel because of dynamic averaging due to diffusion, while it can refocus static dephasing (shown in averaged phases in circles)(modified from Kim and Ugurbil 2003).

The situation is however different at higher high fields, as a results of the different sensitivities to the distribution of vessel sizes within an imaged voxel exhibited by GE and SE sequences. A number of theoretical models and *in vitro* experimental results have shown that, whereas SE measurements are strongly weighted towards vessel diameters on the order of the water diffusion length during the pulse duration such as capillaries and venules (i.e. ≈10μm), GE sequences are much less sensitive to the vessel size (Oja et al. 1999; Boxerman et al. 1995; Weisskoff et al. 1994)(Figure 3.7). An important consequence of this, is that the sensitivity of SE technique is typically two to three times less than that of gradient-echo BOLD, a finding that reflects the

fact that SE methods are only sensitive to the microvascular fraction of the haemodynamic response within imaged voxels (Lee et al. 2002). This phenomenon is important in making SE not viable for high-resolution fMRI because at low magnetic fields, due to the presence of contaminating intra-vascular effects, and especially because of the its low sensitivity compared to GE methods. However, provided that the intravascular contribution to SE imaging is minimised, and sufficient functional contrast is available, the microvascular weighting of SE methods offer the attractive opportunity to increase the spatial specificity of fMRI measures by allowing to image only the microvascular components of the haemodynamic events which are known to be colocalised with the neuronal activity of interest (*supra vide*).

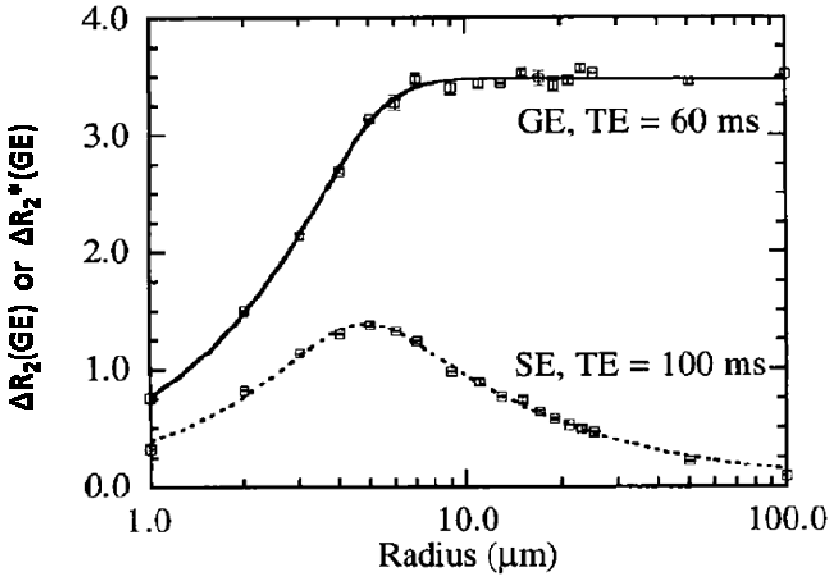

Figure 3.7
Theoretical simulation of ΔR_2^* (TE = 60 ms) and ΔR_2 (TE =100 ms) as a function of vessel diameter, assuming a $\Delta\chi$ of $1x10^{-7}$, corresponding to the administration of a superparamagnetic intravascular contrast agent. (modified from Boxerman et al. 1995). It should be noted that ΔR_2 peaks for microvessels and that ΔR_2^* exceeds ΔR_2 at all radii, reaches a plateau for macrovessels, and is actually greater for macrovessels than for microvessels (Boxerman et al. 1995).

In order to achieve this goal, one experimental option that can be effectively exploited is the use of higher magnetic fields (i.e > 7 Tesla). The use of increased scanner field strengths has the first obvious advantage of improving the functional signal-to-noise ratio (SNR) by augmenting the net magnetisation of the sample. As static field strengths increases linearly, raw signal increases quadratically, whereas thermal noise scales linearly with the filed strength, resulting in a linear increase of SNR with field strength (Huettel et al. 2004). This increased SNR can compensate for the low sensitivity of SE fMRI at low fields, thus permitting to obtain adequate functional SNR for fMRI measurements at sufficiently high fields (i.e. > 4T)(Duong et al. 2002). More importantly, the intravascular blood contribution is almost entirely suppressed at high magnetic fields because the apparent T_2 of blood shortens dramatically with increasing fields (i.e. from 180 to 7 ms at 1.5 and 7 T, respectively), while the gray matter T_2 decreases slightly (from 90 ms to 55 ms, at 1.5 and 7 T, respectively). Therefore, at TEs comparable to the T_2 of tissue, the blood signal is

greatly diminished and thus contributes negligibly to SE BOLD at high fields. Furthermore, theoretical simulations show that at higher magnetic fields the relativity size dependence curve shifts towards an even greater microvascular selectivity for SE acquisition (Boxerman et al. 1995). Thus, the use of high magnetic field has then the advantage of compensating for the reduced functional SNR of SE BOLD measurements, and to eliminate intravascular BOLD contributions, while preserving the microvascular selectivity of SE methods. Collectively, these features make the implementation of SE BOLD methods an attractive alternative to GE BOLDS for high resolution whole-brain imaging of the brain, both in humans (Poser et al. 2010; Boujraf et al. 2009; Thompson et al. 2010) and pre-clinical species (Lee et al. 2002).

Among the SE sequences that have been successfully used to demonstrate these principles, are SE-based echo-planar imaging sequences (SE-EPI) and multiple-refocused sequence, such as FSE (Poser and Norris 2007; Norris et al. 2002). However, SE-EPI sequences suffer from in-plane distortions due to residual T_2* weighting caused by the long EPI readout typically employed (i.e 40 ms), the severity of which increases rapidly with field strength due to the shortened relaxation time (Duong et al. 2002). Alternatively, BOLD fMRI with pure T_2 contrast and no EPI artefacts can be performed by using FSE sequences. Although this approach is associated to longer acquisition times typically exceeding those of a conventional SE-EPI experiment, this practical aspect does not limit the temporal resolution in phMRI experiments like those described in the present thesis, given the slow and sustained temporal dynamics of drug-induced changes in brain function (i.e. in the order of minutes, *infra vide*). On the other hand, the high energy deposition produced by multiple refocusing pulses of FSE is an experimental factor that needs to be controlled. As discussed more in detail in section 2.4.6, this problem can be minimised by using long repetition times, reduced refocusing flip angles in evenly spaced-apart multi-echo sequences like the RARE sequence (Hennig 1988) thus exploiting coherence pathway associated to this scheme. For instance, by employing a 90° refocusing pulse, the energy deposited is one fourth than associated to a traditional 180° pulse, with a moderate cost in terms of SNR (i.e. ≈30% since sin(90°)= 0.71). The use of FSE is thus a valuable alternative to SE-EPI for high-resolution fMRI of the brain whenever low-frequency brain stimulation paradigms are employed.

3.6 Improving Sensitivity: CBV-based fMRI with Exogenous Contrast Agents

The theoretical arguments supporting the use of SE BOLD at high fields to eliminate intravascular BOLD contributions and increase SNR crucially highlight an alternative strategy to achieve the same goal at low fields. The approach relies on the use of exogenous intravascular contrast agents to increase the blood's magnetic susceptibility leading so to generate CBV-based functional contrast. If paramagnetic blood-pool contrast agents with long half-lives are used, it is possible to significantly reduce intravascular T_2 thus eliminating intravascular contributions, and at the same time amplify the spatial range of extravascular magnetic field inhomogeneity associated to the haemodynamic response, thus sensibly increasing the functional

SNR at low fields. An important implication of this approach is that, unlike BOLD contrast which depends on the absolute change in Hb concentration and thus is susceptible to complex haemodynamic and metabolic contributions (i.e. blood flow, blood oxygenation, oxygen extraction) the use of exogenous contrast methods generally rely on the measurement of CBV, a meaningful physiological component of the haemodynamic response. As CBV is also robust marker of basal metabolism (Gaisler-Salomon et al. 2009; Sheth et al. 2004), an important prerogative of this approach is the possibility to offer a multi-parametric assessments of brain function. The same imaging session can thus provide an estimate of basal relative CBV (rCBV), a parameter that can be used for inter-group analysis of resting brain-function, and a subsequent assessment of evoked brain function (through dynamic CBV mapping) elicited by different stimulation paradigms. For these reasons, and with the aim to maximise the functional CNR and spatial selectivity at the field strength (4.7 T) available in our lab, a CBV-based spin-echo protocol was used in all the phMRI studies reported in this experimental thesis.

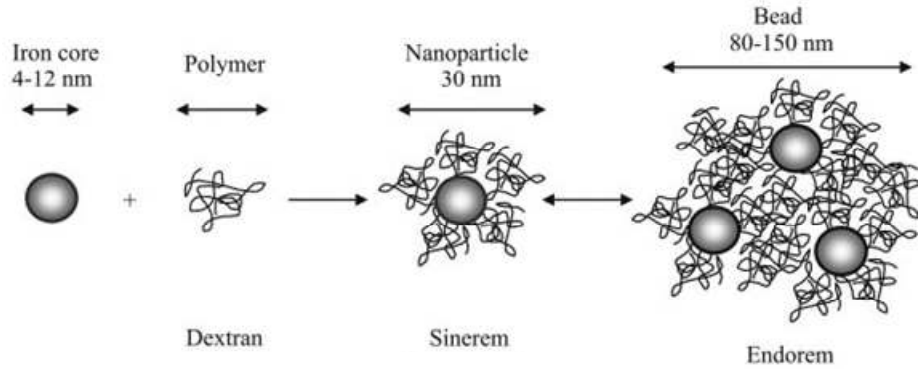

Figure 3.8

Super–paramagnetic iron oxide (SPIO) contrast agents contain a small iron oxide core (4-12) coated with dextran or other chemically inert and bio-compatible materials to form small nanoparticles (ultra-small SPIO, or USPIO) or beads (i.e. Endorem,Guerbet, the agent used in this thesis).

CBV-based techniques use exogenous paramagnetic or superparamagnetic intravascular contrast agents with high susceptibility. Dextran-coated superparamagnetic iron oxide nanoparticles (SPIO) that maintain a steady-state blood concentration permit measurements of relative CBV with good temporal resolution relative to bolus agents, such as gadolinium derivatives (Belliveau et al. 1991). SPIO are a family of MRI contrast agents (reviewed by Wang et al. 2001) that consist of monocrystalline iron oxide cores (4-10 nm) highly coated with dextran (final size is 120-150 nm) to decrease opsonization by plasma proteins, minimizing removal by the reticuloendothelial system and thus producing an extended (i.e. ≥ 3 hr in the rat) blood half-life (Figure 3.8).

Unlike BOLD measurements, however, iron oxide concentration in blood does not change with alterations in blood flow and oxygen consumption induced by neuronal activity. Thus, CBV-based functional methods measure signal perturbations reflecting changes in the particle content of the imaged voxel, which is, under steady-state conditions, solely determined by the changes in CBV consequent to local

cerebrovascular dilation or constriction. As a result, an increase in CBV during stimulation will induce an increase in the content of contrast agents and, consequently, a decrease in MRI signal (Figure 3.9). Importantly, although the change in dHb associated to functional activation may counteract the reduced relaxation rates produced by an increased CBV in individual voxels, *in vivo* experiments (Mandeville et al. 1998; Chen et al. 2001) have shown that this contribution at low fields is not sufficient to neutralize the increased CNR associated to the use of contrast agent, resulting in an overall three-fold CNR increase with respect to conventional GE-BOLD fMRI at the field of the present studies (4.7 T). However, since BOLD CNR increases as a function of field strength, while that of the iron oxide agent does not (the magnetization curve of the superparamagnetic agents used in this thesis (Endorem, Guerbert) is saturated at field strengths of 2T (Kyrtatos et al. 2009)), at sufficiently high fields BOLD may well provide as much CNR as extrinsic injection of a contrast. Interestingly, recent experiments suggest that this equality is achieved roughly at 9.4 T when SE fMRI is used, but that the benefits provided by exogenous agents may persist even at much higher magnetic fields than 9.4 if GE-based CBV-mapping is employed (Mandeville et al. 2004).

As small vessels (including pre-capillary arterioles) dilate vigorously during neural stimulation, whereas large vessels only show negligible dilation (Zaharchuk et al. 1999; Edvinsson and Krause 2002), the use of CBV-based methods has the intrinsic advantage of providing a haemodynamic readout that is more closely related to the actual site of neuronal activation than BOLD fMRI. Since the MRI signal is weaker in voxels containing large vessels due to its high content of contrast agent, signal perturbations following CBV alterations in such voxels are intrinsically less prominent that those detected in parenchymal regions, thus making this technique less susceptible to the effect of large vessels. Moreover, experimental measures and theoretical models have also demonstrated that CBV has methods have more uniform sensitivity to functional changes across brain regions that BOLD methods (Mandeville and Marota 1999). These features make CBV-based measurements an attractive alternative to BOLD fMRI in preclinical species, particularly when used in combination with SE-imaging (Sheth et al. 2004; Duong et al. 2002; Mandeville et al. 2004).

From a theoretical standpoint, the parameters that determine the functional SNR in CBV-based methods are the field strength, the echo time (TE) and contrast agent dose. As mentioned above, since the BOLD contribution is supralinearly dependent on magnetic field while the CBV change remains constant due to full magnetic saturation of SPIO at high fields, the SNR gain of the CBV technique over BOLD is higher at low fields. A seminal work from Mandeville and colleagues (Mandeville et al. 1998) has investigated the theoretical foundations of functional CNR maximisation as a function of TE and contrast agent dose (at a fixed field strength). The authors defined an experimental framework, supported by detailed numerical simulations (Boxerman et al. 1995) where a SPIO agent produces a change in transverse relaxation rate ($\Delta R_2^* = 1/\Delta T_2^*$ or $\Delta R_2 = 1/\Delta T_2$, for GE and SE, respectively) relative to the preinjection baseline proportional to local CBV (V) times some function (f) of the plasma concentration of paramagnetic agent ([P]).

$$\Delta R_2^* = k \bullet f\left([P]\right) \bullet V \tag{3.3}$$

If long TR are used (i.e. negligible T_1-weighting) and SPIO particles reaches a steady state concentration in blood plasma, then Eq. 3.3 reduces to a simple linear relationship between ΔR_2* and CBV at any time *(t)*

$$\Delta R_2^* = K \bullet V(t) \tag{3.4}$$

where the constant K now includes the agent blood concentration and therefore depends on SPIO dose. Importantly, *increases* in ΔR_2* due to increased blood volume (Eq. 3.3) may compete with *decreases* in ΔR_2* due to endogenous deoxyhemoglobin changes associated to the BOLD affect. Therefore, a sufficient amount of contrast agent (typically 10-25 mg/Kg of Fe) must be used so that relaxation rate changes due to exogenous agent greatly exceed BOLD effects. This assumption is implicit in the theoretical discussion that follows, and consistent with our experimental results at the doses of agent used in the studies presented here.

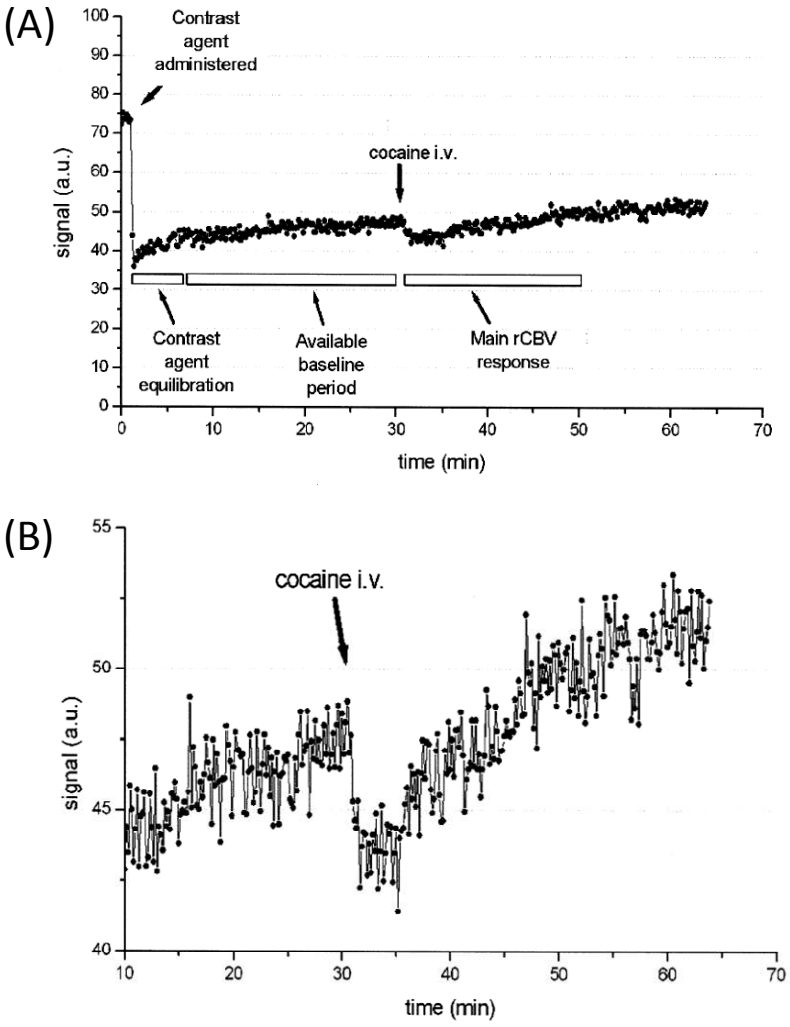

Figure 3.9

(A) Single voxel raw MR signal timecourse from a pharmacological MRI experiment using the SPIO agent Endorem in the rat. T_2-weighted signal changes due to contrast agent administration and washout, and CBV changes following an acute i.v. challenge with the psychostimulant cocaine (B) detail of panel (A).

Percent CBV change during a functional challenge can be simply calculated assuming monoexponential signal decay and negligible competing BOLD signal change. If ΔV(*t*) is the change in volume with respect to V(*0*), and S_{PRE} is the signal before injection of agent, according to Eq 2.58, the signal S(*t*) can be described as

$$S(t) = S_{PRE} \mathrm{e}^{-\mathrm{TE}KV(t)} \tag{3.5}$$

and the corresponding fractional volume change is

$$\frac{\Delta V(t)}{V(0)} = \frac{\Delta R_2^*(t)}{\Delta R_2^*(0)} - 1 = \frac{\ln\left(S(t)/S(0)\right)}{\ln\left(S(t)/S_{PRE}\right)} \tag{3.6}$$

The first expression for percent volume in Eq. 3.6 is general, whereas the second expression requires that the TE is constant throughout the experiment. This second expression states that a functional change in fractional blood plasma volume can be calculated as the natural log of the functional signal change with respect to the reduced baseline signal after injection of agent divided by the log of the signal reduction due to agent injection. Implict in this equation is the fact that the measurement of relative CBV changes entails an estimate of baseline CBV, (i.e. basal CBV prior to any stimulation *V*(0)), an established marker of basal metabolism that can be conveniently used to assess resting brain function in inter-group measurements of altered brain function (Section 4.2, Appendix 5). This characteristic, together with fact that one is able to obtain a direct measurement of a physiologically relevant parameter—CBV, represents an additional advantage of CBV-based methods over traditional BOLD techniques.

In terms of functional contrast to noise ratio (CNR), the same authors (Mandeville et al. 1998) described a simple theoretical model that accounts for the effect of TE and contrast agent dose. If CNR is defined as the signal change during a functional challenge divided by the noise, the CNR for a given physiological response (blood volume change) depends on the TE and the dose of contrast agent that has been administered. As TE or dose increases, the percent signal change with respect to the post-injection baseline increases in magnitude, whereas the SNR decreases. Since the CNR is the product of these quantities, an optimal CNR is achieved by compromising enhancement of percent signal change and reduction of SNR. CNR can be optimized in terms of either agent dose or TE.

Using the assumptions implicit in Eq. 3.6, the CNR for a given hemodynamic response is

$$CNR = S_0 \, \mathrm{e}^{-\mathrm{TE}R_2^*} \, \mathrm{e}^{-\mathrm{TE}KV(0)} \left(\mathrm{e}^{-\mathrm{TE}KV(t)} - 1\right) \tag{3.7}$$

where R_2^* is the (static) relaxation rate before injection of agent and S_0 is the SNR at TE = 0. The term inside parentheses is the fractional signal change during the functional challenge, and the terms outside parentheses define the SNR after agent injection. If Eq. 3.7 is maximized with respect to K (contrast agent dose), it can be demonstrated that the optimal post-injection signal is found to be a slowly varying

function of the relative volume change and is approximately 1/*e* of the preinjection signal for small changes in blood volume (Mandeville et al. 1998). Figure 3.10 shows the calculated relative CNR versus signal drop due to agent injection for a functional response with a 20% increase in blood volume. The optimal signal drop is approximately 60%.

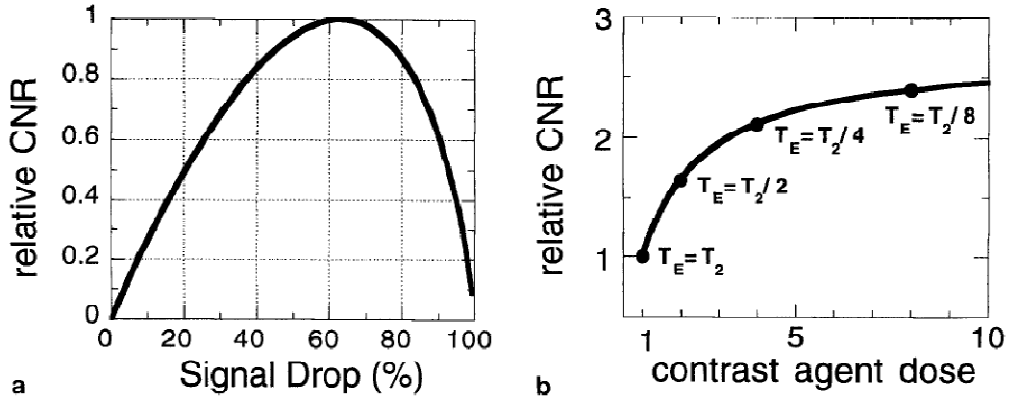

Figure 3.10
Theoretical CNR for functional blood volume studies can be optimized in terms of agent dose or TE. (a) Relative CNR versus signal drop due to agent injection for any fixed TE. (b) Relative CNR and contrast agent dose versus TE relative to preinjection T_2 for an optimal signal drop. Both graphs assume a 20% increase in blood volume (from Mandeville et al. 1998).

Eq. 3.7 can also be maximized with respect to TE for a given contrast agent dose. The optimal TE is then found to be approximately equal to the tissue relaxation time after agent injection

$$\text{Optimal TE} \approx \frac{1}{R_2^* + \Delta R_2^*(0)} \tag{3.8}$$

The maximum CNR that can be obtained using an exogenous agent and T_2-weighted imaging can be predicted from measured SNR and percent volume change and is (for small percent volume changes)

$$\text{maximum CNR} = S_0 = e^{-1}\frac{\Delta V}{V} \tag{3.9}$$

Relative CNR versus dose of contrast agent for an optimal signal drop due to agent injection is shown in Figure 3.8**.** CNR increases in proportion to the SNR before agent injection. A maximum value of CNR, which is a factor of *e* larger than the CNR at TE $=T_2$ is reached at TE = 0. Since the quantity TE x K is fixed to yield the optimal signal drop, the dose of contrast agent approaches infinity as TE approaches zero and relative CNR asymptotically approaches *e*. Therefore, Eq. 3.9 represents the upper limit of CNR, which is not completely obtainable in practice. In summary, these theoretical calculations show that the optimal agent dose drops signal to approximately 40% of its preinjection value for any fixed TE. For a fixed dose, on the other hand, the optimal TE is equal to the T_2, (or T_2*) of the tissue after agent injection.

The application of the theoretical constructs described above is of great practical importance for the experimental implementation of high-resolution fMRI and phMRI small animal species. In the present thesis, the optimized use of SPION and FSE imaging according to the aforesaid principles enabled us to perform high-CNR artefact-free whole-brain functional imaging in rats and mice with an in-plane spatial resolution of 300 μm^2 and 156 μm^2 , respectively, and with adequate TR (typically 26-40 s) to resolve the temporal dynamics of the signal changes produced by the psychoactive substances used in phMRI. This shows how a judicious choice of experimental parameters may enable the implementation of CBV-based approaches that overcome several of the limitations of the BOLD approach in small animals, thus greatly facilitating the preclinical implementation of functional neuroimaging strategies.

Clearly, the biggest disadvantage to the IRON technique is the large amount of iron that must be injected to obtain optimal CNRs (5-20 mg/kg), which hinders a direct methodological translation of this method to the clinic. While iron is relatively nontoxic, such an increase in body iron load may represent an unwarranted cost for the relative benefit of the MR exam. Similar agents to those used in the present work are already being used in humans for imaging liver or splendid lesions. Although no adverse toxicological events have been reported with the human use of SPION, it should be noted that the total iron dose injected is smaller than what is typically employed in CBV imaging (i.e. 0.8–1.8 mg/kg of iron vs. 20 mg/kg in our protocol), and the toxicological effects of such a significant iron increase, if any, are unknown. Preliminary animal research did not highlight any major acute toxic effects with the relatively high doses of SPION used in the present work, even after multiple studies in the same animals over the course of 1 year (Chen et al. 2001; Jenkins et al. 2004). This issue, however, will require further study for potential use in humans. Nevertheless, the tight physiological relationship between CBV-based imaging and the neuro-metabolic processing underlying BOLD fMRI and other neuroimaging measures of neuro-metabolic function (i.e FDG-PET, ASL, perfusion SPECT, or MRI.) make CBV-based imaging a preclinical research tool of unquestionable translational value.

3.7 Statistical Analysis of phMRI time-series

The extrapolation of functionally-meaningful and statistically-significant parameters from raw fMRI image time-series is an active field of research, and a comprehensive description of the potential and pitfalls of the methods available is beyond the scope of this thesis. In this section I will briefly summarize the general approach employed to analyse the phMRI timeseries. A detailed coverage of the theoretical foundations of these methods can be found in specialised texts (Huettel et al. 2004; Friston et al. 2007). Given the lack of established fMRI image-processing tools for preclinical research, image pre-processing and statistical analysis are often implemented by individual researchers through the use of multi-purpose computational platforms for image and signal analysis such as Matlab® or IDL®. This work, together with a crucial appraisal of the theoretical foundations underlying the development of the analytical

approach described here, is the results of a joint effort within the GSK neuroimaging lab, with a fundamental practical and theoretical contribution from Dr A. Schwarz, which I would like to acknowledge.

3.7.1 Experimental Design in phMRI

The strategy in an fMRI (and indeed any) experiment is based on an intervention in a system (brain) and observation of the modulation of the system response (i.e. BOLD effect) resulting from this 'provocation' (i.e. stimulation paradigm). Because fMRI data are not an absolute measure of neuronal activity, all study designs must also provide the opportunity to statistically contrast the neuronal activity of interest with a suitable rest or background condition. As results, a typical fMRI experiment consists in alternating the acquisition of blocks of N fMRI images of the brain while the subject is in an active state, that is, performing a specific task, with the acquisition of blocks of M images while the subject is in a control state (typically, resting). This active-control or ON-OFF cycle constitutes the so-called fMRI stimulation paradigm.

In phMRI studies of the brain, fMRI time series are used to probe the effect of psychoactive compounds upon the central haemodynamic response (Leslie and James 2000). Hence, the simplest experimental design in phMRI involves a comparison between the response to a psychoactive drug injection (i.e. the stimulation paradigm) versus placebo (control state, typically the drug vehicle, i.e. saline). In order to rule out non-negligible contributions of placebo on brain function, this approach usually entails the randomised use of two different group of subjects, of which one receives drug of interest (stimulation paradigm), and the other vehicle (placebo). The functional effect of the drug is then assessed by performing inter-group image statistics. More complex designs can be employed to assess more subtle, second-level effects, that is, the effect of behavioural, genetic, or pharmacological pre-conditioning on the response to a "probe" drug (Sections 4.1-4.4). In such cases, the ultimate readout would be an inter-group assessment of the brain function elicited by the drug, between N differently-conditioned experimental groups.

Operationally, phMRI studies entail the following experimental steps: a) animal preparation, b) phMRI data acquisition, c) image post-processing and d) statistical analysis of phMRI timeseries. Animal preparation consists on the implementation of anaesthetic procedures to minimize the discomfort associated to animal restraint and reduce motion artefacts, as well as the application of monitoring devices aimed to peripherally record physiological parameters that, if not tightly controlled, could confound central haemodynamic readouts (i.e. supra-physiological changes in blood pressure (Gozzi et al. 2006) or arterial blood gases (Steward et al. 2005)).

phMRI timeseries acquisition is usually preceded by the acquisition of high resolution anatomical image of the brain. This scan serves to facilitate the subsequent mapping of each subject's functional timeseries to a common three-dimensional coordinate system, an essential prerequisite to the performance of meaningful voxel-based inter-group statistics. In phMRI studies where the site of activation is often unknown and distributed across different regions, contiguous slices are acquired to obtain a

three-dimensional reference volume. In the rat phMRI studies reported in this thesis, a T_2-weighted RARE reference volume with a FOV of 4 cm, a 256 x 256 image matrix and 16 or 20 1-mm thick contiguous slices where used, yielding a 0.3 mm^2 in-plane and 1 mm longitudinal resolution, respectively.
The anatomical scan is followed by the functional time series acquisition. This scan acquires an epoch of multiple image volumes that allow to follow the evolution of phMRI signal in space and time. Functional time series are typically co-centred with the anatomical reference volume, and acquired with the same spatial coverage (i.e. number of slices). However, their spatial resolution is often reduced as a trade-off for the need to achieve adequate temporal-resolution. In this thesis, this was achieved by reducing the matrix size (128x128, corresponding to an in plane resolution of 0.6 mm^2), and increasing the RARE factor from 8 to 32. The resulting TR was ≈25 seconds for a 20-slice brain-volume. The typical duration of a phMRI experiment is ≈60 min corresponding to ca. 100-120 repetitions.

In the phMRI protocols used here, spin-echo fMRI time-series were sensitised to CBV by infusing a commercially-available SPION agent (Endorem, Guerbert, see Section 3.6). As illustrated in Figure 3.9, contrast agent administration produces a sharp signal drop (≈ 50%) that proportionally reflects “resting state” cerebral blood volume. Resting state CBV is a first important parameter that can be analysed and mapped in the living brain, by virtue of its established relationship with basal metabolic activity of neuronal populations (Sheth et al. 2004). Thus, quantification of basal CBV levels can be used to obtain an estimate of basal neuronal activity, and its modulation by disease or pharmacological states (Section 4.2).

After an appropriate equilibration time, the psychoactive drug of interest (or its vehicle) is injected. Psychoactive compounds typically induce slow but sustained CBV alterations that reflect different pharmaco-dynamic properties of the drug (Bifone and Gozzi 2010). The quantification of the relative CBV (rCBV) change produced by the drug with respect to the per-injection baseline is thus be used a spatio-temporal index of drug-induced neuronal activity. Figure 3.9 also illustrate an important aspect of CBV-based methods. The use of contrast agent is often associated with a drifting background signal, a feature that reflects gradual elimination of contrast agent from the vascular system (contrast agent washout). Therefore, for the phMRI signal to be analysed properly, the drifting contribution of contrast agent washout must be filtered out. In the case of the work presented here, the SPION agent used was shown to give rise to monotonic signal changes amenable to detrending (i.e. rectification of the signal change) by using a mono-exponential input function (described in Schwarz et al. 2003).

3.7.2. Image Pre-Processing

A number of computational procedures, known as pre-processing steps, are operated on fMRI and phMRI data following image reconstruction but prior to statistical analysis. The goals of pre-processing procedures are to reduce unwanted variability in the experimental data and to improve the validity of statistical analysis. Figure 3.11 summarises the pre-processing steps used for image pre-processing in the phMRI experiments depicted in this thesis.

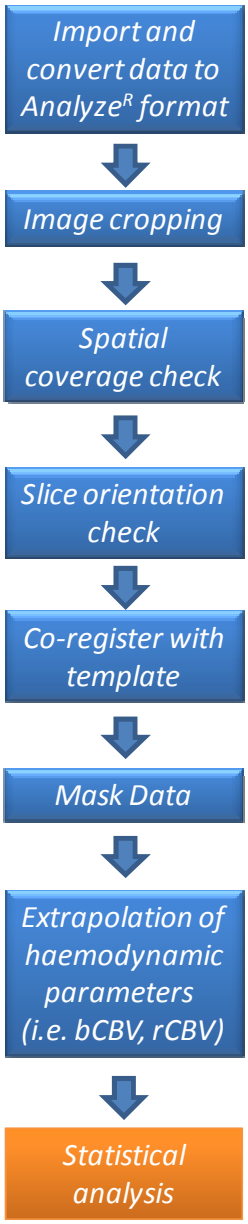

Figure 3.11.

Schematic representation of the image pre-processing workflow applied to the phMRI timeseries produced in this thesis.

Import and convert data to Analyze format. As MRI scanner images are produced in a proprietary format (Bruker), the initial step of the pre-processing pipeline is the conversion into the standard medical imaging format Analyze 7.0. Analyze images are composed of a header file (.hdr) and an image file (.img). The binary header file has fixed size and is organized as a 'C' structure. It contains basic image information such as matrix dimensions, number of slices, volumes (time points), field of view dimension, etcetera. The image file is a flat (uncompressed) binary file containing the actual image data.

Image Cropping. This is an optional step that can be employed to reduce the effective field of view of MRI images, permitting to discard pixels outside the anatomical region of interest. Most MR images are acquired using a substantially larger FOV than necessary, a strategy that is required to reduce the occurrence of "aliasing artefacts" to which frequency-encoded measurements such as MRI are very susceptible. The cropping tools employed in the post-processing pipeline (developed by F. Agosta) returns a reduced versions matrix version of the anatomical and phMRI images (e.g. from 128x128 to 64x64 pixels, respectively) with the obvious advantage of reducing by a factor 4 halving the amount of disk space and computational time required by the subsequent steps.

Spatial coverage check. This step checks the correspondence between the number of slices of the anatomical and the time series image volumes. If inconsistencies arise, the two can be harmonised by removing the exceeding slices. The objective of this step is to make sure the dimension of anatomical and time series brain volumes are identical. This prerequisite is essential for subsequent co-registration to standard stereotaxic template.

Slice orientation check. This step checks for consistency in the dorso-ventral orientation of the images between scans. When discrepant, orientation is rectified by flipping the required image.

Co-register fMRI timeseries to MRI stereotaxic template. In order to allow voxel-wise statistical group comparisons, each subject needs to be mapped on a common three-dimensional coordinate system. Our lab developed and published a stereotaxic MRI template set for the rat brain co-registered with an anatomical atlas (Schwarz et al. 2006a). This consists of an "averaged" MRI rat brain template co-localised with a volumetric reconstruction of the Paxinos and Watson rat brain atlas (Paxinos and Watson 2005), thus enabling the localisation of functional effects in terms of atlas structure and stereotaxic coordinates. Moreover, voxels falling within selected brain structures can be combined to define anatomically based 3D volumes of interest (VOIs), free of operator bias.

In order to use the template, each subject's reference brain volume was mapped on the coordinate set of the brain atlas by means of a rigid-body volumetric transformation involving nine degrees of freedom (three rotation, three translation, three scaling). This was accomplished by using FSL/FLIRT (Smith et al. 2004a), a clinical fMRI software suite developed by the Oxford Centre for Functional MRI of the Brain (http://www.fmrib.ox.ac.uk/). The transformation matrix was then applied to the accompanying fMRI time series. Obviously, an essential prerequisite in order for this procedure to give meaningful result is that all the brain volumes are originally acquired in the same MRI scanner "coordinate system" (i.e. they are co-centred).

Mask data. In order to reduce computational time and improve display of results, non-brain tissue and cerebrospinal fluid (ventricles) were removed from images. This is achieved by multiplying time series data by a binary "brain mask" (1 is brain tissue, 0 all the rest) that accompanies the stereotaxic template (Schwarz et al. 2006a).

*Extrapolation of haemodynamic parameters: basal CBV***.** CBV-weighted phMRI time series signal can be converted on a pixel-wise basis into an index of bCBV through the following transform (section 3.6):

$$CBV(t) = \ln \frac{S(t)}{S_{PRE}} \tag{3.10}$$

where *S(t)* is MRI signal at time t, and S_{PRE} is mean signal prior to contrast agent administration. In order to have a more robust assessment of bCBV, several consecutive bCBV(t) volumes were calculated and averaged into a single representative "mean" bCBV volume covering a small time-window (typically 5-10 min). In order to account for signal drifts reflecting contrast agent washout, the monoexponential signal decay produced by the contrast agent elimination (Schwarz et al. 2003) can be effectively modelled by a linear function over the limited time-window (5-10 min) typically used for bCBV calculation.

Extrapolation of haemodynamic parameters: rCBV. CBV-weighted MRI signal can also be converted into fractional CBV changes (rCBV) relative to a pre-stimulation condition. This step entails the conversion of raw phMRI signal into rCBV timeseries covering the event of interest (i.e. drug or vehicle administration). In this case the effect of the drug is expressed as a ratio between the incremental CBV alteration produced by the drug (i.e. "delta CBV"), and bCBV prior to drug administration, allowing the expression of the change in percentage terms.

As described in section 3.6, CBV-weighted phMRI raw signal can be transformed into rCBV by applying the following transform

$$rCBV(t) = \frac{\ln\left(\frac{S(t)}{B(t)}\right)}{\ln\left(\frac{B(t)}{S_{PRE}}\right)} \tag{3.11}$$

where S(t) is the raw MR signal intensity at time (t), S_{PRE} is signal intensity prior to contrast agent administration, and B(t) is an estimate of the background signal in the absence of transient functional activity. Over long time windows (> 15 min) the fact that the background signal is not constant but reflects elimination of contrast agent from blood compartment must be taken into account. In the case of the contrast agent used in this study, this can be accomplished by detrending the background signal by means of a constrained exponential fit of the form

$$B(t) = S_{PRE} - (S_{PRE} - S_{POST})e^{\frac{1}{T_w}} \tag{3.12}$$

where S_{PRE} and S_{POST} are set to values obtained from the same time course to be detrended, with S_{POST} being the mean signal value of N time points following contrast

agent administration and equilibration, and T_w a known decay time constant which in the case of Endorem is 240 min (Schwarz et al. 2003). It should be noted that the choice of the most appropriate estimation method strictly depends on the time window considered, and dose and type of contrast agent used (Schwarz et al. 2003).

3.7.3 VOI-based Statistics

After image pre-processing, the phMRI timeseries can be subjected to inter-group (i.e. drug vs. vehicle) statistical comparisons. Two complementary approaches are usually employed. One first robust approach relies on the intergroup comparison of phMRI signal-timecourses in anatomical regions or volumes of interest (ROIs, or VOIs, respectively). To this purpose, the brain volume is parcellated into a series of VOIs that coincide with 3D reconstructions of rat brain atlas regions if a stereotaxic MRI template like the one developed in our laboratory is used (Schwarz et al. 2006a). This approach allows, for each subject, to extract a single rCBV time course from individual brain regions that averages all the individual voxels belonging to the same anatomical region (Figure 3.12), free of operator-bias. The phMRI timecourses can then be averaged on a "per group" basis in order to highlight regional differences in magnitude and time-profile of drug induced functional response. By using simple summary measurements (i.e. mean response over time-window or areas under the curve) the phMRI data are then amenable to be analysed for statistically significant effects through the use of standard *post-hoc* statistical tests (i.e. student's t test, ANOVA, Figure 3.13).

VOI analyses have two main advantages over voxelwise methods (see next section). First, because there many fewer VOIs than voxels, the total number of statistical comparisons is greatly reduced, minimising the need for correction for multiple comparisons. Second, each VOI combines data from multiple voxels thus increasing the functional signal-to-noise provided that the VOI is functionally homogenous. The major drawback of to this approach is the need for a subjective input from the experimenter, who is required to manually draw a ROIs, or like in the case of the present work, to select a number of brain meta-regions a priori. A second important problem is the potential mismatching of anatomical and functional regions of the brain. For example, only small portions of an anatomical brain region may contain the functional contribution of interest, and this factor may significantly reduce the functional signal to noise. Conversely, a single anatomical region may contain multiple functional contributions. In this case, it may be beneficial to subdivide the anatomical VOI, which however has the disadvantage of increasing the number of VOI once again raising the statistical issue of multiple comparisons. On the whole, due the variability in function within *any* anatomical region, ROI or VOI-based approaches are typically combined with image-based approaches whenever possible.

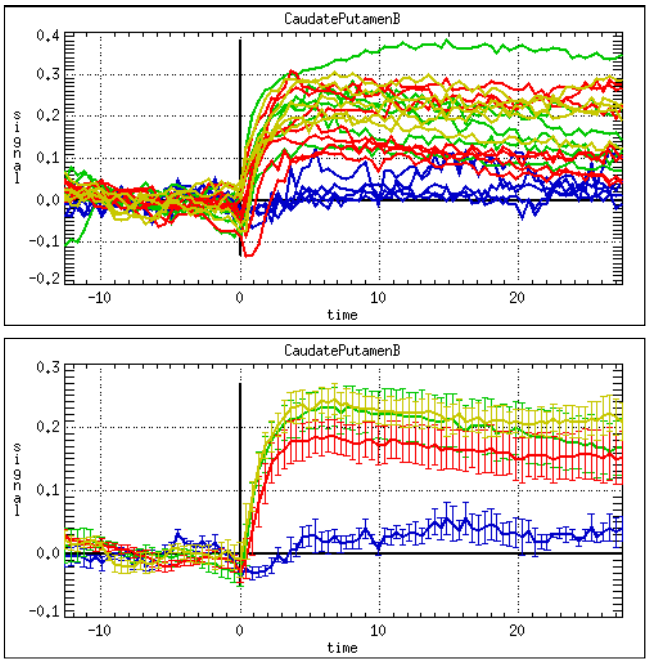

Figure 3.12

Representative temporal profiles of rCBV (signal) following administration of a psycho-stimulant drug (D-amphetamine) or vehicle (control, blue lines) in an anatomical volume of interest (Caudate Putamen) as a function of group pre-treatment Top panel: individual rCBV timecourses, Bottom panel: Mean (±SEM) rCBV response across different groups of experimental subjects.

3.7.4 Image-based Statistics

In order to map regions that exhibit statistically significant changes in brain function upon the administration of an experimental stimulus, voxelwise statistics can be employed. These methods complement VOI-based investigation by providing a detailed three-dimensional spatial description of where in the brain the effect of stimulus is statistically significant.

The main purpose of image-based analysis in phMRI is to permit a voxel-wise comparison of the effect of a drug on fMRI time series across experimental conditions, to produce “activation” or “deactivation” maps. In its simplest form, a typical phMRI experiments entails the comparison of interest is between drug and placebo (vehicle), although second order effects can be equally assessed (i.e. pretreatment- drug vs. control-drug). In this thesis, image-based statistics was implemented with FSL, versatile software suite originally developed for analysis of clinical fMRI images (Smith et al. 2004b).

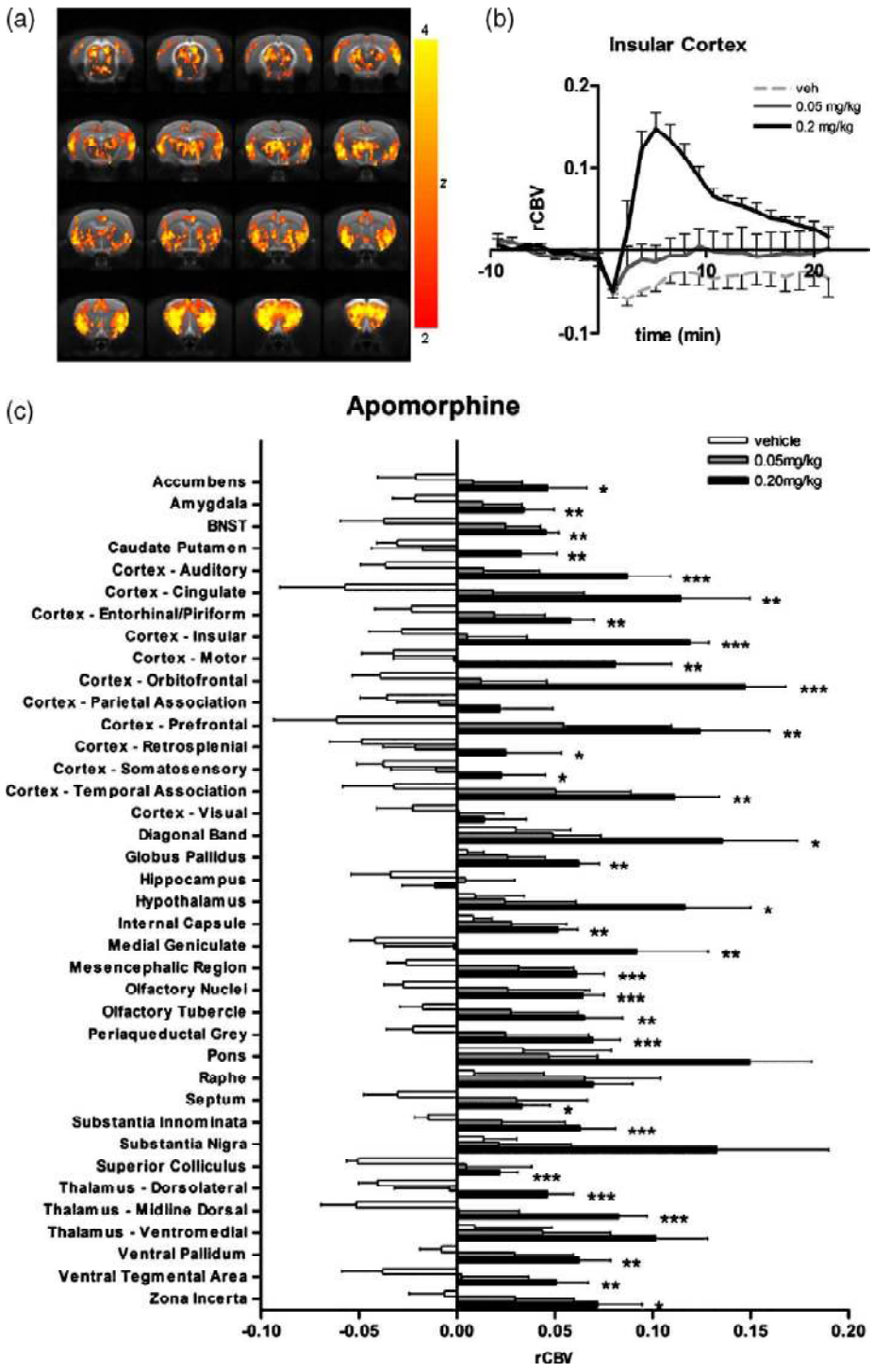

Figure 3.13

*Different ways to analyze and present the results of the statistical analysis of phMRI data (a) Statistical parametric map of the effect of the psycho-stimulant apomorphine versus vehicle, thresholded at a Z score level of 2. (b) Time courses (mean ±SEM at each time point) showing signal changes in each group from the insular cortex VOI, defined using the co-registered atlas. (c) Group mean responses from representative VOIs of interest (statistical significance of two-sided t test comparisons versus vehicle: *P < 0.05, **P < 0.01, ***P < 0.001).*

The main purpose of image-based statistics is to identify a scalar parameter that describes the effect of the stimulus of interest on individual voxel time-series. In most fMRI and phMRI studies statistical parametric maps are generated. These are colour-coded maps that display in each voxel an indicator of the degree of statistical significance (i.e. the probability that each voxels is consistent with the null hypothesis) of stimulus-induced signal changes with respect to a control (baseline) condition. The statistical maps are usually displayed on top of a base image that illustrates the underlying brain anatomy. An arbitrary threshold (usually $\alpha<0.05$ or less) is typically introduced to retain only "significantly" activated (or deactivated) voxels.

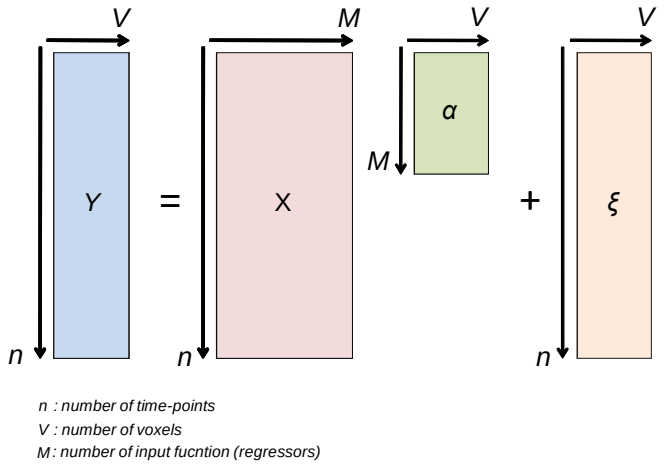

Figure 3.14

Basic principles of the General Linear Model (GLM) in phMRI. The GLM attempts to find the set of experimental parameters (β) for a design matrix X that best accounts for the original data Y.

Voxel-based statistics of fMRI and phMRI data can be effectively performed within the theoretical framework of the "general linear model" (GLM). The GLM is an all-purpose statistical framework that generalizes linear regression by allowing a given signal model (regressor, or input function) to be related to the response variable (i.e. voxel time-course) to assess the effect of interest. This way, GLM can be used to identify f/phMRI time-courses that correlate in time with a signal model reflecting the "stimulation" paradigm used (in phMRI, the presence of drug).

The model is expressed by the equality:

$$y = a_0 + a_1 x_1 + a_2 x_2 + \ldots + a_n x_n + e \qquad (3.12)$$

where in each voxel the data y (i.e. the rCBV time-course in a single voxel), is equal to a weighted combination of several model factors (x_i) plus an additive error term (e). The parameter weights (a_i) indicate how much a factor contributes to the overall data, whereas the parameter a_0 reflects the total contribution of all factors that are held constant throughout the experiment. In solving the linear model equation, the researcher has only one known quantity, the experimental data. The model factors in

phMRI are typically the presence of a drug, which is typically described by a boxcar waveform (e.g., drug off= 0, drug on=1). However, more complex model functions that more closely describe the varying temporal course of drug-induced fMRI responses can be employed to maximise the statistical power of parameter estimation, like for example data-driven model functions identified using wavelet-cluster analysis (Schwarz et al. 2006b). Given the data and a specified set of model factors, the researcher can than calculate what combination of weights serves to minimise the residual error term.

In fMRI, the experimental data are represented as a two dimensional matrix consisting of *n* time points by *V* voxels (Figure 3.14). A design matrix is used to specify the linear model to be evaluated, consisting of *M* model factors, each *n* time points in length. In phMRI the design matrix usually consists of a signal model that can be inferred from experimental design (i.e. drug on–off). The parameter matrix contains *M* rows and V columns, such that each cell indicates amplitude of one of the model factors for a given voxel. Finally the error term is an *n*-by-*V* matrix. Once the design matrix has been set-up for a given experiment, the combination of weights yielding the smallest error term is calculated by computing a cost function, typically least-squares errors (i.e. the sum of squared residuals for each time point). Then, the significance of a model factor for a given voxel can be tested by dividing its associated parameters by the residual error, a quantity that follows the so called "*F distribution",* and so its statistical significance can be evaluated as a function of the available degrees of freedom (i.e. number of independent observations). Conceptually, this process is very similar to a simple correlation analysis, in that it generates an estimate of the "goodness of fit" at each voxel timeseries that can be mapped on a statistical parametric image and that is also amenable to a second-level group comparison. One common way to plot the results of a GLM analysis is by colour-encoding the value *p* (probability of null hypothesis) defining the significance of the regressions in each voxel, or more commonly, by calculating the *z* score associated to each voxels' fit, where *z* is a parameter that gives a measure of the size of the measured effect divided by standard deviation of the sample (Figure 3.15).

In phMRI studies, the output of a GLM analysis typically an individual activation (or deactivation) map showing brain regions whose activity correlates significantly with the input function describing the drug administration paradigm employed (Figure 3.15). However, as phMRI typically imply a comparison between a treated and a control group, a "second level" inter-subject analysis is often performed. An essential prerequisite to this, is that all the subject's images have been mapped into a common three dimensional coordinate space through template co-registration as described above. In order to make inferences about the population from which subjects are drawn, a two-stage random effect analysis is usually performed. In the first stage, voxelwise maps are generated for each subject independently (1^{st} level GLM analysis,

Figure 3.15). In the second stage, the distribution of the individual subjects' statistics is itself tested for significance (Figure 3.16). This can be simply done by using a *t*-test the evaluates whether the individual subjects' summary statistics (e.g. *z* score) are drawn from a distribution with a mean of zero. If the second-stage statistical test is significant at the established *alpha* (significance) value, than it can be concluded that the experimental manipulation (in phMRI, the drug administration) would have an effect on the population from which the subjects were drawn.

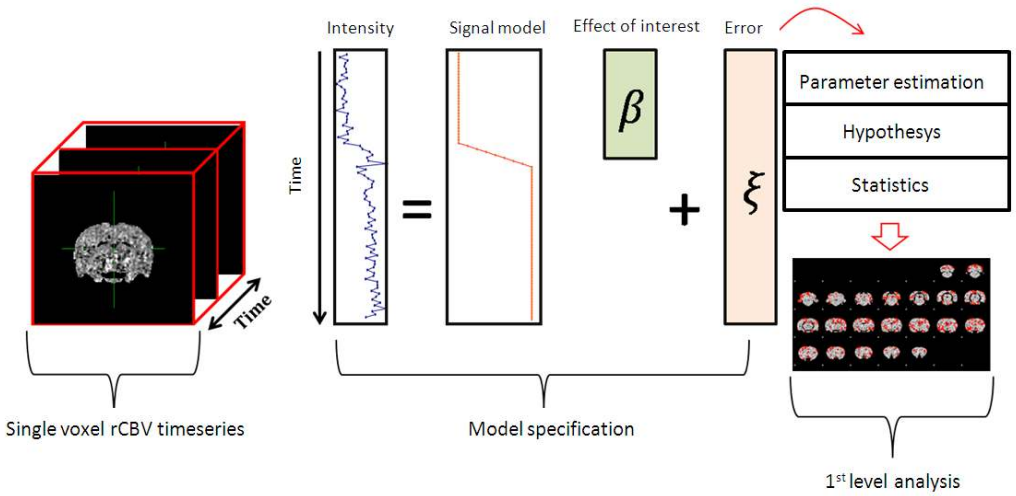

Figure 3.15

Overview of voxel-based 1st level statistical analysis of phMRI timeseries. A signal model is inferred from experimental design and used within the GLM to generate estimates of the coefficients of interest that minimise the error term of the GLM equation. The result of this process is a degree of statistical significance versus a control condition (no drug) at each rCBV time series voxel that can be superimposed on an anatomical image to generate a map of goodness of fit of the chosen regressor at each voxel.

Voxelwise analysis of bCBV data can be likewise performed using GLM approaches. However, bCBV data are not expressed as time-series but reflect an individual summary measurements the averages bCBV over a defined time-window to yield a single bCBV brain volume per subject. In order to perform group analysis of these data within a GLM framework, individual bCBV volumes can be serially concatenated group-wise, and statistical comparisons between groups can be simply performed by using an input function that captures the experimental parameters of interest. In the simple case of two different groups of subjects (say control, and disease state), this would results in a "pseudo-time-series" of concatenated volumes that is analysed using an input function of "zeros" corresponding to control, and "ones" corresponding to the disease state group. The results of this simple first-level analysis will yield maps of voxels where the bCBV is significantly different between groups.

Images-based analysis is usually associated with additional image pre-processing steps that are typically incorporated in the software packages used for statistical analysis. One important step that is often introduced is spatial smoothing. The purpose of

spatial smoothing is to improve the signal to noise by blurring sharp edges and suppress spurious signal contributions. Spatial smoothing is achieved by convolving individual images with a Gaussian Kernel which effectively acts as a low-pass spatial filter. If judiciously performed (i.e. the extent of the filter matches the activation extent), spatial smoothing results in an augmented contrast-to-noise ratio and improved statistical power by increasing the normality of the data (Huettel et al. 2004).

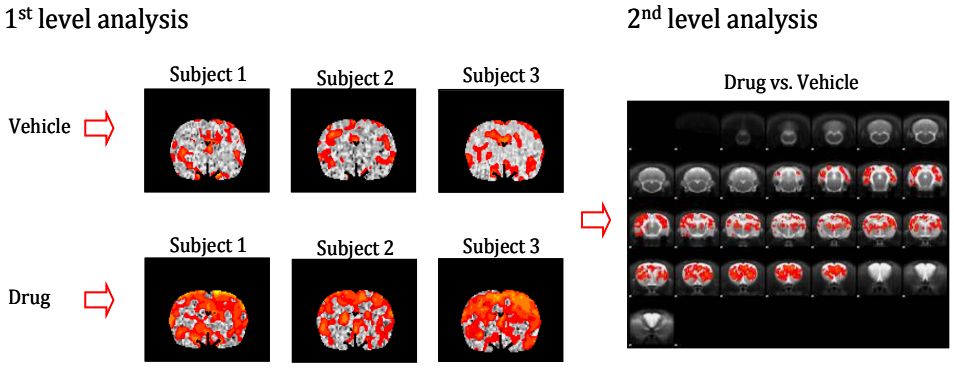

Figure 3.16

Inter-group (2nd level) analysis in phMRI; The distribution of the individual subjects' statistics (i.e. the results of the 1st level analysis) is itself tested for significance on a voxel-base.

An important issue related to voxelwise analysis is the problem of multiple statistical comparisons. As typical fMRI data sets may contain about 100.000 voxels, with an alpha level of 0.05, as many as 5000 voxels are expected to be flagged as significantly activated due to chance alone (false positives). Hence, all voxel based statistical methods should be accompanied by corrections for multiple comparisons. An approach that is gaining acceptance in the imaging community and that has been implemented in the software employed to analyse the phMRI studies of this thesis, is based on the use of *random field theory*. This approach is more conservative than standard strategies relying on the use of stricter alpha values based on the number of independent tests (i.e. the "Bonferroni method"). Indeed, in fMRI images voxels are not completely independent. Time courses in adjacent voxels tend to be highly correlated, as haemodynamic responses spans relatively large regions, and spatial smoothing during pre-processing ensures that no voxel is independent of its neighbours. As a result, methods like the Bonferroni correction, where the alpha level is decreased proportionally to the number *n* of independent tests ($\alpha_{Bon}=\alpha/n$) greatly overestimates the number of independent statistical tests, resulting in an alpha value that is much too conservative. To determine a better correction factor, Worsley and colleagues (Worsley et al. 1992) applied the theory of Gaussian random fields to fMRI data. Random field theory estimates the number of independent statistical tests based upon spatial correlation, or smoothness, of the experimental data, a factor that depends both on the spatial smoothing applied and the intrinsic degree of correlation.

Based on smoothness, a parameter expressed in number of voxels, the number of independent tests in a data can be calculated, a value known as *resolution element*, or *resel*. With even small smoothenss in the data, this value will be much less than the original number of voxels. From the number of resells, one can estimate how many clusters of activity should be found by chance at a given statistical threshold, and use this computation to adjust the significance levels of the maps to obtain a cluster-corrected alpha-level (Smith et al. 2004a; Worsley et al. 1992). A more detailed description of random field theory and cluster correction can be found in specialised texts (Huettel et al. 2004; Friston 1996; Worsley et al. 1992).

4 - Probing Brain Function with Pharmacological MRI

The development of fMRI methods has revolutionised neuroscience, providing clinicians and researchers with a method to investigate the spatio-temporal patterns of neuro-functional activity with unprecedented accuracy. Although primarily developed for human investigations, there exists significant scope for the application of fMRI in preclinical species. For example, fMRI methods can be applied to investigate the physiological basis of the fMRI responses, and to validate the imaging endpoint for clinical investigation. More importantly, animal models may provide useful tools to understand and demonstrate the construct-validity of disease models, and to test the effects of putative medicines on the activity of specific brain circuits thought to be implicated in aspects of the human disease. Hence, the translational potential of a non-invasive imaging technique like fMRI is big and attractive for both basic and applied brain research.

However, a number of experimental constraints hamper the application of fMRI methods to small laboratory animals. Firstly, imaging experiments in rodents require the use of anaesthesia to prevent motion artefacts and to reduce animal stress (Flecknell 1987). Moreover, the vast repertoire of paradigms used to probe cognitive or emotional aspects of brain function in freely moving and behaving animals cannot be applied under the constrained experimental conditions of an fMRI experiment. As a result, the development of fMRI-based translational paradigms has lagged, with most of the preclinical fMRI research being reduced to the employment of basic somato-sensory stimulation paradigms of restricted translational value.

An interesting approach to overcome some of these limitations relies on pharmacological manipulation, and has been dubbed “pharmacological MRI” (phMRI) (Leslie and James 2000), i.e. fMRI as applied to map spatio-temporal patterns of brain activity induced by pharmacological challenges. Originally develop to study the circuital basis of pharmacological activity, the approach has demonstrated the ability to elicit robust and reliable fMRI signals even under anaesthesia, and to enable selective stimulation of different neurotransmitter systems (Jenkins et al. 2003).

Building upon the homology between brain circuits in humans and laboratory animals, phMRI techniques thus offer the attractive opportunity of significantly expanding the stimulation repertoire available to preclinical fMRI research, by allowing to selectively probe specific aspects of brain function under different experimental settings. Within this framework, my research activity has been dedicated to the development of refined phMRI approaches with the aim to broaden

the scope of application of preclinical fMRI both as a translational technique, when applied to clinically-relevant disease models, and more generally as a broad-spectrum platform for the pre-clinical investigation of brain activity and its functional topology under a number of preconditioning states. The results of this research highlight four significant examples of the translational potential and versatility of the technique both for applied and basic neuroscience research.

In a first group of studies, we developed a phMRI assay to map the circuitry activated by NMDAR antagonists in the rat. These compounds (i.e ketamine and PCP) are widely exploited pre-clinically and more recently in clinical research to model schizophrenia symptoms and to provide experimental models that may prove useful in the development of novel treatments for the human disorder. The results of this research (Section 4.1) showed a conserved cortico-limbo-thalamic circuit that is activated by NMDAR antagonists both in human volunteers and rodent species, and that can be modulated by existing and novel antipsychotic drugs.

The translational potential of phMRI measurements has been further corroborated by a second group of studies, where a multi-parametric phMRI-based approach was applied to investigate multiple facets of brain function in a rodent cocaine self-administration model, a behavioural paradigm of established construct-validity for research of drug addiction. This line of investigation (Section 4.2) highlighted specific basal and reactive brain functional alterations that are present both in human addicts and rat chronically self-administering cocaine, thus further underscoring the translational potential of the method.

In a third line of research, the combined use of advanced neuro-genetic targeting strategies and fMRI has proven successful in establishing direct correlations between cells, circuit and complex behaviours in genetically engineered mouse lines. These studies (Section 4.3) have led to the identification of a novel cell population in the amygdala that controls the behavioural response to fear through the recruitment of cholinergic circuits.

Finally, the phMRI approach has proven a powerful tool to explore functional connectivity in rodents, and to map a variety of different neurotransmitter pathways by performing measures of correlated phMRI responses in spatially remote brain areas. This latter aspect has also provided a useful playground to explore novel statistical methods of analysis of functional connectivity represented in terms of complex networks (Section 4.4).

4.1 phMRI of Phencyclidine: Imaging the Circuit of Psychosis and its Modulation

Schizophrenia is a debilitating mental disorder, characterised by abnormalities of thought and behaviour. Recent biochemical evidence suggests a significant patho-physiological contribution of glutamatergic alterations in specific symptomatic manifestations of the disease. The cornerstone of this hypothesis is the observation that glutamate N-methyl-D-Aspartate receptor (NMDAr) antagonists (i.e Phencyclidine – PCP, or ketamine) can induce perceptual abnormalities and psychotic symptoms in healthy humans resembling those observed in schizophrenic patients, a finding that has led to the hypothesis that a decreased NMDAR function may be a predisposing or even causative factor for this disabling disease (Kristiansen et al. 2007; Farber 2003). NMDAr antagonists are thought to exert their action through a selective disinhibition of GABAergic interneurons leading to a dysregulated glutamatergic activity (Figure 4.1).

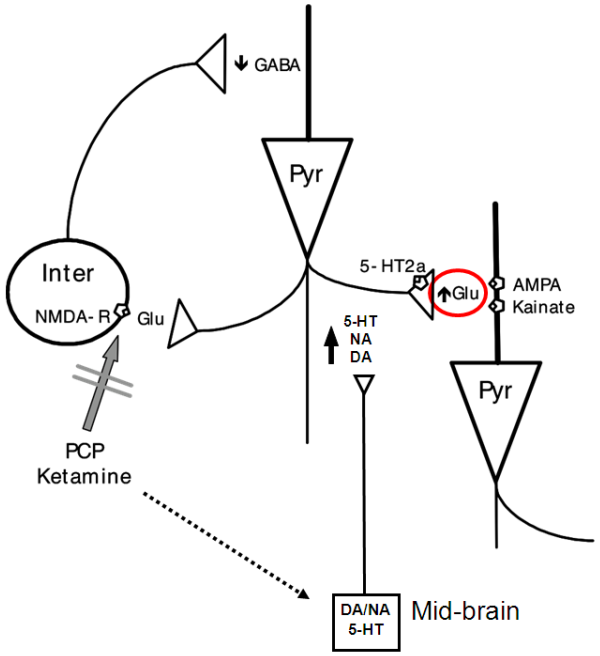

Figure 4.1

Model of the local neuronal circuit that is postulated to be involved in the psychotomimetic cascade elicited by ketamine and PCP (Large 2007; Gozzi et al. 2008a). GABAergic interneurons receive input and thereby exert inhibitory control on pyramidal cells (Pyr) through recurrent projections. In the presence of NMDAr antagonists, (i.e. PCP and ketamine) this local feedback inhibition becomes selectively disrupted (Greene 2001), an effect leading to an aberrant glutamatergic activity of pyramidal cells which may cascade to downstream neurotransmitter systems (DA: dopamine, 5-HT: serotonin, NA: noradrenaline)

The similarity between NMDAR antagonist-induced psychosis and schizophrenia is also widely exploited pre-clinically to model schizophrenia symptoms and to provide experimental models that may prove useful in the development of novel treatments for the human disorder. Specifically, the ability of drugs to inhibit behaviours induced

by NMDAR antagonists may be interpreted as a pharmacodynamic signal of pharmacological activity, or as a predictor of the efficacy of novel pharmacological treatments for schizophrenia (Large 2007). Within this framework, non-invasive neuroimaging techniques like phMRI can be applied to spatially-resolve the neuronal circuitry engaged by glutamate NMDAR antagonism in humans and preclinical species, thus providing a valuable translational tool for schizophrenia and psychosis research.

The use of NMDAr antagonists to model schizophrenia symptoms in preclinical models is however complicated by the strong dose-dependence of the effects they exert. Indeed, at sufficiently high doses PCP and ketamine act as anaesthetics and their psychotogenic effects arise only at lower, sub-anaesthetic doses (Krystal et al. 1994; Morris et al. 2005). As rodent neuroimaging studies are typically performed under anaesthesia, the interaction of NMDAr antagonists with the anaesthetic agents needs to be carefully assessed in order to identify workable doses and anaesthetic regimens.

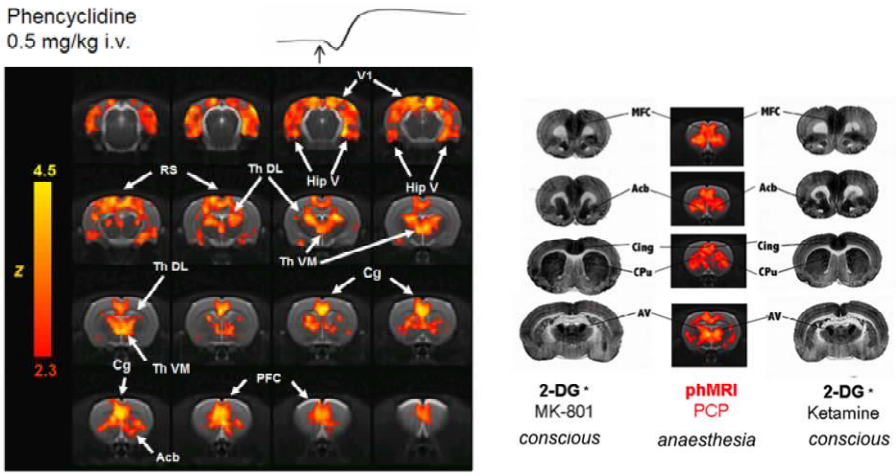

Figure 4.2

Left: Map of the cortico-limbo-thalamic loop activated by PCP in the rat brain (Appendix 2, Gozzi et al. 2008b). Right: Spatial correspondence of the regions activated by PCP and the 2-DG uptake produced by the PCP analogous MK-801 and ketamine in freely moving animals (Appendix 1, Gozzi et al. 2008c) (PFC or MFC, medial–prefrontal cortex; Acb, nucleus accumbens; Cing, cingulate cortex; CPu, caudate putamen; Rs, retrosplenial cortex; AV, anteroventral thalamus, MD, mediodorsal thalamus).

We developed a translational phMRI paradigm allowing a high-resolution investigation mapping of the circuits that are recruited by PCP in the rat. The role of potential experimental confounds (PCP dose and anaesthetic level) was systematically evaluated, in a series of experiments where the phMRI response to PCP in halothane-anaesthetised rats was mapped for varying levels of anaesthesia and different PCP challenge doses (Appendix 1, Gozzi et al. 2008c). As expected, both anatomical distribution and sign of the response depended strongly on anaesthetic

level and challenge dose, with sustained and widespread deactivation at higher PCP doses or anaesthesia levels, a signal of positive interaction between the drug and the anaesthetic agent (Appendix 1). However, at appropriate combinations of PCP and anaesthetic dose a focal and robust pattern of activation was observed in cortico-limbo-thalamic areas, including visual, orbitofrontal, cingulate cortices, the amygdala, dorsolateral and ventromedial thalamus, ventral and posterior hippocampus and basal ganglia.

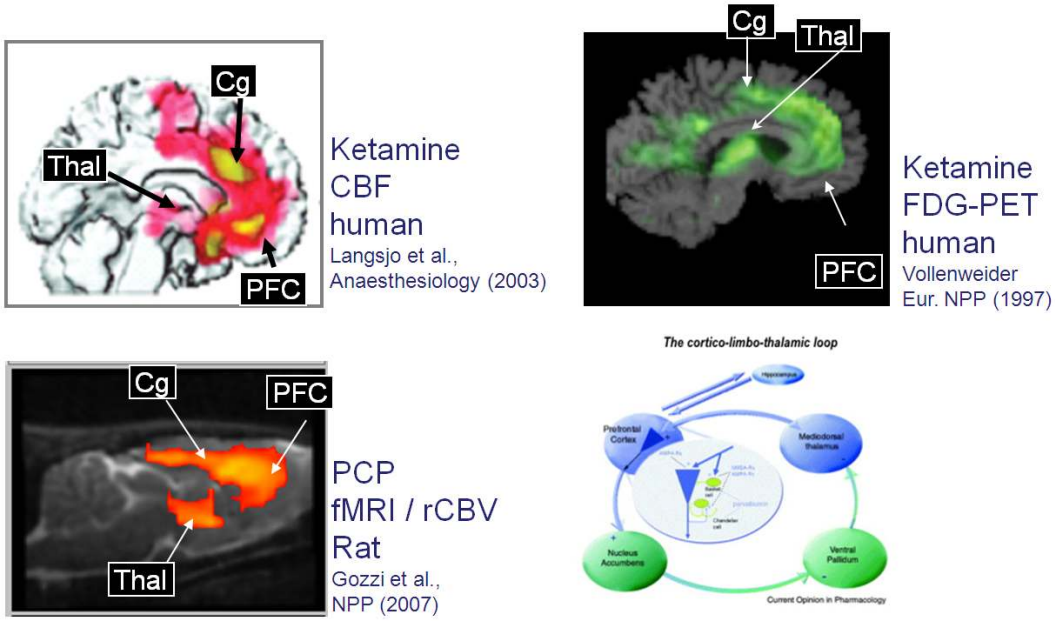

Figure 4.3

Conservation of the neural circuitry activated by acute administration of NMDAr antagonists in the rat (PCP) and human (Ketamine) brain. The results delineate the involvement of a focal and well-characterised cortico-limbo-thalamic network (Morris et al. 2005). PFC: prefrontal cortex; Cg: cingulate cortex; Thal: thalamus.

Notably, the activation pattern highlighted in these studies is consistent with that observed in conscious rats with 2-deoxyglucose autoradiography (Duncan et al. 1998b; Duncan et al. 1999; Duncan et al. 1998a; Miyamoto et al. 2000), single unit electrophysiological recording (Homayoun et al. 2005), [14C]-iodoantipyrine CBF measurements (Cavazzuti et al. 1987) and immediate-early gene expression (Nakki et al. 1996). Thus, a judicious choice of anaesthetic regimen and drug dose appears to preserve the neuro-anatomical substrates stimulated by NMDAR antagonists in conscious subjects. Importantly, a good correspondence (Figure 4.3) was also found between these animal findings and the patterns of brain activity measured in humans under ketamine infusion using either metabolic (FDG-PET) or haemodynamic (BOLD) neuroimaging techniques (Deakin et al. 2008; Gozzi et al. 2008b; Langsjo et al. 2003). Hence, the circuitry recruited by acute NMDAR antagonism appears to be consistent across species and imaging modalities, thus making the use of NMDAr antagonists an attractive translational paradigm (Figure 4.1).

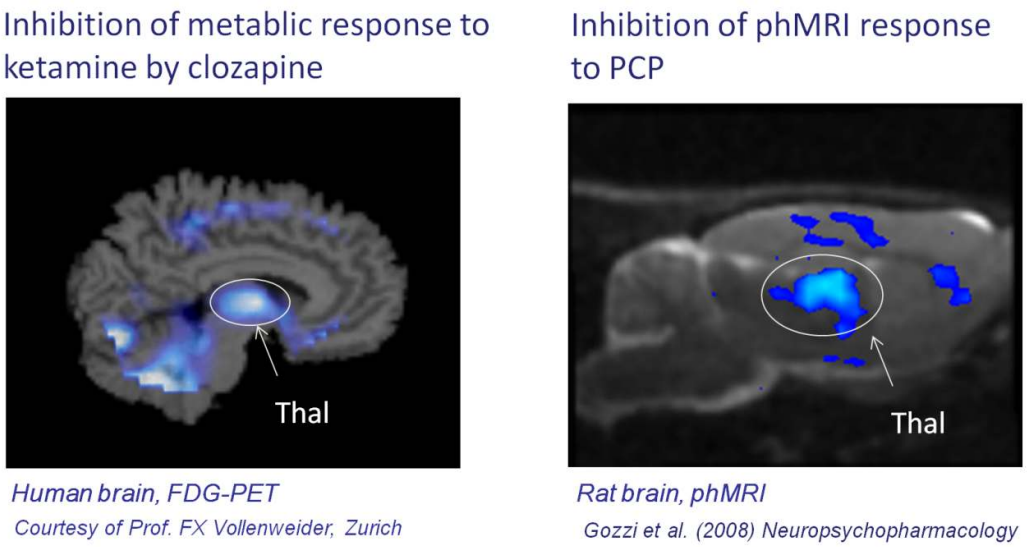

Figure 4.4

The antipsychotic clozapine produces a focal thalamic inhibition of the functional response to NMDAr antagonism both in the human (left) and in the rat brain (right) (Appendix 2, Gozzi et al. 2008b).

The focal nature and anatomical localisation of the pattern of activation produced by NMDAR antagonism may provide important information regarding the circuitry mediating psychosis. A number of clinical neuroimaging studies show evidence of a strong correlation between fronto-thalamo-hippocampal hyperactivity and cognitive and perceptual alterations observed in unmedicated schizophrenia patients (Silbersweig et al. 1995; Liddle et al. 2000; Parellada et al. 1994; Ngan et al. 2002; Soyka et al. 2005). Moreover, functional impairment of limbic cortical areas such as cingulate and retrosplenial cortices has been associated with the development of thought disorder, disturbance of consciousness, and overall cognitive decline (Mitelman et al. 2005; Kircher and Thienel 2005). Likewise, the identification of robust foci of activation in the thalamus is in agreement with recent evidence supporting a critical role of thalamic gating disturbance in the pathophysiology of schizophrenia (Clinton and Meador-Woodruff 2004). Finally, PCP-induced activation of mesolimbic and nigrostriatal structures is in good agreement with the classical dopamine hypothesis of schizophrenia, where dysregulation of dopamine transmission is implicated in the onset of positive symptoms (Carlsson et al. 1999). These observations demonstrate a significant degree of correspondence between the brain areas activated by PCP challenge, and some of the key brain circuits that are thought to be dysfunctional in schizophrenia. This suggests that phMRI with NMDAR antagonists may provide a useful paradigm to study the neuroanatomical substrate of psychosis, and to test the effects of existing and putative antipsychotics on these circuits.

We therefore investigated the modulatory effects of several antipsychotic agents with distinct pharmacological mechanisms on the patterns of activation induced by PCP in the rat (Appendix 2, Gozzi et al. 2008b). Dopaminergic agents like the dopamine D_2 receptor antagonists raclopride did not significantly affect the response to PCP, consistent with a downstream implication of the dopamine system with respect to the mechanism that elicits the phMRI response to the PCP challenge. On the other hand, agents known to inhibit aberrant glutamatergic activity, like metabotropic glutamate receptors (mGluR2/3) agonists LY354740, or the sodium channel blocker lamotrigine, suppressed entirely the activation induced by PCP, thus indicating a primary role of glutamatergic neurotransmission in the functional response to PCP. Consistent with this notion, in another study (Appendix 3, Gozzi et al. 2008a), we showed that stimulation of the glycine co-agonist site of the NMDAR either by direct agonism with D-serine, or by blockade of glycine re-uptake with the glycine transporter type 1 (GlyT-1) inhibitor SSR504734 completely prevented PCP-induced phMRI activation in anaesthetised rats. Some of these findings in animal models have been confirmed in psychobiological (Anand et al. 2000) or neuroimaging (Deakin et al. 2008) studies with the NMDAR antagonist ketamine in humans. Interestingly, the mGluR2/3 receptor agonist LY2140023 was shown to provide significant therapeutic benefit to schizophrenia patients in a randomised phase-II clinical trial (Patil et al. 2007), a finding that has not been replicated in a recent second study, where however a larger-than-anticipated effect in the placebo group was observed (Kinon et al. 2010). Although further research is needed to ascertain the exact therapeutic contribution of this mechanism in schizophrenia, the limited clinical data produced so far support a putative physio-pathological role of NMDAR dysfunction and the translational use of neuroimaging assays exploiting the psychotogenic effects of NMDAR antagonists.

The ability of neuroimaging methods to resolve the anatomical distribution of the pattern of activation is critical to identify the neuronal substrate of drugs with multi-receptor targets. In one study performed in our lab, (Appendix 2, Gozzi et al. 2008b), pre-treatment with the prototypical second-generation antipsychotic clozapine, a drug characterized by a complex receptor profile (Meltzer 1996), resulted in a region-dependent modulation of the phMRI response to PCP, with complete suppression of the functional response in the thalamus (Appendix 2, Gozzi et al. 2008b). Importantly, analogous thalamic effects were observed when clozapine was used as a pretreatment to ketamine in human volunteers (FX Vollenweider, Zurich, personal communication, Figure 4.4). In the light of the key role of altered thalamic gating to the etio-pathology of schizophrenia, it is tempting to interpret the region-dependent effect of clozapine as a mechanistic marker of its superior antipsychotic efficacy, particularly in refractory patients.

Individual components of the complex profiles of many antipsychotics can be studied using the PCP/phMRI paradigm in combination with selective tool compounds. In another study (Appendix 4, Gozzi et al. 2010a), selective serotonin $5HT_{2A}$ receptor antagonism, an important component of clozapine and other second generation antipsychotics, was shown to regionally inhibit the pattern of activation produced by PCP in the septo-fronto-hippocampal circuit (Figure 4.5). This observation is of particular interest given the ample clinical evidence suggesting a correlation between fronto-hippocampal hyperactivity and cognitive and perceptual alterations in unmedicated schizophrenia patients (Silbersweig et al. 1995; Liddle et al. 2000; Parellada et al. 1994; Ngan et al. 2002; Soyka et al. 2005; Medoff et al. 2001). Notably, glucose metabolism studies using PET demonstrated a tight correlation between depression of cortico-hippocampal activity and antipsychotic action elicited by a single-dose of the atypical anti-psychotic risperidone (Liddle et al. 2000), thus corroborating the clinical significance of this circuit in schizophrenia. Collectively, all these pre-clinical and clinical findings support the use of NMDAR antagonist in combination with phMRI as a valuable translational paradigm to study the neuropathological processes that might contribute to the symptoms of schizophrenia, and to investigate how these processes are modulated by antipsychotic agents.

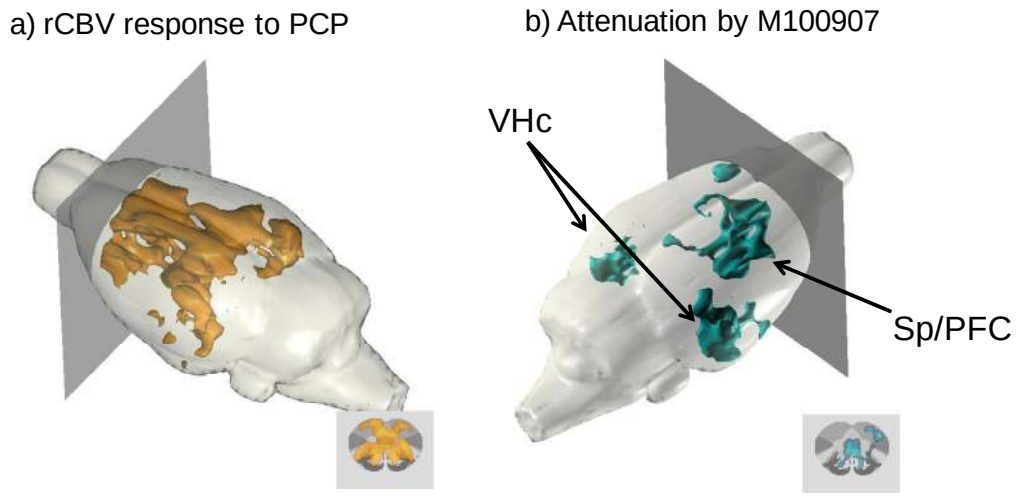

Figure 4.5

The selective 5-HT_{2A} antagonist M100907 selectively inhibits the functional response to the NMDAr antagonist PCP in the fronto-septo-hippocampal circuit (Appendix 2, Gozzi et al. 2010a).

4.2 Multi-parametric Assessment of Brain Function in Disease Models: the Cocaine Self-Administration Paradigm

Chronic cocaine use produces complex and long-lasting neurobiological changes that are thought to underlie the loss of control over drug intake that defines cocaine dependence (Koob et al. 1998). A number of clinical imaging studies have started to shed light on the nature of these complex neuro-adaptational changes. For example, reduced fronto-striatal perfusion and metabolism in abstinent cocaine abusers have been consistently observed (Strickland et al. 1993; London et al. 1999; Volkow et al. 1992). It has been proposed that disrupted function of frontal regions may contribute to the persistent neuropsychological deficits and the impaired control over drug taking that frequently triggers relapse (Strickland et al. 1993; Kalivas 2004). Moreover, several positron emission tomography (PET) studies with selective D_2 dopamine (DA) ligands have demonstrated persistent decreased dopaminergic responsivity in components of the "reward circuit" in cocaine addicts, an abnormality that may contribute to the decreased sensitivity to natural reinforcers experienced by these subjects (Volkow et al. 2007). Finally, recent research suggests that altered functional connectivity of catecholamine circuits may underlie the lower recruitment of subcortical resources and impaired inhibition of cortical function observed in cocaine abusers, a finding that describes novel pathways for the neuroadaptational processes associated to addictive states (Tomasi et al. 2010; Gu et al. 2010).

Cocaine addiction can be effectively modelled in experimental paradigms where rodents are trained to self-administer the drug. These models reproduce several hallmark features of drug addiction, including compulsive drug seeking, uncontrolled drug use, and increased motivation to self-administer the drug (Vanderschuren and Everitt 2004; Ahmed and Koob 1998; Paterson and Markou 2003). These features make these models an experimental tool of excellent face-validity to investigate the neuroplastic events associated to voluntary drug-intake at a cellular and behavioural level (Roberts et al. 2007). However, specific clinical correlates of cocaine addiction, such as the blunted DA responsivity of striatal areas observed in PET studies, do not appear to be adequately modelled by traditional limited-access time-limited cocaine SA paradigms, where instead "sensitised" (i.e. increased) dopaminergic responses are typically observed (reviewed by Narendran and Martinez 2008). Moreover, the exact degree to which these models replicate the multiple neuro-functional alterations observed in human neuroimaging studies remains unknown.

In order to address these questions, we have used a multi-parametric MRI protocol to map basal and evoked brain function in a rat model of chronic cocaine self-administration (SA) (Appendix 5). A prolonged (52 days), extended-access (12 hours) SA protocol was employed to model the characteristics of high-dose, chronic cocaine abuse in humans (Gawin and Ellinwood 1988), and repeated abstinence periods were

introduced to minimize the acute toxic effects of the drug. We measured basal cerebral blood volume (bCBV) as an indirect indicator of basal brain function, and assessed the reactivity of dopaminergic system by mapping the phMRI response to an acute challenge with the dopamine-releaser D-amphetamine. Moreover, correlation analysis (Section 4.4) between resting (bCBV) and amphetamine-evoked (rCBV) responses was performed in an attempt to identify disregulation in circuits that control the recruitment and functional responsiveness of specific brain areas. Finally, post mortem histo-pathological examinations were carried out to assess the potential contribution of direct vascular and neurotoxic effects of cocaine to the imaging findings.

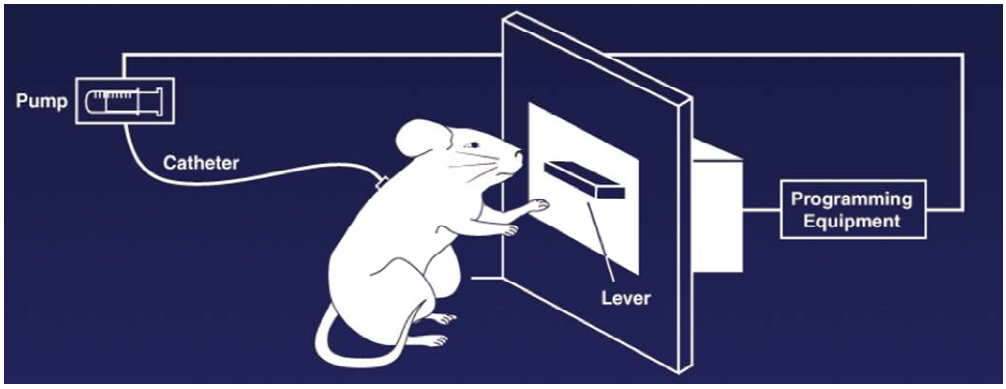

Figure 4.6

Cocaine self-administration paradigms are employed to mimic the cellular, behavioural and neuro-adaptational effects of long-term cocaine intake in laboratory animals. The experimental subjects are trained to press a lever that induces a self-injection of behaviourally active doses of the drug (modified from Caine et al. 1993).

Rats chronically exposed to cocaine exhibited significantly reduced bCBV in regions that play a key contribution in higher cognitive functions and inhibitory control (fronto-cortical areas), craving and anticipation (fronto-hippocampal areas) and reward (mesolimbic areas, Figure 4.7). These data highlight an excellent agreement with clinical neuroimaging research of cocaine addiction, where reduced frontal and striatal perfusion during protracted withdrawal has been observed by several investigators (Strickland et al. 1993; Tumeh et al. 1990; London et al. 1999; Volkow et al. 1992; Volkow et al. 1988) and found to correlate with cognitive impairment, compulsion and loss of inhibitory control over drug which frequently triggers relapse (Strickland et al. 1993; Kalivas 2004; Kalivas et al. 2005). Importantly, analogous cognitive deficits have been observed in rats allowed extended (but not limited) access to cocaine (Briand et al. 2008), a phenomenon that involved working memory and sustained attention tasks (two prefrontal-cortex-dependent tasks) as well as object recognition measures (a hippocampus dependent task).

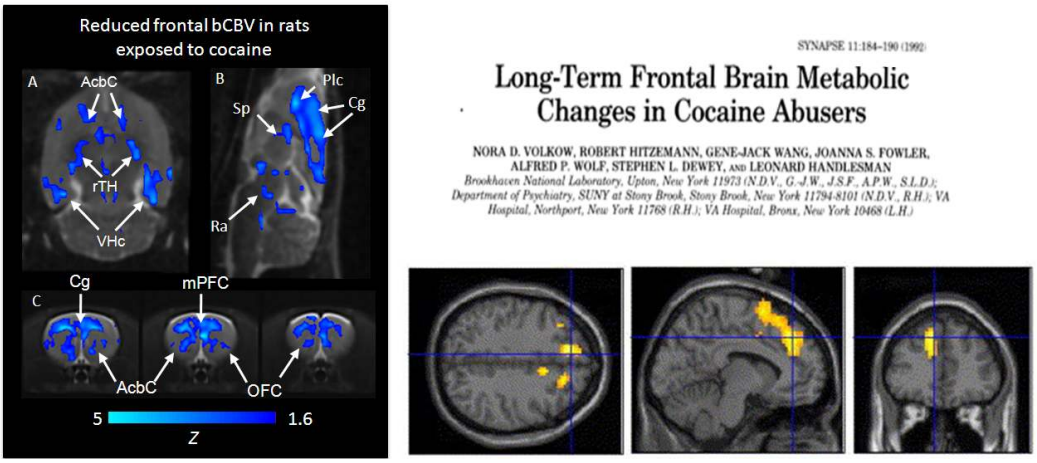

Figure 4.7

Chronic cocaine intake produces reduced frontal bCBV in the rat brain (Right, Gozzi et al., submitted), an effect that correlates well with clinical findings of reduced frontal perfusion (bottom panel, Tucker et al. 2004) and metabolism (Volkow et al. 1992) in cocaine addicts.

The SA group also exhibited a weak but significant reduction in striatal response to D-amphetamine, an effect that was significantly correlated with the total cocaine intake (Figure 4.8). Since previous phMRI studies (reviewed by Knutson and Gibbs 2007) have provided robust evidence that the striatal haemodynamic response produced by D-amphetamine reflect primarily dopaminergic effects, this finding points towards a reduced-responsivity of ventro-striatal dopaminergic function analogous to that demonstrated in PET studies in humans (Narendran and Martinez 2008). These results provide for the first time a plausible preclinical neuroimaging correlate of one of the most replicated clinical manifestation of cocaine addiction, which is believed to play a key contribution to the anhedonia and amotivation reported by drug-addicted subjects during protracted withdrawal (Volkow et al. 1997). Importantly, this result documents a potentially important correspondence between clinical and preclinical neuro-adaptational changes induced by cocaine on DA systems, an aspect that does not appear to be adequately modelled by traditional cocaine exposure paradigms, where “sensitised” (i.e. increased) dopaminergic responses are typically observed (reviewed by Narendran and Martinez 2008).

Finally, correlation analysis between resting (bCBV) and amphetamine-evoked (rCBV) responses revealed an inverse relationship between bCBV in the reticular thalamus and posterior thalamus, and frontal activation due to d-amphetamine in control subjects but not in the cocaine group (Appendix 5). The presence of an inverse relationship between tonic reticular thalamic activity and evoked frontal function is consistent with the functional connectivity of these regions (Paxinos 2008) and the GABAergic composition of the reticular thalamus (Paxinos 2008). As prefrontal projections to the thalami reticular nucleus have been suggested to play a unique circuit for attentional mechanisms (Zikopoulos and Barbas 2006) we speculate that

the loss of correlation between basal and evoked function in cocaine SA subjects may be indicative of an altered inhibitory interplay between these structures which may underlie some of the attentional deficits observed in rats allowed extended access to cocaine (Briand et al. 2008). Importantly, histopathological examinations did not show significant vascular or cellular aberrations n the brain of SA subjects, thus ruling out major unspecific pathological or vascular contributions to the imaging findings.

Taken together, these findings provide evidence of altered brain function in rats that underwent prolonged and extended access cocaine self-administration. Consistent with clinical neuroimaging findings, cocaine-exposed animals revealed reduced basal brain function in fronto-cortical and thalamic areas, and attenuated responsivity in striatal regions upon challenge with the DA releaser D-amphetamine, an effect that was significantly correlated with the total cocaine intake. The consistency of these findings with neuroimaging measures in cocaine-addicted patients supports the use of prolonged and extended-access SA paradigms in the rat to investigate the neuro-adaptations underlying cocaine-addiction, and highlight an important contribution of phMRI approaches to facilitate translational research of drug addiction.

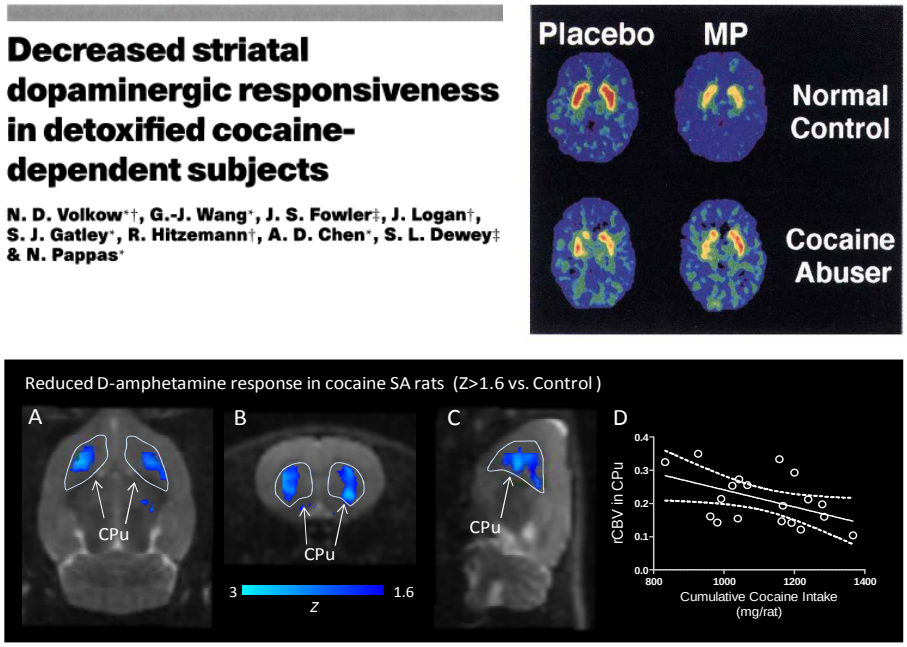

Figure 4.8

Top: Chronic cocaine intake is associated with reduced dopaminergic responsiveness in striatal regions, a finding originally described by Volkow et al (1997) using PET and the dopamine-releasing agent methylphenidate (MP) as molecular probe. Similar findings were observed in the rat brain (Gozzi et al., submitted) using phMRI with the dopamine release amphetamine (bottom, A,B,C). The effect was significantly correlated to the cumulative amount of cocaine self-administered by the subjects

4.3 Linking Circuit and Behaviour: Mapping the Circuit of Fear with Pharmacogenetic Silencing and phMRI

Recent advancements in mouse genetics have led to the development of methods to induce transient and cell-type-specific silencing of neuronal activity *in vivo (Luo et al. 2008; Lee et al. 2010)*. In combination with behavioural observations, this novel approach provides a powerful means to assess the functional contributions of specific neuronal population to specific behaviours. Crucially, if combined with spatially-resolved techniques such as fMRI, these methods offer the unprecedented opportunity to reveal the circuital basis of specific behaviours.

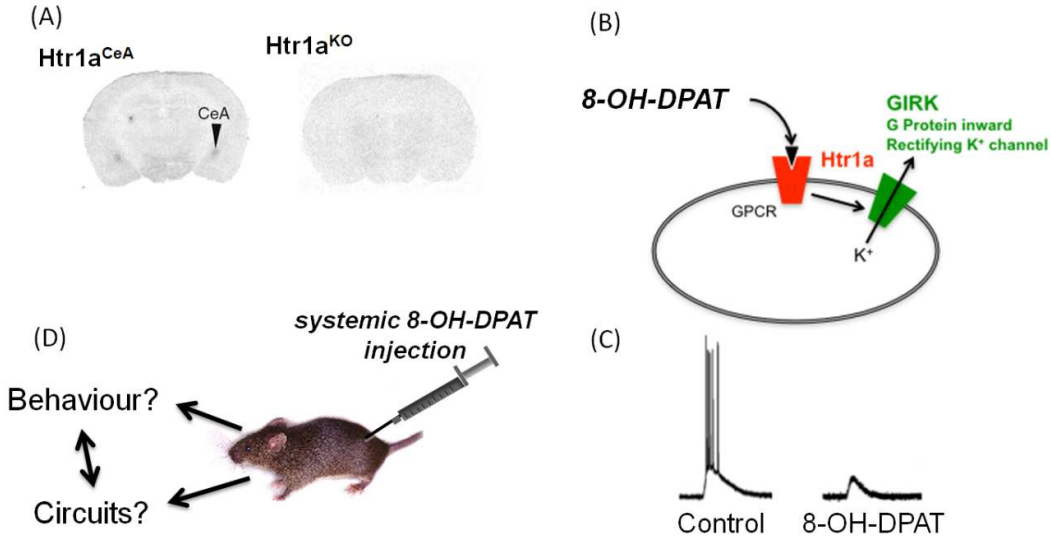

Figure 4.9

Pharmacogenetic silencing of a discrete neuronal population ("Type I") in the central nucleus of the amygdala (CeA). (A) A mouse line expressing the serotonin receptor Htr1a only in selected neurons of the CeA has been devised by Dr. C. Gross and T. Tsetsenis at EMBL Monterotondo (Tsetsenis et al. 2007). (B) The Htr1a receptor is coupled to GIRK potassium channels, and its activation by selective agonists (i.e. by the compound 8-OH-DPAT) (C) induces rapid and reversible membrane hyper-polarization of the cells expressing the receptor. (D) Systemically-administered Htr1aR agonists can be used to obtain cell-specific inhibition of spontaneous neuronal firing in behaving animals and correlate the behavioural output with phMRI measures of circuital activation.

In a work performed in collaboration with Dr Gross (EMBL, Rome) we have provided the first demonstration of the combination of fMRI and tissue-specific pharmacogenetic silencing (Figure 4.9) to spatially resolve behaviour-specific circuits controlled by focal neuronal populations in the mouse brain (Appendix 6, Gozzi et al. 2010b). Specifically, we combined phMRI, functional connectivity analysis (Section 4.4), c-Fos mapping and behavioural measures to examine the effect of inhibition of neural activity in a subset of neurons of the central nucleus of the amygdala (CeA), a key structure involved in the control of emotional and fear responses (Aggleton 1992;

LeDoux 2000; Davis and Whalen 2001). Reversible suppression of neural activity in a subset ("Type-I") of CeA neurons was achieved by inducing tissue-specific re-expression of the serotonin 1A receptor (Htr1a) in mice devoid of the endogenous receptor, a strategy recently described by Gross and co-workers (Tsetsenis et al. 2007). The Htr1aR is coupled to GIRK potassium channels, and its activation induces rapid and reversible membrane hyper-polarization of the cells expressing the receptor. Hence, the use of systemically-administered Htr1aR agonists (like the selective compound 8-OH-DPAT) can be exploited to obtain cell-specific inhibition of spontaneous neuronal firing in behaving animals (Tsetsenis et al. 2007). At the same time, the pharmaco-genetic inhibition strategy is optimally-suited to be implemented as an phMRI paradigm to map the downstream functional effects of CeA silencing, and to correlate the observed circuital responses with the behavioural and cellular events associated to the silencing of Type-I amygdala neurons.

By using this approach, we were able to identify a novel pathway in the mammalian brain apt to regulate passive and more active components of fear responses (Appendix 6, Gozzi et al. 2010b). Specifically, selective inhibition of CeA Type-I neurons led to decreased conditioned freezing behaviour, and widespread increased cortical arousal as visualized by phMRI upon acute administration of the selective Htr1AR agonist 8-OH-DPAT (Figure 4.10). Inter-subject functional connectivity analysis of phMRI time-courses was critical in resolving the neuronal circuitry underlying the increased cortical activity. Significant correlation was found between the CeA and several ventral forebrain cholinergic nuclei such as the substantia innominata and the diagonal band, and the same cholinergic nuclei exhibited tight correlations with the cortical areas activated upon inhibition of type-I CeA neurons. The involvement of the cholinergic system was confirmed in additional phMRI studies showing that the cortical arousal was blocked by central (but not peripheral) cholinergic antagonists. Remarkably, an analysis of the behavioural correlates of cortical activation in $Htr1a^{CeA}$ mice highlighted a pivotal role of type-I CeA cells as suppressors of cholinergic- activity and exploratory behaviour and promoters of freezing (passive) fear responses, thus leading to the identification of a novel neural pathway that biases fear responses toward either passive or active coping strategies.

Methodologically, this work expands the applicability of phMRI and functional connectivity analyses to genetically-modified mouse models, and provides at the same time a first, compelling demonstration of the combined use neuroimaging methods and advanced pharmaco-genetic systems as a new powerful paradigm to identify and resolve behaviourally-relevant neural circuits in the living brain.

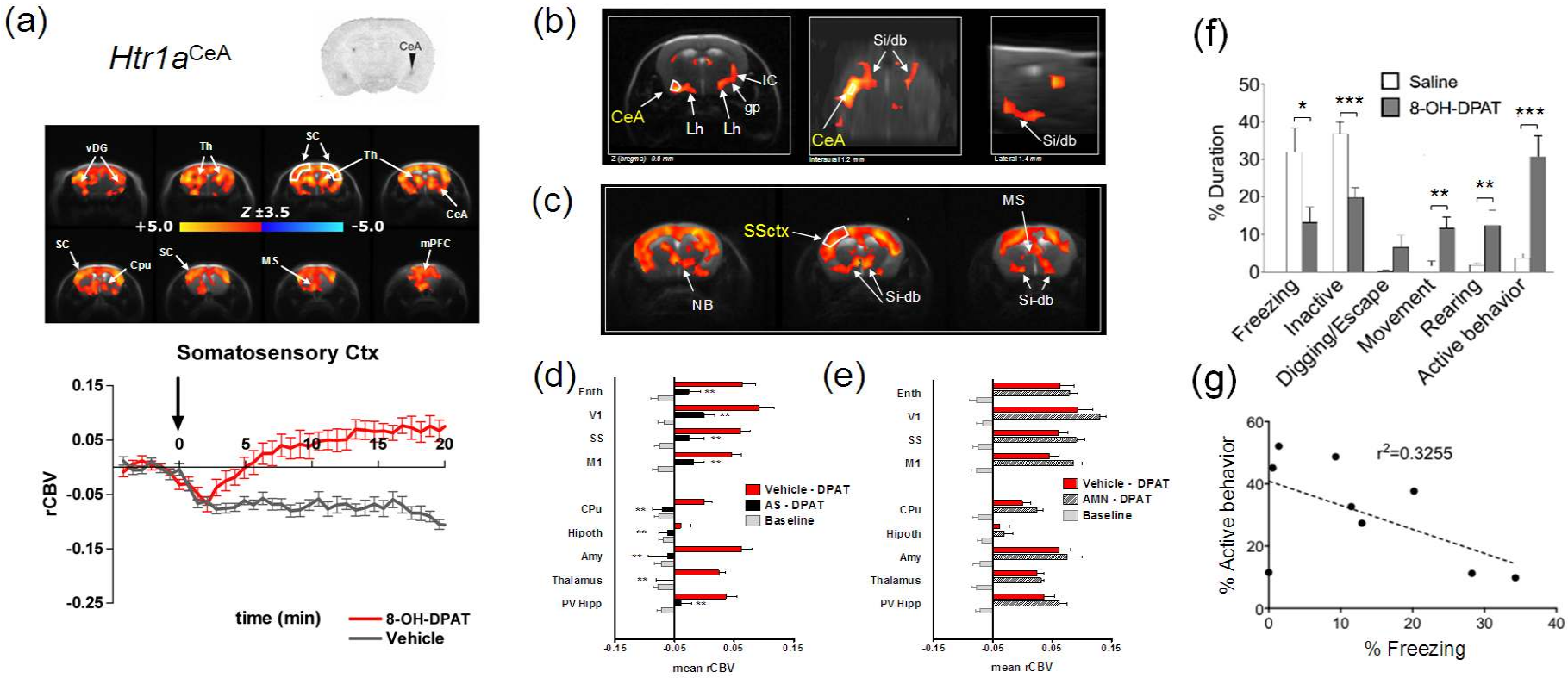

Figure 4.10

(a) Cortical arousal following suppression of type-I CeA cells. (b,c) Ventral forebrain cholinergic neurons are a downstream target of the CeA. Maps of 8-OH-DPATinduced rCBV response significantly correlated with CeA (b) or somatosensory cortex (c) in Htr1aCeA mice (d,e) Cortical arousal depends on central cholinergic neurotransmission. Pretreatment with atropine sulphate (AS, d) but not the non-brain penetrant salt AMN, (e) suppressed the mean rCBV response to 8-OH-DPAT (f, g) Decreased passive and increased active behavioural responses to conditioned aversive stimulus (adapted from Gozzi et al. 2010b, Appendix 6).

4.4 Functional Connectivity Analysis of Brain Circuits with phMRI

Functional Magnetic Resonance Imaging has been instrumental to study brain functional segregation, i.e. the functional specialization of discrete brain regions engaged by specific stimuli (Posner et al. 1988). However, while the evidence of functional specialization of brain cortical regions appears compelling, even the simplest sensorimotor task involves the integrated activity of multiple brain areas (Luria 1973), a notion consistent with the dicothomic principles of functional segregation and integration underlying the brain's functional organization. Hence, multivariate analyses of fMRI time series can be applied to assess *interactivity* among different structures (Rogers et al. 2007; Friston et al. 1994). These approaches rely on the evaluation of some definition of correlation or covariance between spatially remote neurofunctional events. In this context, statistical dependencies among signals originating in different brain regions are interpreted in terms of *functional connectivity*, as opposed to *structural connectivity*, which denotes the presence of physical neuronal connections between remote brain structures (Ramnani et al. 2004).

The inception of fMRI has significantly expanded the repertoire of methods to study functional interactivity in the human brain. The recent discovery that spontaneous, low frequency fluctuations in the fMRI signals from the human brain at rest exhibit coherent patterns within defined networks has opened an interesting avenue of investigation, often referred to as "resting-state fMRI"(Beckmann et al. 2005). By way of example, a network of functional connectivity corresponding to brain regions whose activity is higher at rest than during an experimental task has been identified, and interpreted as evidence in support of the existence of a "default mode" of baseline brain function (Greicius et al. 2003). Interestingly, alterations in resting state functional connectivity have been observed under a number of pathological conditions, including Alzheimer's disease (Li et al. 2002), multiple sclerosis (Lowe et al. 2002) and schizophrenia (Zhou et al. 2008).

While there is a large body of work assessing functional connectivity in the human brain, the extension of these methods to pre-clinical species, and particularly to rodents, is very recent (Bifone et al. 2010). Several studies in laboratory animals have followed the path of human resting state fMRI. Synchronous low-frequency fluctuations were detected in bilateral primary somatosensory cortex in the rat brain at rest under different anaesthetic conditions (Pawela et al. 2009; Pawela et al. 2008; Zhao et al. 2008). All these studies used a seed-correlation region approach (i.e. signal time-course correlations were computed with respect to a specific region chosen by the experimenter a priori) and demonstrated encouraging correlations between bilaterally symmetrical cortical regions. However, coherent networks of

connectivity akin to those observed in humans (e.g. the default mode network) have not been observed in the rat using this method to date. Whether this reflects experimental impediments (e.g. the use of anaesthesia, or high stress-levels due to restraint) or rather a different functional architecture of the rodent brain with respect to that of higher species such as primates is the subject for further investigation.

A conceptually different approach to the study of functional connectivity in rodents has been explored in our lab using pharmacological MRI. The strategy has proven very effective in determining the circuital and neurochemical basis of pharmacologically-evoked fMRI responses. Several recent studies using this approach have shown exquisite delineation of focal patterns of correlated responses corresponding to key neurotransmitter pathways (Schwarz et al. 2007b; Schwarz et al. 2007a; Schwarz et al. 2007c; Schwarz et al. 2008; Schwarz et al. 2009). Moreover, network analysis of functional connectivity patterns obtained with phMRI has provided the first evidence of organized networks of functional connectivity in the rat brain, thus demonstrating the potential of this method to explore the brain functional architecture.

4.4.1 Correlation Analysis in phMRI

Functional connectivity analysis of phMRI data requires image analysis approaches that are substantially different from those applied to study low frequency spontaneous fluctuations. The approach relies on a calculation of interregional correlations in the response amplitude across subjects (Schwarz et al. 2007b), in the fashion of the procedures applied in metabolic PET or autoradiography studies (Horwitz et al. 1984; Soncrant et al. 1986). Schematically, the correlation analysis procedure used in phMRI studies can be summarized in terms of the following steps. First, individual subject time series are co-registered to a common stereotaxic space (Schwarz et al. 2006a). Time courses from individual image voxels are then extracted for each subject, and suitable regressors are fitted to the data to determine response amplitudes. These values provide voxel-specific vectors of response amplitude across subjects. Inter-subject correlations are then calculated for each voxel in reference to a selected ‘seed’ region, using the vector of response amplitudes from step B. Finally, statistical correlation maps, i.e. maps of voxels whose response amplitude correlates significantly (in a statistical sense) with those in the reference region are generated. This approach leverages variations in the spatial profile of the response observed across subjects following drug challenge. Figure 4.11 provides an outline of this process, and an exaggerated visual impression of the intersubject variability in the phMRI response profile.

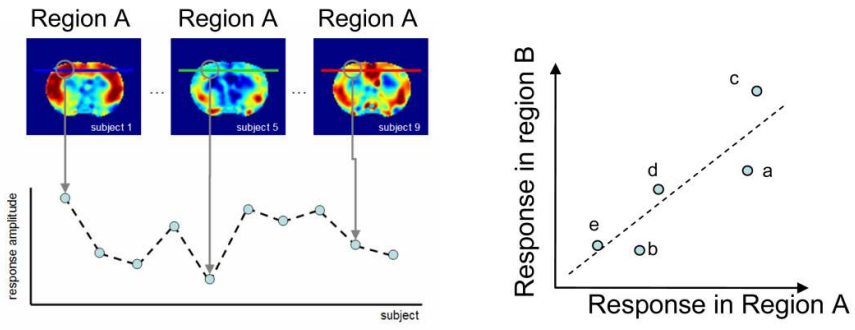

Figure 4.11

Schematic overview of the principle underlying across-subject functional correlation. Different subjects show different spatial profiles of responses to the pharmacological challenge. This variability is leveraged to extract response vectors for each image voxel (left-hand panel). Intersubject correlations are then calculated for each pair of image voxels or for a voxel in reference to a seed region.

The first demonstration of this approach applied correlation analysis of rCBV changes in the rat induced by acute challenge with D-amphetamine and fluoxetine, two widely used drugs that target key monoaminergic systems (Schwarz et al. 2007b). D-amphetamine stimulates the pre-synaptic release of dopamine, and the psychoactive and reinforcing properties of the compound are thought to be mediated by stimulation of the mesolimbic dopamine pathway, a small bundle of neurons originating from the ventral vegmental area (VTA) in the midbrain. Consistent with this hypothesis, correlation maps of phMRI responses referenced to the VTA clearly delineated the parallel major axes of this pathway forward through the ventromedial thalamus to the ventral striatum (Figure 4.12). In the same work, correlation analysis of the phMRI response to fluoxetine, a clinically effective antidepressant, revealed a focal delineation of major ascending serotonergic projections to the forebrain and cortex, in keeping with the drug's mechanism of action. This study represented the first *in vivo* demonstration of functional connectivity in discrete neurotransmitter systems. The correlation analysis was guided by a judicious choice of seed region that was informed by previous knowledge of the systems under investigation. However, similar findings were obtained using a hypothesis-free k-means cluster analysis without prior definition of a seed correlation region (Schwarz et al. 2006a), an optimization-based method that minimizes a distance measure between the *n* response vectors. This result significantly expands the scope of application of the approach, by allowing the implementation of computational approaches free of operator bias.

In the phMRI approach, a drug challenge serves the purpose of eliciting a brain response whose intersubject variability provides a basis to calculate interregional correlations. From a pharmacological point of view, it is also important to ascertain whether drug treatment can *modulate* brain functional connectivity, since this might shed light on the drug mechanism of action at a systems level. One interesting

approach to addressing this problem has been proposed by our lab (2007c), whereby the effects of a compound of interest (DA D_3 receptor antagonist) was shown to produce a region-dependent modulation of the correlated responses to a different probe compound (D-amphetamine). Methodologically, this study extended the applicability of inter-subject functional connectivity analyses of phMRI data to antagonist-agonist experiments, where modulations in the correlation structure underlying the response to a probe signal may be detected.

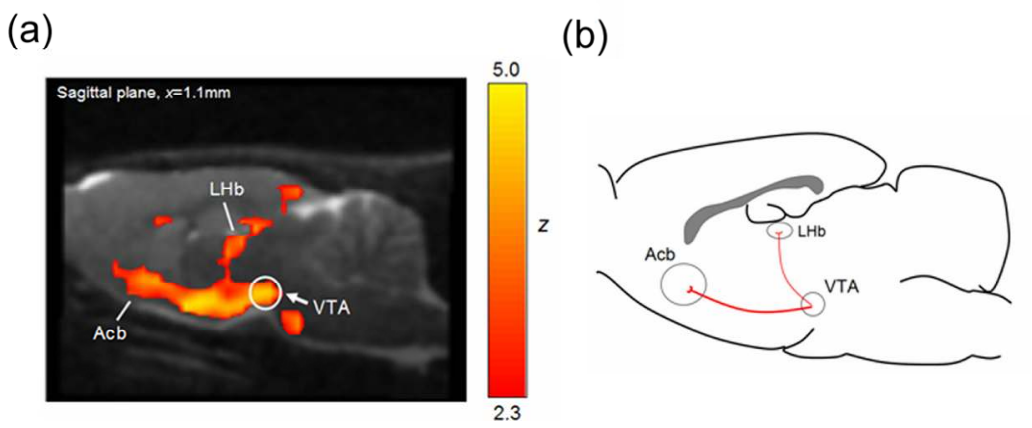

Figure 4.12

(a) Map of the responses to D-amphetamine covarying (across-subjects) with that in the ventral tegmental area (VTA). (b) The pattern of connectivity delineates the mesolimbic DA pathway extending forward to the striatum.

4.4.2 Complex Network Analysis of Functional Connectivity in the Rat Brain

Functional connectivity analyses of neuroimaging data aim to elucidate relationships between signals originating in spatially distinct brain regions. This emphasis on interaction between different brain structures is a good conceptual match for representing the data as a graph, or network, of nodes and links. In this representation, image voxels or parcellated brain regions represent the nodes, and a measure of similarity or correlation in their responses defines the edges linking the nodes (Salvador et al. 2005; Eguiluz et al. 2005; Achard et al. 2006; Achard and Bullmore 2007). In recent years, networks from a wide variety of fields have been characterized and found to exhibit rich behaviours beyond those of simple random networks; accordingly, they are referred to as 'complex networks' (Strogatz 2001). Network analysis of functional connectivity data to date has concentrated on the characterization of global properties of the network, which can reveal much about the properties of the system. For example, networks derived from human brain imaging data have been shown to possess a scale-free degree distribution and exhibit 'small world' behaviour–a finding that has implications for information transfer in the brain(Bullmore and Sporns 2009).

Complex networks of functional connectivity derived from phMRI data in the rat have been recently investigated in our laboratory (Schwarz et al. 2008; Schwarz et al. 2009). In these works, the nodes were defined as individual image voxels (0.128 mm^3) in the 3D image volume, and the strength of the *edge* between each pair of nodes was based on the Pearson correlation coefficient between the inter-subject response amplitude vectors in the two voxels. This value was converted into an equivalent *z*-statistic using Fisher's *r*-to-*z* transformation. The magnitudes of these normalized correlation values were used to describe the strength of the correlation between each pair of nodes and used to construct an edge weight matrix. Finally, the edge weight matrix was thresholded and binarised to define a binary adjacency matrix. Analysis of the structural properties of the resulting networks outlined interesting topological features, including a small-world structure, and a long tailed distribution of node degrees (i.e. number of connections for certain node), indicative of the presence of hubs, namely a subset of highly connected nodes in cortical regions.

Beyond global characterization, the coexistence of functional segregation and integration in brain activity suggest that some degree of modularity i.e., sub-networks or clusters of more tightly linked nodes, might exist within functional connectivity networks. This concept originated in the study of social relationships and has been consequently dubbed "community" structure. The first application of this concept to the analysis of brain functional connectivity networks has been recently demonstrated using phMRI data in rodents challenged with fluoxetine (Schwarz et al. 2008). In this work, a community structure algorithm, based on maximization of a mathematical formalism of 'modularity,' (Newman and Girvan 2004; Newman 2006) was applied to resolve functionally and anatomically segregated communities within a functional connectivity network derived from phMRI responses. The method was applied to identify number and composition of subnetworks within a widely distribute network of functional connectivity obtained under pharmacological challenge with the antidepressant fluoxetine. For a certain partition of the network, *Q* measures the difference between the fraction of the edges connecting nodes within communities and the same fraction in the case of a randomly connected network with the same partition. The closer the value of *Q* is to its theoretical maximum 1, the stronger the community structure, i.e. the more modular the network. The application of this method to the functional connectivity network in the rat challenged with fluoxetine revealed three communities of nodes (Figure 4.13). The pixels in the two largest communities were symmetrically distributed between the left and right hemispheres and their distributions corresponded closely to known anatomical and functional subdivisions of the rat brain. Interestingly, one of the communities comprised nodes corresponding primarily to sub-cortical structures – striatum, thalamus and amygdala – but also regions of the hippocampus and

entorhinal, medial pre-frontal and cingulate cortices. The finding of pixels in the cingulate and prefrontal areas grouped with those in striatal and thalamic structures is consistent with the fact that these cortical regions are the main cortical target of input from the basal ganglia via extensive reciprocal connections with the thalamus (Uylings et al. 2003). These cortical regions are anatomically similar to other regions of the cortex yet *functionally* distinct. Similarly, pixels in the entorhinal cortex and in the hippocampus were assigned to the same community, reflecting the dense connections between these structures. Most other cortical nodes, including those located in the motor, somatosensory and visual cortices, were assigned to a second community (Figure 4.13b), while a third community (Figure 4.13c) mainly comprised pixels near the brain edge, the ventricles and in white matter and the cerebellum.

The community structure approach is somewhat akin to other multivariate methods, like Principal Component Analysis and Independent Component Analysis, which have been extensively applied to seek structure within imaging data in a model-independent way (Friston 1997; McKeown et al. 1998; Beckmann and Smith 2004). Unlike these, however, this community structure approach explicitly takes into account the topology of the functional connections, with communities defined on the basis of link density and distribution. This concept may be more readily interpretable in biological terms than measures such as the orthogonality (Friston et al. 1993; Friston 1997) or statistical independence (McKeown et al. 1998) of spatial modes that are optimized by other algorithms.

A key point in this approach is that the identification of communities within a functional imaging network contains information on both segregation and integration. A partition of the overall network into smaller sub-units suggests a degree of functional segregation in the response, whereas the set of brain regions – not necessarily contiguous – identified within each sub-network reflects their integrated action in response to the experimental stimulus. Importantly, the value of the modularity Q provides a measure of the degree of functional segregation in the network and may provide the basis for an operational definition of this.

This first demonstration of the potential of community structure analysis of functional connectivity in pre-clinical species has been rapidly translated to human functional connectivity, and several studies extending this approach to resting state fMRI have subsequently appeared in the literature (Meunier et al. 2009; Bullmore and Sporns 2009). However, a few questions remain open and are the object of active investigation. For example, the origin of structured patterns of correlated responses is still largely unknown. Specifically, it is unclear whether the patterns of functional connectivity reflect interregional correlations induced by the drug challenge itself, or the intrinsic organization of the brain, perhaps determined by the structure of the underlying neuronal substrate. A follow-up paper applied community

structure analysis to address this question (Appendix 7, Schwarz et al. 2009). To this end, three different pharmacological challenges (D-amphetamine, fluoxetine and nicotine) were investigated, and the emergent communities under different pharmacological conditions were compared to discriminate between connectivity patterns that are stimulus-specific and those independent of the particular neurotransmitter system(s) engaged by the drug, which may thus correspond to general features of the rat brain functional architecture. Interestingly, common features across all three networks revealed two groups of tightly coupled brain structures that responded as functional units independent of the drug, including a network involving the prefrontal cortex and sub-cortical regions extending from the striatum to the amygdala. This suggests that this network of functional connectivity may reflect a general feature of the brain organization, and is consistent with evidence showing strong intrinsic connectivity between neurons in these brain structures. Hence, structural connectivity of the neuronal substrate appears to constraint functional connectivity, and stimulus independent patterns of functional connectivity reflect the structure of large scale neuronal wiring in the rat brain.

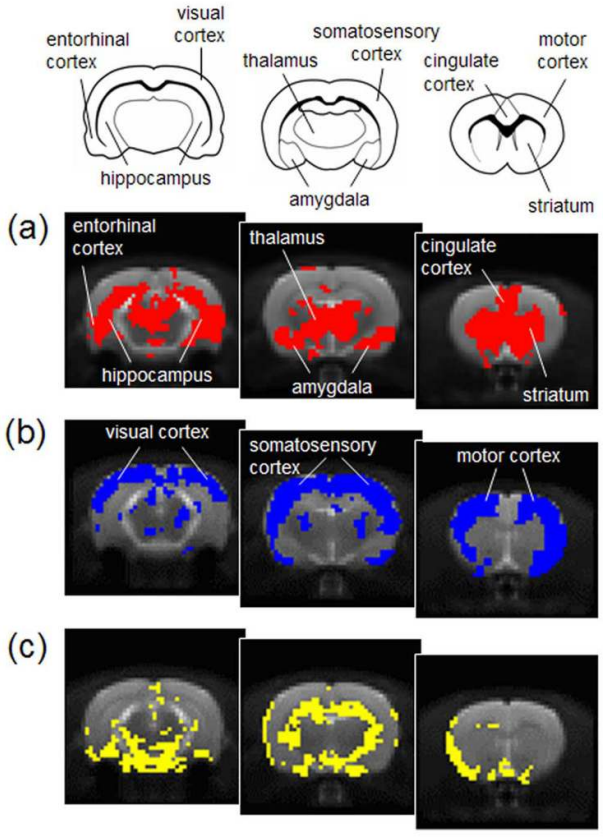

Figure 4.13

Anatomical representation of the three communities identified by modularity maximization in a functional network derived from phMRI responses to fluoxetine.

4.5 Conclusion

Functional Magnetic Resonance Imaging methods have been extensively applied over the last 20 years to study the human brain and its functional organization in healthy and disease states. A strong rationale exists for the extension of this approach to animal models as a translational tool to bridge clinical and preclinical research. Within this framework, the use of pharmacological MRI, i.e. the application of fMRI to map spatio-temporal patterns of brain activity induced by pharmacological agents, shows potential as a means to overcome the limited stimulation repertoire available in anesthetised rodents. The main merits of this approach lie in its ability to elicit robust and reliable activations even under anaesthesia conditions required to reduce motion artefacts and animal stress, and to enable selective stimulation of different neurotransmitter systems, thus providing a playground to study the neurochemical basis of fMRI responses.

My three years' research has focused on the development of refined preclinical phMRI paradigms to focally probe different facets of brain function under a variety of experimental conditions. The results of this effort highlighted encouraging correspondences in the circuits that are recruited by psychotogenic agents, or altered by prolonged drug use, across species and image modality, thus strongly corroborating the translational potential of the approach. Importantly, the combination of this technique with advanced neuro-genetic targeting strategies has been instrumental to unequivocally disclose the circuital determinants of specific behaviours, an approach that is expected to significantly advance our understanding of the neurobiological basis of behaviour. Finally, the application of network partitioning methods to phMRI measures of functional connectivity have made it possible for the first time to resolve biologically and anatomically meaningful patterns of correlated responses in the rat brain, thus providing a novel and powerful method to investigate the brain functional architecture in pre-clinical species.

While fMRI in preclinical species has been driven by imaging applications in humans, the methodological gap between the clinical and the preclinical arenas is closing, with increasingly sophisticated approaches now available for animal studies. The few examples shown here support the use of phMRI approaches as a translational tool, and paves the way to the integrated implementation of phMRI and advance genetic manipulation as a novel powerful platform for basic neurobiological research. Like any contemporary research, the work presented in this dissertation is still in progress. Hopefully, the incremental progress reported in the present studies will motivate the application of phMRI across different areas of basic and applied neurosciences, and provide a basis for future investigations that will help elucidate

the pathological mechanisms of neuro-psychiatric disorders, and guide the development of innovative and more effective therapies.

Appendix 1

Appendix 1

Available online at www.sciencedirect.com
ScienceDirect
Magnetic Resonance Imaging 26 (2008) 999–1006
MAGNETIC RESONANCE IMAGING

Drug–anaesthetic interaction in phMRI: the case of the psychotomimetic agent phencyclidine

Alessandro Gozzi[a,*], Adam Schwarz[a], Valerio Crestan[b], Angelo Bifone[c]

[a]Department of Biology, Psychiatry CEDD, GlaxoSmithKline Medicines Research Centre, 37135 Verona, Italy
[b]Laboratory Animal Sciences, Psychiatry CEDD, GlaxoSmithKline Medicines Research Centre, 37135 Verona, Italy
[c]CPDM, Psychiatry CEDD, GlaxoSmithKline Medicines Research Centre, 37135 Verona, Italy

Received 16 November 2007; accepted 14 January 2008

Abstract

Pharmacological magnetic resonance imaging (phMRI) provides a powerful means to map the effects of drugs on brain activity, with important applications in pharmacological research. However, phMRI studies in preclinical species are often conducted under general anaesthesia as a means to avoid head motion and to minimise the stress induced by the procedure. Under these conditions, the phMRI response to the drug of interest may be affected by interactions with the anaesthetic agent, with consequences for the interpretation of the data. Here, we have investigated the phMRI response to phencyclidine (PCP), an NMDA receptor blocker, in the halothane-anaesthetised rat for varying levels of anaesthesia and different PCP challenge doses. PCP induces psychotic-like symptoms in humans and laboratory animals and is widely applied as a pharmacological model of schizophrenia. However, PCP possesses anaesthetic properties per se, and its interactions with halothane might result in significant effects on the phMRI activation patterns. We observed two qualitatively different patterns of phMRI response. At 0.5 mg/kg iv PCP and 0.8% halothane maintenance anaesthesia, the lowest doses explored, an activation of discrete cortico-limbo-thalamic structures was observed, consistent with neuroimaging studies in humans and 2-deoxyglucose functional mapping in conscious animal models. However, higher anaesthetic concentrations or higher PCP challenge doses resulted in complete abolition of the positive response and in a widespread cortical deactivation (negative response). In the intermediate regime, we observed a dichotomic behaviour, with individual subjects showing one pattern or the other. These findings indicate a dose-dependent drug–anaesthetic interaction, with a complete reversal of the effects of PCP at higher challenge doses or HT concentrations.

Keywords: Phencyclidine; PCP; phMRI; fMRI; Rat; Anaesthesia; Anesthesia; Halothane; CBV; NMDA; Schizophrenia

1. Introduction

Pharmacological magnetic resonance imaging (phMRI) tracks signal changes that reflect a central haemodynamic response to acute drug challenges and may be considered as a surrogate for changes in the underlying neuronal activity [1]. Recent years have seen an increasing application of phMRI to study central effects of drugs on the central nervous system in humans and animal models. In preclinical species, phMRI techniques have been successfully applied to map the central effects produced by a number of psychoactive drugs belonging to different pharmacological classes, including psychostimulant [2,3], antidepressant [4] and anxiolytic compounds [5]. phMRI studies in rodents are often conducted under general anaesthesia as a means to avoid head motion and to minimise the stress induced by restraint. However, the phMRI response to the drug of interest may be affected by interactions with the anaesthetic agent, with consequences for the interpretation of the data. Previous studies have addressed specific issues related to the use of general anaesthesia in phMRI, such as potential perturbations of cerebrovascular autoregulation following the administration of vasoactive compounds [6] or the effect of specific anaesthetics on neurotransmitter function [7]. Potential

* Corresponding author. Department of Neuroimaging, GSK Psychiatry CEDD, 37100 Verona, Italy. Tel.: +39 0458219233; fax: +39 0458218073.
E-mail address: alessandro.gozzi@gsk.com (A. Gozzi).

0730-725X/$ – see front matter © 2008 Elsevier Inc. All rights reserved.
doi:10.1016/j.mri.2008.01.012

Appendix 1

interactions between the anaesthetic and the drug challenge represent another potential confound that can affect the interpretation of the results. The investigation of these effects becomes particularly important when the compounds under investigation are known to possess anaesthetic properties per se, like in the case of the psychotogenic drugs phencyclidine (PCP) or ketamine [8,9].

Acute administration of PCP or ketamine, two drugs acting as NMDA receptor (NMDAR) antagonists, induces psychotic symptoms in healthy subjects [10] and can trigger psychotic episodes in schizophrenic patients [11]. These observations have led to the hypothesis that some aspects of schizophrenia may be due to deficient glutamatergic neurotransmission [12] and have prompted considerable research effort to develop medications for schizophrenia based on this putative mechanism. Glycinergic drugs [13] and AMPAkines [14] represent the best-known examples of novel therapeutic strategies explicitly aimed to enhance glutamatergic neurotransmission. The similarity between NMDAR antagonist-induced psychosis and schizophrenia has also been widely exploited preclinically to provide models to aid the development of novel treatments for the disorder. In these studies, the ability of drugs to inhibit behaviours induced by NMDAR antagonists is assessed in an attempt to predict the efficacy of novel pharmacological treatments for schizophrenia [15]. The application of imaging techniques to map the neuronal substrate underlying these effects can help assess the neurofunctional basis and the predictive value of the use of NMDAR antagonists to mimic schizophrenia.

Recent neuroimaging studies have examined the regional effects of NMDAR antagonists in the human brain. Langsjo et al. [16] reported robust dose-dependent relative cerebral blood flow (rCBF) increases in the anterior cingulate, thalamus, putamen and frontal cortex in healthy volunteers receiving ketamine. Consistent findings were observed by McKie et al. [17] using BOLD fMRI. Recent phMRI studies performed in our lab showed the activation of discrete cortico-limbo-thalamic structures by acute PCP challenge in the halothane-anaesthetised rat, an effect that could be antagonised by antipsychotics and glutamate-release modulators [18]. Littlewood et al. [19] reported an increase in the BOLD response in the hippocampus, retrosplenial cortex and orbital cortex of isoflurane-anaesthetised rats challenged with ketamine. However, no attempt has yet been made to investigate the potential interaction between NMDAR and anaesthesia in phMRI studies.

In the current study, we have investigated the relative cerebral blood volume (rCBV) response to PCP in the halothane-anaesthetised rat for varying concentrations of anaesthesia and different PCP challenge doses. The phMRI protocol used has been previously employed by ourselves and other groups to map the central haemodynamic response to a number of neuroactive compounds [3,18,20–23].

2. Methods

All in vivo studies were conducted in accordance with Italian laws (DL 116, 1992 Ministero della Sanità, Roma). Animal research protocols were also reviewed and consented to by a local animal care committee, in accordance with the guidelines of the *Principles of Laboratory Animal Care* (NIH publication 86-23, revised 1985). The studies were performed on male Sprague–Dawley rats [mean (±S.E.M.) weight, 293±33 g; Charles River, Como, Italy]. Animals had free access to standard rat chow and tap water and were housed in groups of five in solid-bottom cages with sawdust litter. Room temperature (20–22°C), relative humidity (45–65%) and dark–light cycles (12 h each, lights on at 0600 h) were automatically controlled. After arrival, rats were allowed to acclimatise for at least 5 days.

Animal preparation/monitoring and MRI acquisition in each phMRI study have been described previously [18]. Briefly, rats were anaesthetised with 3% halothane in a 30%:70% O_2:N_2 gas mixture, tracheotomised and artificially ventilated with a mechanical respirator. The left femoral artery and vein were cannulated, and the animal was paralysed with a 0.25-mg/kg iv bolus of D-tubocurarine followed by a continuous infusion of 0.25 mg/kg/h through the artery. All wounds were infiltrated with 1% lidocaine before incision. After surgery, the rat was secured into a customised stereotactic holder, and the halothane level was set to 0.8% or 1% (see Section 2.2). The ventilation parameters were adjusted to maintain physiological arterial blood gas levels according to p_aCO_2 and p_aO_2 measurements performed during the study. A statistical comparison of p_aCO_2 values using ANOVA and Fisher's LSD test for multiple comparisons did not reveal any significant difference between pre- and post-MRI p_aCO_2 values or between treatment groups. A magnetic-resonance-compatible thermocouple probe was used to measure rectal temperature. The body temperature of all subjects was maintained within physiological range (37±0.8°C) throughout the experiment, by using a water heating system incorporated in the stereotactic holder. Mean arterial blood pressure (MABP) was monitored continually through the femoral artery. At the end of the experiment, the animals were euthanised with an overdose of anaesthetic followed by cervical dislocation.

2.1. rCBV measurement

MRI data were acquired using a Bruker Avance 4.7-T system, a 72-mm birdcage resonator for radiofrequency pulse transmit and a Bruker curved "Rat Brain" quadrature receive coil. The MR acquisition for each subject comprised T_2-weighted anatomical images using the RARE sequence (Hennig et al., 1986) (TR_{eff}=5000 ms, TE_{eff}=76 ms, RARE factor=8, FOV=40 mm, 256×256 matrix, 16 contiguous 1-mm slices) followed by a time-series acquisition with the same spatial coverage and similar parameters (TR_{eff}=2700 ms, TE_{eff}=110 ms, RARE factor=32) but with a lower

Appendix 1

in-plane spatial resolution (128×128) giving a functional pixel volume of ~0.1 mm^3. The use of T_2-weighted images for the time-series acquisition minimises sensitivity to both large blood vessels and inhomogeneities of the static magnetic field (Boxerman et al., 1995) and also ensured that the geometry of the time-series images matched the anatomical reference images, facilitating subsequent image analysis. Four successive scans were averaged for a resulting time resolution of 80 s. Following five reference images, 2.67 ml/kg of the blood pool contrast agent Endorem (Guerbet, France) was injected so that subsequent signal changes would reflect alterations in rCBV [24]. Prior to the challenge injection, an equilibration period of at least 15 min was allowed. The MRI data were acquired over a period of at least 20 min following the PCP challenge.

2.2. Study design

A total of 32 male Sprague–Dawley rats (250–350 g) underwent phMRI of acute PCP challenge. Rats were randomly assigned to one of four arms:

1. Maintenance anaesthesia concentration, 0.8%; PCP challenge dose, 0.5 mg/kg (n=6) [0.8% HT, 0.5 mg/kg PCP]
2. Maintenance anaesthesia concentration, 0.8%; PCP challenge dose, 1 mg/kg (n=12) [0.8% HT, 1 mg/kg PCP]
3. Maintenance anaesthesia concentration, 1%; PCP challenge dose, 0.5 mg/kg (n=5) [1% HT, 0.5 mg/kg PCP]
4. Maintenance anaesthesia concentration, 1%; PCP challenge dose, 1 mg/kg (n=5) [1% HT, 1 mg/kg PCP]

A fifth group of animals was imaged at 0.8% halothane and challenged with vehicle (saline, n=4). This cohort of animals was used as baseline reference for all the other four arms of the study. Previous experiments in our lab performed at various halothane concentrations did not show any significant difference in baseline rCBV profile following the administration of saline. PCP (Sigma, Milan) and vehicle were injected at a rate of 1 ml/min. Drug quantities refer to the salt form of the compound. Both the PCP doses tested are subanaesthetic and behaviourally effective in freely moving rats [25]. The study was performed using a single halothane vaporiser calibrated against an external reference for accuracy (2B, Varese, Italy). MABP and heart rate were monitored throughout the experiments to assess the level of anaesthesia. Moreover, a pilot study that was performed without neuromuscular blockade showed stable cardiovascular parameters (heart rate and blood pressure) under all experimental conditions used in this study, suggesting that the anaesthetic regimens used are adequate for maintenance.

2.3. Data analysis

The rCBV time-series image data for each experiment were analysed within the framework of the general linear model. Signal intensity changes in the time series were converted into fractional rCBV on a pixel-wise basis, using a constrained exponential model of the gradual elimination of contrast agent from the blood pool [26]. Individual subjects in each study were spatially normalised by a 9-degree-of-freedom affine transformation mapping their T_2-weighted anatomical images to a stereotaxic rat brain MRI template set [27] and applying the resulting transformation matrix to the accompanying rCBV time series. rCBV time series for the PCP challenge were calculated covering 8 min (6 time points) preinjection baseline and 21 min 20 s (16 time points) postinjection window, normalised to a common injection time point. Image-based time-series analysis was carried out using FEAT (FMRI Expert Analysis Tool) Version 5.63, part of FSL (FMRIB's Software Library, www.fmrib.ox.ac.uk/fsl) with 0.8 mm spatial smoothing (≈2.5× in-plane voxel dimension), and using a model function identified by wavelet cluster analysis across all animals in the cohort, capturing the temporal profile of the signal change induced by PCP challenge in each group [28,29]. The design matrix also included the temporal derivative of this regressor and a linear ramp (both orthogonalised to the regressor of interest). The coefficients of the model function thus provided a map of rCBV response amplitude for each injection in each subject. Higher-level group comparisons were carried out using FLAME (FMRIB's Local Analysis of Mixed Effects); Z (Gaussianised T/F) statistic images were thresholded using clusters determined by Z>2.3 and a corrected cluster significance threshold of P=.01 [30,31].

The anatomical distribution of the rCBV changes in both the activation and attenuation maps was used as a guide for the selection of VOIs, which were used to quantify the response to the challenge. VOI time courses were extracted from unsmoothed rCBV time-series data using a 3D digital reconstruction of a rat brain atlas coregistered with the MRI template [27], using custom in-house software written in IDL (Research Systems Inc., Boulder, CO). Pretreatment and PCP administration produced transient alterations of MABP, whose peak magnitude was well within the CBF autoregulation range (60–120 mmHg) under halothane anaesthesia. Experiments performed in our lab using the same anaesthetic protocol applied here have shown that pharmacologically evoked MABP changes within the autoregulation range mentioned above do not result in significant central rCBV response [6].

3. Results

The different combinations of PCP dose and anaesthetic level resulted in significant differences in the sign and magnitude of the rCBV changes observed. The spatiotemporal response pattern in each animal followed one of two distinct profiles. In the [0.8% HT, 0.5 mg/kg PCP] arm, predominantly positive rCBV changes were observed, distributed in a reproducible pattern involving discrete cortical and subcortical areas (Figs. 1 and 2). Strong foci of activation were observed in cortico-limbic areas such as the medial–prefrontal, cingulate, orbitofrontal and

Appendix 1

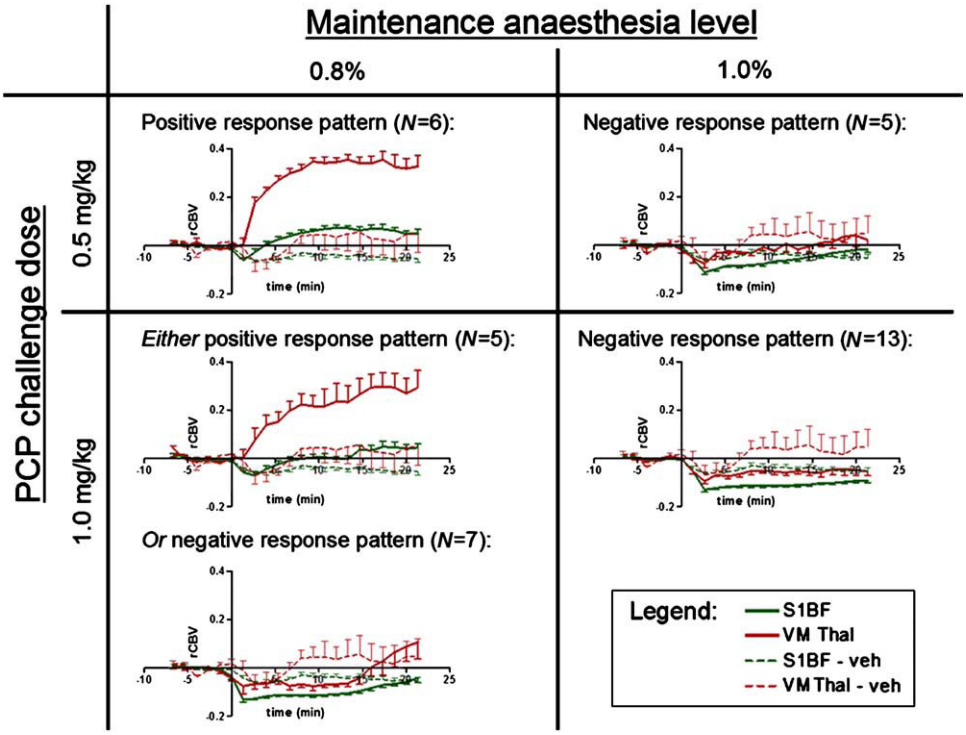

Fig. 1. Summary of study arms and observed responses. Group time courses (mean±S.E.M) are shown for two representative VOIs: the somatosensory cortex (S1BF region; S1BF) and the ventromedial thalamus (VM Thal). rCBV data from four rats challenged with saline were used as baseline reference.

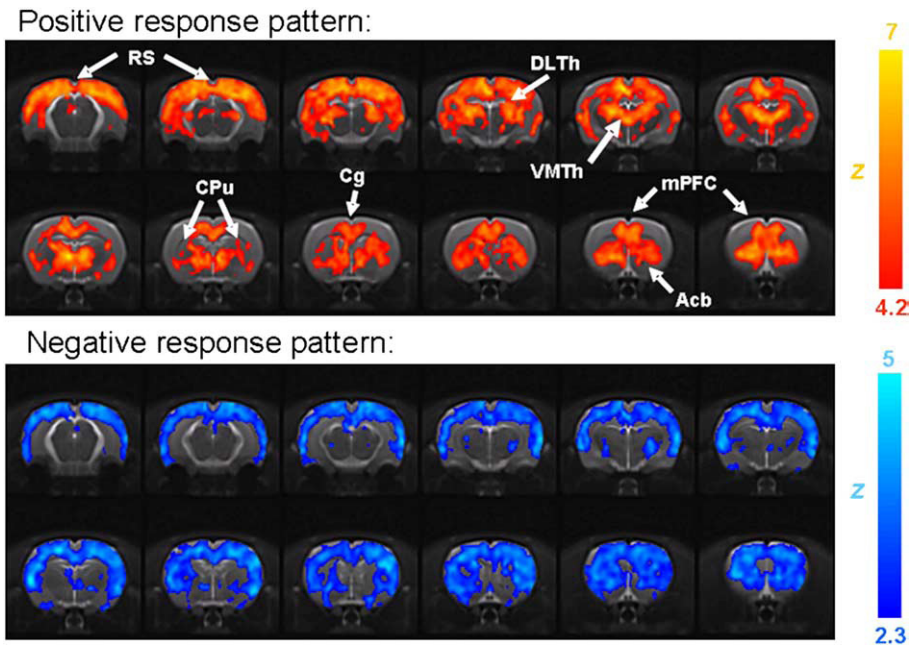

Fig. 2. Representative group activation maps indicating the two characteristic activation signatures observed, depending on the challenge dose and anaesthetic level. Top panel: anatomical distribution of the rCBV changes produced by acute PCP challenge (0.5 mg/kg iv) at a maintenance anaesthesia level of 0.8%. Bottom panel: anatomical distribution of the rCBV changes produced by acute PCP challenge (1 mg/kg iv) at a maintenance anaesthesia level of 1%. *Z* statistics thresholding levels are reported on the right. The significance of the effect has been calculated versus vehicle baseline. Yellow or orange indicates increased rCBV versus vehicle baseline; blue indicates reduced rCBV versus vehicle baseline. RS, retrosplenial cortex; Cg, cingulate cortex; DL/VM Th, dorsolateral/ventromedial thalamus; CPu, caudate putamen; mPFC, medial prefrontal cortex; Acb, nucleus accumbens.

Appendix 1

retrosplenial cortices, with extension into the motor, visual, parietal and temporal association and rhinal cortical areas. Robust activation was also detected in several subcortical nuclei, including the medial and lateral habenula; the amygdala; the anterodorsal, dorsolateral and ventromedial thalamus; the posteroventral hippocampus; the dorsal striatum; and the nucleus accumbens. The time course of PCP-induced activation was similarly sustained in all the activated regions. No significant alterations in rCBV were observed in the somatosensory, piriform and insular cortices; hypothalamus; superior colliculi; or cerebellum.

At a higher dose of PCP, in the [0.8% HT, 1.0 mg/kg PCP] arm, the response was mixed, while 5/12 of the animals showed a positive response similar to that described above (if slightly weaker); the remaining 7/12 evidenced no positive rCBV changes but rather a different response pattern comprising a decrease in rCBV localised to cortical regions (Fig. 1).

At the higher maintenance anaesthetic level, in both [1.0% HT, 0.5 mg/kg PCP] and [1.0% HT, 1.0 mg/kg PCP] arms, PCP produced widespread cortical deactivation. The effect was weak (approximately −8%) but sustained and lasted throughout the time window examined (20 min). No positive rCBV changes were observed in either group in any of the brain regions examined.

As observed in previous rCBV studies, the administration of vehicle produced a slight and transient alteration of rCBV, probably the result of a transitory dilution of the intravascular contrast agent. Both vehicle and PCP administration produced transient changes in MABP. The magnitude of these changes was well within the range of CBF autoregulation (60–120 mmHg) within which abrupt pharmacological manipulation of arterial blood pressure can be homeostatically compensated without producing significant alterations of CBV [6].

4. Discussion

In the present study, we investigated the rCBV response to PCP in the halothane-anaesthetised rat for varying levels of anaesthesia and different PCP challenge doses. We found that the anatomical distribution and the direction of the rCBV response produced by PCP in the halothane-anaesthetised rat depend on both the anaesthetic concentration and PCP challenge dose. Two distinct activation patterns, characterised by a different direction and anatomical distribution of the rCBV response, were observed. At the lowest PCP and halothane doses explored (0.5 mg/kg PCP and 0.8% halothane), robust and reproducible rCBV increases were measured in several cortico-limbo-thalamic structures. At higher PCP or anaesthetic doses, no positive rCBV changes were detected, and a widespread pattern of cortical deactivation became predominant. These findings indicate a dose-dependent drug–anaesthetic interaction, with a complete reversal of the effects of PCP at higher challenge doses or HT levels.

Recent years have seen an increasing application of phMRI to study central effects of drugs on the central nervous system in humans and animal models. The need to avoid head motion and to minimise stress induced by restraint has prompted the development of phMRI protocols in anaesthetised animals [7]. Previous studies have specifically addressed specific issues related to the use of general anaesthesia in phMRI, such as potential perturbations of CBF autoregulation [6,32] or the effect of specific anaesthetics on neurotransmitter function [7]. One further issue that can complicate the interpretation of the results is the occurrence of potential interactions between the drug challenge and the anaesthetic. Such interactions can be compound dependent and dose dependent and, therefore, difficult to predict. Consequently, a systematic investigation of the sign and spatiotemporal distribution of the response for varying levels of anaesthesia and challenge dose may be required to assess the potential influence of these effects on the specific phMRI readout of interest. Such studies are particularly important when the compounds to be examined are known to possess anaesthetic properties per se, like in the case of the psychotogenic drugs PCP or ketamine [8,9].

The observation that changes in anaesthetic level or challenge dose can produce a complete reversal of the effects of PCP is not paralleled by analogous studies using different classes of psychoactive compounds. For instance, experiments performed in our lab showed that increasing the level of halothane anaesthesia from 0.8% to 1% did not substantially affect the magnitude and distribution of amphetamine- or nicotine-induced rCBV response (Gozzi, unpublished results). Similar observations can be inferred from the literature, where acute challenge with amphetamine has been shown to produce consistent patterns of activation at halothane concentrations of 0.8% or 1% (cf. Refs. [33,34]). It should also be emphasised that literature studies often report the use of ranges of anaesthetic significantly wider than those explored in the present study (e.g., HT 1–1.5% [22,35]). The lack of a linear relationship between challenge dose and amplitude of the elicited response is another atypical finding that differentiates PCP from most of the centrally active agents and that testifies to the occurrence of a dose-dependent interaction between PCP and the anaesthetic. This interaction does not appear to be specific to halothane, as preliminary studies performed in isoflurane-anaesthetised rats produced very similar findings at anaesthetic concentrations of 1% and 1.2% (Gozzi, unpublished results).

Consistent with our previous study [18], at 0.5 mg/kg PCP and 0.8% halothane concentration, robust and reproducible rCBV increases were observed in discrete cortical and subcortical structures that have been shown to be activated by NMDAR antagonists in neurofunctional studies performed in conscious rats and in humans. For instance, 2-deoxyglucose functional mapping of the

Appendix 1

NMDAR antagonists MK-801 and ketamine in freely moving animals shows a pattern of increased metabolic activity remarkably similar to the distribution of positive rCBV changes observed in this study (Fig. 3) [36–40]. Moreover, the presence of positive rCBV changes in response to PCP is consistent with the overall excitatory effects observed in freely moving rodents using single-unit recording [41] or [^{14}C]-iodoantipyrine CBF measurements [42]. Very similar patterns of increased activity in non-anaesthetised rodents have also been obtained, measuring immediate-early gene expression. Furthermore, the positive response pattern observed at lower PCP and anaesthetic doses is consistent with the results of neuroimaging studies with ketamine in healthy humans. For instance, Langsjo et al. [16] reported robust dose-dependent rCBF increases in the anterior cingulate, thalamus, putamen and frontal cortex in healthy human volunteers receiving ketamine. Using BOLD fMRI, McKie et al. [17] also reported a very similar pattern in healthy human volunteers. Overall, these findings highlight a significant overlap between the positive rCBV response pattern and metabolic maps of NMDAR antagonists in conscious animals and similarities with respect to regions activated by ketamine in humans. Taken together, these observations suggest that the positive rCBV pattern observed at low PCP (0.5 mg/kg) and anaesthesia doses (halothane 0.8%) is representative of the neurofunctional effects produced by NMDAR blockers in humans and in conscious animals.

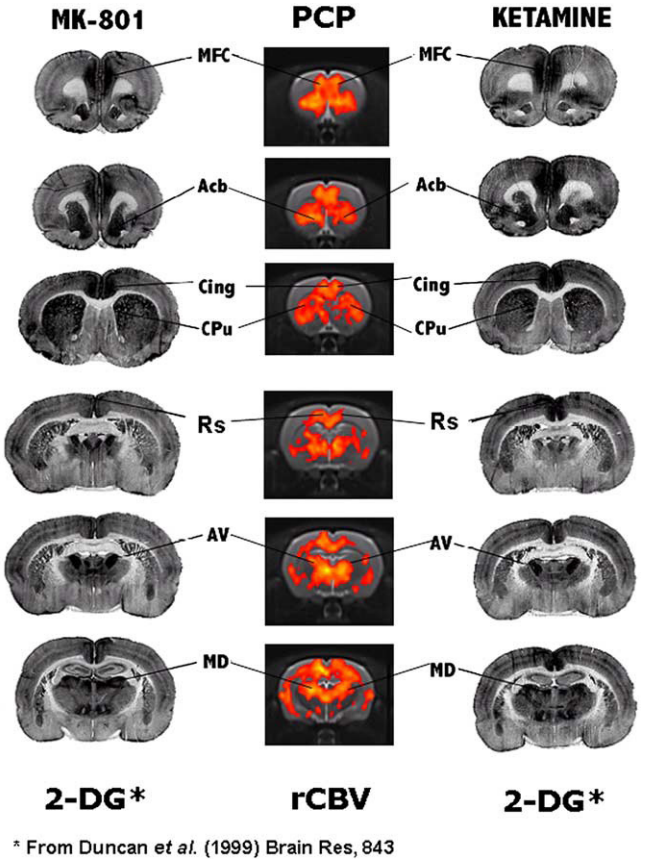

Fig. 3. Spatial correspondence of the regions activated by PCP [0.8% HT; PCP 0.5 mg/kg] and the 2-DG uptake produced by the NMDAR antagonists MK-801 and ketamine in freely moving animals. The 2-DG maps were modified from Duncan et al. [38] with permission (MFC, medial–prefrontal cortex; Acb, nucleus accumbens; Cing, cingulate cortex; CPu, caudate putamen; Rs, retrosplenial cortex; AV, anteroventral thalamus, MD, mediodorsal thalamus).

At higher PCP and/or anaesthetic doses, a markedly different response pattern was observed, comprising a widespread cortical decrease in rCBV. As PCP itself acts as a general anaesthetic at sufficiently high doses [9], the observed cortical deactivation may reflect a synergistic interaction between the drug challenge and the anaesthetic, resulting in widespread suppression of cortical activity. Recent studies have suggested that the psychotogenic action of NMDAR antagonists is a dose-dependent manifestation of a selective inhibition of GABAergic interneurons, resulting in unregulated activity of principal neurons leading to excessive release of glutamate [43,44]. According to this view, by specifically disinhibiting cortical GABA interneurons, subanaesthetic doses of PCP can produce an increased glutamate transmission via non-NMDAR glutamate receptors, thus originating a hyperexcitatory state that is thought to underlie NMDAR-induced psychosis and that, in all probability, forms the basis of the positive rCBV response observed in this study. However, at sufficiently high doses, PCP can produce a general blockade of NMDAR activity in the brain, an effect that outweighs the hyperexcitatory cortical response and that is thought to underlie the analgesic, amnestic and hypnotic properties of the drug. Therefore, as halothane acts primarily by potentiating GABAergic neurotransmission [8,45], the sign (and distribution) of the functional changes produced by PCP may reflect a dose-dependent imbalance between the competing pharmacological action of PCP (via an increase in glutamate neurotransmission) and the anaesthetic (via potentiation of GABAergic inhibition). The presence of a dichotomic response in the [0.8% HT and PCP 1 mg/kg] arm is indicative of how tight the interaction is between these two opposed pharmacological mechanisms in vivo.

Our findings can be of great importance for the interpretation of published results. For instance, Risterucci et al. [46] investigated the functional response to PCP in isoflurane-anaesthetised rats using perfusion imaging and reported the presence of wide areas of decreased perfusion in the cortex and dorsal striatum. As discussed earlier, the presence of decreased cortical perfusion following PCP challenge is at odds with the strong excitatory response observed in neurofunctional studies performed in conscious animals. Considering the high anaesthetic level and PCP used by Risterucci et al. [1.6 minimal alveolar concentration (MAC) of isoflurane vs. 0.8–1 MAC of halothane in this study], and as discussed above in relation to appropriate combination of PCP dose and level of anaesthesia, the findings of their work may reflect a general suppression of cortical activity resulting from the use of a

Appendix 1

relatively high dose of PCP (1 mg/kg) combined with high anaesthetic levels.

In conclusion, our data show a dose-dependent interaction between PCP and maintenance anaesthesia, with a complete reversal of the rCBV response at higher challenge doses or anaesthetic levels. However, the use of lower PCP and halothane doses produces a reproducible pattern of activation that is not qualitatively different from that observed in neuroimaging studies in humans and with 2-deoxyglucose functional mapping in conscious animals. A careful evaluation of the experimental conditions, particularly of the anaesthetic dose, is key to the successful exploitation of phMRI as a preclinical tool to elucidate the neural substrate of psychoactive compounds, particularly when these are prone to significant pharmacological interaction with the anaesthetic.

Acknowledgments

The authors would like to thank Dr. David Sokal for reviewing the manuscript.

References

[1] Wise RG, Tracey I. The role of fMRI in drug discovery. J Magn Reson Imaging 2006;23(6):862–76.
[2] Schwarz AJ, Zocchi A, Reese T, Gozzi A, Garzotti M, Varnier G, et al. Concurrent pharmacological MRI and in situ microdialysis of cocaine reveal a complex relationship between the central hemodynamic response and local dopamine concentration. NeuroImage 2004;23(1): 296–304.
[3] Gozzi A, Schwarz AJ, Reese T, Bertani S, Crestan V, Bifone A. Region-specific effects of nicotine on brain activity: a pharmacological MRI study in the drug-naïve rat. Neuropsychopharmacology 2005; 31(8):1690–703.
[4] Schwarz AJ, Gozzi A, Reese T, Bifone A. In vivo mapping of functional connectivity in neurotransmitter systems using pharmacological MRI. NeuroImage 2007;34(4):1627–36.
[5] Kalisch R, Salome N, Platzer S, Wigger A, Czisch M, Sommer W, et al. High trait anxiety and hyporeactivity to stress of the dorsomedial prefrontal cortex: a combined phMRI and Fos study in rats. NeuroImage 2004;23(1):382–91.
[6] Gozzi A, Ceolin L, Schwarz AJ, Reese T, Bertani S, Bifone A. A multimodality investigation of cerebral haemodynamics and autoregulation in phMRI. Magnetic Resonance Imaging 2007;25(6):826–33.
[7] Steward CA, Marsden CA, Prior MJ, Morris PG, Shah YB. Methodological considerations in rat brain BOLD contrast pharmacological MRI. Psychopharmacology (Berl) 2005;180(4):687–704.
[8] Grasshoff C, Drexler B, Rudolph U, Antkowiak B. Anaesthetic drugs: linking molecular actions to clinical effects. Curr Pharm Des 2006; 12(28):3665–79.
[9] Domino EF. Neurobiology of phencyclidine (Sernyl), a drug with an unusual spectrum of pharmacological activity. Int Rev Neurobiol 1964; 6:303–47.
[10] Adler CM, Malhotra AK, Elman I, Goldberg T, Egan M, Pickar D, et al. Comparison of ketamine-induced thought disorder in healthy volunteers and thought disorder in schizophrenia. Am J Psychiatry 1999;156(10):1646–9.
[11] Lahti AC, Weiler MA, Tamara Michaelidis BA, Parwani A, Tamminga CA. Effects of ketamine in normal and schizophrenic volunteers. Neuropsychopharmacology 2001;25(4):455–67.
[12] Morris BJ, Cochran SM, Pratt JA. PCP: from pharmacology to modelling schizophrenia. Curr Opin Pharmacol 2005;5(1):101–6.
[13] Heresco-Levy U, Javitt DC, Ermilov M, Mordel C, Silipo G, Lichtenstein M. Efficacy of high-dose glycine in the treatment of enduring negative symptoms of schizophrenia. Arch Gen Psychiatry 1999;56(1):29–36.
[14] Goff DC, Leahy L, Berman I, Posever T, Herz L, Leon AC, et al. A placebo-controlled pilot study of the ampakine CX516 added to clozapine in schizophrenia. J Clin Psychopharmacol 2001;21(5):484–7.
[15] Krystal JH, Anand A, Moghaddam B. Effects of NMDA receptor antagonists: implications for the pathophysiology of schizophrenia. Arch Gen Psychiatry 2002;59(7):663–4.
[16] Langsjo JW, Kaisti KK, Aalto S, Hinkka S, Aantaa R, Oikonen V, et al. Effects of subanesthetic doses of ketamine on regional cerebral blood flow, oxygen consumption, and blood volume in humans. Anesthesiology 2003;99(3):614–23.
[17] Deakin JFW, Lees J, McKie S, Hallak JEC, Williams SR, Dursun SM. Glutamate and the neural basis of the subjective effects of ketamine: a pharmaco-magnetic resonance imaging study. Arch Gen Psychiatry 2008;65(2):154–64.
[18] Gozzi A, Large CH, Schwarz A, Bertani S, Crestan V, Bifone A. Differential effects of antipsychotic and glutamatergic agents on the phMRI response to phencyclidine. Neuropsychopharmacology 2007 [in press].
[19] Littlewood CL, Jones N, O'Neil MJ, Mitchell SN, Tricklebank M, Williams MS. Mapping the central effects of ketamine in the rat using pharmacological MRI. Psychopharmacology 2006;186(1):64–81.
[20] Schwarz A, Gozzi A, Reese T, Bertani S, Crestan V, Hagan J, et al. Selective dopamine D(3) receptor antagonist SB-277011-A potentiates phMRI response to acute amphetamine challenge in the rat brain. Synapse 2004;54(1):1–10.
[21] Chen YC, Galpern WR, Brownell AL, Matthews RT, Bogdanov M, Isacson O, et al. Detection of dopaminergic neurotransmitter activity using pharmacologic MRI: correlation with PET, microdialysis, and behavioral data. Magn Reson Med 1997;38(3):389–98.
[22] Dixon AL, Prior M, Morris PM, Shah YB, Joseph MH, Young AM. Dopamine antagonist modulation of amphetamine response as detected using pharmacological MRI. Neuropharmacology 2005;48(2):236–45.
[23] Chen YI, Choi JK, Jenkins BG. Mapping interactions between dopamine and adenosine A2a receptors using pharmacologic MRI. Synapse 2005;55(2):80–8.
[24] Mandeville JB, Marota JJA, Kosofsky BE, Keltner JR, Weissleder R, Rosen B, et al. Dynamic functional imaging of relative cerebral blood volume during rat forepaw stimulation. Magn Reson Med 1998;39: 615–24.
[25] Weissman AD, Dam M, London ED. Alterations in local cerebral glucose utilization induced by phencyclidine. Brain Res 1987; 435(1–2):29–40.
[26] Schwarz AJ, Reese T, Gozzi A, Bifone A. Functional MRI using intravascular contrast agents: detrending of the relative cerebrovascular (rCBV) time course. Magn Reson Imaging 2003;21(10):1191–200.
[27] Schwarz AJ, Danckaert A, Reese T, Gozzi A, Paxinos G, Watson C, et al. A stereotaxic MRI template set for the rat brain with tissue class distribution maps and co-registered anatomical atlas: application to pharmacological MRI. NeuroImage 2006;32(2):538–50.
[28] Schwarz AJ, Whitcher B, Gozzi A, Reese T, Bifone A. Study-level wavelet cluster analysis and data-driven signal models in pharmacological MRI. J Neurosci Methods 2006;159(2):346–60.
[29] Whitcher B, Schwarz AJ, Barjat H, Smart SC, Grundy RI, James MF. Wavelet-based cluster analysis: data-driven grouping of voxel time courses with application to perfusion-weighted and pharmacological MRI of the rat brain. NeuroImage 2005;24(2):281–95.
[30] Friston KJ, Jezzard P, Turner R. Analysis of functional MRI time-series. Human Brain Mapping 1994;1(2):153–71.
[31] Worsley KJ, Evans AC, Marrett S, Neelin P. A three-dimensional statistical analysis for CBF activation studies in human brain. J Cereb Blood Flow Metab 1992;12(6):900–18.
[32] Zaharchuk G, Mandeville JB, Bogdanov Jr AA, Weissleder R, Rosen BR, Marota JJ. Cerebrovascular dynamics of autoregulation and

Appendix 1

hypoperfusion. An MRI study of CBF and changes in total and microvascular cerebral blood volume during hemorrhagic hypotension. Stroke 1999;30(10):2197–204.

[33] Choi JK, Chen YI, Hamel E, Jenkins BG. Brain hemodynamic changes mediated by dopamine receptors: role of the cerebral microvasculature in dopamine-mediated neurovascular coupling. NeuroImage 2006; 30(3):700–12.

[34] Schwarz AJ, Gozzi A, Reese T, Heidbreder CA, Bifone A. Pharmacological modulation of functional connectivity: the correlation structure underlying the phMRI response to D-amphetamine modified by selective dopamine D3 receptor antagonist SB277011A. Magn Reson Imag 2007;25(6):811–20.

[35] Preece MA, Sibson NR, Raley JM, Blamire A, Styles P, Sharp T. Region-specific effects of a tyrosine-free amino acid mixture on amphetamine-induced changes in BOLD fMRI signal in the rat brain. Synapse 2007;61(11):925–32.

[36] Duncan GE, Moy SS, Knapp DJ, Mueller RA, Breese GR. Metabolic mapping of the rat brain after subanesthetic doses of ketamine: potential relevance to schizophrenia. Brain Res 1998;787(2):181–90.

[37] Duncan GE, Leipzig JN, Mailman RB, Lieberman JA. Differential effects of clozapine and haloperidol on ketamine-induced brain metabolic activation. Brain Res 1998;812(1–2):65–75.

[38] Duncan GE, Miyamoto S, Leipzig JN, Lieberman JA. Comparison of brain metabolic activity patterns induced by ketamine, MK-801 and amphetamine in rats: support for NMDA receptor involvement in responses to subanesthetic dose of ketamine. Brain Res 1999; 843(1–2):171–83.

[39] Duncan GE, Miyamoto S, Leipzig JN, Lieberman JA. Comparison of the effects of clozapine, risperidone, and olanzapine on ketamine-induced alterations in regional brain metabolism. J Pharmacol Exp Ther 2000;293(1):8–14.

[40] Miyamoto S, Leipzig JN, Lieberman JA, Duncan GE. Effects of ketamine, MK-801, and amphetamine on regional brain 2-deoxyglucose uptake in freely moving mice. Neuropsychopharmacology 2000; 22(4):400–12.

[41] Homayoun H, Jackson ME, Moghaddam B. Activation of metabotropic glutamate 2/3 receptors reverses the effects of NMDA receptor hypofunction on prefrontal cortex unit activity in awake rats. J Neurophysiol 2005;93(4):1989–2001.

[42] Cavazzuti M, Porro CA, Biral GP, Benassi C, Barbieri GC. Ketamine effects on local cerebral blood flow and metabolism in the rat. J Cereb Blood Flow Metab 1987;7(6):806–11.

[43] Farber NB. The NMDA receptor hypofunction model of psychosis. Ann N Y Acad Sci 2003;1003:119–30.

[44] Greene R. Circuit analysis of NMDAR hypofunction in the hippocampus, in vitro, and psychosis of schizophrenia. Hippocampus 2001; 11(5):569–77.

[45] Mody I, Tanelian DL, MacIver MB. Halothane enhances tonic neuronal inhibition by elevating intracellular calcium. Brain Res 1991;538(2): 319–23.

[46] Risterucci C, Jeanneau K, Schoppenthau S, Bielser T, Kunnecke B, von Kienlin M, et al. Functional magnetic resonance imaging reveals similar brain activity changes in two different animal models of schizophrenia. Psychopharmacology (Berl) 2005;180(4):724–34.

Appendix 2

Appendix 2

Neuropsychopharmacology (2007), 1–14

www.neuropsychopharmacology.org

Differential Effects of Antipsychotic and Glutamatergic Agents on the phMRI Response to Phencyclidine

Alessandro Gozzi*[,1], Charles H Large[2], Adam Schwarz[1], Simone Bertani[2], Valerio Crestan[2] and Angelo Bifone[1]

[1]Department of Biology, Psychiatry CEDD, GlaxoSmithKline Medicines Research Centre, Verona, Italy; [2]Laboratory Animal Science, Psychiatry CEDD, GlaxoSmithKline Medicines Research Centre, Verona, Italy

Acute administration of NMDA receptor (NMDAR) antagonists such as phencyclidine (PCP) or ketamine induces symptoms that closely resemble those of schizophrenia in humans, a finding that has led to the hypothesis that a decreased NMDAR function may be a predisposing or even causative factor in schizophrenia. However, the precise neuropharmacological mechanisms underlying these effects remain to be fully elucidated. Here, we applied pharmacological MRI (phMRI) to examine the brain circuitry underlying the psychotomimetic action of PCP in the anesthetized rat, and investigated how these functional changes are modulated by drugs that possess distinct pharmacological mechanisms. Acute administration of PCP (0.5 mg/kg i.v.) produced robust and sustained positive relative cerebral blood volume (rCBV) changes in discrete cortico-limbo-thalamic regions. Pretreatment with the selective D_2 dopamine antagonist raclopride (0.3 mg/kg i.p.) did not significantly affect the rCBV response to PCP, while the atypical antipsychotic clozapine (5 mg/kg i.p.) produced region-dependent effects, with complete suppression of the rCBV response in the thalamus, and weaker attenuation of the response in cortical and hippocampal structures. The response to PCP was strongly suppressed in all regions by pretreatment with two drugs that can inhibit aberrant glutamatergic activity: the anticonvulsant lamotrigine (10 mg/kg i.p.) and the mGluR2/3 agonist LY354740 (10 mg/kg i.p.). Taken together, our findings corroborate the pivotal role of dysfunctional glutamatergic neurotransmission in the functional response elicited by PCP, while the lack of effect of raclopride argues against a primary role of dopamine D_2 receptor activation in this process. Finally, the thalamic effect of clozapine could be key to elucidating the functional basis of its pharmacological action.

Neuropsychopharmacology advance online publication, 5 September 2007; doi:10.1038/sj.npp.1301547

Keywords: fMRI; phencyclidine; clozapine; raclopride; lamotrigine; LY363740

INTRODUCTION

NMDA receptor (NMDAR) antagonists such as ketamine and phencyclidine (PCP) induce perceptual abnormalities, psychotic symptoms, and mood changes in healthy humans (Adler *et al*, 1999; Javitt and Zukin, 1991). Many of the symptoms induced by NMDR antagonists are considered similar to those of schizophrenia, and include core symptoms, such as thought disorder and hallucinations (Malhotra *et al*, 1996). These compounds have also been shown to exacerbate positive symptoms of patients with schizophrenia (Lahti *et al*, 2001; Malhotra *et al*, 1997b). Moreover, both clinical and experimental evidence suggest that the expression and functionality of NMDAR might be dysregulated in schizophrenia (Kristiansen *et al*, 2007; Millan, 2005). These findings have led to the hypothesis that a decreased NMDAR function may be a predisposing or even causative factor for this disabling disease (Farber, 2003; Greene, 2001). The similarity between NMDAR antagonist-induced psychosis and schizophrenia has also been widely exploited preclinically to provide models to aid the development of novel treatments for the disorder. In these studies, the ability of drugs to inhibit behaviors induced by NMDAR antagonists is assessed in an attempt to predict the efficacy of novel pharmacological treatments for schizophrenia (reviewed by Large, 2007). Therefore, the site and mode of action of NMDAR antagonists in relation to different symptoms or behaviors that they induce is the object of extensive research.

Neuroimaging studies have provided some initial insights into the site of action of NMDAR antagonists in the human brain. Langsjo *et al* (2003) reported robust dose-dependent rCBF increases in the anterior cingulate, thalamus, putamen, and frontal cortex in healthy volunteers receiving ketamine. Consistent findings were observed by McKie *et al* (2007) using BOLD fMRI. Holcomb *et al* (2005) showed that ketamine increased cerebral blood flow (CBF) in the anterior cingulate and frontal cortices in both healthy

*Correspondence: A Gozzi, Neuroimaging, Psychiatry CEDD, GlaxoSmithKline Research Centre, Fleming 4, Verona 37100, Italy,
Tel: + 39 0458219233, Fax: + 39 0458218073,
E-mail: alessandro.2.gozzi@gsk.com
Received 11 May 2007; revised 18 July 2007; accepted 23 July 2007

volunteers and patients with schizophrenia. Earlier studies also reported that low doses of ketamine affect selectively the areas that are thought to be dysfunctional in schizophrenia such as the limbic cortex and basal ganglia (Morris *et al*, 2005; Soyka *et al*, 2005; Tamminga *et al*, 2003). Recent neuroimaging studies have also examined the regional effects of NMDAR antagonists in the rat. Ketamine has been shown to increase the BOLD response in the hippocampus, retrosplenial cortex, and orbital cortex of anesthetized rats; weaker effects were reported in the nucleus accumbens and ventral pallidum (Littlewood *et al*, 2006a). Risterucci *et al* (2005) examined the effects of PCP in the rat using perfusion imaging. They reported increased perfusion in the enthorhinal cortex, nucleus accumbens, thalamus, and ventral pallidum, but decreased perfusion in prefrontal and temporal cortices and dorsal striatum.

Overall, the two studies in rat suggest similarities in the regions of the brain activated by PCP and ketamine, and similarities with respect to regions activated by ketamine in humans. However, no attempt has yet been made to determine the contribution of specific receptor systems to the different regional effects observed in functional studies of NMDAR antagonists. In order to begin to address this question, here we have applied pharmacological MRI (phMRI) methods to investigate the spatio-temporal distribution of relative cerebral blood volume (rCBV) changes induced by acute PCP challenge in the rat, and examined how these changes are modulated by drugs that possess distinct pharmacological mechanisms. As the effect of NMDAR antagonists is thought to involve a dysregulation of glutamatergic neurotransmission (Farber, 2003), we assessed the effect of two drugs that have been suggested to prevent aberrant glutamatergic activity through distinct pharmacological mechanisms: the metabotropic glutamate 2/3 (mGluR2/3) receptor agonist LY354740 and the brain sodium channel blocker lamotrigine. LY354740 has been shown to prevent PCP-induced glutamate release (Moghaddam and Adams, 1998), and to block dose-dependently the behavioral effects of NMDAR antagonists in rodents (Schoepp and Marek, 2002) and in human volunteers (Krystal *et al*, 2005). Lamotrigine (lamictal, Messenheimer, 1995) is a broad-spectrum anticonvulsant that reduces neuronal excitability and glutamatergic transmission (Large *et al*, 2005), and that has been shown to prevent psychotic symptoms and disruption of behavior induced by ketamine or PCP in rodents and human volunteers (Idris *et al*, 2005; Brody *et al*, 2003; Anand *et al*, 2000). Moreover, since NMDAR antagonists may be used in preclinical studies to predict the efficacy of novel antipsychotic drugs, we examined the modulation of PCP response by compounds representative of conventional and atypical antipsychotics. Raclopride, a potent and selective dopamine D_2 receptor antagonist (Lahti *et al*, 1993; Kohler *et al*, 1985), was used to probe the classic mechanism of action of first-generation antipsychotics relying on D_2 dopamine blockade. The contribution of dopamine to the psychotogenic action of PCP is still the subject of debate, with the literature showing inconsistent effects of dopamine D_2 blockers in rodents (Idris *et al*, 2005; Linn *et al*, 2003; Duncan *et al*, 1998a; Corbett *et al*, 1995) and humans (Krystal *et al*, 1999), despite evidence of altered dopamine release following NMDAR antagonist administration (Adams and Moghaddam, 1998). The effect of raclopride was compared with that of clozapine, a prototypical new-generation antipsychotic that, in addition to blocking dopamine D_2 receptors, possesses multiple antagonistic actions at several other receptors (Meltzer, 1996). Clozapine has been reported to reverse the cognitive and social behavior deficits induced by NMDAR antagonists in rodents (Idris *et al*, 2005) and humans (Malhotra *et al*, 1997a). The parallel investigation of drugs representative of the mechanisms of action of typical and atypical antipsychotics is of great interest in light of the wide preclinical use of NMDAR antagonists as a neuropharmacological model to aid the development of novel treatments for schizophrenia. If these drugs also differentially modify regional brain activation, then it may be possible to link regions to behaviors and to identify the neurofunctional basis of the pharmacological action of antipsychotic drugs.

METHODS

Animal Preparation

All *in vivo* studies were conducted in accordance with the Italian laws (DL 116, 1992 Ministero della Sanità, Roma). Animal research protocols were also reviewed and consented to by a local animal care committee, in accordance with the guidelines of the Principles of Laboratory Animal Care (NIH publication 86–23, revised 1985). The studies were performed on male Sprague–Dawley rats (mean ± SEM, 293 ± 33 g, Charles River, Como, Italy). Animals had free access to standard rat chow and tap water and were housed in groups of five in solid bottom cages with sawdust litter. Room temperature (20–22°C), relative humidity (45–65%), and dark–light cycles (12 h each, lights on at 0600 hours) were automatically controlled. After arrival, rats were allowed to acclimatize for at least 5 days.

Animal preparation/monitoring and MRI acquisition in each phMRI study were similar to previous studies (Gozzi *et al*, 2005). Briefly, rats were anesthetized with 3% halothane in a 30% : 70% $O_2 : N_2$ gas mixture, tracheotomized, and artificially ventilated with a mechanical respirator. The left femoral artery and vein were cannulated and animals were paralyzed with a 0.25 mg/kg i.v. bolus of D-tubocurarine followed by a continuous infusion of 0.25 mg/kg/h through the artery. All wounds were infiltrated with 1% lidocaine before incision. A PE50 cannula was also inserted intraperitoneally for drug pretreatment. After surgery the rat was secured into a customized stereotactic holder (Bruker, Ettlingen, Germany) and the halothane level set to 0.8%. The ventilation parameters were adjusted to maintain physiological arterial blood gases levels according to p_aCO_2 and p_aO_2 measurements performed during the study. A statistical comparison of p_aCO_2 values using ANOVA and a Fisher's LSD test for multiple comparisons did not reveal any significant difference between pre- and post-MRI p_aCO_2 values, or between treatment groups. A magnetic resonance-compatible thermocouple probe was used to measure rectal temperature. The body temperature of all subjects was maintained within physiological range (37 ± 0.8°C) throughout the experiment, by using a water heating system incorporated in the stereotactic holder. Mean arterial blood pressure (MABP) was monitored continually through the femoral artery. At the end of the

experiment, the animals were euthanized with an overdose of anesthetic followed by cervical dislocation.

rCBV Measurement

MRI data were acquired using a Bruker Avance 4.7 Tesla system, a 72 mm birdcage resonator for radio frequency pulse transmit and a Bruker curved 'Rat Brain' quadrature receive coil. The MR acquisition for each subject comprised T_2-weighted anatomical images using the RARE sequence (Hennig *et al*, 1986) ($TR_{eff} = 5000$ ms, $TE_{eff} = 76$ ms, RARE factor 8, FOV 40 mm, 256 × 256 matrix, 16 contiguous 1 mm slices) followed by a time series acquisition with the same spatial coverage and similar parameters ($TR_{eff} = 2700$ ms, $TE_{eff} = 110$ ms, RARE factor 32), but with a lower in-plane spatial resolution (128 × 128) giving a functional pixel volume of $\sim 0.1\ mm^3$. The use of T_2-weighted images for the time-series acquisition minimizes sensitivity to both large blood vessels and inhomogeneities of the static magnetic field (Boxerman *et al*, 1995), and also ensured that the geometry of the time-series images matched the anatomical reference images, facilitating subsequent image analysis. Two successive scans were averaged for a resulting time resolution of 40 s. Following five reference images, 2.67 ml/kg of the blood pool contrast agent Endorem (Guerbet, France) was injected so that subsequent signal changes would reflect alterations in relative rCBV (Mandeville *et al*, 1998). Prior to the injection of drug pretreatment, an equilibration period of 15 min was allowed. Experiments (see below) were performed following an antagonist–agonist design, with intraperitoneal injection of drug (or vehicle) pretreatment followed by PCP challenge (or vehicle) 30 min later. The MRI data were acquired over a period of at least 20 min following the administration of the PCP challenge.

Experiments and Compounds

Rats were randomly assigned to one of the following treatment groups:

(1) Intraperitoneal preadministration of vehicle (water, 1 ml/kg) followed by an intravenous challenge with PCP (phencyclidine hydrochloride, Sigma-Aldrich, Italy, 0.5 mg/kg, 1 ml/rat) 30 min later ($n = 24$);
(2) Intraperitoneal preadministration of raclopride (*S*(−)-raclopride (+)-tartrate, Sigma-Aldrich, Italy, 0.3 mg/kg) followed by an intravenous challenge with PCP (0.5 mg/kg) 30 min later ($n = 6$);
(3) Intraperitoneal preadministration of clozapine (Sigma-Aldrich, Italy, 5 mg/kg) followed by an intravenous challenge with PCP (0.5 mg/kg) 30 min later ($n = 7$);
(4) Intraperitoneal preadministration of LY354740 (GSK, Italy, 10 mg/kg) followed by an intravenous challenge with PCP (0.5 mg/kg) 30 min later ($n = 7$);
(5) Intraperitoneal preadministration of lamotrigine (lamictal, lamotrigine isothionate, GSK, Italy, 10 mg/kg free base) followed by an intravenous challenge with PCP (0.5 mg/kg) 30 min later ($n = 6$);
(6) Intraperitoneal preadministration of vehicle (water) followed by an intravenous challenge with vehicle (saline, 1 ml/rat) 30 min later ($n = 6$). This group of rats was used as double-negative control group (baseline).

All the compounds were injected at a rate of 1 ml/min. PCP was dissolved in saline, while all the pretreatments were dissolved in water. Clozapine was dissolved in a few drops of 1 N HC1 and brought to volume with water. The final pH of the clozapine solution was adjusted to 7 with a few microliters of 1 N NaOH. The doses chosen for the different drugs were based on previously published *in vivo* studies. PCP at 0.5 mg/kg i.v. has been shown to elicit robust behavioral and metabolic (2DG) effects in freely moving rats (Weissman *et al*, 1987). The dose of raclopride used in this study (0.3 mg/kg i.p.) produces ~75% dopamine D_2 receptor occupancy, a value that ensures a robust antipsychotic response without inducing cataleptic behavior (Wadenberg *et al*, 2000). The dose of clozapine tested (5 mg/kg i.p.) has been shown to produce a D_2 receptor occupancy of approximately 40% (see Kapur *et al*, 2003; Schotte *et al*, 1993, 1996), with one study showing a slightly lower value (*ca.* 25%, Mukherjee *et al*, 2001). These values are consistent with those determined in schizophrenic patients treated with clozapine (eg 16–68% in Kapur *et al*, 1999; 20–67% in Nordstrom *et al*, 1995). The same dose of clozapine ensures serotonin 5-HT_{2A} receptor occupancy analogous to the one measured in the clinical condition (*ca.* 80 *vs* 84–94%, Nordstrom *et al*, 1995; Schotte *et al*, 1995). Clozapine at 5 mg/kg i.p. has also been shown to prevent the behavioral and metabolic effects of PCP and other NMDAR antagonists in freely moving rats (Idris *et al*, 2005; Duncan *et al*, 1998a, 2000; Corbett *et al*, 1995; Bakshi *et al*, 1994). Therefore, the dose selected produces robust pharmacological effects while maintaining its 'atypicality' with regard to the degree of D_2 receptor occupancy, a feature that differentiates this clozapine from atypical antipsychotics and most new-generation neuroleptics such as risperidone and olanzapine (Kapur *et al*, 1999). LY354740 at 10 mg/kg i.p. has been shown to prevent the behavioral and neurochemical effects of PCP (Schoepp and Marek, 2002). Lamotrigine was given at a nonsedative dose (10 mg/kg i.p.), which was recently shown to affect PCP-induced disruption of a reversal learning task in rats (Idris *et al*, 2005).

Data Analysis

The rCBV time-series image data for each experiment were analyzed within the framework of the general linear model (GLM). Signal intensity changes in the time series were converted into fractional rCBV on a pixel-wise basis, using a constrained exponential model of the gradual elimination of contrast agent from the blood pool (Schwarz *et al*, 2003). Individual subjects in each study were spatially normalized by a nine-degree-of-freedom affine transformation mapping their T_2-weighted anatomical images to a stereotaxic rat brain MRI template set (Schwarz *et al*, 2006a) and applying the resulting transformation matrix to the accompanying rCBV time series. RCBV time series for the PCP challenge were calculated covering 8 min (12 time points) preinjection baseline and 20 min (30 time points) postinjection window, normalized to a common injection time point. RCBV time series were also calculated for the pretreatment covering 6 min (9 time points) preinjection baseline and 20 min (30 time points) postinjection window normalized to a common injection time point. Image-based time series analysis was performed using FEAT (FMRI Expert Analysis Tool) Version 5.63, part of FSL (FMRIB's Software Library,

www.fmrib.ox.ac.uk/fsl) with 0.8 mm spatial smoothing ($\approx 2.5 \times$ in-plane voxel dimension) and using a model function identified by Wavelet Cluster Analysis (WCA) across all animals in the cohort, capturing the temporal profile of the signal change induced by PCP challenge in each group (Figure 1 inset shows the model function chosen for PCP response in vehicle–PCP group) (Schwarz *et al*, 2006b; Whitcher *et al*, 2005). The design matrix also included the temporal derivative of this regressor and a linear ramp (both orthogonalized to the regressor of interest). The coefficients of the model function thus provided a map of rCBV response amplitude for each injection in each subject. Higher level group comparisons were performed using FLAME (FMRIB's Local Analysis of Mixed Effects); Z (Gaussianized T/F) statistic images were thresholded using clusters determined by $Z > 2.3$ and a corrected cluster significance threshold of $p = 0.01$ (Friston *et al*, 1994; Worsley *et al*, 1992). Maps of the attenuation of the PCP response by pretreatments were created comparing the rCBV response of the vehicle–PCP group (group 1) *vs* each pretreated group (groups 2–5). Attenuation maps were also thresholded using clusters determined by $Z > 2.3$ and a corrected cluster significance threshold (P_c) of $p = 0.01$. The anatomical distribution of the rCBV changes in both the activation and attenuation maps was used as guide for a selection of VOIs, which were used to quantify and compare the efficacy of the pretreatment.

VOI time courses for both the pretreatment and the PCP challenge were extracted from unsmoothed rCBV time series data using a 3D digital reconstruction of a rat brain atlas (Paxinos and Watson, 1998) co-registered with the MRI template (Schwarz *et al*, 2006a), using custom in-house software written in IDL (Research Systems Inc., Boulder, Colorado). A list with the anatomical definition of the VOIs examined that has been previously described can be found in nucleus accumbens (*Acb*); caudate putamen (*Cpu*); antero-dorsal region of the hippocampus (regions of hippocampus dorsal to a line 5.5 mm ventral from bregma, Figures 25–35 in Paxinos and Watson (1998), *hippocampus AD*); postero-dorsal region of the hippocampus (regions of hippocampus dorsal to a line 5.5 mm ventral from bregma, Figures 36–45 in Paxinos and Watson (1998), excluding subiculum and DG region in Figure 45, *hippocampus PD*); ventral hippocampus (regions of hippocampus greater than 5.5 mm ventral from bregma, Figures 36–45 in Paxinos and Watson (1998), excluding subiculum and DG region in Figure 45, *hippocampus V*); posterior layers of the dentate gyrus (DG and PoDG regions, Figures 45–47 in Paxinos and Watson (1998), *hippocampus PDG*); dorso-lateral thalamus (*thalamus DL*); medio-dorsal thalamus (*thalamus MD*); ventro-medial thalamus (*thalamus VM*); lateral hypothalamus (*LH*); ventro-lateral part of latero-dorsal thalamus (*LDVL*); dorso-medial part of latero-dorsal thalamus (*LDDM*); hypothalamus (*Hth*); medial prefrontal cortex

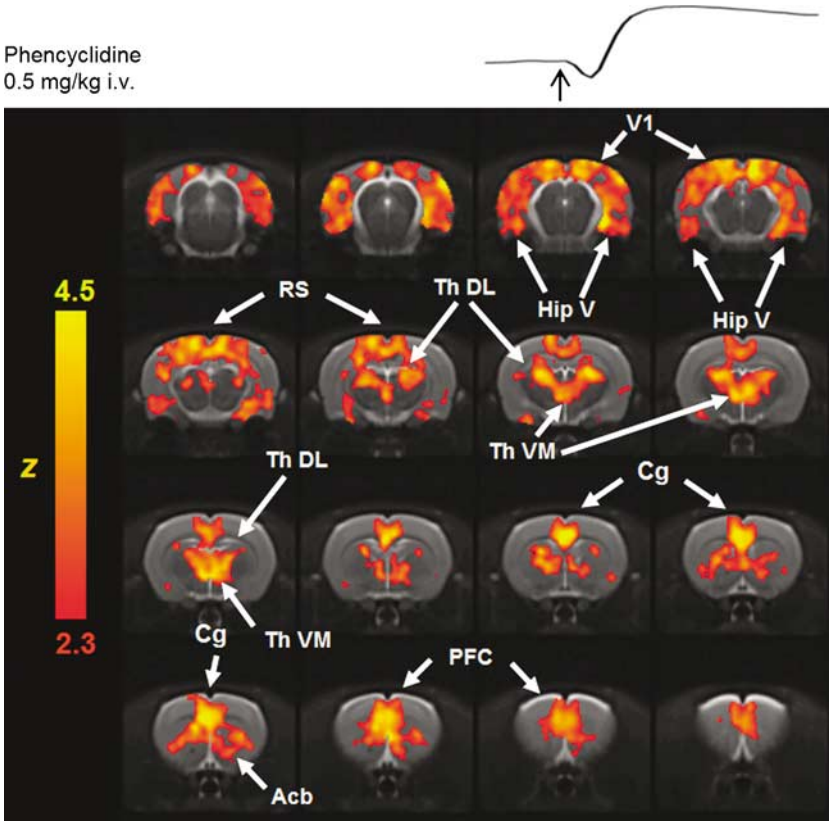

Figure 1 Maps of rCBV response following acute phencyclidine (PCP) challenge (0.5 mg/kg i.v.; $n = 24$) relative to vehicle ($n = 6$). Orange/yellow indicated increased rCBV *vs* baseline (vehicle). The temporal profile of the regressor used as a signal model in the general linear model (GLM) analysis (see Methods) is shown at the top right of the activation map, with an arrow indicating the time of injection. (Abbreviations: V1, primary visual cortex; VHip, ventral hippocampus; RS, retrosplenial cortex; DLth, dorso-lateral thalamus; VMth, ventro-medial thalamus; Cg, cingulate cortex, Acb, nucleus accumbens; mPFC, medial prefrontal cortex.)

(*PFC*); cingulate cortex (*Cg*); orbito-frontal cortex (*OFC*); retrosplenial cortex (*RS*); motor cortex (*MC*); primary somatosensory cortex (*S1*); primary visual cortex (*V1*); entorhinal cortex (includes ectorhinal and perirhinal areas) (*Ent*); piriform cortex (includes both Pir layer and adjacent tissue, *Pir*); insular cortex (*Ins*); parietal association cortex (*PtA*); temporal association cortex (*TeA*); ventral tegmental area (*VTA*); substantia nigra (*SN*); raphe nuclei (*raphe*); superior colliculi (*SupCo*); pons (*pons*); amygdala (includes basolateral and basomedial and medial amygdaloid nuclei plus central nucleus of the amygdala, *Amy*).

For each VOI time course, the average rCBV over a 16 min time window covering the peak response to PCP (4–20 min post injection) was used as a summary statistic of the relative change. The effect of pretreatment on the magnitude of average rCBV in different VOIs was assessed by a one-way ANOVA followed by a Dunnett's test *vs* group 1. Threshold for statistical significance was considered as $p = 0.05$. Results are quoted and displayed as mean ± SEM unless otherwise indicated.

The rCBV time profiles of the intraperitoneal pretreatment *per se* did not show clear or sustained signal changes compared to vehicle for all the compounds in any of the VOIs examined (PFC, RS, V1, S1, Pir, Ins, OFC, Ent cortices, LD and VM thalami, Hth, Hc, Cpu, Acb, septum, VTA, SupCo, Amy, SN).

Pretreatment and PCP administration produced transient alterations of MABP whose peak magnitude was well within the CBF autoregulation range 60–120 mm Hg under halothane anesthesia. Experiments performed in our lab using the same anesthetic protocol applied here have shown that pharmacologically evoked MABP changes within the autoregulation range mentioned above do not result in significant central rCBV response (Gozzi *et al*, 2007a).

RESULTS

PCP (0.5 mg/kg) induced a robust activation of distinct cortico-limbo-thalamic structures (Figure 1). Significant positive rCBV changes ($Z > 2.3$ *vs* vehicle, cluster correction at $p = 0.05$) were observed in limbic cortical regions (medial prefrontal, cingulate, orbito-frontal, and retrosplenial cortices), with extension into the motor, visual, parietal-, and temporal association and rhinal cortices. Significant foci of activation were also observed in specific subcortical structures, including the medial and lateral habenula, amygdala, antero-dorsal, dorso-lateral and ventro-medial thalamus, postero-dorsal, antero-dorsal and ventral and posterior hippocampus, the dorsal striatum, and the nucleus accumbens. The time course of PCP-induced activation was similar in all the activated regions (eg medial prefrontal cortex, hippocampus, and latero-dorsal thalamus, Figure 2), with a brief dip followed by a rapid increase in rCBV that reached a plateau within 5 min of drug injection, and remained sustained over the period examined. In nonactivated regions (eg somatosensory cortex, Figure 2), the transient dip was not followed by any appreciable increase in rCBV with respect to control animals challenged with vehicle (baseline). The magnitude of the rCBV response to PCP was region-dependent, with the largest response in specific subregions of the cortex and the thalamus (eg mean rCBV increase at peak in cingulate $+17.7 \pm 1.7\%$ and prefrontal cortex $+14.9 \pm 1.6\%$, respectively; $+19.0 \pm 1.6\%$ and $+19.3 \pm 2.3\%$ in ventro-medial and dorso-lateral thalami, respectively). Smaller changes in rCBV were observed in other cortical areas (eg visual cortex $+11.9 \pm 1.2\%$) and subcortical structures (eg ventral hippocampus $+10.0 \pm 1.2\%$). These effects are summarized in Figure 3. PCP did not produce significant changes in rCBV with respect to vehicle in the somatosensory, piriform and insular cortices, hypothalamus, superior colliculi, or cerebellum.

PCP administration produced a rapid rise in MABP ($+8.9 \pm 3.3$ mm Hg, peak 1 min post injection) followed by an undershoot (-6.9 ± 2.1 mm Hg), which returned to preinjection baseline (99.2 ± 3.1 mm Hg) about 10–12 min post injection. Intraperitoneal preadministration of vehicle also produced a transient (≈ 2 min) change in arterial blood pressure (-30 mm Hg). The injection of vehicle produced negligible rCBV changes *per se* in all the brain regions examined.

Clozapine

Preadministration of clozapine (5 mg/kg i.p.) significantly inhibited the rCBV response to PCP in the cortex, thalamus, antero-dorsal hippocampus, and striatum (Figure 4). The degree of inhibition varied by region, with foci of strong inhibition in the dorso-lateral and ventro-medial thalami ($p = 0.0002$ and 0.001, respectively), areas of moderate inhibition in the medial prefrontal ($p = 0.02$), cingulate ($p = 0.01$), and visual cortices ($p = 0.01$), and regions of weak and nonsignificant inhibition in the ventral hippocampus and posterior dentate gyrus ($p = 0.30$ and 0.18, respectively). These effects could also be clearly seen in the rCBV time courses (Figures 2 and 4). Cortical regions such as the medial prefrontal cingulate, retrosplenial, temporal association, and visual cortices showed an attenuated, but sustained response to PCP, which lasted throughout the time window examined. In areas of stronger inhibition by clozapine, such as the latero-dorsal and ventro-medial thalami and dorsal striatum, no appreciable rCBV response to PCP was observed. Total suppression of PCP activation was also observed in strongly responding subthalamic nuclei such as the LDVL and LDDM (dorso-medial and ventro-lateral part of latero-dorsal thalamus, $p = 0.0003$ and 0.00008 respectively). A trend for a subregional specificity in clozapine response was also observed in the hippocampus. Clozapine significantly inhibited PCP activation in the antero-dorsal and posterior dorsal hippocampus ($p = 0.02$ in both regions). However, clozapine did not significantly inhibit PCP-induced activation of the ventral hippocampus or posterior dentate gyrus. Within the basal ganglia, clozapine significantly inhibited PCP-induced activation in the striatum ($p = 0.006$), but failed to suppress activation in the nucleus accumbens ($p = 0.35$).

Preadministration of clozapine was followed by a gradual decrease in MABP (-25.6 ± 8.3 mm Hg), which plateaued 4–6 min after injection. The effect persisted for more than 30 min and was still present at the time of PCP challenge. The rCBV changes produced by preadministration of clozapine *per se* were negligible in all the brain regions examined (Figure 5).

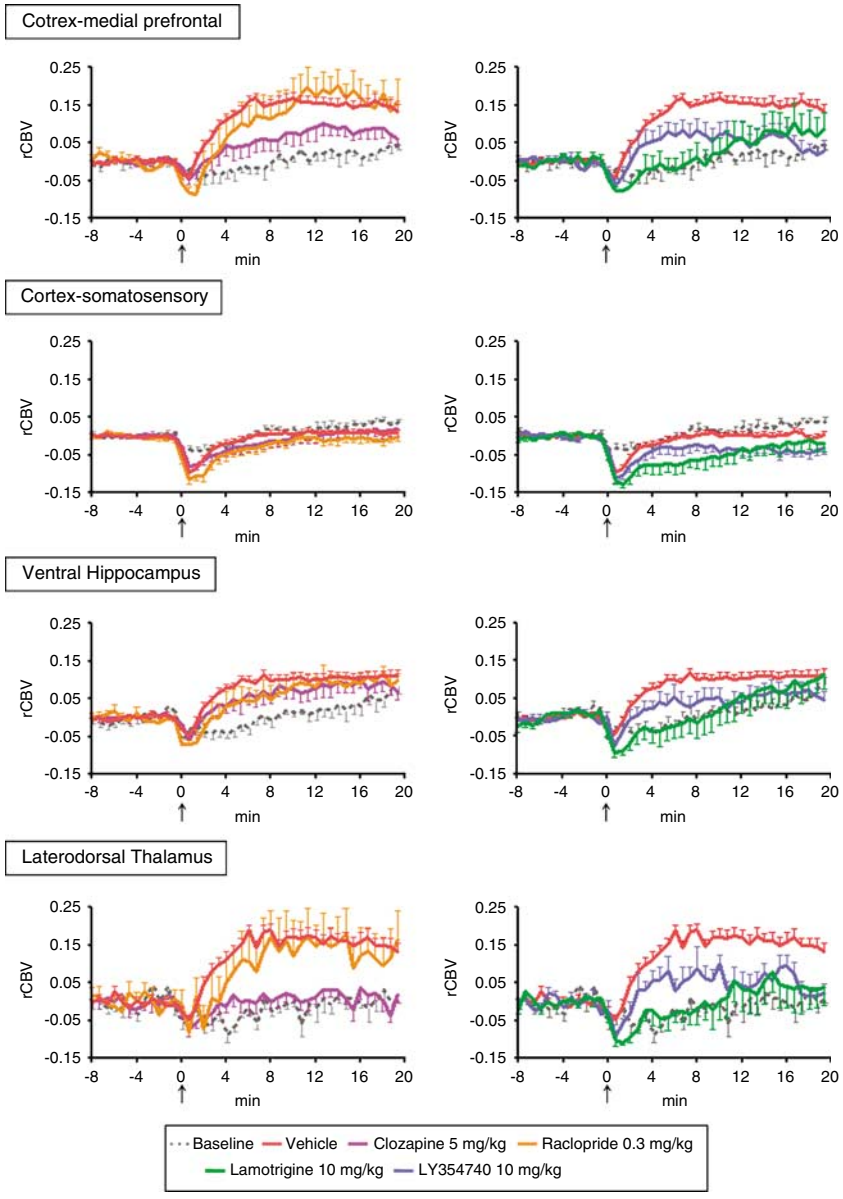

Figure 2 rCBV time course following phencyclidine (PCP) injection as a function of pretreatment in four representative brain structures. Arrows indicate the time of PCP injection. Baseline data were obtained in animals pretreated and challenged with vehicle (saline). Data are plotted as mean ± SEM within each group. (clozapine–PCP $n=7$; raclopride–PCP $n=6$; lamotrigine–PCP $n=6$, LY354740–PCP $n=7$; vehicle–PCP $n=24$.)

Raclopride

Intraperitoneal pretreatment with raclopride (0.3 mg/kg) did not significantly attenuate the response to PCP in any of the regions examined (Figures 2 and 4). However, a trend toward attenuation was observed in the dorso-lateral thalamus ($p=0.10$, Figure 4), caudate putamen, and nucleus accumbens ($p=0.08$ and 0.11, respectively; Figure 4). Equally, the time course of rCBV changes following PCP administration in raclopride-treated rats was not significantly modified compared to control, in either the regions activated by PCP (eg thalamus, limbic cortex, hippocampus) or those not activated by PCP (eg somatosensory cortex, Figures 2 and 4). Raclopride did not produce significant alterations of basal MABP, with respect to vehicle, and the rCBV changes produced by preadministration of raclopride *per se* were negligible in all the brain regions examined (Figure 5).

LY354740

LY354740 (10 mg/kg i.p.) induced a significant inhibition of the rCBV response to PCP in all the activated regions examined (Figures 2 and 4). The inhibition was marked in all activated cortical areas ($p<0.001$ in all regions examined, Figure 4). Marked inhibition was also observed in the ventro-medial thalamus ($p=0.009$) and dorsal hippocampus ($p=0.002$). Significant inhibition was observed also in mesolimbic areas such as the striatum and the nucleus accumbens ($p=0.02$ and 0.04, respectively). Time course analysis of rCBV changes showed a significant inhibition of the response to PCP in animals pretreated with

Appendix 2

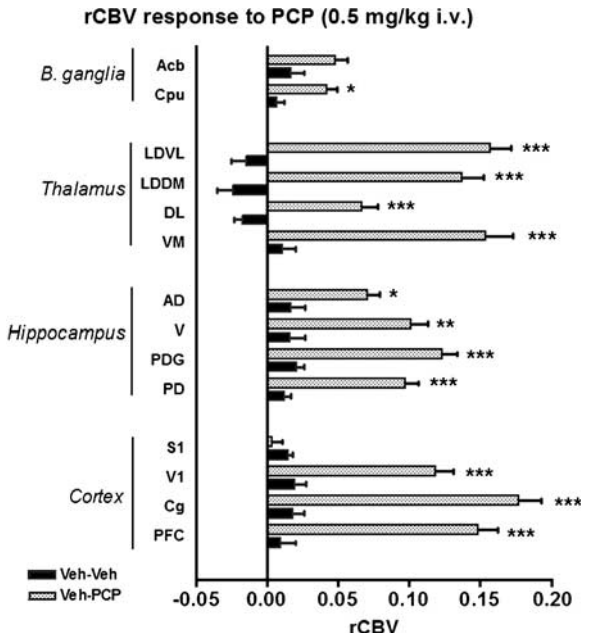

Figure 3 rCBV response to PCP in representative VOIs. The effect was plotted as mean rCBV over a 16 min time window covering the peak response to phencyclidine (PCP) (4–20 min post injection). Baseline data of control animals pretreated and challenged with vehicle are reported for comparison (vehicle–vehicle). $*p<0.05$, $**p<0.01$, $***p<0.001$, *vs* vehicle–vehicle. (Abbreviations: Acb, nucleus accumbens; Cpu, caudate putamen; LDVL ventro-lateral part of latero-dorsal thalamus, LDDM dorso-medial part of latero-dorsal thalamus, DL, dorso-lateral thalamus; VM, ventro-medial thalamus, AD, antero-dorsal hippocampus; V, ventral hippocampus; PDG, posterior dentate gyrus; PD, postero-dorsal hippocampus; S1, primary somatosensory cortex; V1, primary visual cortex; Cg, cingulate cortex; PFC, medial prefrontal cortex.)

LY354740 both in the amplitude and the duration of the response (Figure 2). As observed with lamotrigine, weak but sustained rCBV decreases in cortical areas were observed upon the injection of PCP after LY354740 pretreatment, particularly in the motor and somatosensory regions (eg somatosensory cortex, $p=0.01$, Figures 2 and 4). LY354740 did not produce significant alterations of basal MABP, with respect to vehicle, and the rCBV changes produced by preadministration of LY354740 *per se* were negligible in all the brain regions examined (Figure 5).

Lamotrigine

Lamotrigine (10 mg/kg i.p.) significantly inhibited the activation induced by PCP in all regions (Figures 2 and 4). The effect was particularly marked in strongly responding cortical regions, such as prefrontal, cingulate, and retrosplenial cortices, where preadministration of lamotrigine completely suppressed the PCP response ($p=0.002$, 0.0003, and 0.002, respectively). Robust or complete suppression was also observed in key subcortical structures including the ventro-medial and dorso-lateral thalamus ($p=0.004$ and 0.003, respectively), the hippocampus ($p<0.02$ in all the hippocampal regions examined), and the dorsal striatum ($p=0.006$). Time course analysis of rCBV changes showed robust inhibition of the response to PCP over the period examined (Figure 2). Weak but sustained rCBV decreases in cortical areas were observed upon the injection of PCP after lamotrigine pretreatment, particularly in the motor and somatosensory regions (eg somatosensory cortex, $p=0.005$, Figures 2 and 4).

The administration of lamotrigine did not produce significant alterations of basal MABP with respect to vehicle, and the rCBV changes produced by preadministration of lamotrigine *per se* were negligible in all the brain regions examined (Figure 5).

DISCUSSION

Acute administration of NMDAR antagonists like phencyclidine (PCP) or ketamine induces symptoms that closely resemble those of schizophrenia in humans, a finding that led to the hypothesis that a decreased NMDAR function may be a predisposing or even causative factor in schizophrenia. However, the brain circuitry and the precise neuropharmacological mechanisms underlying these effects remain to be fully elucidated. Here, we applied phMRI to examine the brain circuitry underlying the psychotomimetic action of PCP, and investigated how these functional changes are modulated by drugs that possess distinct pharmacological mechanisms. Acute administration of PCP produced robust activation of cortico-limbo-thalamic regions. Pretreatment with the selective D_2 dopamine antagonist raclopride did not significantly affect the rCBV response to PCP, while the atypical antipsychotic clozapine produced region-dependent effects, with complete suppression of the rCBV response in the thalamus, and weaker attenuation of the response in cortical and hippocampal structures. The response to PCP was also strongly suppressed by pretreatment with two drugs that can prevent aberrant glutamatergic activity: the anticonvulsant lamotrigine and the mGluR2/3 agonist LY354740.

rCBV Response to PCP

Acute administration of PCP produced a robust and reproducible increase in rCBV in discrete cortico-limbic, thalamic, and hippocampal regions. Multiple lines of evidence argue that the rCBV changes observed reflect underlying neuronal activation. First, the observed rCBV increases are unlikely to be the result of global hemodynamic effects, since PCP induced a sustained activation of discrete cortical and subcortical structures, with no effects in other regions. Next, PCP and the intraperitoneal pretreatments induced only modest and transient alterations of arterial blood pressure. The magnitude of these changes under halothane anesthesia was well within the range (60–120 mm Hg) within which abrupt pharmacological manipulation of MABP can be homeostatically compensated without producing significant alterations of CBV (Gozzi *et al*, 2007a). Finally, the observed pattern of rCBV changes is consistent with the results from studies of the functional effects of NMDAR antagonists performed with a variety of other measures in *ex vivo* experiments that should not be sensitive to hemodynamic confounds; eg ^{14}C-2-deoxyglucose (2DG) uptake and immediate early gene expression (Duncan *et al*, 1999c, d; Nakki *et al*, 1996).

The use of anesthetic is a putative confound that can potentially affect the sign and distribution of the functional response. This aspect has been extensively studied in our

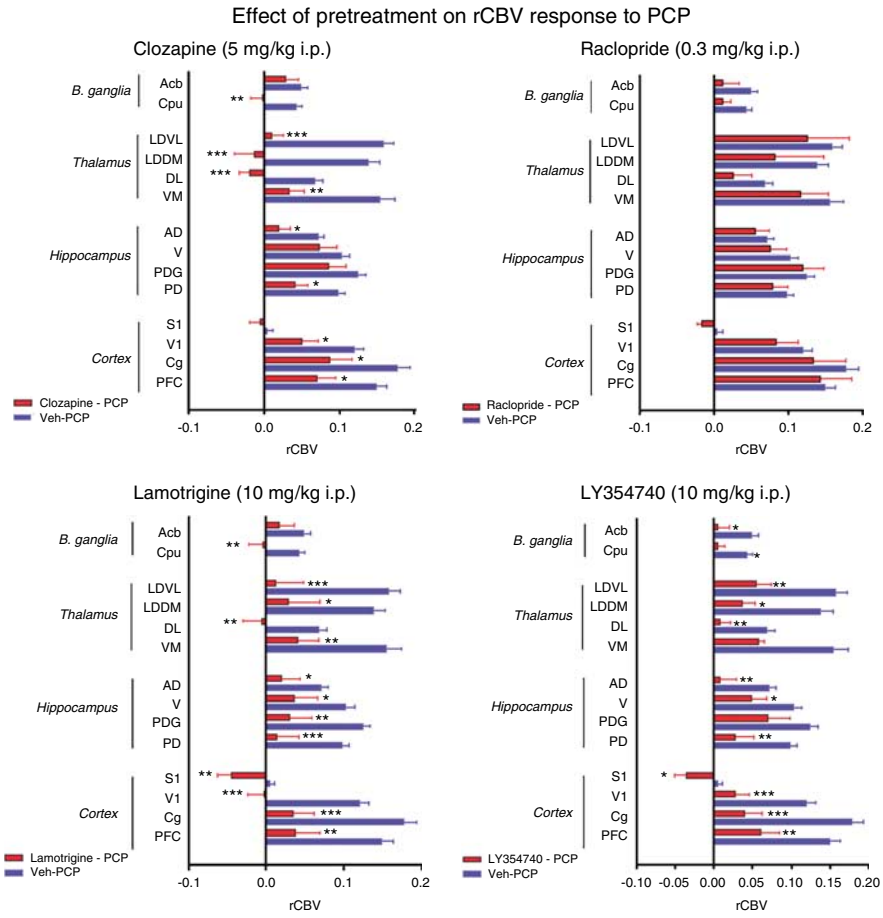

Figure 4 Effect of pretreatment on the rCBV response to phencyclidine (PCP) in representative VOIs. Data are expressed as mean ± SEM (clozapine–PCP $n=7$; raclopride–PCP $n=6$; lamotrigine–PCP $n=6$; LY354740–PCP $n=7$; vehicle–PCP $n=24$). *$p<0.05$, **$p<0.01$, ***$p<0.001$, *vs* vehicle–PCP. (Abbreviations: Acb, nucleus accumbens; Cpu, caudate putamen; LDVL, ventro-lateral part of latero-dorsal thalamus; LDDM, dorso-medial part of latero-dorsal thalamus; DL, dorso-lateral thalamus; VM, ventro-medial thalamus; AD, antero-dorsal hippocampus; V, ventral hippocampus; PDG, posterior dentate gyrus; PD, postero-dorsal hippocampus; S1, primary somatosensory cortex; V1, primary visual cortex; Cg, cingulate cortex; PFC, medial prefrontal cortex.)

lab through a comprehensive series of studies aimed to identify a dose of PCP and an anesthetic level that resulted in a pattern of activation consistent with the result of neurofunctional studies performed in conscious animals (eg single unit recording, [^{14}C]-iodoantipyrine CBF measurements, 2-deoxyglucose uptake etc). This work has highlighted a critical interaction between PCP and maintenance anesthetic, with the appearance of widespread brain deactivation as the level of anesthesia or PCP dose is increased. However, when rats were imaged under 0.8% halothane anesthesia and challenged with a subanesthetic dose of PCP (0.5 mg/kg i.v.), robust and reproducible activation of discrete cortico-limbo-thalamic structures was observed (Gozzi *et al*, 2007b). These conditions were, therefore, used in the present study. Several lines of evidence support the suggestion that the observed pattern of activation is representative of the central effects of PCP in freely moving animals and in humans. First, the observation of *activation* in response to PCP is consistent with the excitatory effects of NMDAR antagonists observed in freely moving rodents, measured with single unit recording (Homayoun *et al*, 2005), [^{14}C]-iodoantipyrine CBF measurements (Cavazzuti *et al*, 1987), and 2DG (Miyamoto *et al*, 2000; Duncan *et al*, 1998a, b, 1999b, 2000; Weissman *et al*, 1987; Meibach *et al*, 1979). Second, the anatomical distribution of rCBV changes is consistent with regions of increased 2DG uptake in conscious rats upon injection of NMDAr antagonist such as PCP, ketamine, or MK-801 (Duncan *et al*, 1999a). Third, the pattern of functional changes described in the present work is very similar to that observed in neuroimaging studies of the effects of ketamine in healthy humans. For example, Langsjo *et al* (2003) reported robust dose-dependent rCBF increases in the anterior cingulate, thalamus, putamen, and frontal cortex in healthy human volunteers receiving ketamine. McKie *et al* (2007) using BOLD fMRI also report a similar pattern in healthy human volunteers. Taken together, these observations suggest that the level of anesthesia (and dose of PCP) used in the present study did not qualitatively affect the central effects of PCP.

Other groups have also examined the regional effects of NMDAR antagonists in the rat brain using neuroimaging techniques. Subanesthetic doses of ketamine in isoflurane-anesthetized rats were shown to increase the BOLD response in the hippocampus, the retrosplenial and orbital cortices, the nucleus accumbens, and the ventral pallidum (Littlewood *et al*, 2006a, b), regions that have also been identified in the present study. Risterucci *et al* (2005)

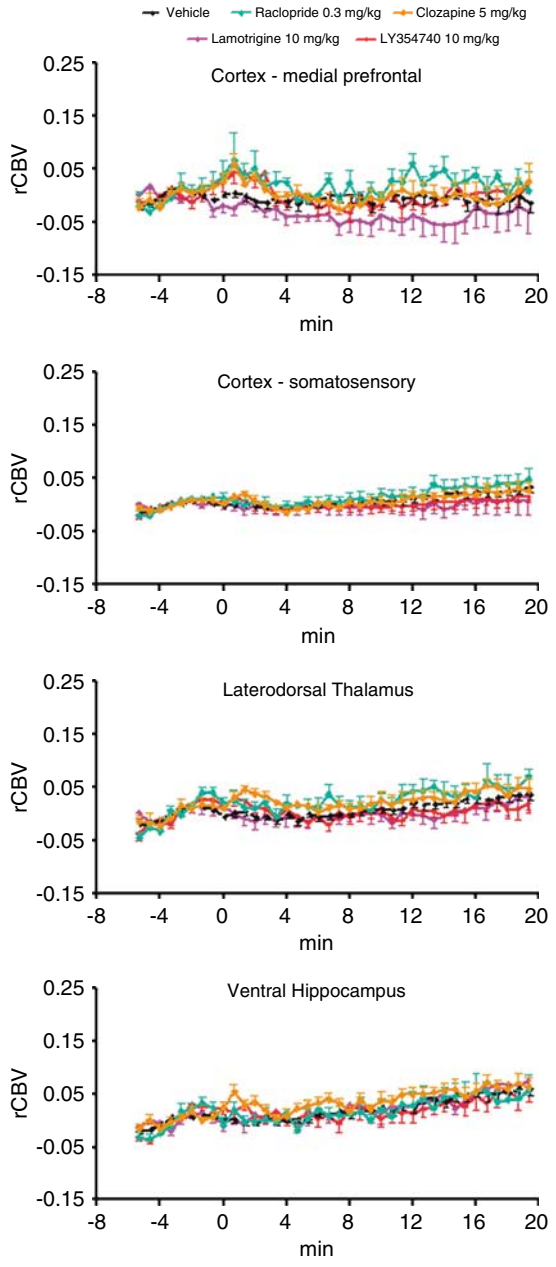

Figure 5 Effect of pretreatment *per se* on basal rCBV in four representative brain regions. Drugs were administered at time 0. Data are plotted as mean ± SEM within each group.

investigated the functional response to PCP in isoflurane-anesthetized rats using perfusion imaging. Similar to the present study, they reported increased perfusion in the enthorhinal cortex, nucleus accumbens shell, thalamus, and ventral pallidum; however, they reported decreased perfusion in prefrontal and temporal cortices and dorsal striatum, and no change in the hippocampus. The presence of areas of decreased perfusion in limbic cortical structures is at odds with our results. A possible explanation for this discrepancy is the use of a higher level of anesthetic (1.6 MAC (minimum alveolar concentration) of isoflurane) than that used in the present study (0.8 MAC (minimum alveolar concentration) of halothane). As PCP itself acts as a general anesthetic at sufficiently high doses, and as discussed earlier in relation to appropriate combination of PCP dose and level of anesthesia, the findings by Risterucci might reflect a general suppression of cortical activity resulting from the use of a higher dose of PCP combined with high levels of isoflurane (Gozzi *et al*, 2007b).

PCP altered rCBV in well-defined neural structures, such as the prefrontal cortex, hippocampus, amygdala, and thalamus, which are known to form a cortico-limbo-thalamic loop that has been the subject of research into the underlying neuropathological basis of schizophrenia (Large, 2007). While acute administration of PCP is unlikely to mimic comprehensively a complex multifactorial disease like schizophrenia, at some level PCP may, however, modify neural function in these key circuits to induce some symptoms in healthy humans that are remarkably similar to symptoms of psychosis. For instance, functional impairment of limbic cortical areas has been shown to be coupled to the decline in executive functioning that is often experienced by patients with schizophrenia (Kircher and Thienel, 2005). Similarly, dysfunction of the posterior cingulate and retrosplenial cortices has been associated with the development of thought disorder, disturbance of consciousness, and overall cognitive decline (Mitelman *et al*, 2005). Dysregulation of the amygdala–hippocampus complex has been linked to symptoms of affect, such as the inability to recognize emotional faces (Mancini-Marie *et al*, 2004; Schneider *et al*, 1998). Furthermore, aberrant hippocampal activity has been associated with memory impairment, which is observed in patients with schizophrenia (Kircher and Thienel, 2005). Likewise, the identification of focal activation by PCP of areas of the thalamus is in agreement with recent evidence supporting a critical role for this region in the pathophysiology of schizophrenia (Clinton and Meador-Woodruff, 2004). Finally, PCP-induced activation of mesolimbic and nigrostriatal structures is in good agreement with the classical dopamine hypothesis of schizophrenia, where dysregulation of accumbens dopamine transmission is implicated in the onset of positive symptoms. Overall, these observations suggest a degree of overlap between the regions that are affected by PCP, and some of the key brain circuits that may be dysfunctional in schizophrenia. Consequently, the use of PCP combined with functional neuroimaging provides a valuable approach to identifying neuropathological processes that might contribute to the symptoms of schizophrenia. Importantly, the approach is also ideally suited for investigating the site of action of existing and future antipsychotic drugs.

Effect of Antipsychotic Drugs

Among the atypical antipsychotic agents, clozapine possesses superior efficacy in the treatment of patients with schizophrenia, especially in those refractory to therapy with conventional D_2 receptor antagonists (Tandon and Fleischhacker, 2005; Kane *et al*, 1988). In the present study, pretreatment with clozapine produced a profound suppression of the response to PCP in specific brain structures, such as the cingulate and medial prefrontal cortex, the thalamus, the antero-dorsal hippocampus, and the striatum. Our results are consistent with preclinical work examining the effects of clozapine on NMDAR function. Studies have shown that clozapine, but not the D_2 receptor antagonist

haloperidol, reversed deficits in cognitive and social behavior induced by NMDAR agonists in rodents, primates (Idris *et al*, 2005; Gaisler-Salomon and Weiner, 2003; Linn *et al*, 2003; Qiao *et al*, 2001), and humans (Malhotra *et al*, 1997a). Similar findings have been reported using functional readouts such as 2DG uptake (Duncan *et al*, 1998a, 2000).

The pharmacological profile of clozapine is broad, including affinity for D_1 and D_2 dopamine receptors, and potent antagonist action at affinity for 5-HT_{2A}, 5-HT_{2C}, 5-HT_6, 5-HT_7, α_1- and α_2-adenergic, histamine H_1, and muscarinic M_1 receptors (Meltzer, 1996). Classically, D_2 receptor blockade has been considered to be the key pharmacological mechanism underlying clozapine efficacy. However, in the present study, pretreatment with the selective dopamine D_2 antagonist raclopride did not produce significant inhibition of the response to PCP in any of the regions analyzed. Raclopride was given at a subcataleptic dose that is expected to produce $\sim$75% dopamine D_2 receptor occupancy (Wadenberg *et al*, 2000), a value that is in line with the threshold of occupancy (65–70%) required for therapeutic effect in patients with schizophrenia (Farde *et al*, 1992). The same dose of raclopride has also been shown to be active in tests classically considered to reflect *in vivo* blockade of DA transmission, such as D-amphetamine-induced hyperlocomotion (Mark *et al*, 2004; Maurel-Remy *et al*, 1995). In contrast, the dose of clozapine tested in the present study would be expected to occupy just 40% of dopamine D_2 receptors (Kapur *et al*, 2003; Mukherjee *et al*, 2001), a value that is also consistent with the occupancies determined in schizophrenic patients treated with clozapine (eg 16–68% in Kapur *et al*, 1999; 20–67% in Nordstrom *et al*, 1995). Thus, the lack of inhibitory effect of raclopride at a dose that significantly blocks dopamine D_2 neurotransmission argues against a primary role for dopamine D_2 receptors in the generation of psychotic symptoms by NMDAR antagonists, and suggests that the efficacy of clozapine in the models is not due to D_2 receptor blockade. Consistent with the present observations with raclopride, NMDAR antagonists are reported to increase dopamine release in limbic and frontal cortical brain areas (Adams and Moghaddam, 1998; Hertel *et al*, 1995), but dopamine D_2 receptor antagonists or dopamine depletion was unable to prevent the behavioral effects induced by NMDAR antagonists in rodents (Idris *et al*, 2005; Linn *et al*, 2003; Carlsson *et al*, 1999; Duncan *et al*, 1998a; Corbett *et al*, 1995) and humans (Krystal *et al*, 1999). These findings also underscore a potential limitation in the validity of the NMDAR deficit model as a tool to predict the therapeutic efficacy of antipsychotic agents relying on blockade of D_2 dopamine receptors.

Clozapine also has affinity for dopamine D_1 receptors, although it is still unclear whether the drug acts as an agonist or antagonist (Tauscher *et al*, 2004). D_1 receptor activation by other drugs has also been shown to promote NMDAR function (Flores-Hernandez *et al*, 2002; Morari *et al*, 1994). Alternatively, or in addition, clozapine may potentiate NMDAR activation by elevating synaptic levels of glycine through inhibition of type 1 glycine transporters (GlyT-1) (Javitt *et al*, 2005). Such a mechanism could also be implicated in the focal effect of clozapine in the thalamus, given the high level of Gly-T1 receptor expression in this region, with respect to the cortex and other limbic areas (Zafra *et al*, 1995). Thus the efficacy of clozapine in the present study might arise through a direct or indirect enhancement of NMDAR function, counteracting the effect of NMDAR block by PCP.

Clozapine has a high affinity for 5-HT_{2A} receptors so it is also possible that these receptors mediate the efficacy of the drug in the present model, perhaps via an indirect modulatory effect on cortical glutamate neurotransmission (Seeman, 2002; Aghajanian and Marek, 1999). This is also consistent with the strong effects observed with lamotrigine and LY354740, which are also thought to act via the inhibition of glutamate transmission. However, direct studies of the effects of clozapine on glutamate release have produced conflicting results, with both increased (Yamamoto and Cooperman, 1994; Daly and Moghaddam, 1993) and decreased (Yang and Wang, 2005) levels of cortical glutamate observed following the administration of clozapine to rats.

The observation from the present study that clozapine produces a stronger effect in the thalamus, compared to the cortex or limbic brain areas, is of particular interest and suggests a regional selectivity that might be key to understanding the functional basis of its pharmacological action. It can be speculated that the superior therapeutic efficacy of clozapine with respect to other antipsychotics (Tandon and Fleischhacker, 2005; Breier *et al*, 1994; Kane *et al*, 1988) might be at least partly mediated by a more effective restoration (or preservation) of thalamic function. This hypothesis would be consistent with the recent neuropathological and neuroimaging evidence pointing to structural and metabolic abnormalities in the thalamus giving rise to deficits in sensory processing and some symptoms of psychosis (Sim *et al*, 2006; Clinton and Meador-Woodruff, 2004). The regional specificity of clozapine might also provide an additional clue as to the contribution of specific receptor systems to its mechanism of action. For example, serotonin 5-HT_7 receptors are highly expressed in the thalamus, and are known to be inhibited by clozapine (Heidmann *et al*, 1998). It is, therefore, tempting to speculate that 5-HT_7 receptors might be implicated in the focal effect of clozapine on the thalamus. Consistent with this hypothesis, a recent study showed that the selective serotonin 5-HT_7 agonist SB269970A prevented deficits in reversal learning induced by PCP in rats (Neill *et al*, 2006). It is also noteworthy that recent genetic or post mortem studies have implicated 5-HT_7 receptors in the pathology underlying schizophrenia (Dean *et al*, 2006; Ikeda *et al*, 2006; East *et al*, 2002).

Effect of LY354740

LY354740 produced a potent and widespread suppression of the rCBV response to PCP. This compound is a selective metabotropic glutamate (mGlu) 2/3 receptor agonist that can prevent glutamate hyperexcitation by decreasing the evoked release of glutamate from forebrain and limbic glutamatergic synapses (Schoepp and Marek, 2002; Cartmell and Schoepp, 2000). Consistent with this, LY354740 has been shown to inhibit increases in glutamate induced by the depolarizing agent veratridine in the striatum of freely moving rats (Battaglia *et al*, 1997), and reduce the response to electrically evoked glutamate release in a manner

consistent with a presynaptic site of action (Capogna, 2004; Kilbride *et al*, 1998). Agonists of mGluR2/3 such as LY354740 can antagonize the behavioral and neurochemical effects of PCP in rodents (Lorrain *et al*, 2003; Cartmell *et al*, 1999; Moghaddam and Adams, 1998) and produce a dose-dependent suppression of ketamine-induced impairment of working memory by ketamine in human volunteers (Krystal *et al*, 2005). Our results show a significant inhibition of the amplitude of the response to PCP in most of the activated regions, an effect that parallels the preclinical and clinical findings mentioned above.

The results with LY354740, a compound that can modulate glutamate release, add to a growing body of evidence that implicates glutamate transmission and an aberrant activity of glutamatergic neurons (eg cortical and hippocampal pyramidal cells) in the behavioral and neurometabolic effects of NMDA antagonists. Electrophysiological and neurotoxicological studies suggest that the cognitive, psychotomimetic, and eventually neurodegenerative actions of NMDA antagonists are dose-dependent manifestations of a general inhibition of GABAergic interneurons, resulting in unregulated activity of principal neurons leading to excessive release of glutamate (Farber, 2003; Greene, 2001). By selectively disinhibiting cortical interneurons, psychotogenic doses of NMDA can produce an increased glutamate transmission via non-NMDA glutamate receptors over major excitatory projections from the cortex to the basal forebrain and the thalamus, thus originating a hyperexcitatory state that is thought to underlie NMDA-induced psychosis. Our findings that LY354740 completely suppressed the response to PCP are in agreement with this theory. It is noteworthy that the response suppression was widespread and affected all the activated regions, suggesting that disruption of glutamate transmission may occur early in the cascade of events leading from NMDAR blockade to psychomimetic reaction.

The observation that LY354740 can produce anxiolytic effects on rodents (Ferris *et al*, 2001) has led some authors to hypothesize a direct involvement of mGluR2/3 receptors in GABA neurotransmission. However, neurophysiological and neuroanatomical studies do not provide evidence of a direct modulation of GABAergic activity by mGluR2/3 agonists, and preclinical data suggest that the anxiolytic action of LY354740 is probably mediated by an inhibition of glutamate release from excitatory inputs to crucial brain structures, such as the amygdala and hypothalamus (reviewed by Swanson *et al*, 2005). Moreover, drugs that do directly enhance GABAergic inhibition (eg sodium valproate, diazepam, lorazepam) do not prevent the effects of NMDAR antagonists in either rodents or humans (Large, 2007; Krystal *et al*, 1998), thus suggesting that GABA-enhancement alone is not sufficient to prevent the psychotomimetic action of NMDA antagonists (Large, 2007). Taken together, these findings point to a modulation of glutamate release as the most plausible mechanism by which LY354740 can inhibit the psychotomimetic effects of PCP.

Effect of Lamotrigine

Lamotrigine is a broad spectrum anticonvulsant that inhibits voltage-gated sodium channels in a use-dependent manner; the drug has also been shown to reduce neuronal excitability and glutamatergic transmission (Large *et al*, 2005). Studies in rodents show that acute treatment with lamotrigine can prevent the disruption of behavior induced by NMDA antagonists (Large *et al*, 2005), and in healthy human volunteers lamotrigine has been shown to attenuate positive, negative, and cognitive effects of ketamine (Anand *et al*, 2000). In the present study, pretreatment with lamotrigine produced a potent and widespread inhibition of the rCBV response to PCP in all the activated regions, which is consistent with recent results showing that lamotrigine pretreatment can reduce the BOLD response to ketamine in healthy human volunteers (McKie *et al*, 2007).

Several studies have shown that PCP, ketamine, and other NMDAR antagonists can induce aberrant glutamatergic neurotransmission by altering the firing of cortical neurons in rats (Jodo *et al*, 2005; Jackson *et al*, 2004; Tamminga *et al*, 2003; Shi and Zhang, 2003). Thus the efficacy of lamotrigine in these models and in the present study supports the hypothesis that the psychotomimetic effects of NMDAR antagonists arise through dysregulation of cortical neural activity and possibly an increase in excitatory transmission. However, since glutamate release is intimately linked to the underlying pattern of neuronal activity, it is not yet clear whether lamotrigine effects are directed at one or the other. Despite this, the efficacy of lamotrigine underscores once more a central role of dysregulation of cortical neuronal activity and glutamate release in the psychotomimetic effect of NMDAR antagonists. The widespread effect of lamotrigine, reducing the PCP-induced rCBV response in all brain areas, further indicates that the inhibition of activity and/or glutamate transmission lies proximal to the primary effect of NMDAR antagonists.

In conclusion, we investigated the spatio-temporal distribution of changes in rCBV induced by acute challenge with PCP in the anesthetized rat and examined how these effects are modulated by drugs that differentially modify NMDAR antagonist-induced behaviors. PCP produced increases in rCBV in discrete cortico-limbo-thalamic regions. This effect was strongly suppressed by pretreatment with compounds that can reduce neuronal excitability and modulate glutamatergic transmission such as the sodium channel blocker lamotrigine and the mGluR2/3 agonist LY354740, thus corroborating the pivotal role of cortical glutamatergic neurotransmission in the psychotomimetic action of NMDAR antagonists. Pretreatment with the selective D_2 dopamine antagonist raclopride did not significantly affect the response to PCP, a finding that argues against a primary role for dopamine D_2 receptors in the functional response elicited by NMDAR antagonists. Finally, clozapine produced a region-dependent suppression of PCP response, with moderate but significant inhibition in the cortex, and total response suppression in the thalamus. This regional effect of NMDAR antagonists could be key to elucidating the functional basis of clozapine pharmacological action.

DISCLOSURE/CONFLICT OF INTEREST

We declare that, except for income received from my primary employer, no financial support or compensation has been received from any individual or corporate entity

over the past 3 years for research or professional service and there are no personal financial holdings that could be perceived as constituting a potential conflict of interest.

REFERENCES

Adams B, Moghaddam B (1998). Corticolimbic dopamine neurotransmission is temporally dissociated from the cognitive and locomotor effects of phencyclidine. *J Neurosci* **18**: 5545–5554.

Adler CM, Malhotra AK, Elman I, Goldberg T, Egan M, Pickar D *et al* (1999). Comparison of ketamine-induced thought disorder in healthy volunteers and thought disorder in schizophrenia. *Am J Psychiatry* **156**: 1646–1649.

Aghajanian GK, Marek GJ (1999). Serotonin, via 5-HT2A receptors, increases EPSCs in layer V pyramidal cells of prefrontal cortex by an asynchronous mode of glutamate release. *Brain Res* **825**: 161–171.

Anand A, Charney DS, Oren DA, Berman RM, Hu XS, Cappiello A *et al* (2000). Attenuation of the neuropsychiatric effects of ketamine with lamotrigine: support for hyperglutamatergic effects of N-methyl-D-aspartate receptor antagonists. *Arch Gen Psychiatry* **57**: 270–276.

Bakshi VP, Swerdlow NR, Geyer MA (1994). Clozapine antagonizes phencyclidine-induced deficits in sensorimotor gating of the startle response. *J Pharmacol Exp Ther* **271**: 787–794.

Battaglia G, Monn JA, Schoepp DD (1997). *In vivo* inhibition of veratridine-evoked release of striatal excitatory amino acids by the group II metabotropic glutamate receptor agonist LY354740 in rats. *Neurosci Lett* **229**: 161–164.

Boxerman JL, Hamberg LM, Rosen BR, Weisskoff RM (1995). MR contrast due to intravascular magnetic susceptibility perturbations. *Magn Reson Med* **34**: 555–566.

Breier A, Buchanan RW, Kirkpatrick B, Davis OR, Irish D, Summerfelt A *et al* (1994). Effects of clozapine on positive and negative symptoms in outpatients with schizophrenia. *Am J Psychiatry* **151**: 20–26.

Brody SA, Geyer MA, Large CH (2003). Lamotrigine prevents ketamine but not amphetamine-induced deficits in prepulse inhibition in mice. *Psychopharmacology (Berl)* **169**: 240–246.

Capogna M (2004). Distinct properties of presynaptic group II and III metabotropic glutamate receptor-mediated inhibition of perforant pathway-CA1 EPSCs. *Eur J Neurosci* **19**: 2847–2858.

Carlsson A, Waters N, Carlsson ML (1999). Neurotransmitter interactions in schizophrenia—therapeutic implications. *Biol Psychiatry* **46**: 1388–1395.

Cartmell J, Monn JA, Schoepp DD (1999). The metabotropic glutamate 2/3 receptor agonists LY354740 and LY379268 selectively attenuate phencyclidine *versus* d-amphetamine motor behaviors in rats. *J Pharmacol Exp Ther* **291**: 161–170.

Cartmell J, Schoepp DD (2000). Regulation of neurotransmitter release by metabotropic glutamate receptors. *J Neurochem* **75**: 889–907.

Cavazzuti M, Porro CA, Biral GP, Benassi C, Barbieri GC (1987). Ketamine effects on local cerebral blood flow and metabolism in the rat. *J Cereb Blood Flow Metab* **7**: 806–811.

Clinton SM, Meador-Woodruff JH (2004). Thalamic dysfunction in schizophrenia: neurochemical, neuropathological, and *in vivo* imaging abnormalities. *Schizophr Res* **69**: 237–253.

Corbett R, Camacho F, Woods AT, Kerman LL, Fishkin RJ, Brooks K *et al* (1995). Antipsychotic agents antagonize non-competitive N-methyl-D-aspartate antagonist-induced behaviors. *Psychopharmacology (Berl)* **120**: 67–74.

Daly DA, Moghaddam B (1993). Actions of clozapine and haloperidol on the extracellular levels of excitatory amino acids in the prefrontal cortex and striatum of conscious rats. *Neurosci Lett* **152**: 61–64.

Dean B, Pavey G, Thomas D, Scarr E (2006). Cortical serotonin7, 1D and 1F receptors: effects of schizophrenia, suicide and antipsychotic drug treatment. *Schizophr Res* **88**: 265–274.

Duncan GE, Leipzig JN, Mailman RB, Lieberman JA (1998a). Differential effects of clozapine and haloperidol on ketamine-induced brain metabolic activation. *Brain Res* **812**: 65–75.

Duncan GE, Miyamoto S, Leipzig JN, Lieberman JA (1999a). Comparison of brain metabolic activity patterns induced by ketamine, MK-801 and amphetamine in rats: support for NMDA receptor involvement in responses to subanesthetic dose of ketamine. *Brain Res* **843**: 171–183.

Duncan GE, Miyamoto S, Leipzig JN, Lieberman JA (1999b). Comparison of brain metabolic activity patterns induced by ketamine, MK-801 and amphetamine in rats: support for NMDA receptor involvement in responses to subanesthetic dose of ketamine. *Brain Res* **843**: 171–183.

Duncan GE, Miyamoto S, Leipzig JN, Lieberman JA (1999c). Comparison of brain metabolic activity patterns induced by ketamine, MK-801 and amphetamine in rats: support for NMDA receptor involvement in responses to subanesthetic dose of ketamine. *Brain Res* **843**: 171–183.

Duncan GE, Miyamoto S, Leipzig JN, Lieberman JA (1999d). Comparison of brain metabolic activity patterns induced by ketamine, MK-801 and amphetamine in rats: support for NMDA receptor involvement in responses to subanesthetic dose of ketamine. *Brain Res* **843**: 171–183.

Duncan GE, Miyamoto S, Leipzig JN, Lieberman JA (2000). Comparison of the effects of clozapine, risperidone, and olanzapine on ketamine-induced alterations in regional brain metabolism. *J Pharmacol Exp Ther* **293**: 8–14.

Duncan GE, Moy SS, Knapp DJ, Mueller RA, Breese GR (1998b). Metabolic mapping of the rat brain after subanesthetic doses of ketamine: potential relevance to schizophrenia. *Brain Res* **787**: 181–190.

East SZ, Burnet PWJ, Kerwin RW, Harrison PJ (2002). An RT-PCR study of 5-HT6 and 5-HT7 receptor mRNAs in the hippocampal formation and prefrontal cortex in schizophrenia. *Schizophr Res* **57**: 15–26.

Farber NB (2003). The NMDA receptor hypofunction model of psychosis. *Ann NY Acad Sci* **1003**: 119–130.

Farde L, Nordstrom AL, Wiesel FA, Pauli S, Halldin C, Sedvall G (1992). Positron emission tomographic analysis of central D1 and D2 dopamine receptor occupancy in patients treated with classical neuroleptics and clozapine. Relation to extrapyramidal side effects. *Arch Gen Psychiatry* **49**: 538–544.

Ferris P, Seward E, Dawson GR (2001). Interactions between LY354740, a Group II metabotropic agonist and the GABAA-benzodiazepine receptor complex in the rat elevated plus-maze. *J Psychopharmacol* **15**: 76–82.

Flores-Hernandez J, Cepeda C, Hernandez-Echeagaray E, Calvert CR, Jokel ES, Fienberg AA *et al* (2002). Dopamine enhancement of NMDA currents in dissociated medium-sized striatal neurons: role of D1 receptors and DARPP-32. *J Neurophysiol* **88**: 3010–3020.

Friston KJ, Jezzard P, Turner R (1994). Analysis of functional MRI time-series. *Hum Brain Mapp* **1**: 153–171.

Gaisler-Salomon I, Weiner I (2003). Systemic administration of MK-801 produces an abnormally persistent latent inhibition which is reversed by clozapine but not haloperidol. *Psychopharmacology* **V166**: 333–342.

Gozzi A, Ceolin L, Schwarz AJ, Reese T, Bertani S, Bifone A (2007a). A multimodality investigation of cerebral haemodynamics and autoregulation in phMRI. *Magn Reson Imaging* **25**: 826–833.

Gozzi A, Schwarz AJ, Reese T, Bertani S, Crestan V, Bifone A (2005). Region-specific effects of nicotine on brain activity: a pharmacological MRI study in the drug-naïve rat. *Neuropsychopharmacology* **31**: 1690–1703.

Gozzi A, Schwarz AJ, Reese T, Crestan V, Bifone A (2007b). Drug-anaesthetic interaction in pharmacological MRI: the case of the psychotogenic agent phencyclidine, Book of abstracts: 15th Annual Meeting of the International Society of Magnetic Resonance in Medicine: P2000.

Greene R (2001). Circuit analysis of NMDAR hypofunction in the hippocampus, *in vitro*, and psychosis of schizophrenia. *Hippocampus* **11**: 569–577.

Heidmann DEA, Szot P, Kohen R, Hamblin MW (1998). Function and distribution of three rat 5-hydroxytryptamine7 (5-HT7) receptor isoforms produced by alternative splicing. *Neuropharmacology* **37**: 1621–1632.

Hennig J, Nauerth A, Friedburg H (1986). RARE imaging: a fast imaging method for clinical MR. *Magn Reson Med* **3**: 823–833.

Hertel P, Mathe JM, Nomikos GG, Iurlo M, Mathe AA, Svensson TH (1995). Effects of d-amphetamine and phencyclidine on behavior and extracellular concentrations of neurotensin and dopamine in the ventral striatum and the medial prefrontal cortex of the rat. *Behav Brain Res* **72**: 103–114.

Holcomb HH, Lahti AC, Medoff DR, Cullen T, Tamminga CA (2005). Effects of noncompetitive NMDA receptor blockade on anterior cingulate cerebral blood flow in volunteers with schizophrenia. *Neuropsychopharmacology* **30**: 2275–2282.

Homayoun H, Jackson ME, Moghaddam B (2005). Activation of metabotropic glutamate 2/3 receptors reverses the effects of NMDA receptor hypofunction on prefrontal cortex unit activity in awake rats. *J Neurophysiol* **93**: 1989–2001.

Idris NF, Repeto P, Neill JC, Large CH (2005). Investigation of the effects of lamotrigine and clozapine in improving reversal-learning impairments induced by acute phencyclidine and D-amphetamine in the rat. *Psychopharmacology (Berl)* **179**: 336–348.

Ikeda M, Iwata N, Kitajima T, Suzuki T, Yamanouchi Y, Kinoshita Y *et al* (2006). Positive association of the serotonin 5-HT7 receptor gene with schizophrenia in a Japanese population. *Neuropsychopharmacology* **31**: 866–871.

Jackson ME, Homayoun H, Moghaddam B (2004). NMDA receptor hypofunction produces concomitant firing rate potentiation and burst activity reduction in the prefrontal cortex. *Proc Natl Acad Sci USA* **101**: 8467–8472.

Javitt DC, Duncan L, Balla A, Sershen H (2005). Inhibition of system A-mediated glycine transport in cortical synaptosomes by therapeutic concentrations of clozapine: implications for mechanisms of action. *Mol Psychiatry* **10**: 275–287.

Javitt DC, Zukin SR (1991). Recent advances in the phencyclidine model of schizophrenia. *Am J Psychiatry* **148**: 1301–1308.

Jodo E, Suzuki Y, Katayama T, Hoshino KY, Takeuchi S, Niwa SI *et al* (2005). Activation of medial prefrontal cortex by phencyclidine is mediated via a hippocampo-prefrontal pathway. *Cereb Cortex* **15**: 663–669.

Kane J, Honigfeld G, Singer J, Meltzer H (1988). Clozapine for the treatment-resistant schizophrenic. A double-blind comparison with chlorpromazine. *Arch Gen Psychiatry* **45**: 789–796.

Kapur S, VanderSpek SC, Brownlee BA, Nobrega JN (2003). Antipsychotic dosing in preclinical models is often unrepresentative of the clinical condition: a suggested solution based on *in vivo* occupancy. *J Pharmacol Exp Ther* **305**: 625–631.

Kapur S, Zipursky RB, Remington G (1999). Clinical and theoretical implications of 5-HT2 and D2 receptor occupancy of clozapine, risperidone, and olanzapine in schizophrenia. *Am J Psychiatry* **156**: 286–293.

Kilbride J, Huang LQ, Rowan MJ, Anwyl R (1998). Presynaptic inhibitory action of the group II metabotropic glutamate receptor agonists, LY354740 and DCG-IV. *Eur J Pharmacol* **356**: 149–157.

Kircher TT, Thienel R (2005). Functional brain imaging of symptoms and cognition in schizophrenia. *Prog Brain Res* **150**: 299–308.

Kohler C, Hall H, Ogren SO, Gawell L (1985). Specific *in vitro* and *in vivo* binding of 3H-raclopride a potent substituted benzamide drug with high affinity for dopamine D-2 receptors in the rat brain. *Biochem Pharmacol* **34**: 2251–2259.

Kristiansen LV, Huerta I, Beneyto M, Meador-Woodruff JH (2007). NMDA receptors and schizophrenia. *Curr Opin Pharmacol* **7**: 48–55.

Krystal JH, Abi-Saab W, Perry E, D'Souza DC, Liu N, Gueorguieva R *et al* (2005). Preliminary evidence of attenuation of the disruptive effects of the NMDA glutamate receptor antagonist, ketamine, on working memory by pretreatment with the group II metabotropic glutamate receptor agonist, LY354740, in healthy human subjects. *Psychopharmacology (Berl)* **179**: 303–309.

Krystal JH, D'Souza DC, Karper LP, Bennett A, Abi-Dargham A, Abi-Saab D *et al* (1999). Interactive effects of subanesthetic ketamine and haloperidol in healthy humans. *Psychopharmacology (Berl)* **145**: 193–204.

Krystal JH, Karper LP, Bennett A, D'Souza DC, Abi-Dargham A, Morrissey K *et al* (1998). Interactive effects of subanesthetic ketamine and subhypnotic lorazepam in humans. *Psychopharmacology (Berl)* **135**: 213–229.

Lahti AC, Weiler MA, Tamara Michaelidis BA, Parwani A, Tamminga CA (2001). Effects of ketamine in normal and schizophrenic volunteers. *Neuropsychopharmacology* **25**: 455–467.

Lahti RA, Evans DL, Stratman NC, Figur LM (1993). Dopamine D4 *versus* D2 receptor selectivity of dopamine receptor antagonists: possible therapeutic implications. *Eur J Pharmacol* **236**: 483–486.

Langsjo JW, Kaisti KK, Aalto S, Hinkka S, Aantaa R, Oikonen V *et al* (2003). Effects of subanesthetic doses of ketamine on regional cerebral blood flow, oxygen consumption, and blood volume in humans. *Anesthesiology* **99**: 614–623.

Large CH (2007). Do NMDA receptor antagonist models of schizophrenia predict the clinical efficacy of antipsychotic drugs? *J Psychopharmacol* **21**: 283–301.

Large CH, Webster EL, Goff DC (2005). The potential role of lamotrigine in schizophrenia. *Psychopharmacology (Berl)* **181**: 415–436.

Linn S, Negi S, Gerum V, Javitt C (2003). Reversal of phencyclidine-induced prepulse inhibition deficits by clozapine in monkeys. *Psychopharmacology* **V169**: 234–239.

Littlewood CL, Jones N, O'Neil MJ, Mitchell SN, Tricklebank M, Williams MS (2006a). Mapping the central effects of ketamine in the rat using pharmacological MRI. *Psychopharmacology* **V186**: 64–81.

Littlewood CL, Diana C, Dixon AL, Dix SL, White CT, O'neill MJ *et al* (2006b). Using the BOLD MR signal to differentiate the stereoisomers of ketamine in the rat. *NeuroImage* **32**: 1733–1746.

Lorrain DS, Baccei CS, Bristow LJ, Anderson JJ, Varney MA (2003). Effects of ketamine and N-methyl-D-aspartate on glutamate and dopamine release in the rat prefrontal cortex: modulation by a group II selective metabotropic glutamate receptor agonist LY379268. *Neuroscience* **117**: 697–706.

Malhotra AK, Adler CM, Kennison SD, Elman I, Pickar D, Breier A (1997a). Clozapine blunts N-methyl-D-aspartate antagonist-induced psychosis: a study with ketamine. *Biol Psychiatry* **42**: 664–668.

Malhotra AK, Pinals DA, Adler CM, Elman I, Clifton A, Pickar D *et al* (1997b). Ketamine-induced exacerbation of psychotic symptoms and cognitive impairment in neuroleptic-free schizophrenics. *Neuropsychopharmacology* **17**: 141–150.

Malhotra AK, Pinals DA, Weingartner H, Sirocco K, Missar CD, Pickar D *et al* (1996). NMDA receptor function and human cognition: the effects of ketamine in healthy volunteers. *Neuropsychopharmacology* **14**: 301–307.

Mancini-Marie A, Stip E, Fahim C, Mensour B, Leroux JM, Beaudoin G *et al* (2004). Fusiform gyrus and possible impairment of the recognition of emotional expression in schizophrenia subjects with blunted affect: a fMRI preliminary report. *Brain Cogn* **54**: 153–155.

Mandeville JB, Marota JJA, Kosofsky BE, Keltner JR, Weissleder R, Rosen B *et al* (1998). Dynamic functional imaging of relative cerebral blood volume during rat forepaw stimulation. *Magn Reson Med* **39**: 615–624.

Mark JM, Laetitia S, Alain G, Didier C, Mauricette B (2004). The role of dopamine D 3 compared with D 2 receptors in the control of locomotor activity: a combined behavioural and neurochemical analysis with novel, selective antagonists in rats. *Psychopharmacology* **V174**: 341–357.

Maurel-Remy S, Bervoets K, Millan MJ (1995). Blockade of phencyclidine-induced hyperlocomotion by clozapine and MDL 100 907 in rats reflects antagonism of 5-HT2A receptors. *Eur J Pharmacol* **280**: R9–R11.

McKie S, Lees J, Hallak J, Deakin JF, Williams SCR (2007). Pretreatment by lamotrigine attenuates the ketamine-induced BOLD response in healthy volunteers: a phMRI study. Book of abstracts: 15th Annual Meeting of the International Society of Magnetic Resonance in Medicine: p 24.

Meibach RC, Glick SD, Cox R, Maayani S (1979). Localisation of phencyclidine-induced changes in brain energy metabolism. *Nature* **282**: 625–626.

Meltzer HY (1996). Pre-clinical pharmacology of atypical antipsychotic drugs: a selective review. *Br J Psychiatry Suppl* **29**: 23–31.

Messenheimer JA (1995). Lamotrigine. *Epilepsia* **36**(Suppl 2): S87–S94.

Millan M (2005). N-Methyl-d-aspartate receptors as a target for improved antipsychotic agents: novel insights and clinical perspectives. *Psychopharmacology* **179**: 30–53.

Mitelman SA, Shihabuddin L, Brickman AM, Hazlett EA, Buchsbaum MS (2005). Volume of the cingulate and outcome in schizophrenia. *Schizophr Res* **72**: 91–108.

Miyamoto S, Leipzig JN, Lieberman JA, Duncan GE (2000). Effects of ketamine, MK-801, and amphetamine on regional brain 2-deoxyglucose uptake in freely moving mice. *Neuropsychopharmacology* **22**: 400–412.

Moghaddam B, Adams BW (1998). Reversal of phencyclidine effects by a group II metabotropic glutamate receptor agonist in rats. *Science* **281**: 1349–1352.

Morari M, O'Connor WT, Ungerstedt U, Fuxe K (1994). Dopamine D1 and D2 receptor antagonism differentially modulates stimulation of striatal neurotransmitter levels by acid. *Eur J Pharmacol* **256**: 23–30.

Morris BJ, Cochran SM, Pratt JA (2005). PCP: from pharmacology to modelling schizophrenia. *Curr Opin Pharmacol* **5**: 101–106.

Mukherjee J, Christian BT, Narayanan TK, Shi B, Mantil J (2001). Evaluation of dopamine D-2 receptor occupancy by clozapine, risperidone, and haloperidol *in vivo* in the rodent and nonhuman primate brain using 18F-fallypride. *Neuropsychopharmacology* **25**: 476–488.

Nakki R, Sharp FR, Sagar SM, Honkaniemi J (1996). Effects of phencyclidine on immediate early gene expression in the brain. *J Neurosci Res* **45**: 13–27.

Neill JC, Jones DN, Hagan JJ, Thomas DR (2006). Antagonism at 5-HT7 receptors attenuates a PCP-induced reversal learning deficit in the rat. *Schizophr Res* **81**(Suppl): 233.

Nordstrom AL, Farde L, Nyberg S, Karlsson P, Halldin C, Sedvall G (1995). D1, D2, and 5-HT2 receptor occupancy in relation to clozapine serum concentration: a PET study of schizophrenic patients. *Am J Psychiatry* **152**: 1444–1449.

Paxinos G, Watson C (1998). *The Rat Brain in Stereotactic Coordinates*. Academic Press: San Diego.

Qiao H, Noda Y, Kamei H, Nagai T, Furukawa H, Miura H *et al* (2001). Clozapine, but not haloperidol, reverses social behavior deficit in mice during withdrawal from chronic phencyclidine treatment. *NeuroReport* **12**: 11–15.

Risterucci C, Jeanneau K, Schoppenthau S, Bielser T, Kunnecke B, von Kienlin M *et al* (2005). Functional magnetic resonance imaging reveals similar brain activity changes in two different animal models of schizophrenia. *Psychopharmacology (Berl)* **180**: 724–734.

Schneider F, Weiss U, Kessler C, Salloum JB, Posse S, Grodd W *et al* (1998). Differential amygdala activation in schizophrenia during sadness. *Schizophr Res* **34**: 133–142.

Schoepp DD, Marek GJ (2002). Preclinical pharmacology of mGlu2/3 receptor agonists: novel agents for schizophrenia? *Curr Drug Targets CNS Neurol Disord* **1**: 215–225.

Schotte A, Bonaventure P, Janssen PF, Leysen JE (1995). *In vitro* receptor binding and *in vivo* receptor occupancy in rat and guinea pig brain: risperidone compared with antipsychotics hitherto used. *Jpn J Pharmacol* **69**: 399–412.

Schotte A, Janssen P, Gommeren W, Luyten W, Gompel P, Lesage A *et al* (1996). Risperidone compared with new and reference antipsychotic drugs: *in vitro* and *in vivo* receptor binding. *Psychopharmacology* **124**: 57–73.

Schotte A, Janssen PF, Megens AA, Leysen JE (1993). Occupancy of central neurotransmitter receptors by risperidone, clozapine and haloperidol, measured *ex vivo* by quantitative autoradiography. *Brain Res* **631**: 191–202.

Schwarz AJ, Danckaert A, Reese T, Gozzi A, Paxinos G, Watson C *et al* (2006a). A stereotaxic MRI template set for the rat brain with tissue class distribution maps and co-registered anatomical atlas: application to pharmacological MRI. *NeuroImage* **32**: 538–550.

Schwarz AJ, Reese T, Gozzi A, Bifone A (2003). Functional MRI using intravascular contrast agents: detrending of the relative cerebrovascular (rCBV) time course. *Magn Reson Imaging* **21**: 1191–1200.

Schwarz AJ, Whitcher B, Gozzi A, Reese T, Bifone A (2006b). Study-level wavelet cluster analysis and data-driven signal models in pharmacological MRI. *J Neurosci Methods* **159**: 346–360.

Seeman P (2002). Atypical antipsychotics: mechanism of action. *Can J Psychiatry* **47**: 27–38.

Shi WX, Zhang XX (2003). Dendritic glutamate-induced bursting in the prefrontal cortex: further characterization and effects of phencyclidine. *J Pharmacol Exp Ther* **305**: 680–687.

Sim K, Cullen T, Ongur D, Heckers S (2006). Testing models of thalamic dysfunction in schizophrenia using neuroimaging. *J Neural Transm* **V113**: 907–928.

Soyka M, Koch W, Moller HJ, Ruther T, Tatsch K (2005). Hypermetabolic pattern in frontal cortex and other brain regions in unmedicated schizophrenia patients. Results from a FDG-PET study. *Eur Arch Psychiatry Clin Neurosci* **255**: 308–312.

Swanson CJ, Bures M, Johnson MP, Linden AM, Monn JA, Schoepp DD (2005). Metabotropic glutamate receptors as novel targets for anxiety and stress disorders. *Nat Rev Drug Discov* **4**: 131–144.

Tamminga CA, Lahti AC, Medoff DR, Gao XM, Holcomb HH (2003). Evaluating glutamatergic transmission in schizophrenia. *Ann NY Acad Sci* **1003**: 113–118.

Tandon R, Fleischhacker W (2005). Comparative efficacy of antipsychotics in the treatment of schizophrenia: a critical assessment. *Schizophr Res* **79**: 145–155.

Tauscher J, Hussain T, Agid O, Verhoeff NP, Wilson AA, Houle S *et al* (2004). Equivalent occupancy of dopamine D1 and D2 receptors with clozapine: differentiation from other atypical antipsychotics. *Am J Psychiatry* **161**: 1620–1625.

Wadenberg ML, Kapur S, Soliman A, Jones C, Vaccarino F (2000). Dopamine D2 receptor occupancy predicts catalepsy and the suppression of conditioned avoidance response behavior in rats. *Psychopharmacology (Berl)* **150**: 422–429.

Weissman AD, Dam M, London ED (1987). Alterations in local cerebral glucose utilization induced by phencyclidine. *Brain Res* **435**: 29–40.

Whitcher B, Schwarz AJ, Barjat H, Smart SC, Grundy RI, James MF (2005). Wavelet-based cluster analysis: data-driven grouping of voxel time courses with application to perfusion-weighted and pharmacological MRI of the rat brain. *NeuroImage* **24**: 281–295.

Worsley KJ, Evans AC, Marrett S, Neelin P (1992). A three-dimensional statistical analysis for CBF activation studies in human brain. *J Cereb Blood Flow Metab* **12**: 900–918.

Yamamoto BK, Cooperman MA (1994). Differential effects of chronic antipsychotic drug treatment on extracellular glutamate and dopamine concentrations. *J Neurosci* **14**: 4159–4166.

Yang TT, Wang SJ (2005). Effects of haloperidol and clozapine on glutamate release from nerve terminals isolated from rat prefrontal cortex. *Synapse* **56**: 12–20.

Zafra F, Aragon C, Olivares L, Danbolt NC, Gimenez C, Storm-Mathisen J (1995). Glycine transporters are differentially expressed among CNS cells. *J Neurosci* **15**: 3952–3969.

Appendix 3

Psychopharmacology
DOI 10.1007/s00213-008-1271-z

ORIGINAL INVESTIGATION

Pharmacological stimulation of NMDA receptors via co-agonist site suppresses fMRI response to phencyclidine in the rat

Alessandro Gozzi · Hugh Herdon · Adam Schwarz · Simone Bertani · Valerio Crestan · Giuliano Turrini · Angelo Bifone

Received: 12 March 2008 / Accepted: 21 July 2008

Abstract
Rationale Increasing experimental evidence suggests that impaired *N*-methyl-D-aspartic acid (NMDA) receptor (NMDAr) function could be a key pathophysiological determinant of schizophrenia. Agonists at the allosteric glycine (Gly) binding site of the NMDA complex can promote NMDAr activity, a strategy that could provide therapeutic efficacy for the disorder. NMDAr antagonists like phencyclidine (PCP) can induce psychotic and dissociative symptoms similar to those observed in schizophrenia and are therefore widely used experimentally to impair NMDA neurotransmission in vivo.
Objectives In the present study, we used pharmacological magnetic resonance imaging (phMRI) to investigate the modulatory effects of endogenous and exogenous agonists at the NMDAr Gly site on the spatiotemporal patterns of brain activation induced by acute PCP challenge in the rat. The drugs investigated were D-serine, an endogenous agonist of the NMDAr Gly site, and SSR504734, a potent Gly transporter type 1 (GlyT-1) inhibitor that can potentiate NMDAr function by increasing synaptic levels of Gly.
Results Acute administration of PCP induced robust and sustained activation of discrete cortico-limbo-thalamic circuits. Pretreatment with D-serine (1 g/kg) or SSR504734 (10 mg/kg) completely inhibited PCP-induced functional activation. This effect was accompanied by weak but sustained *deactivation* particularly in cortical areas.
Conclusions These findings suggest that agents that stimulate NMDAr via Gly co-agonist site can potentiate NMDAr activity in the living brain and corroborate the potential for this class of drugs to provide selective enhancement of NMDAr neurotransmission in schizophrenia.

Keywords fMRI · Glycine · PCP · D-serine · Gly-T1 · phMRI · SSR504734 · CBV

A. Gozzi · H. Herdon · A. Schwarz
Biology, Neurosciences CEDD,
GlaxoSmithKline Medicines Research Centre,
Verona, Italy

S. Bertani · V. Crestan · G. Turrini
Laboratory Animal Science, Neurosciences CEDD,
GlaxoSmithKline Medicines Research Centre,
Verona, Italy

A. Bifone
CPDM, Neurosciences CEDD,
GlaxoSmithKline Medicines Research Centre,
Verona, Italy

A. Gozzi (✉)
Neuroimaging, GSK Neurosciences CEDD,
Fleming 4,
37100 Verona, Italy
e-mail: alessandro.2.gozzi@gsk.com

Introduction

Accumulating clinical and experimental evidence suggests that impaired expression and functionality of the *N*-methyl-D-aspartate receptor (NMDAr) could be a key pathophysiological determinant of schizophrenia (Kristiansen et al. 2007). This observation has prompted considerable research effort to develop novel medications aimed to enhance NMDAr functionality in vivo. The NMDAr is unique among ligand-gated ion channels because its functional activation requires the presence of glutamate, the primary receptor ligand, and glycine (Gly), an obligatory co-agonist that binds to a separate modulatory site of the receptor complex (Leeson and Iversen 1994).

Several in vitro studies have demonstrated that agents that directly bind to the Gly co-agonist site such as Gly itself, the endogenous co-agonist D-serine, or the partial agonist cycloserine can dose-dependently promote NMDAr neurotransmission (Millan 2002). NMDAr activity can also be promoted by increasing endogenous glycine levels in proximity of the NMDAr receptor by using Gly transporter (GlyT) inhibitors, which can raise synaptic Gly levels by preventing its removal from the synaptic cleft (Javitt 2007). Two high-affinity Gly transporter subtypes, referred to as GlyT-1 and GlyT-2, have been identified which share approximately 50% amino acid sequence identity (Sur and Kinney 2007). The distribution of GlyT-2 is relatively restricted, being present mainly on inhibitory glycinergic neurons in the spinal cord, brainstem, and cerebellum. In contrast, GlyT-1 is more widely expressed throughout the body, with expression in the central nervous system (CNS) being much greater than it is in the periphery. Within the CNS, GlyT-1 is expressed on both glial and neuronal cells around the synapses where it provides the principal high-affinity transport system controlling extracellular glycine levels (Sur and Kinney 2007). By inhibiting GlyT-1 and raising the extracellular glycine concentration, it is possible to strengthen NMDAr-mediated synaptic inputs and still retain the temporal and spatial specificity of activation of NMDA receptors, since this is governed by the synaptic release of glutamate which is still required to activate the receptor. Thus, GlyT-1 inhibitors have the potential to provide selective enhancement of NMDAr activity and have been shown to promote downstream processes related to NMDAr function, e.g., synaptic plasticity (Kinney et al. 2003). As a result, a number of chemically diverse GlyT-1 inhibitors have been developed that can raise extracellular glycine levels and potentiate NMDA receptor-related activity (Sur and Kinney 2007).

A prerequisite for the successful exploitation of these mechanisms in vivo is the presence of non-saturating levels of Gly under homeostatic conditions. This aspect has been the object of a considerable debate in recent years. Early studies reporting the detection of high extracellular Gly levels in the brain (3–10 μM) led to the proposal that tonic Gly levels could be saturating under physiological conditions (Thomson 1990; Westergren et al. 1994). This hypothesis has been challenged by subsequent electrophysiology studies where in vitro and in vivo NMDAr potentiation was induced by administration of agents that stimulate Gly co-agonist site (Kinney et al. 2003; Martina et al. 2003; Chen et al. 2003). These data seem to support the view that the effective Gly concentration in the synaptic cleft could be much lower (nM range), due to the action of Gly transporters strategically placed around the synapse (Javitt and Heresco-Levy 2000). However, some controversy still exists as to the nature and role of the interaction of Gly and the NMDAr in vivo, with multiple studies showing the lack of modulatory effects following the application of Gly site agonists (Long et al. 2007; Meur et al. 2007; Obrenovitch et al. 1997). Such discrepant results have led some authors to propose that the degree of NMDA Gly site saturation might be region-dependent (Li and Han 2007; Ballard et al. 2002).

NMDA receptor antagonists like ketamine or phencyclidine (PCP) can be used experimentally to induce impairment of NMDAr neurotransmission in vivo. Acute administration of these compounds produces robust and well-characterized behavioral and neurofunctional effects (Krystal et al. 2002) that can be reversed or prevented by agents that stimulate NMDAr activity, including glycinergic agents (Large 2007). In the present study, we applied pharmacological magnetic resonance imaging (phMRI) to examine if compounds that stimulate the Gly-binding site on the NMDAr can modulate the spatio-temporal pattern of response to an acute PCP challenge in the rat brain. phMRI is a noninvasive technique that measures central hemodynamic changes to acute drug challenges as surrogate for changes in the underlying neuronal activity and can therefore be employed to investigate drug–receptor interactions in the living brain and at a systems level (Jenkins et al. 2003; Gozzi et al. 2005). The drugs investigated were D-serine, an endogenous agonist of the NMDAr Gly site (Nishikawa 2005) and SSR504734, a potent Gly transporter type 1 (GlyT-1) inhibitor that potentiates NMDAr function by increasing extracellular levels of Gly (Depoortere et al. 2005).

Materials and methods

Animal preparation

All in vivo studies were conducted in accordance with the Italian laws (DL 116, 1992 Ministero della Sanità, Roma). Animal research protocols were also reviewed and consented to by the GSK animal care committee, in accordance with the guidelines of the Principles of Laboratory Animal Care (NIH publication 86-23, revised 1985). The studies were performed on male Sprague–Dawley rats (mean± SEM, 293±5 g, Charles River, Como, Italy). Animals had free access to standard rat chow and tap water and were housed in groups of five in solid-bottom cages with sawdust litter. Room temperature (20–22°C), relative humidity (45–65%), and dark–light cycles (12 h each, lights on at 0600 hours) were automatically controlled. After arrival, rats were allowed to acclimatize for at least 5 days.

Animal preparation/monitoring and MRI acquisition in each phMRI study were similar to previous studies (Gozzi

et al. 2008b). Briefly, rats were anesthetized with 3% halothane in a 30:70% O_2:N_2 gas mixture, tracheotomized and artificially ventilated with a mechanical respirator. The left femoral artery and vein were cannulated and animal paralyzed with a 0.25-mg/kg i.v. bolus of D-tubocurarine followed by a continuous infusion of 0.25 mg/kg/h through the artery. A PE50 cannula was inserted intraperitoneally for drug pretreatment. Average duration of surgery was 25–35 min. After surgery, the rat was secured into a customized stereotactic holder (Bruker, Ettlingen, Germany) and the halothane level set to 0.8%. The ventilation parameters were adjusted to maintain physiological arterial blood gas levels according to p_aCO_2 and p_aO_2 measurements performed prior to and at the end of the fMRI time-series acquisition. No statistically significant difference between pre- and post-acquisition p_aCO_2 values for each of the experimental groups was found ($p>0.23$, all groups). A student *t* test corrected for multiple comparisons using the Benajmini–-Hochberg method did not evidence any statistically significant intergroup difference between pre- or post-acquisition p_aCO_2 values. Moreover, linear regression analysis did not show significant correlation between the amplitude of the relative cerebral blood volume (rCBV) response to PCP (expressed as 4–20 min postinjection average in the medial prefrontal cortex) and p_aCO_2 levels, when these were expressed as basal values, or pre- and post- acquisition difference ($P>.19$, $r<.33$). A magnetic resonance-compatible thermocouple probe was used to measure rectal temperature. The body temperature of all subjects was maintained within physiological range (37± 0.8°C) throughout the experiment, by using a water-heating system incorporated in the stereotactic holder. Mean arterial blood pressure (MABP) was monitored continually through the femoral artery. At the end of the experiment, the animals were euthanized with an overdose of anesthetic followed by cervical dislocation.

Relative cerebral volume measurement

MRI data were acquired using a Bruker Avance 4.7 Tesla system, a 72-mm birdcage resonator for radiofrequency pulse transmit and a Bruker curved "Rat Brain" quadrature receive coil. The MR acquisition for each subject comprised T_2-weighted anatomical images using the RARE sequence (Hennig et al. 1986) (TR_{eff}=5,000 ms, TE_{eff} = 76 ms, RARE factor 8, FOV 40 mm, 256×256 matrix, 16 contiguous 1 mm slices) followed by a time-series acquisition with the same spatial coverage and similar parameters (TR_{eff} =2,700 ms, TE_{eff} =110 ms, RARE factor 32), but with a lower in-plane spatial resolution (128×128) giving a functional pixel volume of ~0.1 mm^3. Two successive scans were averaged for a resulting time resolution of 40 s.

In each experiment, intraperitoneal injection of drug (or vehicle) was followed by PCP challenge (or vehicle) 30 min (groups 3–5, see below) or 24 h later (groups 1–2). In the latter case, animals were pretreated outside the magnet and underwent surgical preparation for MRI acquisition 22.5 h later. In these subjects, the start of the rCBV time series was timed to allow PCP administration to take place 24 h post-i.p. pretreatment. Total MRI time-series acquisition time was 80-min (120 repetitions) for all groups. Following five reference images, 2.67 ml/kg of the blood pool contrast agent Endorem (Guerbet, France) was injected so that subsequent signal changes would reflect alterations in relative cerebral blood volume (rCBV; Mandeville et al. 1998). In groups 3–5, prior to the injection of i.p. drug pretreatment, an equilibration period of 15 min (23 images) was allowed. PCP challenge (groups 1–4) was administered at image 73, ensuring a 30-min delay between i.p. pretreatment (when present, groups 3–5) and the subsequent intravenous PCP bolus. The MRI data were acquired over a period of 30 min following the administration of the PCP challenge.

Compounds and experimental arms

D-serine study A 24-h delay between pretreatment and challenge was used to ensure a stable elevation of D-serine levels in the brain (Hashimoto and Chiba 2004). Rats were randomly assigned to one of the following groups:

(1) intraperitoneal pretreatment with vehicle (water 2 ml/kg $n=5$) and intravenous challenge with PCP (0.5 mg/kg, 1 ml/rat IV) 24 h later
(2) intraperitoneal pretreatment with D-serine (10 mmol–1 g/kg, $n=8$) and intravenous challenge with PCP (0.5 mg/kg, 1 ml/rat IV) 24 h later

SSR504734 study Rats were randomly assigned to one of the three following groups

(3) intraperitoneal pretreatment with vehicle (water, $n=6$, 1 ml/kg) and intravenous challenge with PCP (0.5 mg/kg, 1 ml/rat IV) 30 min later
(4) intraperitoneal pretreatment with SSR504734 (10 mg/kg, $n=5$) and intravenous administration of PCP (0.5 mg/kg, 1 ml/rat IV) 30 min later
(5) intraperitoneal pretreatment with water (1 ml/kg; $n=6$) and intravenous challenge with saline (1 ml/rat) 30 min later. This group served as reference rCBV baseline for PCP in both studies.

D-serine and phencyclidine hydrochloride (PCP) were purchased at Sigma-Aldrich (Milan- Italy). SSR504734 was synthesized by GSK department of Medicinal Chemistry. All the compounds were injected at a rate of 1 ml/min.

Compound injection was followed by administration of 0.4 ml of saline to flush the intravenous line. The doses chosen for the different drugs were based on previously published in vivo studies. PCP at 0.5 mg/kg i.v. produces robust fMRI activation of discrete cortico-limbo-thalamic structures in the anesthetized rat (Gozzi et al. 2008b). The same dose of PCP has also been reported to elicit robust behavioral and metabolic (2-deoxyglucose) effects in freely moving rats (Weissman et al. 1987; Gozzi et al. 2008b). The dose of SSR504734 tested (10 mg/kg i.p.) exhibited robust efficacy in NMDA-antagonist models of schizophrenia (Depoortere et al. 2005). The pretreatment scheme and dose of D-serine used have been reported to produce robust and sustained D-serine elevation in the brain (Hashimoto and Chiba 2004). Similar amounts of D-serine have been shown to be effective in preventing PCP-induced cognitive deficits (Andersen and Pouzet 2004) and stereotyped behavior in freely moving rats (Tanii et al. 1994).

Data analysis

rCBV time-series image data for each experiment were analyzed within the framework of the general linear model (GLM) to obtain *Z* statistic maps (Worsley et al. 1992). The maps thus obtained were used to guide the selection of activated/deactivated regions for subsequent volume of interest (VOI)-based quantification and comparison of efficacy of pretreatments.

Signal intensity changes in the time series were converted into fractional rCBV on a pixel-wise basis, using a constrained exponential model of the gradual elimination of contrast agent from the blood pool (Schwarz et al. 2003). Individual subjects in each study were spatially normalized by a 9-*df* affine transformation mapping their T2-weighted anatomical images to a stereotaxic rat brain MRI template set (Schwarz et al. 2006a) and applying the resulting transformation matrix to the accompanying rCBV time series. rCBV time series for the PCP or vehicle challenge (groups 1–5) were calculated covering 8 min (12 timepoints) prechallenge baseline and 25 min (38 timepoints) postchallenge window, normalized to a common injection timepoint. Image-based time series analysis was carried out using FMRI Expert Analysis Tool (FEAT) Version 5.63, part of FSL (FMRIB's Software Library, www.fmrib.ox.ac.uk/fsl) with 0.8 mm spatial smoothing (≈2.5 × in-plane voxel dimension) and using a model function identified by wavelet cluster analysis (WCA) across all animals in the cohort, capturing the temporal profile of the signal change induced by PCP challenge in each group (Whitcher et al. 2005; Schwarz et al. 2006b). The design matrix also included the temporal derivative of this regressor and a linear ramp (both orthogonalized to the regressor of interest) with the aim to capture additional variance due to slight deviations in individual subjects or brain regions from the signal model time course as described more in detail in Schwarz et al. (2006b). The model function obtained for groups 1 and 3 (vehicle-PCP) was very similar to the one previously described in a similar phMRI experiment (Gozzi et al. 2008b), while groups 2 and 4 exhibited a negative model function that described well the profile of the sustained negative rCBV changes produced by PCP after drug pretreatment (see Fig. 2, SS cortex). The coefficients of the model function thus provided a map of rCBV response amplitude for each injection in each subject. Higher-level group comparisons were carried out using FMRIB's local analysis of mixed effects (FLAME); *Z* (Gaussianised *T*/*F*) statistic images were thresholded using clusters determined by $Z>2.33$ (study 1) or $Z>1.96$ (study 2) and a corrected cluster significance threshold of $p=0.05$ (Worsley et al. 1992; Friston et al. 1994).

To rule out the presence of significant short-lived contributions to the pattern of activation produced by PCP in the different groups, we performed an additional GLM analysis using a regressor that we identified retaining only high temporal frequency components in the WCA analysis with the aim to capture subtle short-lived responses like those induced by vehicle injection. This analysis did not highlight any significantly activated or deactivated voxel vs. vehicle–vehicle baseline for any of the groups analyzed ($Z>1.6$, cluster correction $p=0.05$).

rCBV maps were displayed using different *Z* scores to better highlight the high degree of spatial overlap in the anatomical distribution of PCP-induced response in the two independent studies. The lower statistical threshold used for D-serine study reflects a higher variance and a lower mean response observed in some of the regions activated by PCP in the vehicle-PCP cohort of this study with respect to the corresponding group in SSR504734 study (group 3, see Fig. 3). However, a formal comparison of the magnitude of the response in the two vehicle-pretreated groups is beyond the scope of the study, as the two experiments were performed at different times, using different animal batches and presented differences in the pretreatment protocol (see "Materials and methods" section). We therefore opted for different *Z* scores in order to highlight the substantial correspondence between the neural circuitry activated by PCP in the two control groups.

VOI time courses for the PCP challenge were extracted from unsmoothed rCBV time-series data using a 3D digital reconstruction of a rat brain atlas (Paxinos and Watson 1998) co-registered with the MRI template (Schwarz et al. 2006a), using custom in-house software written in IDL (Research Systems, Boulder, CO, USA). A list of the VOIs examined and their anatomical definitions can be found in Gozzi et al. (2008b). For each VOI timecourse, the average

rCBV over a 16-min time window covering the peak response to PCP (4–20 min postinjection) was used as a summary statistic of the relative change. The effect of pretreatment on the magnitude of average rCBV in different VOIs was assessed by a one-way analysis of variance (ANOVA) followed by a Dunnett's test versus vehicle (group 5). Threshold for statistical significance was considered as $p=0.05$. Results are quoted and displayed as mean±SEM unless otherwise indicated.

As subjects from groups 3–5 received the pretreatment during the phMRI time-series acquisition, VOI timecourses of pretreatment per se were examined to exclude the presence of rCBV "ceiling" or "floor" effects that might have influenced or prevented the subsequent response to PCP. To this end, rCBV timecourses were also calculated for the pretreatment over a time-window covering 6 min (eight timepoints) preinjection baseline and 21 min (32 timepoints) postinjection window normalized to a common injection timepoint. VOI timecourses were extracted from unsmoothed rCBV time series in the same regions examined for the PCP challenge. This procedure could not be applied to subjects from groups 1 and 2, as these animals received the pretreatment outside the magnet. In these subjects, we therefore examined if the pretreatment produced alterations of basal (resting-state) CBV, which was calculated as previously described (Mandeville et al. 2001) using images 0–5 as precontrast period (0–3.3 min prior to contras agent injection) and images 20–25 as postcontrast (and postequilibration) period (13.3–16.6 min time-window; approximately 30 min prior to PCP challenge). Basal CBV values were then extracted using the digitized brain atlas (Schwarz et al. 2006a) for all the VOIs previously analyzed for PCP effects. The presence of statistically significant differences in mean basal CBV difference between groups 1 and 2 in each of the VOI examined was assessed with ANOVA followed by a Fisher least significant difference test for multiple comparisons.

Pretreatment and PCP administration produced transient alterations of MABP whose peak magnitude was well within the cerebral blood flow (CBF) autoregulation range 60–120 mmHg under 0.8% halothane anesthesia. Previous experiments performed at the same anesthetic doses used here have shown that positive or negative pharmacologically evoked MABP changes within the autoregulation range mentioned above do not result in significant central rCBV response (Gozzi et al. 2007; Zaharchuk et al. 1999; Gozzi et al. 2005)

Results

Vehicle-pretreated animals (groups 1 and 3) showed a robust and sustained rCBV response to PCP in distinct

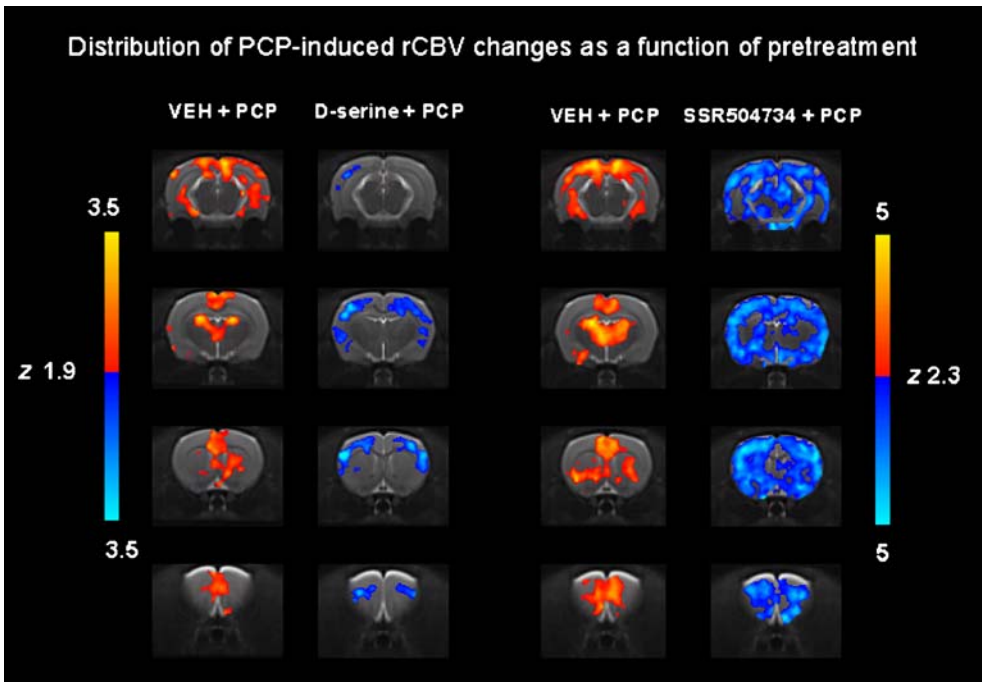

Fig. 1 Anatomical distribution of the rCBV response to acute PCP challenge (0.5 mg/kg i.v.) as a function of pretreatment. Form *left to right*, maps correspond to experimental groups nr *1* (vehicle-PCP, $n=5$), *2* (D-serine 1 g/kg-PCP, $n=8$), *3* (vehicle-PCP, $n=6$), and *4* (SSR504734 10 mg/kg-PCP, $n=5$), respectively. Groups 1 and 2 received i.p. pretreatment 24 h prior to PCP challenge, while groups nr. 3 and 4 were pretreated during the fMRI time-series acquisition 30 min before PCP. *Orange/yellow* indicate increased rCBV versus baseline (vehicle–vehicle). *Blue* indicates decreased rCBV versus baseline. An annotated version of a representative vehicle-PCP activation map can be found in Gozzi et al. (2008b)

corticolimbo-thalamic structures (Figs. 1, 2, and 3). Significant signal increases were observed in limbic cortical regions (medial prefrontal, cingulate, orbitofrontal, and retrosplenial cortices), with extension into the motor, visual, parietal- and temporal-association and rhinal cortices. Significant foci of activation were also observed in specific subcortical structures, including the medial and lateral habenula, amygdala, anterodorsal, dorsolateral and ventromedial thalamus, posterodorsal, anterodorsal and ventral and posterior hippocampus, the dorsal striatum and the nucleus accumbens (Fig. 1). The overall time-profile of PCP-induced activation was similar in all the activated regions (Fig. 2), with a brief dip followed by a rapid increase in rCBV that reached a plateau within 5 min of drug injection, and remained sustained over the period examined. The magnitude of the rCBV response to PCP was region dependent, with the largest response in cortical and thalamic regions. In nonactivated regions (e.g., somatosensory cortex, Fig. 2), the transient dip was not followed by any appreciable increase in rCBV with respect to control animals challenged with vehicle (baseline). The regional distribution and time-profile of PCP in the two control groups pretreated with vehicle (groups 1 and 3) were comparable, although a trend for a stronger and less variable response was apparent in group 3 (SSR504734 study).

Pre-administration of D-serine (1 g/kg i.p.) significantly inhibited the positive rCBV response to PCP in all the activated regions examined (Figs. 1–3). The effect did not appear to be region specific, with significant suppression taking place in all the major cortical and subcortical structures. Small but sustained rCBV decreases in cortical areas were observed upon injection of PCP in D-serine pre-administered animals particularly in motor and somatosensory areas of the cortex. These effects could be best seen in the rCBV timecourses (Fig. 2). Pretreatment of D-serine per se did not produce significant alterations of basal (resting-state) CBV prior to the PCP challenge in any of the VOIs examined (Fig. 4; $p>0.18$, all regions).

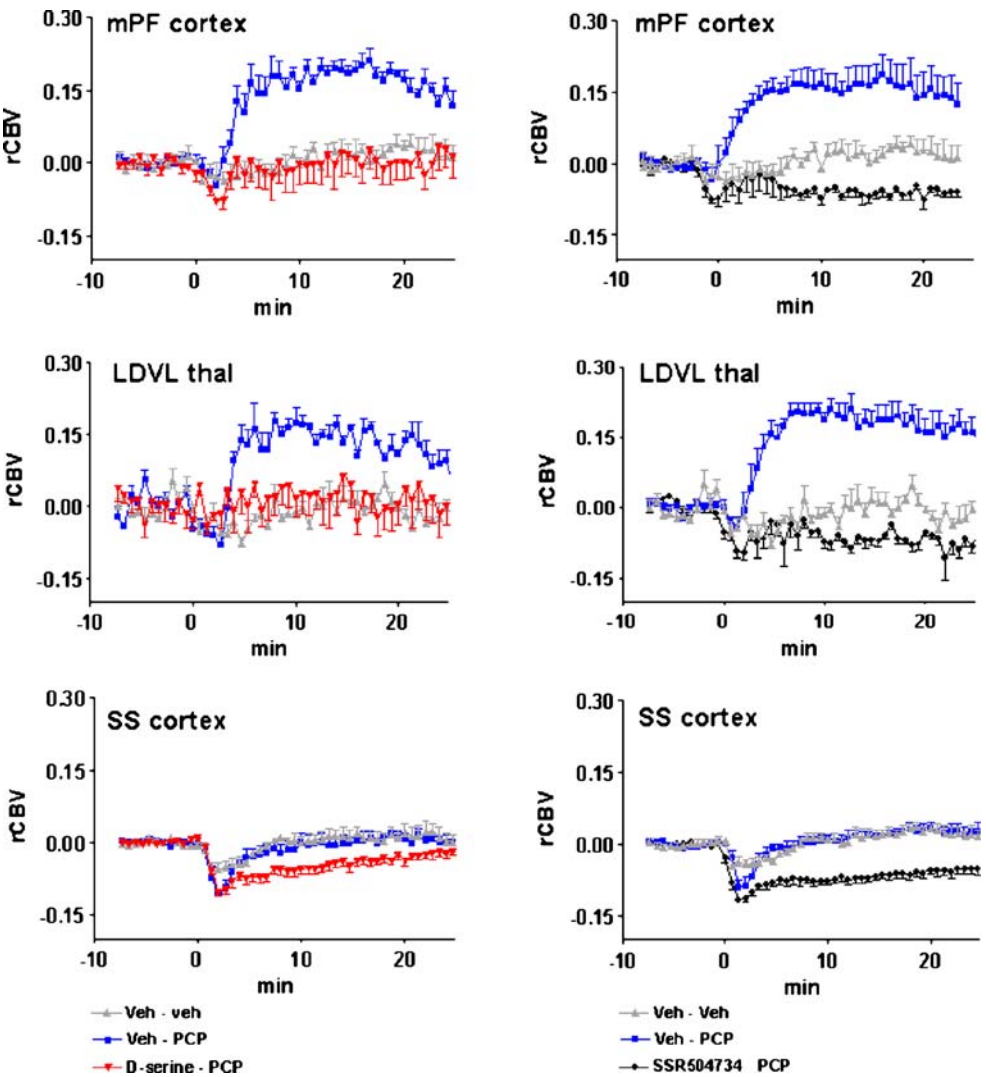

Fig. 2 rCBV timecourse following PCP injection in representative brain structures. PCP was administered at time 0. Baseline data were obtained in animals pretreated and challenged with vehicle (saline, group 5). Data are plotted as mean±SEM within each group. *Left* Veh–Veh (group 5) $n=6$; Veh–PCP (group 1) $n=5$, D-serine 1 g/kg–PCP (group 2) $n=8$; *Right*: Veh–Veh (group 5) $n=6$; Veh–PCP (group 3) $n=6$; SSR504734 10 mg/kg–PCP (group 4) $n=5$ (*mPF* Medial prefrontal cortex, *LDVL thal* ventrolateral part of laterodorsal thalamus, *SS* somatosensory cortex)

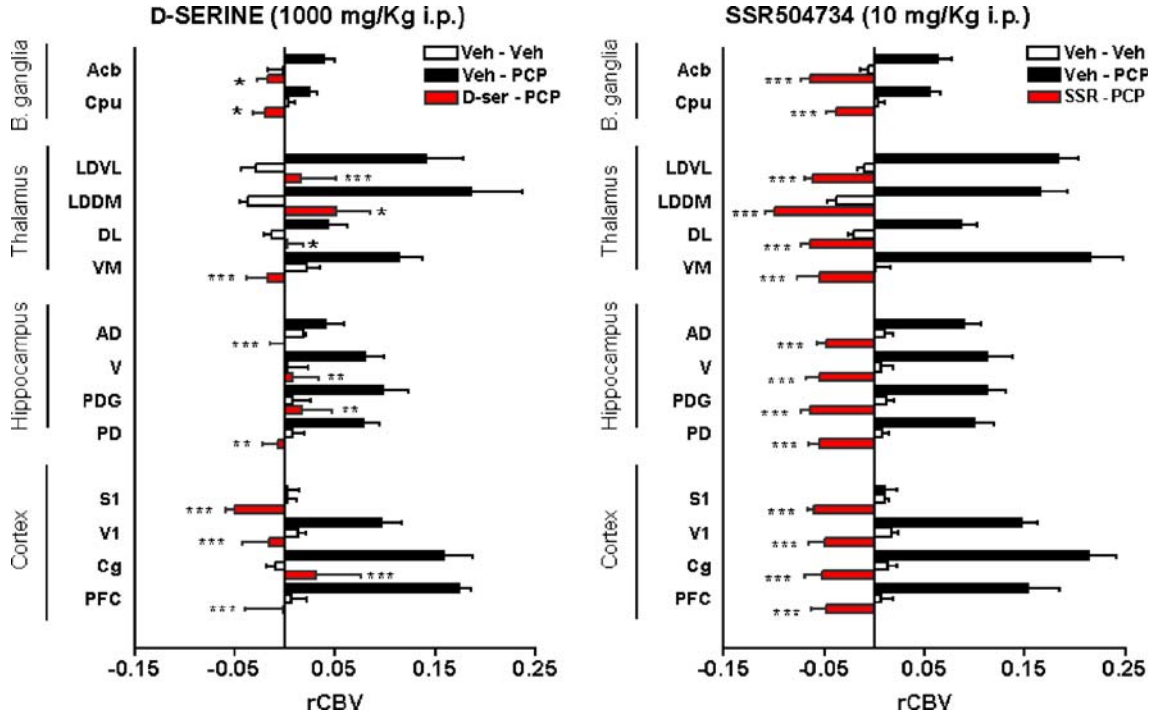

Fig. 3 Magnitude of rCBV response to PCP in representative regions of interest. The effect was plotted as mean rCBV over a 16-min time window covering the peak response to PCP (4–20 min postinjection). Baseline data of control animals pretreated and challenged with vehicle are reported for comparison (Veh–Veh). *$p<0.05$, **$p<0.01$, ***$p<0.001$ versus Veh–Veh. *Left*: Veh–Veh (group 5) $n=6$; Veh–PCP (group 1) $n=5$, D-serine 1 g/kg–PCP (group 2) $n=8$; *Right*: Veh–Veh (group 5) $n=6$; Veh–PCP (group 4) $n=6$; SSR504734 10 mg/kg–PCP (group 5) $n=5$. (*Acb* Nucleus accumbens, *Cpu* caudate putamen, *LDVL* ventrolateral part of laterodorsal thalamus, *LDDM* dorsomedial part of laterodorsal thalamus, *DL* dorsolateral thalamus, *VM* ventromedial thalamus, *AD* anterodorsal hippocampus, *V* ventral hippocampus, *PDG* posterior dentate gyrus, *PD* posterodorsal hippocampus, *S1* primary somatosensory cortex, *V1* primary visual cortex, *Cg* cingulate cortex, *PFC* medial prefrontal cortex)

Pretreatment with the Gly-TI inhibitor SSR504734 (10 mg/kg i.p.) completely suppressed positive rCBV response to PCP in all the brain regions examined (Figs. 1–3). The effect did not show region dependence with robust and sustained response inhibition in both cortical and subcortical areas. The inhibitory action of SSR504734 was accompanied by widespread and sustained negative rCBV changes following PCP injection in all the subjects treated. The administration of SSR504734 per se gave rise to small, short-lived (2–8 min) rCBV increases in most of the cortical and subcortical regions examined (Fig. 5). The increase was small and transient, and at the time of PCP challenge, no clear basal rCBV alteration was present in any of the regions examined.

Discussion

NMDA receptor antagonists like ketamine or phencyclidine (PCP) are widely used experimentally to investigate NMDAr neurotransmission in vivo. Acute administration of these drugs produces a complex cascade of neurobehavioral effects that, in humans, present in the form of psychotic symptoms very similar to those observed in schizophrenia. (Malhotra et al. 1996; Krystal et al. 2002) Recent phMRI studies performed in our lab have shown the activation of discrete corticolimbo-thalamic circuits following acute PCP challenge in the anesthetized rat (Gozzi et al. 2008b, a). The same experimental protocol was used here to test if this effect could be modulated by agents that stimulate NMDAr function by acting at the Gly co-agonist site. Consistent with our two preceding studies, acute administration of PCP elicited spatially selective functional activation of distinct cortico-thalamic and hippocampal areas. The magnitude and timecourse of PCP-induced rCBV changes in the two control (vehicle-pretreated) groups of this study were comparable to those observed in previous studies, a finding that is of interest per se as it testifies to the reproducibility of the experimental paradigm used and underscores the potential of phMRI as a tool to explore system-level pharmacology in the living brain.

Pretreatment with the endogenous NMDAr co-agonist D-serine produced robust and widespread inhibition of the functional activation elicited by PCP. This finding suggests that stimulation of NMDAr Gly site can strengthen NMDAR glutamatergic neurotransmission in vivo, and

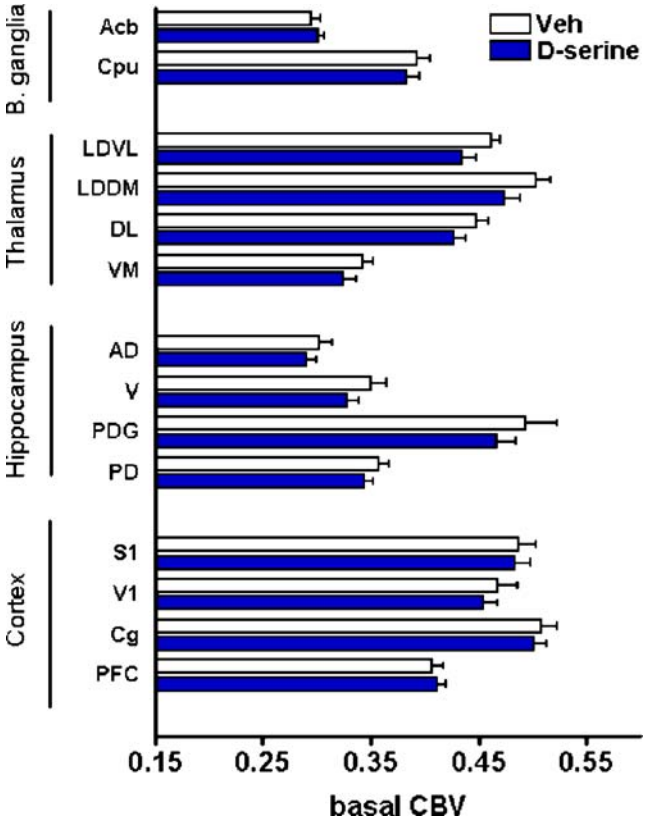

Fig. 4 Effect of pretreatment with D-serine per se (1 g/kg i.p.) on basal CBV in representative brain regions. Data are plotted as mean± SEM within each group

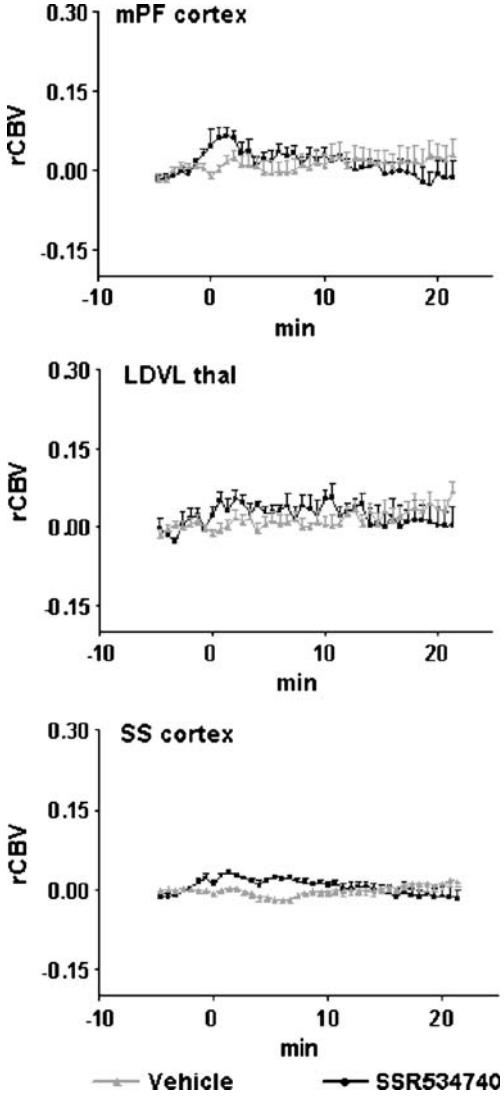

Fig. 5 Effect of pretreatment with SSR504734 per se (10 mg/kg i.p.) on rCBV baseline in three representative brain regions. SSR504734 (group 4, $n=5$) or vehicle (groups 3 and 5, $n=12$) were administered at time 0. Data are plotted as mean±SEM within each group

corroborates the hypothesis that the Gly sites of NMDAr are not tonically saturated under homeostatic conditions in vivo. Consistent with our results, a number of previous reports have shown the ability of similar doses of D-serine to antagonize both the acute and chronic neuro-behavioral effects of PCP in freely moving rodents (Tanii et al. 1994; Nilsson et al. 1997; Andersen and Pouzet 2004; Karasawa et al. 2008; Hashimoto et al. 2008). The anatomical distribution of the D-serine inhibitory effect revealed widespread general inhibition of PCP response, with no clear signs of regional-dependence. This observation would argue against the hypothesis that NMDAr Gly sites could present variable region-dependent degrees of saturation in the brain, at least as far as the regions activated by PCP are concerned. However, it is still unclear which of the neurofunctional effects of PCP reflect local impairment of NMDA neurotransmission and which originate in remote brain structures through long-range afferent/efferent terminals. Until the relative contribution of these complementary mechanisms is fully clarified, it will not be possible to determine the exact local or global nature of an inhibitory action like the one produced by D-serine.

The dose and administration scheme of D-serine used in this study were selected from the work by Hashimoto and Chiba (2004) who demonstrated a slow but sustained increase in the CNS levels of the amino acid following systemic administration, with a plateau 6 h postinjection that remains elevated for the subsequent 24 h. D-serine slow pharmacokinetics correlates well with the results of preliminary experiments performed in our lab showing the inability of the same dose of D-serine to produce significant effects after intraperitoneal administration 30 min prior to the PCP challenge (A. Gozzi, unpublished results). The time-dependence of the inhibitory action of D-serine on PCP therefore provides an indirect confirmation of the specific pharmacological nature of the inhibitory action observed.

D-serine has been reported to elicit basal CBV increases in the hippocampus of isoflurane-anesthetized rat 2 h postintraperitoneal administration (Panizzutti et al. 2005).

In the present study, the drug did not produce significant changes in baseline CBV 23 h after i.p. administration. The absence of significant CBV alterations in spite of the presence of elevated D-serine levels in the CNS (Hashimoto and Chiba 2004) is not totally unexpected, as prior phMRI studies have demonstrated that the profile of hemodynamic response to a drug challenge does not necessarily correlate with its pharmacokinetic exposure (Schwarz et al. 2004). This finding also permits to rule out the presence of "ceiling" or "floor" rCBV alterations that could have prevented the subsequent response to PCP. Similar considerations apply to SSR504734, which induced weak- and short-lived rCBV increases in cortical and subcortical areas that returned to preinjection baseline values well before the PCP challenge.

Consistent with the results of D-serine, pretreatment with the selective GlyT-1 inhibitor SSR504734 completely blocked the positive functional response to PCP. The inhibition appeared to be robust and generalized, with complete suppression of the positive rCBV response in all the brain regions examined. This finding adds to previous preclinical evidence showing that glycinergic stimulation of the NMDAr can antagonize the neurofunctional and psychotogenic effects produced by PCP and other NMDAr antagonists in rodents. For example, Depoortere et al. (2005) showed that SSR504734 can significantly inhibit NMDA antagonist-induced brain metabolic activity, EEG perturbations, and locomotor hyperactivity. Similar results have been reported for other GlyT-1 inhibitors (Harsing et al. 2003; Hashimoto et al. 2008; Karasawa et al. 2008) suggesting that the effect of SSR504734 is related to its mechanism of action, rather than being specific to a particular molecular moiety. These findings are consistent with the view by which high-capacity astroglial GLYT-1 exert a stringent control of Gly levels within the synaptic cleft (Zafra et al. 1995) and are thus responsible for keeping the effective synaptic concentrations of Gly well below the micromolar range measured in the extracellular space (Javitt 2007).

An interesting finding of the present study was the detection of significant PCP-induced rCBV decreases (i.e., deactivation) following the administration of PCP in rats pretreated with D-serine or SSR504734. The effect was more pronounced and spatially extended in animals receiving SSR504734 with respect to D-serine, the latter showing significant deactivation only in somatosensory cortical regions. The origin and significance of this negative response to PCP are not entirely clear. Additional studies performed in our lab with chemically diverse Gly-TI inhibitors produced analogous effects (A Gozzi, unpublished results). The degree of deactivation also appeared to be dose-dependent. This feature was however not observed with antipsychotic drugs like clozapine or with compounds that inhibit the PCP response by modulating presynaptically glutamate release (Gozzi et al. 2008b), suggesting that the effect could be specific to this particular pharmacological

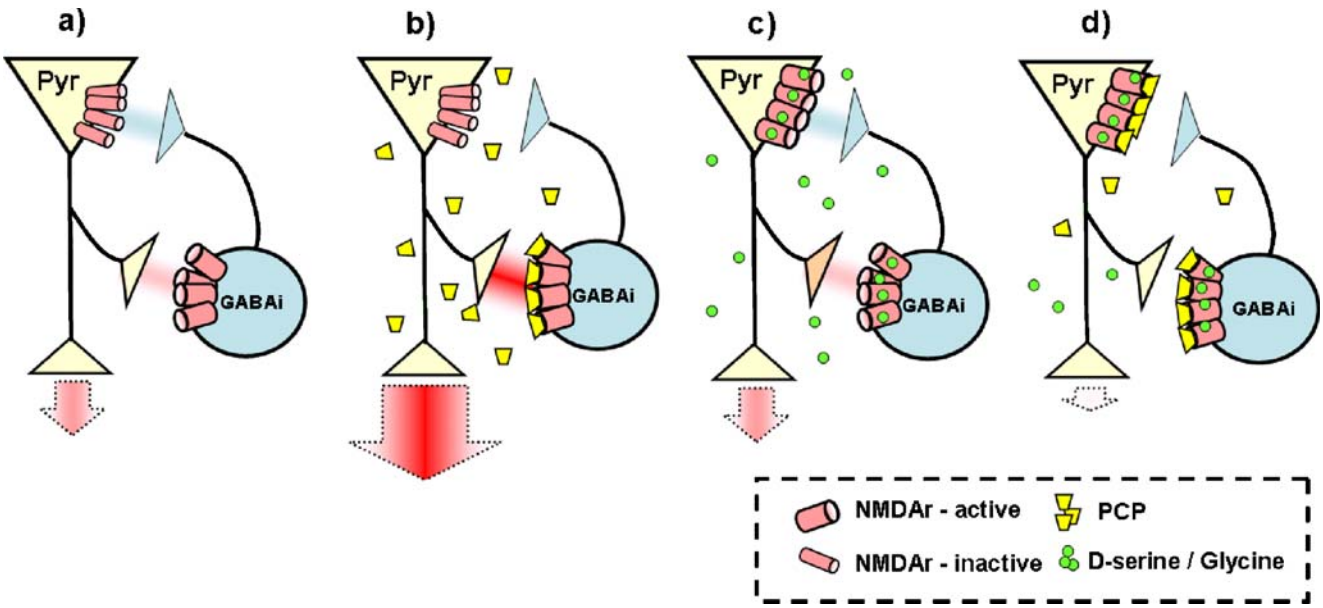

Fig. 6 Model of the local neuronal circuit disinhibition in response to PCP and putative modulatory effect of glycinergic agents on circuit dynamics. **a** GABAergic interneurons (GABAi) receive input and thereby exert inhibitory control on pyramidal cells (Pyr) through recurrent projections. **b** In the presence of PCP, this local feedback inhibition becomes selectively disrupted. As PCP is a use-dependent NMDAr channel blocker, this effect may reflect higher tonic activity of GABA NMDAr pool, resulting in a large population of open NMDAr channels accessible to the antagonist. **c** Allosteric modulators of NMDAr like D-serine or glycine, by increasing opening frequency of NMDAr pyramidal pool can alter this balance and make pyramidal NMDAr more accessible to the antagonistic action of PCP thus leading to generalized depression of NMDAr neurotransmission in the brain (**d**)

mechanism. A tentative explanation of this finding may lie in the basic neuropharmacological mechanisms governing the psychotomimetic reaction to PCP. As comprehensively reviewed by Greene (2001), electrophysiology data strongly suggest that the functional and behavioral effects of NMDAr antagonists are mediated by a dose-dependent disinhibition of cortical projection cell firing (e.g., pyramidal neurons, Fig. 6). This phenomenon appears to reflect selective antagonization by PCP of NMDAr located on the GABAergic interneurons responsible for recurrent inhibitory feedback onto pyramidal cells (Homayoun and Moghaddam 2007). Two main mechanisms are thought to significantly contribute to this selective neuropharmacological action. First, NMDAr on interneurons are not as strongly voltage sensitive as pyramidal NMDAr, probably a consequence of a different NMDAr subunit composition (Greene 2001; Grunze et al. 1996). As a result, tonic pyramidal neurotransmission is intrinsically much less susceptible to NMDAr antagonism than the corresponding recurrent inhibitory circuit. This is because pyramidal neurons require a significant depolarizing influence (usually form other synaptic inputs) to activate NMDAr-dependent conductance by removal of the voltage-sensitive Mg^{++} blocking the NMDAr channel. The functional contribution of this phenomenon is probably magnified by a second contributing mechanism, namely, the fact that PCP acts primarily by binding to a site that resides within the NMDA channel (MacDonald et al. 1991). As a result, PCP will exert a stronger pharmacological inhibition in the channel pool that is most active (i.e., GABAergic interneurons) compared to the one that is less active (i.e., pyramidal cells; Fig. 6b). Thus, if the NMDAr of interneurons are more active, then PCP-induced selective blockade of these channels might occur prior to reaching a neuropharmacological equilibrium or can even preclude ever reaching equilibrium. According to this model, agents that stimulate the NMDAr Gly site may alter this equilibrium by increasing the opening frequency of pyramidal NMDAr channels (Fig. 6c) and thereby promote PCP-induced blockade of NMDAr-mediated excitatory input onto pyramidal cells. This effect can, in turn, counterbalance and/or outweigh the inhibitory action of PCP on GABAergic interneurons, leading to generalized antagonism of all NMDA-dependent neurotransmission (Fig. 6d), an effect that would functionally reflect in widespread depression of brain activity similar to that observed in subjects pretreated with SSR534740 and, to a lower extent, in the cortex of subjects treated with D-serine. According to this view, the widespread pattern of deactivation observed in rats pretreated with SSR534740 would also argue against the hypothesis that NMDAr Gly sites could present region-dependent degrees of saturation in the brain.

The use of the anesthetic may represent a confound that can, in principle, affect the magnitude and distribution of the functional response to drugs. This aspect has been discussed in greater detail in a dedicated study (Gozzi et al. 2008a). It is, however, noteworthy to emphasize here the striking correspondence that we found between the pattern of activation produced by PCP in this protocol and the results of neuroimaging and 2-deoxyglucose functional mapping in conscious animal models, a result that strongly suggests that the functional changes mapped are representative of the central effects of PCP in freely moving animals and in humans. The consistency between our results with D-serine and SSR534740 and those obtained in the behavioral models discussed above provides an ulterior indirect confirmation of this argument.

In conclusion, our results show that D-serine and SSR504734 can significantly inhibit the fMRI response to acute PCP challenge in the rat. These findings are consistent with the hypothesis that pharmacological stimulation of NMDA receptors via Gly co-agonist site can potentiate NMDAr neurotransmission in the living brain. These results are consistent with previous findings suggesting that Gly levels in vivo are not saturating under homeostatic conditions. The efficacy of the Gly-TI inhibitor shows a potential for this class of drugs to provide selective enhancement of NMDAr activity, a pharmacological strategy that can be exploited therapeutically to restore NMDAr hypofunctionality in schizophrenia.

References

Andersen JD, Pouzet B (2004) Spatial memory deficits induced by perinatal treatment of rats with PCP and reversal effect of D-serine. Neuropsychopharmacology 29:1080–1090

Ballard TM, Pauly-Evers M, Higgins GA, Ouagazzal AM, Mutel V, Borroni E et al (2002) Severe impairment of NMDA receptor function in mice carrying targeted point mutations in the glycine binding site results in drug-resistant nonhabituating hyperactivity. J Neurosci 22:6713–6723

Chen L, Muhlhauser M, Yang CR (2003) Glycine tranporter-1 blockade potentiates NMDA-mediated responses in rat prefrontal cortical neurons in vitro and in vivo. J Neurophysiol 89:691–703

Depoortere R, Dargazanli G, Estenne-Bouhtou G, Coste A, Lanneau C, Desvignes C et al (2005) Neurochemical, electrophysiological and pharmacological profiles of the selective inhibitor of the glycine transporter-1 SSR504734, a potential new type of antipsychotic. Neuropsychopharmacology 30:1963–1985

Friston KJ, Jezzard P, Turner R (1994) Analysis of functional MRI time-series. Hum Brain Mapp 1:153–171

Gozzi A, Schwarz AJ, Reese T, Bertani S, Crestan V, Bifone A (2005) Region-specific effects of nicotine on brain activity: a pharmacological MRI study in the drug-naïve rat. Neuropsychopharmacology 31:1690–1703

Gozzi A, Ceolin L, Schwarz AJ, Reese T, Bertani S, Bifone A (2007) A multimodality investigation of cerebral haemodynamics and autoregulation in phMRI. Magn Reson Imaging 25:826–833

Gozzi A, Schwarz AJ, Reese T, Crestan V, Bifone A (2008a) Drug-anaesthetic interaction in phMRI: the case of the pyschotomimetic agent phencyclidine. Magn Reson Imag. doi:10.1016/j.mri.2008.01.012

Gozzi A, Large CH, Schwarz A, Bertani S, Crestan V, Bifone A (2008b) Differential effects of antipsychotic and glutamatergic agents on the phMRI response to phencyclidine. Neuropsychopharmacology 33:1690–1703

Greene R (2001) Circuit analysis of NMDAR hypofunction in the hippocampus, in vitro, and psychosis of schizophrenia. Hippocampus 11:569–577

Grunze HC, Rainnie DG, Hasselmo ME, Barkai E, Hearn EF, McCarley RW et al (1996) NMDA-dependent modulation of CA1 local circuit inhibition. J Neurosci 16:2034–2043

Harsing LG, Gacsalyi I, Szabo G, Schmidt E, Sziray N, Sebban C et al (2003) The glycine transporter-1 inhibitors NFPS and Org 24461: a pharmacological study. Pharmacol Biochem Behav 74:811–825

Hashimoto A, Chiba Y (2004) Effect of systemic administration of -serine on the levels of - and -serine in several brain areas and periphery of rat. Eur J Pharmacol 495:153–158

Hashimoto K, Fujita Y, Ishima T, Chaki S, Iyo M (2008) Phencyclidine-induced cognitive deficits in mice are improved by subsequent subchronic administration of the glycine transporter-1 inhibitor NFPS and d-serine. Eur Neuropsychopharmacol 18:414–421

Hennig J, Nauerth A, Friedburg H (1986) RARE imaging: a fast imaging method for clinical MR. Magn Reson Med 3:823–833

Homayoun H, Moghaddam B (2007) NMDA receptor hypofunction produces opposite effects on prefrontal cortex interneurons and pyramidal neurons. J Neurosci 27:11496–11500

Javitt DC (2007) Glutamate and Schizophrenia: Phencyclidine, N [hyphen (true graphic)]Methyl[hyphen (true graphic)]d[hyphen (true graphic)]Aspartate Receptors, and Dopamine-Glutamate Interactions. In: Anissa Abi[hyphen (true graphic) (ed). International Review of NeurobiologyIntegrating the Neurobiology of Schizophrenia. Academic, pp 69–108

Javitt DC, Heresco-Levy U (2000) Are glycine sites saturated in vivo? Arch Gen Psychiatry 57:1181–1183

Jenkins BG, Chen Y-CI, Mandeville JB (2003) Pharmacological magnetic resonance imaging (phMRI). In: van Bruggen N, Roberts T (eds) Biomedical imaging in experimental neuroscience. CRC Press, New York, pp 155–209

Karasawa Ji, Hashimoto K, Chaki S (2008) d-Serine and a glycine transporter inhibitor improve MK-801-induced cognitive deficits in a novel object recognition test in rats. Behav Brain Res 186:78–83

Kinney GG, Sur C, Burno M, Mallorga PJ, Williams JB, Figueroa DJ et al (2003) The glycine transporter type 1 inhibitor *N*-[3-(4′-fluorophenyl)-3-(4′-phenylphenoxy)propyl]sarcosine potentiates NMDA receptor-mediated responses in vivo and produces an antipsychotic profile in rodent behavior. J Neurosci 23:7586–7591

Kristiansen LV, Huerta I, Beneyto M, Meador-Woodruff JH (2007) NMDA receptors and schizophrenia. Curr Opin Pharmacol 7:48–55

Krystal JH, Anand A, Moghaddam B (2002) Effects of NMDA receptor antagonists: implications for the pathophysiology of schizophrenia. Arch Gen Psychiatry 59:663–664

Large CH (2007) Do NMDA receptor antagonist models of schizophrenia predict the clinical efficacy of antipsychotic drugs? J Psychopharmacol 21:283–301

Leeson PD, Iversen LL (1994) The glycine site on the NMDA receptor: structure–activity relationships and therapeutic potential. J Med Chem 37:4053–4067

Li YH, Han TZ (2007) Glycine binding sites of presynaptic NMDA receptors may tonically regulate glutamate release in the rat visual cortex. J Neurophysiol 97:817–823

Long KD, Mastropaolo J, Rosse RB, Deutsch SI (2007) Exogenously administered d-serine failed to potentiate the ability of MK-801 to antagonize electrically precipitated seizures in nonhandled control and stressed mice. Eur Neuropsychopharmacol 17:53–57

MacDonald JF, Bartlett MC, Mody I, Pahapill P, Reynolds JN, Salter MW et al (1991) Actions of ketamine, phencyclidine and MK-801 on NMDA receptor currents in cultured mouse hippocampal neurones. J Physiol 432:483–508

Malhotra AK, Pinals DA, Weingartner H, Sirocco K, Missar CD, Pickar D et al (1996) NMDA receptor function and human cognition: the effects of ketamine in healthy volunteers. Neuropsychopharmacology 14:301–307

Mandeville JB, Marota JJA, Kosofsky BE, Keltner JR, Weissleder R, Rosen B et al (1998) Dynamic functional imaging of relative cerebral blood volume during rat forepaw stimulation. Magn Reson Med 39:615–624

Mandeville JB, Jenkins BG, Kosofsky BE, Moskowitz MA, Rosen B, Marota JJA (2001) Regional sensitivity and coupling of BOLD and CBV changes during stimulation of rat brain. Magn Reson Med 45:443–447

Martina M, Krasteniakov NV, Bergeron R (2003) D-Serine differently modulates NMDA receptor function in rat CA1 hippocampal pyramidal cells and interneurons. J Physiol 548:411–423

Meur KL, Galante M, Angulo MC, Audinat E (2007) Tonic activation of NMDA receptors by ambient glutamate of non-synaptic origin in the rat hippocampus. J Physiol 580:373–383

Millan MJ (2002) *N*-methyl-D-aspartate receptor-coupled glycineB receptors in the pathogenesis and treatment of schizophrenia: a critical review. Curr Drug Targets CNS Neurol Disord 1:191–213

Nilsson M, Carlsson A, Carlsson ML (1997) Glycine and D-serine decrease MK-801-induced hyperactivity in mice. J Neural Transm 104:1195–1205

Nishikawa T (2005) Metabolism and functional roles of endogenous D-serine in mammalian brains. Biol Pharm Bull 28:1561–1565

Obrenovitch TP, Hardy AM, Urenjak J (1997) High extracellular glycine does not potentiate *N*-methyl-aspartate-evoked depolarization in vivo. Brain Res 746:190–194

Panizzutti R, Rausch M, Zurbrugg S, Baumann D, Beckmann N, Rudin M (2005) The pharmacological stimulation of NMDA receptors via co-agonist site: an fMRI study in the rat brain. Neuroscience Letters 380:111–115

Paxinos G, Watson C (1998) The rat brain in stereotactic coordinates. Academic Press, San Diego

Schwarz AJ, Reese T, Gozzi A, Bifone A (2003) Functional MRI using intravascular contrast agents: detrending of the relative cerebrovascular (rCBV) time course. Magn Reson Imaging 21:1191–1200

Schwarz AJ, Zocchi A, Reese T, Gozzi A, Garzotti M, Varnier G et al (2004) Concurrent pharmacological MRI and in situ microdialysis of cocaine reveal a complex relationship between the central hemodynamic response and local dopamine concentration. Neuroimage 23:296–304

Schwarz AJ, Danckaert A, Reese T, Gozzi A, Paxinos G, Watson C et al (2006a) A stereotaxic MRI template set for the rat brain with tissue class distribution maps and co-registered anatomical atlas: application to pharmacological MRI. NeuroImage 32:538–550

Schwarz AJ, Whitcher B, Gozzi A, Reese T, Bifone A (2006b) Study-level wavelet cluster analysis and data-driven signal models in pharmacological MRI. J Neurosci Methods 159:346–360

Sur C, Kinney GG (2007) Glycine transporter 1 inhibitors and modulation of NMDA receptor-mediated excitatory neurotransmission. Curr Drug Targets 8:643–649

Tanii Y, Nishikawa T, Hashimoto A, Takahashi K (1994) Stereoselective antagonism by enantiomers of alanine and serine of phencyclidine-induced hyperactivity, stereotypy and ataxia in the rat. J Pharmacol Exp Ther 269:1040–1048

Thomson AM (1990) Glycine is a coagonist at the NMDA receptor/channel complex. Prog Neurobiol 35:53–74

Weissman AD, Dam M, London ED (1987) Alterations in local cerebral glucose utilization induced by phencyclidine. Brain Res 435:29–40

Westergren I, Nystrom B, Hamberger A, Nordborg C, Johansson BB (1994) Concentrations of amino acids in extracellular fluid after opening of the blood–brain barrier by intracarotid infusion of protamine sulfate. J Neurochem 62:159–165

Whitcher B, Schwarz AJ, Barjat H, Smart SC, Grundy RI, James MF (2005) Wavelet-based cluster analysis: data-driven grouping of voxel time courses with application to perfusion-weighted and MRI of the rat brain. Neuroimage 24:281–295

Worsley KJ, Evans AC, Marrett S, Neelin P (1992) A three-dimensional statistical analysis for CBF activation studies in human brain. J Cereb Blood Flow Metab 12:900–918

Zafra F, Aragon C, Olivares L, Danbolt NC, Gimenez C, Storm-Mathisen J (1995) Glycine transporters are differentially expressed among CNS cells. J Neurosci 15:3952–3969

Zaharchuk G, Mandeville JB, Bogdanov Jr AA, Weissleder R, Rosen BR, Marota JJ (1999) Cerebrovascular dynamics of autoregulation and hypoperfusion. An MRI study of CBF and changes in total and microvascular cerebral blood volume during hemorrhagic hypotension. Stroke 30:2197–2204

Appendix 4

Psychopharmacology (2010) 209:37–50
DOI 10.1007/s00213-009-1772-4

ORIGINAL INVESTIGATION

Antagonism at serotonin 5-HT_{2A} receptors modulates functional activity of frontohippocampal circuit

Alessandro Gozzi · Valerio Crestan · Giuliano Turrini · Marcel Clemens · Angelo Bifone

Received: 31 July 2009 / Accepted: 20 December 2009 / Published online: 29 January 2010

Abstract
Rationale Several second-generation antipsychotics are characterised by a significant antagonistic effect at serotonin 5-HT_{2A} receptors (5-HT_{2A}R), a feature that has been associated with lower incidence of extra-pyramidal symptoms and a putative amelioration of positive and negative symptoms experienced by schizophrenic patients. However, the neurofunctional substrate of 5-HT_{2A} antagonism and its exact contribution to the complex pharmacological profile of these drugs remain to be elucidated.
Objectives Here, we used pharmacological magnetic resonance imaging to map the modulatory effects of the selective 5-HT_{2A}R antagonist Ml00907 on the spatiotemporal patterns of brain activity elicited by acute phencyclidine (PCP) challenge in the rat. PCP is a non-competitive NMDA receptor antagonist that induces dysregulation of corticolimbic glutamatergic neurotransmission and produces cognitive impairment and psychotic-like symptoms reminiscent of those observed in schizophrenia.
Results Pre-administration of M100907 produced focal and region-dependent attenuation of PCP-induced response in frontoseptohippocampal areas. As early studies highlighted a permissive role of 5-HT_{2A}R on frontal dopamine release, the role of post-synaptic dopamine D_1 receptors on PCP-induced response was examined by using the potent antagonist SCH23390. Interestingly, SCH23390 did not affect PCP's response in any of the regions examined. This finding rules out a significant contribution of dopamine in the functional changes mapped and, indirectly, the inhibitory effect of M100907, in favour of a glutamatergic origin.
Conclusions Our data expand recent evidence suggesting a key role of 5-HT_{2A}R in modulating glutamate-mediated cognitive performance in the prefrontal cortex and highlight the whole frontoseptohippocampal circuit as a key functional substrate of 5-HT_{2A}R antagonism in normal and disease states.

Keywords fMRI · Phencyclidine · M100907 · phMRI · Schizophrenia · Cognition

Electronic supplementary material The online version of this article (doi:10.1007/s00213-009-1772-4) contains supplementary material, which is available to authorized users.

A. Gozzi · M. Clemens · A. Bifone
Biology, Neurosciences CEDD,
GlaxoSmithKline Medicines Research Centre,
Verona, Italy

V. Crestan · G. Turrini
Laboratory Animal Science, Neurosciences CEDD,
GlaxoSmithKline Medicines Research Centre,
Verona, Italy

A. Gozzi (✉)
Neuroimaging, GSK Neurosciences CEDD,
Fleming 4,
37100 Verona, Italy
e-mail: alessandro.gozzi@gsk.com

Present Address:
M. Clemens
Osservatorio Astronomico di Padova,
Padova, Italy

Introduction

Schizophrenia is a disabling psychiatric disorder characterised by complex and severe symptoms, including psychosis, hallucinations, cognitive deficits and mood alterations. Whilst the first antipsychotic agents targeted selectively the dopamine system through dopamine D_2 receptors, second-generation antipsychotics (SGA; e.g. clozapine) are characterised by a multifaceted pharmacological

profile, including multiple antagonist or inverse agonist properties at several neuroreceptor systems including serotonin, noradrenaline and histamine (Seeman 2002). This complexity makes it difficult to unravel the role and pharmacological contribution of individual target receptors, and despite almost two decades of active research since the identification of the first atypical antipsychotic clozapine, the precise mechanism responsible for the therapeutic effect of these molecules remains elusive.

The observation that several SGA present relatively low dopamine D_2 receptors affinity but high affinity for serotonin (5-HT) receptors has stimulated great interest in the neurophysiological role of this neurotransmitter in schizophrenia (Meltzer 1996). In particular, it has been suggested that the relatively high affinity of clozapine for the 5-HT_{2A} receptor (5-HT_{2A}R) may contribute to its reduced side effect liability and to its greater efficacy in therapy-resistant schizophrenia (Tandon and Fleischhacker 2005; Ichikawa and Meltzer 1999; Meltzer et al. 1989).

Pre-clinical experimental evidence indicates the possibility of a significant role for $5HT_{2A}$ receptors in modulating specific effects of SGA. Early studies showed that systemic or local administration of selective 5-HT_{2A}R antagonists in the rat medial prefrontal cortex stimulates dopamine efflux (Schmidt and Fadayel 1995). This finding has led to the hypothesis of a permissive role of 5-HT_{2A}R on frontal dopamine release as a contributory factor for a potentially superior cognitive effect of novel generation antipsychotics over classic dopamine D2 receptor antagonists (Kuroki et al. 1999; Ichikawa and Meltzer 1999). This hypothesis, however, has not been consistently confirmed in clinical studies, and the benefit exerted by SGA medications on cognitive performance remains questionable (Davidson et al. 1999). Recent studies have revealed an additional contribution of 5-HT_{2A}R as modulators of glutamatergic neurotransmission in frontocortical areas (Scruggs et al. 2000, 2003; Zhai et al. 2002), an effect that seems to be relevant for the control of attentional and cognitive performance of rat prefrontal cortex (Carli et al. 2005; Mirjana et al. 2004) and could exert a direct anti-psychotic effect in disease states involving hyperglutamatergic neurotransmission (Coyle 2006). However, most of the studies that investigated the neurobehavioural correlates of frontal 5-HT_{2A}R antagonism have employed local impairment of NMDA and/or 5-HT_{2A}R activity through in situ administration of pharmacological agents (Mirjana et al. 2004; Martin-Ruiz et al. 2001; Ceglia et al. 2004). Whilst this approach is valuable in linking discrete receptor populations with the cellular determinants of behaviour, its pharmacological significance is severely limited by the local nature of the manipulations employed, which neglects potentially important afferent and efferent contributions of a complex receptor system like 5-HT_{2A}. Moreover, the wide distribution of 5-HT_{2A}R in the brain (Hoyer et al. 1986) and its pre- and post-synaptic location at different neuronal sub-types (Meltzer et al. 2003) make it difficult to predict the overall functional effect and exact neuronal substrates of $5HT_{2A}$R antagonism in the living brain. As most of the pre-clinical research so far has focused on the role of the receptor in frontal areas, the function and possible contributions of the wide extra-frontal 5-HT_{2A}R pool has remained virtually unexplored.

Non-invasive neuroimaging techniques such as pharmacological magnetic resonance imaging (phMRI) simultaneously integrate multiple functional contributions from widely distributed receptor populations, providing a spatially resolved description of pharmacological activity that is not straightforwardly related to receptor distribution and density (Jenkins et al. 2003; Gozzi et al. 2006; Honey and Bullmore 2004). In an attempt to identify the circuits modulated by 5-HT_{2A}R antagonism in the living brain, we used a rat phMRI protocol to map the modulatory effect of the selective 5-HT_{2A}R antagonist M100907 (Kehne et al. 1996) on the spatiotemporal pattern of response to an acute challenge with the *N*-methyl-D-aspartic acid receptor (NMDAR) antagonist phencyclidine (PCP). NMDAR antagonists like ketamine and PCP induce perceptual abnormalities, psychosis-like symptoms and mood changes in healthy humans and patients with schizophrenia (Malhotra et al. 1997; Adler et al. 1999; Allen and Young 1978), a finding that has led to the hypothesis that a decreased NMDAR function may be a pre-disposing or even causative factor in schizophrenia (Kristiansen et al. 2007; Krystal et al. 2002). The behavioural and functional effects of NMDAR antagonists are thought to arise primarily from a dose-dependent disinhibition of thalamocortical glutamatergic neurotransmission (Greene 2001; Large 2007), an event that cascades to involve several neurotransmitter systems including serotonin and dopamine (Greene 2001; Large 2007; Moghaddam et al. 1997). Recent neuroimaging studies have demonstrated the ability of NMDAR antagonists to elicit focal corticolimbothalamic activation in pre-clinical species (Gozzi et al. 2008b; Littlewood et al. 2006) and humans (Langsjo et al. 2003; Deakin et al. 2008), an effect totally suppressed by agents that modulate glutamate neurotransmission and regionally attenuated by atypical antipsychotics like clozapine (Gozzi et al. 2008a, b). In the present study, we explored the modulatory effect of the selective 5-HT_{2A}R antagonist M100907 on the functional response to PCP as a means to identify and spatially resolve the circuital substrate of 5-HT_{2A}R antagonism in the living brain. This approach allowed us to identify a focal and region-dependent attenuation of PCP-induced response by M100907 in frontoseptohippocampal areas.

Moreover, in an attempt to elucidate the neurochemical determinants of the changes mapped, we examined the role of dopamine D_1 antagonism on the pattern of activation of PCP using the potent antagonist SCH22390 (Neisewander et al. 1998). Dopamine D_1 receptors are crucially involved in the control of cognitive functions processed at a prefrontal level (Robbins 2005). Since M100907 has been reported to stimulate dopamine release in frontal areas (Schmidt and Fadayel 1995), the effect of this drug may involve post-synaptic activation of D_1 dopamine receptors. Given the prevalent role of dopamine D_1 receptors in mediating the fMRI response to dopamine-releasing agents (reviewed by Knutson and Gibbs 2007), by assessing the effect SCH22390, we sought to determine whether the functional response to PCP in our model presents significant contributions of dopaminergic nature. When considered with previous evidence of a negligible role of dopamine D_2 receptors in the same experimental setup (Gozzi et al. 2008b), a lack of modulatory effect by SCH233990 would strongly argue against a predominant contribution of dopamine in the functional response to PCP mapped and, in turn, in the inhibitory effect of M100907. In the light of the established facilitatory role of 5-HT_{2A}R on pyramidal glutamate neurotransmission (Scruggs et al. 2000, 2003; Zhai et al. 2002), this finding would thus provide important indirect evidence supporting a glutamatergic origin of the effects mapped with M100907.

Materials and methods

Animal preparation

The studies were performed on male Sprague–Dawley rats (250–350 g, Charles River, Como, Italy). Animal preparation/monitoring and MRI acquisition have been previously described in greater detail (Gozzi et al. 2008b). Briefly, rats were anaesthetised with 3% halothane, tracheotomised and artificially ventilated with a mechanical respirator. The left femoral artery and vein were cannulated and animal paralysed with a 0.25-mg/kg i.v. bolus of D-tubocurarine followed by a continuous infusion of 0.25 mg/kg/h through the artery. After surgery, halothane level was set to 0.8%. Arterial blood samples (0.5 ml) were taken immediately prior to and at the end of the fMRI time series acquisition, and p_aCO_2 and p_aO_2 were measured using a blood gas analyser (Table SI). No statistically significant difference in mean pre- and post-acquisition p_aCO_2 values for each pair of PCP-challenged groups was found ($p>0.33$, all groups; ANOVA, followed by Fisher's least significant difference (LSD) test for multiple comparisons). The body temperature of all subjects was maintained within physiological range (37±0.8°C) throughout the experiment by using a water heating system. Mean arterial blood pressure (MABP) was monitored continually through a transducer placed in the femoral artery.

rCBV measurement

MRI acquisition parameters have been previously described in greater detail (Gozzi et al. 2008a). Images were acquired using a Bruker Avance 4.7-T system. The MR acquisition for each subject comprised T_2-weighted anatomical images using the rapid acquisition relaxation enhanced (RARE) sequence (Hennig et al. 1986; TR=5,000 ms, TE_{eff}=76 ms, RARE factor 8, FOV 40 mm, 256×256 matrix, 16 contiguous 1 mm slices) followed by a time series acquisition with same spatial coverage (TR_{eff}=2,700 ms, TE_{eff}=110 ms, RARE factor 32, 128×128 matrix, NA=2, dt=40).

Total MRI time-series acquisition time was 77 min (110 repetitions) for all groups. Following six reference images, 2.67 ml/kg of the blood pool contrast agent Endorem (Guerbet, France) was injected so that subsequent signal changes would reflect alterations in relative cerebral blood volume (rCBV; Mandeville et al. 1998).

Compounds, doses and experimental design

In order to allow for a better randomisation and keep the study manageable, drugs were tested in two separate studies. PCP challenge was administered 30 or 20 min after i.p. or s.c. pre-treatment (see below), and MRI data were acquired over a period of 30 min following the administration of the PCP challenge. Male SD rats were randomly assigned to one of the groups below.

M100907 1.5 mg/kg study

1. Intraperitoneal pre-treatment with vehicle (water 1 ml/kg) followed by intravenous challenge with PCP (0.5 mg/kg, 1 ml/rat) 30 min later (n=5)
2. Intraperitoneal pre-treatment with M100907 (1.5 mg/kg) and intravenous challenge with PCP (0.5 mg/kg, 1 ml/rat) 30 min later (n=6)

M100907 0.5 mg/kg study

3. Intraperitoneal pre-treatment with vehicle (saline, 1 ml/kg), followed by intravenous challenge with PCP (0.5 mg/kg, 1 ml/rat) 30 min later (n=8)
4. Intraperitoneal pre-treatment with M100907 (0.5 mg/kg) followed by intravenous administration of PCP (0.5 mg/kg, 1 ml/rat) 30 min later (n=6)

SCH23390 0.5 mg/kg study

5. Subcutaneous pre-treatment with vehicle (water, 1 ml/kg) followed by intravenous challenge with PCP (0.5 mg/kg, 1 ml/rat) 20 min later (n=6)
6. Subcutaneous pre-treatment with SCH23390 (0.1 mg/kg; 1 ml/kg) followed by intravenous challenge with PCP (0.5 mg/kg, 1 ml/rat) 20 min later (n=8)
7. Intraperitoneal pre-treatment with water (1 ml/kg) followed by intravenous challenge with saline (1 ml/rat) 30 min later (n=6). This group served as reference rCBV baseline for PCP in all studies

Phencyclidine hydrochloride was purchased from Tocris (Bristol, UK). M100907 was synthesised by the GSK department of Medicinal Chemistry. All compounds were dissolved in saline and injected at a rate of 1 ml/min. The doses chosen for the different drugs were based on previously published in vivo studies. PCP was tested at a sub-anaesthetic dose (0.5 mg/kg i.v.) that produces robust corticolimbothalamic activation in halothane-anesthetised rat (Gozzi et al. 2008c). The same dose of PCP has also been reported to elicit robust behavioural and metabolic (2-deoxyglucose) effects in conscious and freely-moving rats (Weissman et al. 1987; Gozzi et al. 2008b).

The doses of M100907 used in the present study showed robust effects in multiple behavioural readouts in rodents (reviewed by Kehne et al. 1996). The compound exhibits high potency and excellent selectivity (>100-fold separation at 26 receptors) and has been shown to be devoid of ex vivo receptor binding at alpha1-adrenetrgic or D_2-dopamine receptor at doses 7-fold higher than the maximal dose tested in our experiments (Kehne et al. 1996). SCH23390 is a potent dopamine D_1 antagonist (Andersen et al. 1992). The pre-treatment regimen used with SCH23390 has been reported to produce rapid and sustained exposure in the rat brain (Hietala et al. 1992). The same dose of SCH223390 tested produced robust in vivo antagonism of acute and chronic effect of dopaminergic agents in numerous rat behavioural paradigms (Molloy and Waddington 1984; Garris et al. 1994; Wolf and Xue 1999; Zahrt et al. 1997) whilst minimising the cataleptic and cognitive-impairing effects reported at higher doses (Wadenberg 1992).

Data analysis

rCBV time series image data for each experiment were analysed within the framework of the general linear model as described in greater detail elsewhere (Worsley et al. 1992; Schwarz et al. 2006b). The maps thus obtained were used to guide the selection of activated/deactivated regions for subsequent volume of interest (VOI)-based quantification and comparison of efficacy of pre-treatments.

Signal intensity changes in the time series were converted into fractional rCBV on a pixel-wise basis, using a constrained exponential model of the gradual elimination of contrast agent from the blood pool (Schwarz et al. 2003, 2006b). Individual subjects in each study were spatially normalised by a 9 degree-of-freedom affine transformation mapping their T_2-weighted anatomical images to a stereotaxic rat brain MRI template set (Schwarz et al. 2006a) and applying the resulting transformation matrix to the accompanying rCBV time series. rCBV time series for the PCP or vehicle challenge were calculated covering 8 min (12 time points) pre-challenge baseline and 25 min (38 time points) post-challenge window, normalised to a common injection time point. Image-based time series analysis was carried out using FMRI Expert Analysis Tool Version 5.63, part of FMRIB's Software Library (www.fmrib.ox.ac.uk/fsl) with 0.8 mm spatial smoothing (≈2.5× in-plane voxel dimension) and using a model function identified by Wavelet Cluster Analysis across all animals in the cohort, capturing the temporal profile of the signal change induced by PCP challenge (Whitcher et al. 2005; Schwarz et al. 2006b). As no substantial differences in the temporal profile of PCP-induced changes were observed across PCP-challenged groups (see "Results" section), a common regressor was used (Supplementary Figure 1). Consistent with previous studies, PCP did not produce any significant short-lived or negative signal changes in any of the regions analysed (Gozzi et al. 2008a, b).

The design matrix also included the temporal derivative of this regressor and a linear ramp (both orthogonalised to the regressor of interest) with the aim to capture additional variance due to slight deviations in individual subjects or brain regions from the signal model time course as described in more detail in Schwarz et al. (2006b). The coefficients of the model function thus provided a map of rCBV response amplitude for each injection in each subject. Higher-level group comparisons were carried out using FMRIB's Local Analysis of Mixed Effects; Z (Gaussianised T/F) statistic images were thresholded using clusters determined by Z>2.3 and a corrected cluster significance threshold of p=0.01 (Worsley et al. 1992; Friston et al. 1994). Volumetric three-dimensional reconstructions of activation maps were generated using custom in-house software written in IDL (Research Systems Inc., Boulder, CO, USA).

VOI time courses for the PCP challenge were extracted from unsmoothed rCBV time series data using a 3D digital reconstruction of a rat brain atlas (Paxinos and Watson 1998) co-registered with the MRI template (Schwarz et al. 2006a), using custom in-house software written in IDL (Research Systems Inc., Boulder, CO, USA). A list of the VOIs examined and their anatomical definitions can be

found in (Gozzi et al. 2008b). For each VOI time course, the average rCBV over a 16-min time window covering the peak response to PCP (4–20 min post-injection) was used as a summary statistic of the relative change. The effect of pre-treatment on the magnitude of average rCBV in different VOIs was assessed by a one-way ANOVA followed by Fisher's LSD test for multiple comparisons.

VOI time courses pre- and post-M100907 administration were also examined to assess potential effects of pre-treatment per se on basal CBV. To this end, rCBV time courses were also calculated for the pre-treatment over a time window covering 6 min (8 time points) pre-injection baseline and 22 min (32 time points, groups 1–4 and 7) or 17 min (24 time points, groups 5 and 6) post-injection window normalised to a common injection time point. VOI time courses were extracted from unsmoothed rCBV time series in the same regions examined for the PCP challenge.

Administration of vehicle, SCH23390 or PCP was accompanied by small and transient alterations of MABP. M100907 produced a sustained decrease in MABP that lasted throughout PCP's pre-injection time window (mean MABP≈65 mmHg). In all cases, peak magnitude of the MABP observed was within the cerebral blood flow auto-regulation range measured under the same anaesthetic conditions used in the present study (Gozzi et al. 2007). As shown by us and other groups, positive or negative pharmacologically evoked MABP changes within the auto-regulation range mentioned above do not result in significant central rCBV response when spin-echo MRI sequences are used (Zaharchuk et al. 1999; Gozzi et al. 2006).

Results

Vehicle-pre-treated animals (groups 1 and 3 and 5) showed a robust and sustained rCBV response to PCP in several corticolimbothalamic structures (Figs. 1, 2, 3, 4 and 5), consistent with previous observations (Gozzi et al. 2008b, c). Statistically significant activation was observed in limbic cortical regions with extension into the motor, visual, parietal- and temporal association and rhinal cortices. Additional foci of subcortical activation were observed in the medial and lateral habenula, amygdala, anterodorsal, dorsolateral and ventromedial thalamus, posterodorsal, anterodorsal and ventral and posterior hippocampus, the striatum and the nucleus accumbens. The overall temporal profile of PCP-induced activation was comparable in all the activated regions (Fig. 4; Supplementary Figures 2 and 3). Despite differences in the peak magnitude of PCP response across studies, the spatial distribution and relative amplitude of the regional response to PCP were very consistent and conserved across the different control groups (groups 1, 3 and 5; Figs. 3 and 5).

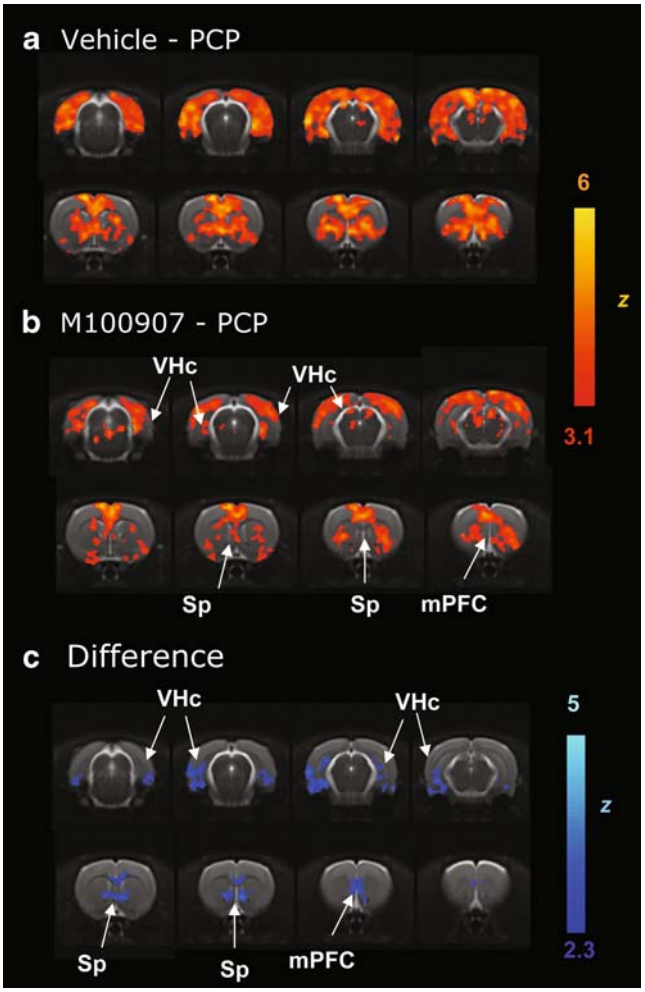

Fig. 1 **a** Anatomical distribution of the rCBV response following acute challenge with PCP (0.5 mg/kg i.v., group 1) with respect to baseline (vehicle–vehicle, group 5). **b** Anatomical distribution of the rCBV response following acute challenge with PCP (0.5 mg/kg i.v., group 1) in animals pre-treated with M100907 with respect to baseline (vehicle–vehicle, group 5). *Orange/yellow* indicates increased rCBV versus baseline (vehicle–vehicle). **c** Map of the regions showing an attenuated PCP response in animals pre-treated with M100907 (1.5 mg/kg i.p., group 1 vs. group 2). *Blue* indicates decreased rCBV versus baseline. *Z* statistics threshold levels are reported beside each map. Maps were cluster-corrected using a $p=0.01$ significance level. *mPFC* medial prefrontal cortex, *Sp* septum, *VHc* ventral hippocampus

Pre-administration of M100907 (1.5 mg/kg i.p.) produced region-dependent and sustained attenuation of PCP-induced rCBV response (Figs. 1, 2, 3 and 4). Foci of significant inhibition were observed in the medial prefrontal cortex, diagonal band, septal nuclei and in ventral hippocampal and peri-hippocampal areas, including the rhinal cortex ($p<0.05$, ANOVA; Figs. 1, 2, 3 and 4). Three-dimensional reconstruction of the areas of attenuation highlighted the involvement of contiguous septofrontal and hippocampal structures (Fig. 2). No areas of increased response to PCP were observed. The lower dose of M100907 (0.5 mg/kg i.p.) did not produce statistically significant attenuation of PCP

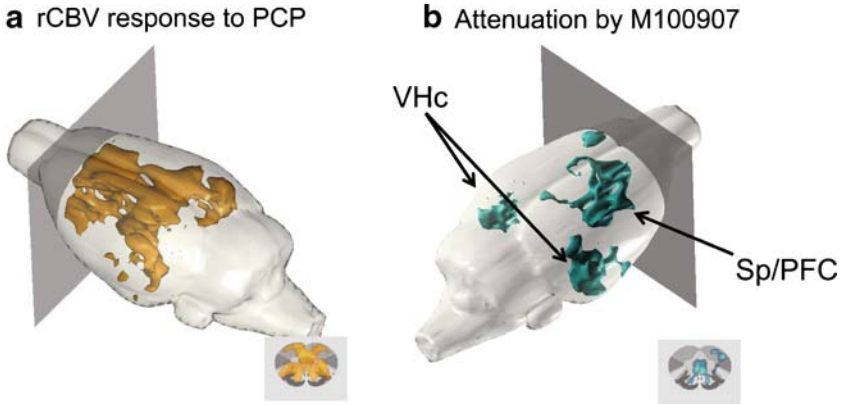

Fig. 2 **a** Volumetric reconstruction of the pattern of rCBV activation produced by acute challenge with PCP with respect to vehicle and **b** attenuating effect of pre-treatment with the selective 5-HT_{2A} antagonist M100907 (1.5 mg/kg i.p.) in frontoseptohippocampal regions. *PFC* medial prefrontal cortex, *VHc* ventral hippocampus, *Sp* septum

response in any of the regions examined ($p>0.28$ all regions; Fig. 3), although a trend was evident in the medial prefrontal cortex ($p<0.09$). This effect was best seen on rCBV time courses (Supplementary Figure 2). Pre-administration of SCH23390 (0.1 mg/kg i.p.) did not produce any significant alteration of PCP response in any of the regions examined ($p>0.24$, all regions; Fig. 5; Supplementary Figure 3).

Administration of M100907 per se (0.5 or 1.5 mg/kg i.p.) produced small (2–8%) and short-lived (4–9 min) rCBV increases in various brain regions, including the medial prefrontal cortex and ventral hippocampus (Supplementary Figures 4 and 5). At the time of PCP challenge, no apparent basal rCBV alteration with respect to vehicle was present in any of the regions examined. Intraperitoneal administration of SCH23390 did not produce visible alteration of basal rCBV with respect to vehicle in any of the regions examined (Supplementary Figure 6).

Discussion

In the present study, we show that selective antagonism of 5-HT_{2A}R induces focal attenuation of PCP-induced activation in frontoseptohippocampal areas of the rat brain. Our results extend previous findings of a role of 5-HT_{2A}R in modulating frontocortical activity (Ceglia et al. 2004; Mirjana et al. 2004) by highlighting the additional involvement of septal and ventral–hippocampal structures

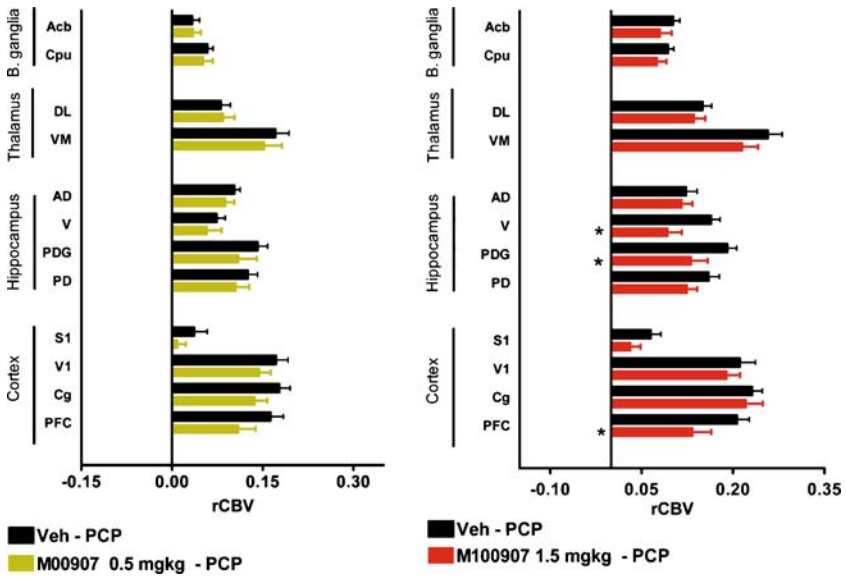

Fig. 3 Magnitude of mean rCBV response ($AUC_{4–20\ min}$) to PCP in representative regions of interest. *Left* Veh-PCP (group 3); Veh-PCP (group 4). *Right* Veh-PCP (group 1), M100907 1.5 mg/kg–PCP (group 2); *$p<0.05$ versus Veh-PCP (group 1), ANOVA followed by Fisher LSD test for multiple comparison. *Acb* nucleus accumbens, *Cpu* caudate putamen, *DL* dorsolateral thalamus, *VM* ventromedial thalamus, *AD* anterodorsal hippocampus, *V* ventral hippocampus, *PDG* posterior dentate gyrus, *PD* posterodorsal hippocampus, *S1* primary somatosensory cortex, *V1* primary visual cortex, *Cg* cingulate cortex, *PFC* medial prefrontal cortex

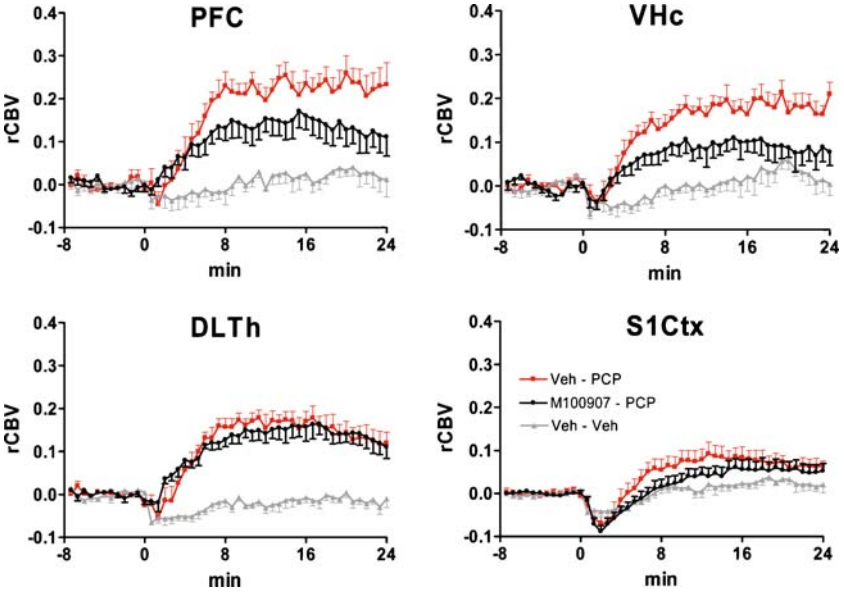

Fig. 4 rCBV time course following PCP injection in representative brain structures. PCP was administered at time 0. Baseline data were obtained in animals pre-treated and challenged with vehicle (saline, group 5). Data are plotted as mean ± SEM within each group. Veh-PCP: group 1, M100907 (1.5 mg/kg i.p.)–PCP: group 2, Veh-Veh: group 7. *PFC* medial prefrontal cortex, *VHc* ventral hippocampus, *DLTh* dorsolateral thalamus, *S1Ctx* primary somatosensory cortex

as integrated substrate of the action of 5-HT_{2A}R antagonism in the living brain. This finding is of particular interest in the light of clinical evidence suggesting a correlation between frontohippocampal hyperactivity and cognitive and perceptual alterations observed in unmedicated schizophrenia patients (Silbersweig et al. 1995; Liddle et al. 2000; Parellada et al. 1994; Ngan et al. 2002; Soyka et al. 2005; Medoff et al. 2001)

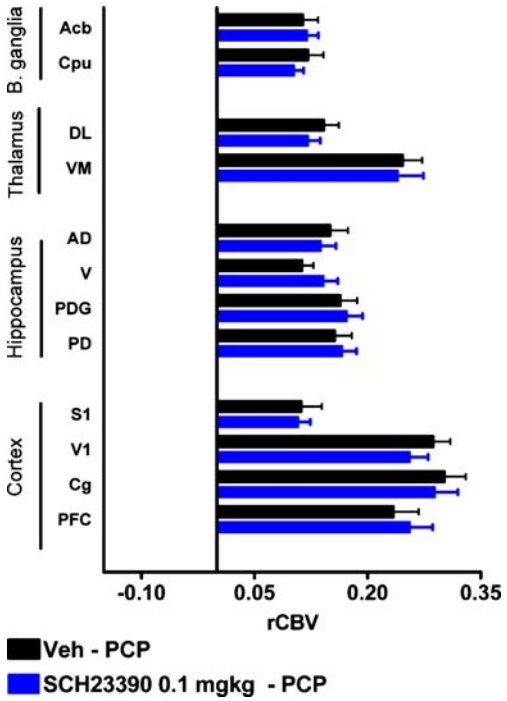

Fig. 5 Magnitude of mean rCBV response ($AUC_{4–20\ min}$) to PCP in representative regions of interest. Veh-PCP (group 5), SCH23390 0.1 mg/kg (group 6). *Acb* nucleus accumbens, *Cpu* caudate putamen, *DL* dorsolateral thalamus, *VM* ventromedial thalamus, *AD* anterodorsal hippocampus, *V* ventral hippocampus, *PDG* posterior dentate gyrus, *PD* posterodorsal hippocampus, *S1* primary somatosensory cortex, *V1* primary visual cortex, *Cg* cingulate cortex, *PFC* medial prefrontal cortex

The observation that 5-HT_{2A}R antagonism affects brain activity in frontohippocampal areas is consistent with previous pre-clinical research. 5-HT_{2A} receptor density in these regions is high (Cornea-Hebert et al. 1999), and immunofluorescence studies have demonstrated marked 5-HT_{2A}R immunoreactivity in GABAergic and cholinergic septohippocampal terminals, as well as in pyramidal and granule cells of the hippocampus (Luttgen et al. 2004). These findings suggest that 5-HT_{2A}R can regulate hippocampal activity both via local pre-synaptic mechanisms and upstream modulation of septal outputs. In agreement with this, electrophysiology studies showed that M100907 and atypical antipsychotic can potently inhibit the excitatory action of serotonin on various septohippocampal neuronal populations (Alreja 1996; Liu and Alreja 1997; Piguet and Galvan 1994; Shen and Andrade 1998). However, the effect does not trivially reflect 5-HT_{2A}R receptor distribution. Indeed, high 5-HT_{2A}R density has been reported in large brain structures such as basal ganglia, thalamus and neocortex (Cornea-Hebert et al. 1999) which did not show significant modulation by M100907. This finding is of interest, as it highlights a discrete circuit whose activity is focally modulated by a widely distributed receptor population, and underscores the possibility to use functional neuroimaging methods to describe specific psychopharmacological contributions in terms of modulation of focal neural circuits.

The functional imaging technique used for this study does not provide direct information on the specific cellular or neurochemical determinants of the modulatory action of

M100907. However, multiple lines of evidence support a glutamatergic origin of the effect mapped. Firstly, 5-HT_{2A}R can positively modulate glutamatergic neurotransmission in frontocortical areas (Ceglia et al. 2004; Scruggs et al. 2000; Aghajanian and Marek 1997), through blockade of 5-HT_{2A} pre-synaptic heteroreceptors (Aghajanian and Marek 2000; Martin-Ruiz et al. 2001). Consistent with this hypothesis, NMDAR antagonists have been shown to induce a dose- and use-dependent hyper-glutamatergic state through de-regulation of pyramidal glutamatergic activity by selectively impairing recurrent feedback from GABAergic inter-neurons (Gozzi et al. 2008a; Greene 2001; Homayoun and Moghaddam 2007). Secondly, compounds that modulate pyramidal glutamate release have been shown to markedly attenuate the functional and behavioural cascade triggered by NMDAR antagonism (Gozzi et al. 2008a, b; Cartmell et al. 1999). In agreement with this, Ceglia et al. (2004) reported the ability of M100907 to prevent the increase in frontocortical glutamate induced by the NMDAR antagonist 3-(*R*)-2-carboxypiperazin-4-propyl-1-phosphonic acid (CPP), an effect that also produced an improvement of CPP-induced impairment in attentional performance. Conversely, little or no inhibitory effect has been observed with drugs that target neurotransmitter systems secondarily activated by the effect of NMDAR antagonism such as dopamine D_2 antagonists (Idris et al. 2005; Gozzi et al. 2008b; Large 2007).

Alternatively, since M100907 has been reported to stimulate dopamine release in frontal areas (Schmidt and Fadayel 1995), the inhibitory effect observed could reflect post-synaptic activation of D_1 dopamine receptors. However, this effect, however, cannot be straightforwardly investigated by using dopamine-mimetic drugs, as these compounds produce robust and widespread haemodynamic alterations that could saturate the subsequent response to a PCP challenge (Choi et al. 2006; Schwarz et al. 2004, 2007). We therefore examined the role of post-synaptic dopamine D_1 receptors on PCP-induced fMRI response examined using a potent D_1 antagonist (SCH23390, 0.1 mg/kg; Andersen et al. 1992). Acute administration of PCP generates disinhibition of corticothalamic glutamatergic neurotransmission, an event that cascades to involve several neurotransmitter systems including serotonin and dopamine (Greene 2001; Large 2007; Moghaddam et al. 1997). Increased dopamine release upon acute administration of NMDAR antagonists has been observed in mesolimbic areas and in frontal regions of the rat (Moghaddam et al. 1997; Javitt et al. 1999). Given the prevalent role of dopamine D_1 receptors in mediating the fMRI response to dopamine-releasing agents (Knutson and Gibbs 2007), by assessing the effect of selective DA antagonists, we sought to determine whether the functional response to PCP in our model presents significant contributions of dopaminergic nature. Interestingly, pre-administration of SCH23390 did not produce any significant alteration of PCP response in any of the regions examined. When considered with previous evidence of a negligible role of dopamine D_2 receptors in the same experimental setup (Gozzi et al. 2008b), this finding strongly argues against a predominant role of dopamine in the functional changes mapped and, in turn, in the inhibitory action observed with M100907. In the light of the established facilitatory role of 5-HT_{2A}R on pyramidal glutamate neurotransmission discussed above, it seems thus likely that that the effect of M100907 reflects a local reduction in glutamatergic neurotransmission. However, whilst this is by far the most plausible neurochemical mechanism, our data do not permit to rule out contributions of PCP-induced serotonergic neurotransmission independent of the neuromodulatory role of the 5-HT_{2A}R on glutamate release

Although a comprehensive discussion of the role of dopamine in the cascade elicited by NMDAR antagonism is beyond the scope of the manuscript, the lack of effect of SCH22390 is of interest per se as it provides additional evidence of a subsidiary role of this neurotransmitter in mediating the neurobehavioural effects of these drugs, a finding observed by numerous investigators using dopamine D_2 antagonists in different experimental models and readouts (Idris et al. 2005; Gozzi et al. 2008b; Krystal et al. 1999; Linn et al. 2003). Our finding extends these results to the D_1 receptor subtype, suggesting that dopaminergic mechanisms are engaged far downstream in the neurofunctional cascade triggered by psychotogenic doses of NMDAR antagonists.

M100907 produced significant attenuation of PCP only at the highest dose (1.5 mg/kg), although a trend in the mPFC was apparent at the lower dose tested (0.5 mg/kg; Fig. 3). As pharmacodynamic studies reported complete inhibition of behavioural response to serotonergic agents at doses of 0.1 mg/kg (Schreiber et al. 1995; Kehne et al. 1996), the presence of significant attenuation only at the higher dose may call into question putative contributions from other receptor types, namely alpha1-adrenergic, dopamine D_2 or 5-HT_{2c}. However, multiple lines of evidence make this hypothesis very unlikely. Firstly, M100907's affinity for D_2 receptors is >2,500-fold lower than 5-HT_{2A} (Kehne et al. 1996). Consistent with this, the drug failed to reduce apomorphine induced climbing in rats, an index of D_2 receptor antagonism, at a dose as high as 8 mg/kg (Kehne et al. 1996; Sorensen et al. 1993). Although the selectivity at alpha$_1$-adrenergic receptor is slightly lower (>100-fold), the drug did not show significant ex vivo receptor binding at alpha$_1$-adrenergic receptors at doses up to 10 mg/kg (Kehne et al. 1996). Moreover, a dose of 16 mg/kg of M100907 (i.e. 10-fold higher than the effective dose of our study) failed to antagonise the acute

cardiovascular effects of the alpha$_1$-adrenergic agonist phenylephrine (Kehne et al. 1996) in a widely used behavioural assay index of alpha$_1$-receptor antagonism (Peroutka et al. 1977). Finally, 1 mg/kg of M100907 did not show significant antagonism of the pre-pulse inhibition-disruptive effect of the potent alpha$_1$-adrenergic agonist cirazoline in two different rat strains (Varty et al. 1999). In the light of these findings, a significant contribution of dopamine D_2 or alpha$_1$-adrenergic receptors appears extremely unlikely.

Secondly, although receptor binding data indicate a >100-fold selectivity over 5-HT$_{2C}$ receptors (Kehne et al. 1996; Palfreyman et al. 1993), in vitro antagonism assays of functional selectivity highlighted a >1,000-fold separation between the two receptors (Kehne et al. 1996). In agreement with this, a number of in vivo studies showed that M100907, at the same or higher doses tested here, did not produce detectable effects in behavioural paradigms sensitive to the action of selective 5-HT$_{2C}$ antagonism (Fletcher et al. 2002; Zaniewska et al. 2007; Hajos et al. 2003), or produced significant effects that were not paralleled by the action of selective 5-HT$_{2C}$ antagonists (Varty et al. 1999). Thirdly, the nature of the behavioural alterations produced by 5-HT$_{2C}$ antagonism in models of NMDAR hypo-function cannot be easily be reconciled with our findings, as several reports showed that 5-HT$_{2C}$ antagonism does not inhibit, but rather exacerbates, the acute effects of NMDAR antagonists (Higgins et al. 2003; Hutson et al. 2000; O'Neill et al. 1999; Wood et al. 2001). These effects have been linked to an increased dopaminergic tone consequent to the blockade of 5- HT$_{2C}$ receptors in several mesocortical areas, including the medial prefrontal cortex (Gobert et al. 2000). However, as discussed above, our data with the dopamine D_1 antagonists SCH23390 argue against a significant contribution of dopaminergic neurotransmission in the functional effect mapped. Moreover, consistent with the hypothesis of an opposing functional role of 5-HT$_{2A}$ and 5-HT$_{2C}$ receptors (Ichikawa and Meltzer 1999), electrophysiology studies demonstrated that 5-HT$_{2C}$ antagonism do not decreases, but rather *increases* the activity of septohippocampal circuit (expressed as theta waves recordings), an effect reversed by selective 5-HT$_{2C}$ agonists (Hajos et al. 2003). In agreement with this, selective 5-HT$_{2C}$ *agonists* have been recently shown to be highly efficacious in inhibiting the behavioural effects of NMDAR antagonism (Marquis et al. 2007).When considered together, these data strongly argue against a significant contribution of 5-HT$_{2C}$ or other spurious receptor systems in the inhibitory effect of M100907 observed in this study.

Based on recent ex vivo receptor occupancy data in the rat frontal cortex, the doses of M100907 used in the present manuscript (1.5 and 0.5 mg/kg i.p.) would be expected to have an estimated receptor occupancy of approximately 100% and 80% at the end 30-min post-PCP time window examined (Knauer et al. 2008). Although the different receptor occupancy alone could explain the lack of response at the low dose, other experimental factors could have contributed to stretch or right-shift the effective dose–efficacy curve. For example, pharmacokinetic studies of M100907 in the rat showed that the compound reaches peak brain concentrations (T_{max}) 32±11 min after its intravenous administration (5 mg/kg; Scott and Heath 1998). Assuming similar parameters following use of intraperitoneal route, the relatively long-time window used to quantify its effect in the present manuscript (30–60 min post-administration) may not be optimally suited to maximise the sensitivity of the measurements. Furthermore, molecular interactions between M100907, PCP and the anaesthetic used (halothane) could also play a significant contribution in vivo. Recent work from (Kapur and Seeman 2002) showed the ability of PCP and ketamine to bind to the high-affinity state of 5-HT$_{2A}$ receptor with micromolar affinity, a value consistent with brain exposure of PCP at the dose used in the present work (Proksch et al. 2000). Moreover, the same authors recently demonstrated that low doses of volatile anaesthetics such as halothane or isoflurane can also bind to (and stimulate) the activity of 5-HT$_{2A}$ receptors (Seeman and Kapur 2003). Thus, simultaneous interactions of PCP and anaesthetic with 5-HT$_{2A}$ receptors may produce significant functional antagonisation or pharmacological displacement of M100907, resulting in the need of higher doses to exert pharmacologically significant effects. Interestingly, a number of studies of 5-HT$_{2A}$ antagonism in PCP models of NMDAR hypo-function showed significant effects only at doses similar to those used in our study (Varty et al. 1999; Habara et al. 2001), whilst studies performed at lower doses do not consistently show effects (Rodefer et al. 2008; Winter et al. 2004; Adams and Moghaddam 2001). This suggests that PCP-5-HT$_{2A}$ receptor interactions might be non-negligible even in absence of anaesthesia. Future experiments using NMDAR antagonist devoid of significant 5-HT$_{2A}$ affinity (i.e. CPP; Lehmann et al. 1987) may be performed to investigate this hypothesis. Nonetheless, it should be emphasised that if these interactions do occur in vivo, they are expected to affect the effectiveness, but not the outcome, of 5-HT$_{2A}$ antagonism in the brain, thus leaving unaltered the functional significance of the effects described in our manuscript.

Whilst the transient state produced by the acute administration of PCP cannot possibly mimic the entire syndrome and course of a multi-factorial disease like schizophrenia, the ability of NMDAR antagonists to produce behavioural effects akin to positive and negative symptoms of the disorder in human volunteers (Krystal et

al. 2003; Adler et al. 1999) suggests that the hyperglutamatergic state produced by these drugs alters neural function in circuits that are relevant for this condition. Importantly, the circuits activated by NMDAR antagonists in rodents and humans as seen with various functional imaging modalities (Deakin et al. 2008; Gozzi et al. 2008c; Langsjo et al. 2003; Vollenweider, personal communication) show a high degree of homology between species and do not appear to be qualitatively affected by the anaesthesia (Gozzi et al. 2008c). Several neuroimaging studies have provided evidence for localised anatomical and functional abnormalities in frontohippocampal areas of schizophrenia patients. Imaging studies of haemodynamic parameters have highlighted increased blood flow and abnormal hippocampal activity at rest and during the performance of memory retrieval tasks (Heckers 2001; Medoff et al. 2001). Similarly, neurometabolic studies in unmedicated schizophrenic patients have highlighted increased tonic frontocortical activity, a feature that has been linked to the sensory flooding, cognitive fragmentation and ego-dissolution seen in both drug-induced and disorder-based psychosis (Parellada et al. 1994; Soyka et al. 2005; Geyer and Vollenweider 2008; Volkow et al. 1986). Thus, the ability of 5-HT_{2A}R antagonism to produce region-selective attenuation of aberrant frontohippocampal states suggests that this pharmacological mechanism might contribute to some of the therapeutic effect of clozapine and other second generation anti-psychotics that possess significant 5-HT_{2A}R affinity (Ichikawa and Meltzer 1999). A few clinical studies have recently addressed the role of selective 5-HT_{2A}R antagonism in schizophrenia patients. In a two multicenter, placebo and haloperidol-controlled studies in USA, M100907 showed statistically significant efficacy on total score versus placebo of positive and negative symptoms (De Paulis 2001; Marder 1999), although the drug was less effective than haloperidol. The effect was not confirmed in a European study involving patients with predominantly negative symptoms, although M100907-treated schizophrenic subjects showed significantly fewer preservative errors in the Wisconsin Card Sorting Test (Roth et al. 2004). A recent placebo-controlled study using a the 5-$HT_{2A/2C}$R antagonist SR46349B produced significant reductions in the positive and negative syndrome scale total and negative scores versus placebo (Meltzer et al. 2004). Likewise, the 5-$HT_{2A/2C}$R antagonist mianserin produced significant improvement in measures of cognitive function (learning, memory and sustained attention) when the drug was tested as add-on therapy in schizophrenic patients (Poyurovsky et al. 2003). Collectively, the limited clinical data available suggest that 5-HT_{2A} antagonism per se may produce mild, but clinically significant antipsychotic effects, involving a moderate improvement of both positive and negative symptoms. This is in agreement with our observation that the 5-HT_{2A}R antagonist M100907, unlike glutamatergic compounds (Gozzi et al. 2008a, b), is unable to entirely suppress the functional cascade produced by PCP in the rat brain, but selectively reduces PCP-induced activation in the frontoseptohippocampal circuit, a key substrate of higher cognitive functions that appears to be tonically hyper-activated in drug-induced and disorder-based psychosis. Consistent findings have been reproduced in pre-clinical behavioural models, where 5-HT_{2A}R receptor antagonists do not consistently antagonise the entire spectrum of behavioural and neurochemical responses produced by NMDAR antagonists in the rat (Large 2007; Adams and Moghaddam 2001) but have been shown to improve frontocortical functions (Mirjana et al. 2004; Winstanley et al. 2003). Of interest, glucose metabolism studies using positron emission tomography highlighted a tight correlation between depression of corticohippocampal activity and antipsychotic action elicited by a single dose of the atypical anti-psychotics risperidone (Liddle et al. 2000). Whilst multiple receptor contributions are likely to contribute to this effect, this finding is important as it suggests that the circuital mechanism identified in our study may be of clinical significance.

In conclusion, we have shown that 5-HT_{2A}R antagonist reduces PCP-induced activation in discrete brain regions, including frontal cortex, septum and ventral–hippocampal areas. These results are consistent with pre-clinical studies highlighting a key role of 5-HT_{2A}R in modulating glutamate-mediated cognitive performance in the rodent prefrontal cortex and extend those findings by highlighting a role of the frontoseptohippocampal circuit as an integrated substrate of the action of $5HT_{2A}$ antagonism in the living brain. Collectively, pre-clinical and clinical research provide converging evidence that 5-HT_{2A}R antagonism can exert a region-selective modulation of frontoseptohippocampal activity that might be of clinical benefit when the circuit is functionally hyperactive.

Acknowledgements The author would like to thank Dr. Mauro Corsi for critically reviewing the manuscript.

Disclosure/conflict of interest The author(s) declare that, except for income received from my primary employer, no financial support or compensation has been received from any individual or corporate entity over the past 3 years for research or professional service and there are no personal financial holdings that could be perceived as constituting a potential conflict of interest.

References

Adams BW, Moghaddam B (2001) Effect of clozapine, haloperidol, or M100907 on phencyclidine-activated glutamate efflux in the prefrontal cortex. Biol Psychiatry 50:750–757

Adler CM, Malhotra AK, Elman I, Goldberg T, Egan M, Pickar D, Breier A (1999) Comparison of ketamine-induced thought disorder in healthy volunteers and thought disorder in schizophrenia. Am J Psychiatry 156:1646–1649

Aghajanian GK, Marek GJ (1997) Serotonin induces excitatory postsynaptic potentials in apical dendrites of neocortical pyramidal cells. Neuropharmacology 36:589–599

Aghajanian GK, Marek GJ (2000) Serotonin model of schizophrenia: emerging role of glutamate mechanisms. Brain Res Rev 31:302–312

Allen RM, Young SJ (1978) Phencyclidine-induced psychosis. Am J Psychiatry 135:1081–1084

Alreja M (1996) Excitatory actions of serotonin on GABAergic neurons of the medial septum and diagonal band of Broca. Synapse 22:15–27

Andersen PH, Gronvald FC, Hohlweg R, Hansen LB, Guddal E, Braestrup C, Nielsen EB (1992) NNC-112, NNC-687 and NNC-756, new selective and highly potent dopamine D1 receptor antagonists. Eur J Pharmacol 219:45–52

Carli M, Baviera M, Invernizzi RW, Balducci C (2005) Dissociable contribution of 5-HT1A and 5-HT2A receptors in the medial prefrontal cortex to different aspects of executive control such as impulsivity and compulsive perseveration in rats. Neuropsychopharmacology 31:757–767

Cartmell J, Monn JA, Schoepp DD (1999) The metabotropic glutamate 2/3 receptor agonists LY354740 and LY379268 selectively attenuate phencyclidine versus d-amphetamine motor behaviors in rats. J Pharmacol Exp Ther 291:161–170

Ceglia I, Carli M, Baviera M, Renoldi G, Calcagno E, Invernizzi RW (2004) The 5-HT2A receptor antagonist M100, 907 prevents extracellular glutamate rising in response to NMDA receptor blockade in the mPFC. J Neurochem 91:189–199

Choi JK, Chen YI, Hamel E, Jenkins BG (2006) Brain hemodynamic changes mediated by dopamine receptors: role of the cerebral microvasculature in dopamine-mediated neurovascular coupling. NeuroImage 30:700–712

Cornea-Hebert V, Riad M, Wu C, Singh SK, Descarries L (1999) Cellular and subcellular distribution of the serotonin 5-HT2A receptor in the central nervous system of adult rat. J Comp Neurol 409:187–209

Coyle J (2006) Glutamate and schizophrenia: beyond the dopamine hypothesis. Cell Mol Neurobiol 26:363–382

Davidson RJ, Abercrombie H, Nitschke JB, Putnam K (1999) Regional brain function, emotion and disorders of emotion. Curr Opin Neurobiol 9:228–234

De Paulis T (2001) M-100907 (Aventis). Curr Opin Investig Drugs 2:123–132

Deakin JFW, Lees J, McKie S, Hallak JEC, Williams SR, Dursun SM (2008) Glutamate and the neural basis of the subjective effects of ketamine: a pharmaco-magnetic resonance imaging study. Arch Gen Psychiatry 65:154–164

Fletcher PJ, Grottick AJ, Higgins GA (2002) Differential effects of the 5-HT(2A) receptor antagonist M100907 and the 5-HT(2C) receptor antagonist SB242084 on cocaine-induced locomotor activity, cocaine self-administration and cocaine-induced reinstatement of responding. Neuropsychopharmacology 27:576–586

Friston KJ, Jezzard P, Turner R (1994) Analysis of functional MRI time-series. Hum Brain Mapp 1:153–171

Garris PA, Ciolkowski EL, Pastore P, Wightman RM (1994) Efflux of dopamine from the synaptic cleft in the nucleus accumbens of the rat brain. J Neurosci 14:6084–6093

Geyer MA, Vollenweider FX (2008) Serotonin research: contributions to understanding psychoses. Trends Pharmacol Sci 29:445–453

Gobert A, Rivet JM, Lejeune F, Newman-Tancredi A, dhumeau-Auclair A, Nicolas JP, Cistarelli L, Melon C, Millan MJ (2000) Serotonin(2C) receptors tonically suppress the activity of mesocortical dopaminergic and adrenergic, but not serotonergic, pathways: a combined dialysis and electrophysiological analysis in the rat. Synapse 36:205–221

Gozzi A, Schwarz A, Reese T, Bertani S, Crestan V, Bifone A (2006) Region-specific effects of nicotine on brain activity: a pharmacological MRI study in the drug-naïve rat. Neuropsychopharmacology 31:1690–1703

Gozzi A, Ceolin L, Schwarz A, Reese T, Bertani S, Bifone A (2007) A multimodality investigation of cerebral haemodynamics and autoregulation in phMRI. Magn Reson Imaging 25:826–833

Gozzi A, Herdon H, Schwarz A, Bertani S, Crestan V, Turrini G, Bifone A (2008a) Pharmacological stimulation of NMDA receptors via co-agonist site suppresses fMRI response to phencyclidine in the rat. Psychopharmacology 201:273–284

Gozzi A, Large C, Schwarz A, Bertani S, Crestan V, Bifone A (2008b) Differential effects of antipsychotic and glutamatergic agents on the phMRI response to phencyclidine. Neuropsychopharmacology 33:1690–1703

Gozzi A, Schwarz AJ, Reese T, Crestan V, Bifone A (2008c) Drug-anaesthetic interaction in phMRI: the case of the pyschotomimetic agent phencyclidine. Magn Reson Imag 26:999–1006

Greene R (2001) Circuit analysis of NMDAR hypofunction in the hippocampus, in vitro, and psychosis of schizophrenia. Hippocampus 11:569–577

Habara T, Hamamura T, Miki M, Ohashi K, Kuroda S (2001) M100907, a selective 5-HT(2A) receptor antagonist, attenuates phencyclidine-induced Fos expression in discrete regions of rat brain. Eur J Pharmacol 417:189–194

Hajos M, Hoffmann WE, Weaver RJ (2003) Regulation of septo-hippocampal activity by 5-hydroxytryptamine2C receptors. J Pharmacol Exp Ther 306:605–615

Heckers S (2001) Neuroimaging studies of the hippocampus in schizophrenia. Hippocampus 11:520–528

Hennig J, Nauerth A, Friedburg H (1986) RARE imaging: a fast imaging method for clinical MR. Magn Reson Med 3:823–833

Hietala J, Sepp T, Lappalainen J, Syvlahti E (1992) Quantification of SCH 39166, a novel selective D1 dopamine receptor antagonist, in rat brain and blood. Psychopharmacology 106:455–458

Higgins GA, Enderlin M, Haman M, Fletcher PJ (2003) The 5-HT2A receptor antagonist M100, 907 attenuates motor and 'impulsive-type' behaviours produced by NMDA receptor antagonism. Psychopharmacology 170:309–319

Homayoun H, Moghaddam B (2007) NMDA receptor hypofunction produces opposite effects on prefrontal cortex interneurons and pyramidal neurons. J Neurosci 27:11496–11500

Honey G, Bullmore E (2004) Human pharmacological MRI. Trends Pharmacol Sci 25:366–374

Hoyer D, Pazos A, Probst A, Palacios JM (1986) Serotonin receptors in the human brain. II. Characterization and autoradiographic localization of 5-HT1C and 5-HT2 recognition sites. Brain Res 376:97–107

Hutson PH, Barton CL, Jay M, Blurton P, Burkamp F, Clarkson R, Bristow LJ (2000) Activation of mesolimbic dopamine function by phencyclidine is enhanced by 5-HT2C/2B receptor antagonists: neurochemical and behavioural studies. Neuropharmacology 39:2318–2328

Ichikawa J, Meltzer HY (1999) Relationship between dopaminergic and serotonergic neuronal activity in the frontal cortex and the action of typical and atypical antipsychotic drugs. Eur Arch Psychiatry Clin Neurosci 249:S90–S98

Idris NF, Repeto P, Neill JC, Large CH (2005) Investigation of the effects of lamotrigine and clozapine in improving reversal-learning impairments induced by acute phencyclidine and D-amphetamine in the rat. Psychopharmacology (Berl) 179:336–348

Javitt DC, Balla A, Sershen H, Lajtha A (1999) Reversal of phencyclidine-induced effects by glycine and glycine transport inhibitors. Biol Psychiatry 45:668–679

Jenkins BG, Chen Y-CI, Mandeville JB (2003) Pharmacological magnetic resonance imaging (phMRI). In: van Bruggen N, Roberts T (eds) Biomedical imaging in experimental neuroscience. CRC, New York, pp 155–209

Kapur S, Seeman P (2002) NMDA receptor antagonists ketamine and PCP have direct effects on the dopamine D(2) and serotonin 5-HT(2)receptors-implications for models of schizophrenia. Mol Psychiatry 7:837–844

Kehne JH, Baron BM, Carr AA, Chaney SF, Elands J, Feldman DJ, Frank RA, van Giersbergen PL, McCloskey TC, Johnson MP, McCarty DR, Poirot M, Senyah Y, Siegel BW, Widmaier C (1996) Preclinical characterization of the potential of the putative atypical antipsychotic MDL 100, 907 as a potent 5-HT2A antagonist with a favorable CNS safety profile. J Pharmacol Exp Ther 277:968–981

Knauer CS, Campbell JE, Galvan B, Bowman C, Osgood S, Buist S, Buchholz L, Henry B, Wong EHF, Shahid M, Grimwood S (2008) Validation of a rat in vivo [3H]M100907 binding assay to determine a translatable measure of 5-HT2A receptor occupancy. Eur J Pharmacol 591:136–141

Knutson B, Gibbs S (2007) Linking nucleus accumbens dopamine and blood oxygenation. Psychopharmacology 191:813–822

Kristiansen LV, Huerta I, Beneyto M, Meador-Woodruff JH (2007) NMDA receptors and schizophrenia. Curr Opin Pharmacol 7:48–55

Krystal JH, D'Souza DC, Karper LP, Bennett A, Abi-Dargham A, Abi-Saab D, Cassello K, Bowers MB Jr, Vegso S, Heninger GR, Charney DS (1999) Interactive effects of subanesthetic ketamine and haloperidol in healthy humans. Psychopharmacology (Berl) 145:193–204

Krystal JH, Anand A, Moghaddam B (2002) Effects of NMDA receptor antagonists: implications for the pathophysiology of schizophrenia. Arch Gen Psychiatry 59:663–664

Krystal JH, D'Souza DC, Mathalon D, Perry E, Belger A, Hoffman R (2003) NMDA receptor antagonist effects, cortical glutamatergic function, and schizophrenia: toward a paradigm shift in medication development. Psychopharmacology (Berl) 169:215–233

Kuroki T, Meltzer HY, Ichikawa J (1999) Effects of antipsychotic drugs on extracellular dopamine levels in rat medial prefrontal cortex and nucleus accumbens. J Pharmacol Exp Ther 288:774–781

Langsjo JW, Kaisti KK, Aalto S, Hinkka S, Aantaa R, Oikonen V, Sipila H, Kurki T, Silvanto M, Scheinin H (2003) Effects of subanesthetic doses of ketamine on regional cerebral blood flow, oxygen consumption, and blood volume in humans. Anesthesiology 99:614–623

Large CH (2007) Do NMDA receptor antagonist models of schizophrenia predict the clinical efficacy of antipsychotic drugs? J Psychopharmacol 21:283–301

Lehmann J, Schneider J, McPherson S, Murphy DE, Bernard P, Tsai C, Bennett DA, Pastor G, Steel DJ, Boehm C (1987) CPP, a selective N-methyl-D-aspartate (NMDA)-type receptor antagonist: characterization in vitro and in vivo. J Pharmacol Exp Ther 240:737–746

Liddle PF, Lane CJ, Ngan E (2000) Immediate effects of risperidone on cortico-striato-thalamic loops and the hippocampus. Br J Psychiatry 177:402–407

Linn S, Negi S, Gerum V, Javitt C (2003) Reversal of phencyclidine-induced prepulse inhibition deficits by clozapine in monkeys. Psychopharmacology V169:234–239

Littlewood CL, Jones N, O'Neil MJ, Mitchell SN, Tricklebank M, Williams MS (2006) Mapping the central effects of ketamine in the rat using pharmacological MRI. Psychopharmacology V186:64–81

Liu W, Alreja M (1997) Atypical antipsychotics block the excitatory effects of serotonin in septohippocampal neurons in the rat. Neuroscience 79:369–382

Luttgen M, Ove Ígren S, Br M (2004) Chemical identity of 5-HT2A receptor immunoreactive neurons of the rat septal complex and dorsal hippocampus. Brain Res 1010:156–165

Malhotra AK, Pinals DA, Adler CM, Elman I, Clifton A, Pickar D, Breier A (1997) Ketamine-induced exacerbation of psychotic symptoms and cognitive impairment in neuroleptic-free schizophrenics. Neuropsychopharmacology 17:141–150

Mandeville JB, Marota JJA, Kosofsky BE, Keltner JR, Weissleder R, Rosen B, Weisskoff R (1998) Dynamic functional imaging of relative cerebral blood volume during rat forepaw stimulation. Magn Reson Med 39:615–624

Marder SR (1999) Limitations of dopamine-D_2 antagonists and the search for novel antipsychotic strategies. Neuropsychopharmacology 21:S117–S121

Marquis KL, Sabb AL, Logue SF, Brennan JA, Piesla MJ, Comery TA, Grauer SM, Ashby CR Jr, Nguyen HQ, Dawson LA, Barrett JE, Stack G, Meltzer HY, Harrison BL, Rosenzweig-Lipson S (2007) WAY-163909 [(7bR, 10aR)-1, 2, 3, 4, 8, 9, 10, 10a-octahydro-7bH-cyclopenta-[b][1, 4]diazepino[6, 7, 1hi]indole]: a novel 5-hydroxytryptamine 2C receptor-selective agonist with preclinical antipsychotic-like activity. J Pharmacol Exp Ther 320:486–496

Martin-Ruiz R, Puig MV, Celada P, Shapiro DA, Roth BL, Mengod G, Artigas F (2001) Control of serotonergic function in medial prefrontal cortex by serotonin-2A receptors through a glutamate-dependent mechanism. J Neurosci 21:9856–9866

Medoff DR, Holcomb HH, Lahti AC, Tamminga CA (2001) Probing the human hippocampus using rCBF: contrasts in schizophrenia. Hippocampus 11:543–550

Meltzer HY (1996) Pre-clinical pharmacology of atypical antipsychotic drugs: a selective review. Br J Psychiatry 168(Suppl 29):23–31

Meltzer HY, Matsubara S, Lee JC (1989) Classification of typical and atypical antipsychotic drugs on the basis of dopamine D-1, D-2 and serotonin2 pKi values. J Pharmacol Exp Ther 251:238–246

Meltzer HY, Li Z, Kaneda Y, Ichikawa J (2003) Serotonin receptors: their key role in drugs to treat schizophrenia. Prog Neuropsychopharmacol Biol Psychiatry 27:1159–1172

Meltzer HY, Arvanitis L, Bauer D, Rein W (2004) Placebo-controlled evaluation of four novel compounds for the treatment of schizophrenia and schizoaffective disorder. Am J Psychiatry 161:975–984

Mirjana C, Baviera M, Invernizzi RW, Balducci C (2004) The serotonin 5-HT2A receptors antagonist M100907 prevents impairment in attentional performance by NMDA receptor blockade in the rat prefrontal cortex. Neuropsychopharmacology 29:1637–1647

Moghaddam B, Adams B, Verma A, Daly D (1997) Activation of glutamatergic neurotransmission by ketamine: a novel step in the pathway from NMDA receptor blockade to dopaminergic and cognitive disruptions associated with the prefrontal cortex. The Journal of Neuroscience: The Official Journal of the Society for Neuroscience 17:2921–2927

Molloy AG, Waddington JL (1984) Dopaminergic behaviour stereospecifically promoted by the D1 agonist R-SK & F 38393 and selectively blocked by the D1 antagonist SCH 23390. Psychopharmacology 82:409–410

Neisewander JL, Fuchs RA, O'Dell LE, Khroyan TV (1998) Effects of SCH-23390 on dopamine D1 receptor occupancy and locomotion produced by intraaccumbens cocaine infusion. Synapse 30:194–204

Ngan ETC, Lane CJ, Ruth TJ, Liddle PF (2002) Immediate and delayed effects of risperidone on cerebral metabolism in

neuroleptic naive schizophrenic patients: correlations with symptom change. J Neurol Neurosurg Psychiatry 72:106–110

O'Neill MF, Heron-Maxwell CL, Shaw G (1999) 5-HT2 receptor antagonism reduces hyperactivity induced by amphetamine, cocaine, and MK-801 but not D1 agonist C-APB. Pharmacol Biochem Behav 63:237–243

Palfreyman MG, Schmidt CJ, Sorensen SM, Dudley MW, Kehne JH, Moser P, Gittos MW, Carr AA (1993) Electrophysiological, biochemical and behavioral evidence for 5-HT2 and 5-HT3 mediated control of dopaminergic function. Psychopharmacology (Berl) 112:S60–S67

Parellada E, Catafau AM, Bernardo M, Lomena F, Gonzalez-Monclus E, Setoain J (1994) Prefrontal dysfunction in young acute neuroleptic-naive schizophrenic patients: a resting and activation SPECT study. Psychiatry Res 55:131–139

Paxinos G, Watson C (1998) The rat brain in stereotactic coordinates. Academic, San Diego

Peroutka SJ, U'Prichard DC, Greenberg DA, Snyder SH (1977) Neuroleptic drug interactions with norepinephrine alpha receptor binding sites in rat brain. Neuropharmacology 16:549–556

Piguet P, Galvan M (1994) Transient and long-lasting actions of 5-HT on rat dentate gyrus neurones in vitro. J Physiol 481(Pt 3):629–639

Poyurovsky M, Koren D, Gonopolsky I, Schneidman M, Fuchs C, Weizman A, Weizman R (2003) Effect of the 5-HT2 antagonist mianserin on cognitive dysfunction in chronic schizophrenia patients: an add-on, double-blind placebo-controlled study. Eur Neuropsychopharmacol 13:123–128

Proksch JW, Gentry WB, Owens SM (2000) The effect of rate of drug administration on the extent and time course of phencyclidine distribution in rat brain, testis, and serum. Drug Metab Dispos 28:742–747

Robbins TW (2005) Chemistry of the mind: neurochemical modulation of prefrontal cortical function. J Comp Neurol 493:140–146

Rodefer JS, Nguyen TN, Karlsson JJ, Arnt J (2008) Reversal of subchronic PCP-induced deficits in attentional set shifting in rats by sertindole and a 5-HT6 receptor antagonist: comparison among antipsychotics. Neuropsychopharmacology 33:2657–2666

Roth BL, Hanizavareh SM, Blum AE (2004) Serotonin receptors represent highly favorable molecular targets for cognitive enhancement in schizophrenia and other disorders. Psychopharmacology 174:17–24

Schmidt CJ, Fadayel GM (1995) The selective 5-HT2A receptor antagonist, MDL 100, 907, increases dopamine efflux in the prefrontal cortex of the rat. Eur J Pharmacol 273:273–279

Schreiber R, Brocco M, de Lefebvre LB, Monneyron S, Millan MJ (1995) A drug discrimination analysis of the actions of novel serotonin1A receptor ligands in the rat using the 5-HT1A receptor agonist, 8-hydroxy-2-(di-n-propylamino)tetralin. J Pharmacol Exp Ther 275:822–831

Schwarz AJ, Reese T, Gozzi A, Bifone A (2003) Functional MRI using intravascular contrast agents: detrending of the relative cerebrovascular (rCBV) time course. Magn Reson Imaging 21:1191–1200

Schwarz AJ, Zocchi A, Reese T, Gozzi A, Varnier G, Girlanda E, Biscaro B, Bertani S, Crestan V, Heidbreder CA, Bifone A (2004) The relationship between local dopamine changes and phMRI response to acute cocaine challenge in the rat revealed by concurrent in situ microdialysis. In: Book of abstracts: Twelfth Annual Meeting of the International Society of Magnetic Resonance in Medicine 12

Schwarz AJ, Danckaert A, Reese T, Gozzi A, Paxinos G, Watson C, Merlo-Pich EV, Bifone A (2006a) A stereotaxic MRI template set for the rat brain with tissue class distribution maps and co-registered anatomical atlas: application to pharmacological MRI. NeuroImage 32:538–550

Schwarz AJ, Whitcher B, Gozzi A, Reese T, Bifone A (2006b) Study-level wavelet cluster analysis and data-driven signal models in pharmacological MRI. J Neurosci Methods 159:346–360

Schwarz AJ, Gozzi A, Reese T, Heidbreder CA, Bifone A (2007) Pharmacological modulation of functional connectivity: the correlation structure underlying the phMRI response to d-amphetamine modified by selective dopamine D3receptor antagonist SB277011A. Magn Reson Imag 25:811–820

Scott DO, Heath TG (1998) Investigation of the CNS penetration of a potent 5-HT2a receptor antagonist (MDL 100, 907) and an active metabolite (MDL 105, 725) using in vivo microdialysis sampling in the rat. J Pharm Biomed Anal 17:17–25

Scruggs JL, Patel S, Bubser M, Deutch AY (2000) DOI-induced activation of the cortex: dependence on 5-HT2A heteroceptors on thalamocortical glutamatergic neurons. J Neurosci 20:8846–8852

Scruggs JL, Schmidt D, Deutch AY (2003) The hallucinogen 1-[2, 5-dimethoxy-4-iodophenyl]-2-aminopropane (DOI) increases cortical extracellular glutamate levels in rats. Neurosci Lett 346:137–140

Seeman P (2002) Atypical antipsychotics: mechanism of action. Can J Psychiatry 47:27–38

Seeman P, Kapur S (2003) Anesthetics inhibit high-affinity states of dopamine D2 and other G-linked receptors. Synapse 50:35–40

Shen RY, Andrade R (1998) 5-Hydroxytryptamine2 receptor facilitates GABAergic neurotransmission in rat hippocampus. J Pharmacol Exp Ther 285:805–812

Silbersweig DA, Stern E, Frith C, Cahill C, Holmes A, Grootoonk S, Seaward J, McKenna P, Chua SE, Schnorr L (1995) A functional neuroanatomy of hallucinations in schizophrenia. Nature 378:176–179

Sorensen SM, Kehne JH, Fadayel GM, Humphreys TM, Ketteler HJ, Sullivan CK, Taylor VL, Schmidt CJ (1993) Characterization of the 5-HT2 receptor antagonist MDL 100907 as a putative atypical antipsychotic: behavioral, electrophysiological and neurochemical studies. J Pharmacol Exp Ther 266:684–691

Soyka M, Koch W, Möller H, Rüther T, Tatsch K (2005) Hypermetabolic pattern in frontal cortex and other brain regions in unmedicated schizophrenia patients. Eur Arch Psychiatry Clin Neurosci 255:308–312

Tandon R, Fleischhacker W (2005) Comparative efficacy of antipsychotics in the treatment of schizophrenia: a critical assessment. Schizophr Res 79:145–155

Varty GB, Bakshi VP, Geyer MA (1999) M100907, a serotonin 5-HT2A receptor antagonist and putative antipsychotic, blocks dizocilpine-induced prepulse inhibition deficits in Sprague–Dawley and Wistar rats. Neuropsychopharmacology 20:311–321

Volkow ND, Brodie JD, Wolf AP, Angrist B, Russell J, Cancro R (1986) Brain metabolism in patients with schizophrenia before and after acute neuroleptic administration. J Neurol Neurosurg Psychiatry 49:1199–1202

Wadenberg M-L (1992) Antagonism by 8-OH-DPAT, but not ritanserin, of catalepsy induced by SCH 23390 in the rat. J Neural Transm 89:49–59

Weissman AD, Dam M, London ED (1987) Alterations in local cerebral glucose utilization induced by phencyclidine. Brain Res 435:29–40

Whitcher B, Schwarz AJ, Barjat H, Smart SC, Grundy RI, James MF (2005) Wavelet-based cluster analysis: data-driven grouping of voxel time courses with application to perfusion-weighted and pharmacological MRI of the rat brain. Neuroimage 24:281–295

Winstanley CA, Chudasama Y, Dalley JW, Theobald DEH, Glennon JC, Robbins TW (2003) Intra-prefrontal 8-OH-DPAT and M100907 improve visuospatial attention and decrease impulsivity on the five-choice serial reaction time task in rats. Psychopharmacology 167:304–314

Winter JC, Eckler JR, Rabin RA (2004) Serotonergic/glutamatergic interactions: the effects of mGlu2/3 receptor ligands in rats

trained with LSD and PCP as discriminative stimuli. Psychopharmacology (Berl) 172:233–240

Wolf ME, Xue CJ (1999) Amphetamine-induced glutamate efflux in the rat ventral tegmental area is prevented by MK-801, SCH 23390, and ibotenic acid lesions of the prefrontal cortex. J Neurochem 73:1529–1538

Wood MD, Reavill C, Trail B, Wilson A, Stean T, Kennett GA, Lightowler S, Blackburn TP, Thomas D, Gager TL, Riley G, Holland V, Bromidge SM, Forbes IT, Middlemiss DN (2001) SB-243213; a selective 5-HT2C receptor inverse agonist with improved anxiolytic profile: lack of tolerance and withdrawal anxiety. Neuropharmacology 41:186–199

Worsley KJ, Evans AC, Marrett S, Neelin P (1992) A three-dimensional statistical analysis for CBF activation studies in human brain. J Cereb Blood Flow Metab 12:900–918

Zaharchuk G, Mandeville JB, Bogdanov AA Jr, Weissleder R, Rosen BR, Marota JJ (1999) Cerebrovascular dynamics of autoregulation and hypoperfusion. An MRI study of CBF and changes in total and microvascular cerebral blood volume during hemorrhagic hypotension. Stroke 30:2197–2204

Zahrt J, Taylor JR, Mathew RG, Arnsten AF (1997) Supranormal stimulation of D1 dopamine receptors in the rodent prefrontal cortex impairs spatial working memory performance. J Neurosci 17:8528–8535

Zaniewska M, McCreary AC, Przegalinski E, Filip M (2007) Effects of the serotonin 5-HT2A and 5-HT2C receptor ligands on the discriminative stimulus effects of nicotine in rats. Eur J Pharmacol 571:156–165

Zhai Y, George CA, Zhai J, Nisenbaum ES, Johnson MP, Nisenbaum LK (2002) Group II metabotropic glutamate receptor modulation of DOI-induced c-fos mRNA and excitatory responses in the cerebral cortex. Neuropsychopharmacology 28:45–52

All in vivo studies were conducted in accordance with the Italian laws (DL 116, 1992 Ministero della Sanità, Roma). Animal research protocols were also reviewed and consented to by the GSK animal care committee, in accordance with the guidelines of the Principles of Laboratory Animal Care (NIH publication 86-23, revised 1985).

Appendix 5

Appendix 5

The following manuscript is under review by Neuropsychopharamcology

NEUROIMAGING EVIDENCE OF ALTERED FRONTO-CORTICAL AND STRIATAL FUNCTION AFTER PROLONGED COCAINE SELF-ADMINISTRATION IN THE RAT

Alessandro Gozzi[1], Lisa Dacome[2], Michela Tessari[2], Federica Agosta[2], Stefano Lepore[2], Anna Lanzoni[2], Patrizia Cristofori[3], Emilio Merlo Pich, Mauro Corsi[2], Angelo Bifone[1]

[1] Istituto Italiano di Tecnologia, Center for Nanotechnology Innovation @NEST

Piazza San Silvestro 12, 56127, Pisa, Italy

[2] GlaxoSmithKline Medicines Research Centre, Via Fleming 4, Verona, Italy

[3]GlaxoSmithKline Pathology Department , SA Ware, Hertford, UK

Abstract

Cocaine addiction is often modeled in experimental paradigms where rodents learn to self-administer the drug. However, the extent to which these models replicate the functional alterations observed in clinical neuroimaging studies of cocaine addiction remains unknown.

We used Magnetic Resonance Imaging (MRI) to assess basal and evoked brain function in rats subjected to a prolonged, extended-access cocaine self-administration scheme. Specifically, we measured basal cerebral blood volume (bCBV), an established correlate of basal metabolism, and assessed the reactivity of the dopaminergic system by mapping the pharmacological MRI (phMRI) response evoked by the dopamine-releaser amphetamine.

Cocaine-exposed subjects exhibited reduced bCBV in fronto-cortical areas, nucleus accumbens, ventral hippocampus and thalamus. The cocaine group also showed an attenuated functional response to amphetamine in ventro-striatal areas, an effect that was significantly correlated with total cocaine intake. An inverse relationship between bCBV in the reticular thalamus and the frontal response elicited by amphetamine was found in control subjects but not in the cocaine group, suggesting that the inhibitory interplay within this attentional circuit may be compromised by the drug. Importantly, histopathological analysis did not reveal significant alterations of the microvascular bed in the brain of cocaine-exposed subjects, suggesting that the imaging findings cannot be merely ascribed to cocaine-induced vascular damage.

These results document that chronic, extended-access cocaine SA in the rat produces neuroimaging alterations that closely mimic hallmark imaging findings in human cocaine addicts. The functional alterations observed serve as plausible neuro-biological substrate for the behavioral expression of compulsive drug-intake in laboratory animals.

Introduction

Chronic cocaine use produces long-lasting neurobiological changes that are thought to underlie the loss of control over drug intake that defines cocaine dependence (*1*). Human neuroimaging studies have started to shed light on the nature of these changes and their relationship with specific behaviors or symptoms. Reduced fronto-striatal perfusion and metabolism in abstinent cocaine abusers have been reported by multiple investigators (*2-4*). The disrupted function of frontal regions has been linked to the persistent neuropsychological deficits and impaired control over drug taking that frequently triggers relapse (*2, 5*). Positron emission tomography (PET) studies with selective D_2 dopamine (DA) ligands have demonstrated that subjects with cocaine addiction show persistent reduction in D_2 DA receptor availability (*6, 7*) and decreased dopaminergic responsivity in the ventral striatum and other components of the "reward circuit" (*8*), consistent with a decreased sensitivity to natural reinforcers observed in these subjects (*9*). Recent research suggests that altered functional connectivity of catecholamine circuits may underlie the impaired inhibition of cortical function observed in

cocaine abusers, a finding that portrays novel pathways for the neuroadptational processes associated to addictive states (*10, 11*).

Cocaine abuse is often modelled pre-clinically in experimental paradigms where rats are trained to self-administer (SA) the drug. By employing different SA patterns, experimenters have been able to reproduce several hallmark features of drug addiction, including compulsive drug seeking (*12*), uncontrolled drug use (*13*) and increased motivation to self-administer the drug (*14*). These features make these models an experimental tool of excellent face-validity to investigate the neuroplastic events associated to voluntary drug-intake (*15*). However, specific clinical correlates of cocaine addiction, such as the blunted DA responsivity of striatal areas observed in PET studies (*6, 7*), do not appear to be adequately modelled by traditional short-term, limited-access cocaine SA paradigms, where instead "sensitised" (i.e. increased) dopaminergic responses are typically observed (*16*). Moreover, the extent to which these models replicate the multiple neuro-functional alterations observed in human neuroimaging studies remains unknown.

In the present study, we used Magnetic Resonance Imaging (MRI) to map basal and evoked brain function in a rat model of cocaine SA. A prolonged (52 days), extended-access (12 hours) SA protocol was employed to model the characteristics of high-dose, chronic cocaine abuse in humans (*17, 18*). Repeated abstinence periods were introduced to minimize the acute toxic effects of the drug and to ensure sustained motivation to self-administer high doses of cocaine (*15*). After a 10-day detoxification period, we measured microvascular basal cerebral blood volume (bCBV), an indirect indicator of resting brain function (*19, 20*), and assessed the reactivity of dopaminergic system by mapping the functional response elicited by the DA-releaser amphetamine using a CBV-based pharmacological MRI (phMRI) protocol (*21, 22*). Correlation analysis between resting (bCBV) and amphetamine-evoked (rCBV) responses were performed in an attempt to identify disregulation in circuits that control the recruitment and functional responsiveness of specific brain areas. Finally, *post mortem* histo-pathological examinations were carried out to assess the potential contribution of direct vascular and neurotoxic effects of prolonged cocaine SA to the imaging findings.

Methods

Experiments were carried out in accordance with Italian regulations governing animal welfare and protection. Protocols were also reviewed and consented to by a local animal care committee, in accordance with the guidelines of the Principles of Laboratory Animal Care (NIH publication 86-23, revised 1985).

Cocaine self administration

Rats that underwent cocaine SA were tested in operant chambers as previously described (*23*). Each experimental chamber (Med Associates Inc., St. Albans, VT) was fitted with a cue light placed above each lever, and with a 2900-Hz tone module. An infusion pump was connected via an external catheter to a single-channel liquid swivel (Instech Laboratories Inc., Plymouth Meeting, PA). Data acquisition and operant-schedule parameters were controlled by a Med-PC software (Med Associates Inc.).

Cocaine SA procedure

Thirty male Lister-Hooded rats (Charles-River, UK) weighing 275-300 g were individually housed in a temperature and humidity controlled room with water available *ad libitum*. Animals were food-restricted throughout the experiment to maintain a constant body weight of 300 g (± 10 g).

After their arrival, rats were acclimatized for one week and subsequently implanted with a catheter in the jugular vein as previously described (*23*). After a 7-day recovery period, rats were transported to the operant chamber. Cocaine self-administration procedure was initiated under a fixed ratio (FR) 1 schedule of reinforcement. Each press on the active lever was associated with a 0.1 ml infusion of a cocaine hydrochloride solution (300 µg/kg) plus the simultaneous illumination of the stimulus (cue) light and extinction of the chamber light for 20 s. Presses on the "inactive" lever had no programmed consequences. Each drug infusion ("reward delivery") was followed by a 20-s lever retraction. The first three "training" sessions were terminated after either 50 infusions or 2 h from the start of the session. In the subsequent 30 sessions the cocaine access time was extended to 12 hours (6.00 p.m. – 6 a.m.), the unit dose reduced to 0.150 µg/kg/infusion, and FR gradually increased to 3 (sessions 4-6) and eventually to 5 (remaining 27 sessions).

Appendix 5

Subjects that lost catheter patency or appeared unhealthy (i.e. showed signs of infection) were removed from the study (eleven subjects altogether). Repeated 48-72 hrs abstinence periods were introduced on days 16 (session 14, 72 hrs), 23 (session 18, 72 hrs), 31 (session 23, 48 hrs) to minimize the risk of acute cocaine-induced intoxication. Session 30 was followed by a longer (5 days) binge abstinence followed by two additional sessions. Such intervals were introduced due to the necessity to harmonise the timing of MRI scan and self-administration protocol over the

relatively large number of subjects employed. A 10-day detoxification period within the home cage was introduced prior to the imaging experiment.

Vehicle SA procedure

A group of fourteen rats was used as baseline reference group. The subjects were implanted with a jugular catheter and subjected to the same training and SA procedures (including number, duration of SA sessions and abstinence) as described above, except for the use of vehicle (saline, 0.1 ml) instead of cocaine during operant sessions.

Magnetic resonance Imaging

Animal preparation

Imaging studies were performed 10 days after the last SA session. Animal preparation and MRI acquisition parameters have been previously described in greater detail (*21, 22*). Briefly, rats were anaesthetized with 3% halothane, tracheotomised and artificially ventilated with a mechanical respirator. A femoral artery and vein were cannulated and the animals were paralyzed with D-Tubocurarine. After surgery halothane level was set to 0.8%. Arterial blood gases (p_aCO_2 and p_aO_2) were measured prior to and after the fMRI timeseries (Supplementary Table I). No statistically significant difference in mean pre- or post-acquisition p_aCO_2 values between groups was found ($p>0.1$, all groups; one-way ANOVA). The body temperature of all subjects was maintained within physiological range and mean arterial blood pressure (MABP) was monitored continually through the femoral artery.

MR Image acquisition

Anatomical and fMRI timeseries were acquired on a Bruker Avance 4.7 Tesla system. A T_2-weighted anatomical volume was acquired using the RARE sequence (TR= 5461ms, TE_{eff} = 72 ms, RARE factor 8, FOV 40mm, 256x256 matrix, 20 contiguous 1mm slices) followed by a time series acquisition (TR_{eff} = 2700 ms, TE_{eff} = 111 ms, RARE factor 32, dt=27) with same spatial coverage. Total MRI time-series acquisition time was 58-min (128 repetitions) for both groups.

Following five reference images, 2.67ml/kg of the contrast agent Endorem (Guerbet, France) was injected to make the fMRI signal changes sensitive to cerebral blood volume (rCBV) (*24, 25*). D-amphetamine (0.5 mg/kg) was administered intravenously 25 min after contrast agent injection, and MRI data were acquired over a period of 25 min following the challenge. The dose of d-amphetamine was chosen based on previous *in vivo* studies (*22, 26*). The dose ensures robust brain activation, does not produce "ceiling" rCBV responses (*27*) and elicits transient MABP responses that are homeostatically compensated under halothane anaesthesia (*28, 29*)

Data analysis

Basal CBV (bCBV)

bCBV time series image data for each experiment were analyzed within the framework of the general linear model (*30*). Individual subjects were spatially normalized to a stereotaxic rat brain MRI template set (*31*). Signal intensity changes were converted into basal cerebral blood volume (bCBV(*t*)) on a pixel-wise basis as previously described (*24, 32*). bCBV time series were calculated over a 4.5 minute time-window starting 6.8 min after contrast agent injection. Mean bCBV volumes for individual subjects were created by averaging the 10 time-points time-wise. Linear detrending was introduced to account for contrast agent washout (*25*). Voxel-wise group statistics was carried out using FSL (*33*) using multi-level Bayesian inference, with 0.7 mm spatial smoothing, a Z threshold > than 1.6 and a corrected cluster significance threshold of p=0.01.

phMRI response to D-amphetamine

MRI signal intensity changes were converted into fractional CBV (rCBV) as previously described (*24*). rCBV time series for amphetamine challenge were calculated covering 12.5 minute pre-challenge and 24 minutes post-challenge window. Voxel-wise statistics was carried out using FEAT with 0.7 mm spatial smoothing and using a model function (Supplementary Figure 1) capturing the temporal profile of amphetamine-induced rCBV response (*34*). Higher-level group comparisons were carried out with multi-level Bayesian inference and thresholded at Z>1.6 with a corrected cluster significance threshold of p=0.01. In order to specifically test the hypothesis of an altered striatal reactivity to D-amphetamine in cocaine rats, a 3D binary mask of the striatum was generated using a digital reconstruction of the rat brain atlas (*31*) and

used to pre-threshold rCBV time series prior to higher-level FSL analysis. The same analysis was repeated on non-masked rCBV datasets.

Volume of interest (VOI) mean bCBV values and time courses for the amphetamine challenge were extracted as previously described (*31, 35*). Statistical differences in mean bCBV were assessed using a one-way ANOVA test followed by Fisher's test for multiple comparisons.

Correlation analysis

Maps of correlated bCBV and D-amphetamine induced rCBV responses across subjects were calculated within the GLM framework at the group level with reference to bCBV in representative regions using FSL (*36, 37*). A number of representative VOIs were selected based on the results of the inter-group bCBV maps (medial prefrontal, insular, orbitofrontal, somatosensory cortex, caudate putamen, nucleus accumbens, reticular thalamus, posteroventral thalamus). For each VOI, the design matrix comprised a regressor capturing the group mean bCBV signal in the anatomical structure and another containing the zero-meaned bCBV vector across the N subjects in the group from the selected reference structure. Z statistic images were calculated via contrasts capturing positive and negative correlations with the reference response, and were thresholded with $Z>1.6$ and a corrected cluster significance threshold of $p=0.01$. Linear regression plots of correlated bCBV and rCBV responses were calculated by plotting bCBV and mean rCBV response to amphetamine across individual subjects, the latter being expressed as mean response over a 20 minute (4-24 min post injection) time-window.

Histopathology

Histopathological evaluation was performed on 10 cocaine subject and 8 randomly- chosen controls as previously described (*38*). After the MRI experiment, rats were maintained under deep anaesthesia (halothane 5%), and a 15 min aortic perfusion of fixative media (10% buffered formalin) was performed, preceded by a 5 minutes infusion of saline. Perfused brains were removed and stored in fixative solution for further 24-72 hours. Brain trimming was then performed using a brain matrix (ASI-Instruments®) designed for rats weighing 200-400 g. Tissue samples were paraffin-embedded, sectioned into 5 µm-thin slices, and stained with a combination of Haematoxylin-eosin and Luxol Fast Blue (*39*). The slice and brain regions analysed where the cingulate and prefrontal cortex, caudate putamen, corpus callosum, hippocampus (C2), cerebellum (purkinje cells) and substantia nigra. The examination was performed by two study-blind veterinary pathologists.

Appendix 5

Results

Cocaine Self-Administration

All the subjects completed the 33 cocaine SA sessions successfully over a time period of 52 days. The SA schedule used ensured a prolonged and sustained intake of cocaine throughout the study (Figure 1). The average cumulative intake of SA cocaine per subject was 1138.4 ±33.3 mg/rat. Both active level presses and cocaine intake appeared to be rather stable throughout the course of the experiment, although linear regression highlighted a weak but significant ($p<0.03$, $F=4.62$) trend towards an overall increased cocaine intake over time when all homogeneous sessions were compared (sessions 4-31, FR 3-5, binge abstinence intervals 48-72 hrs) (Supplementary Figure 2).

Cocaine SA rats show reduced frontal bCBV

In order to investigate the effect of chronic cocaine administration on basal brain function, we measured bCBV in cocaine SA and control subjects and mapped the regions exhibiting statistically significant differences between groups. Cocaine SA rats showed significantly reduced bCBV in several brain areas compared to control rats (Figure 2 and 3). The effect was prominent in the medial-prefrontal, cingulate, orbitofrontal cortex, septum, ventral hippocampus, in the core region of the nucleus accumbens as well as raphe nuclei and reticular thalamic areas. No difference in total CBV between groups was observed ($p=0.23$, student's t test).

Cocaine SA rats show reduced striatal responsiveness to amphetamine

In order to probe striatal dopaminergic reactivity, cocaine SA and control rats were challenged with the DA releaser amphetamine, and the presence of functional alterations in the magnitude of the rCBV response elicited by the drug was assessed via voxel-wise statistics in sub-cortical areas. Consistent with previous studies (*22*) amphetamine produced robust activation of sub-cortical and cortical areas in both groups of subjects (Figure 4). Cocaine SA rats exhibited an attenuated functional response to amphetamine in the striatum compared to control rats (Figure 5). The magnitude of the striatal response to amphetamine was found to be inversely correlated with cumulative cocaine intake ($p=0.03$, Figure 5). Additional foci of reduced functional response to amphetamine were observed in sensory-motor and orbitofrontal cortex (Supplementary Figure 3). Administration of amphetamine produced transient increases in MABP (Supplementary Figure 4). The effect was not temporally correlated with the functional response, and well within the blood flow autoregulatory range within which vasopressive responses are homeostatically compensated without producing significant rCBV alterations (*28, 29*).

Cocaine SA rats revealed altered thalamo—frontal activity

In an attempt to establish a correlation between basal and evoked functional activity and to investigate dysregulations in the control of these two states, we measured the correlation between bCBV and amphetamine-induced response in control and cocaine SA animals. No correlation between bCBV and amphetamine-induced rCBV responses was found in either group in any of the regions examined, with exception of the reticular and posterior-ventral thalamus which revealed, in control subjects, an inverse relationship with amphetamine-induced rCBV in fronto-cortical areas (Supplementary Figure 5). This correlation appeared to be disrupted in the cocaine SA group (Figure 6).

Cocaine SA brains do not present microvascular alterations

A histopathological evaluation of brain white and grey matter, glial and interstitial compartments, as well as macro- and micro-vascular, ependymal and meningeal structures did not highlight any neurocellular, interstitial or microvascular lesions in either group. Specifically, no signs of cellular pyknosis or atrophy, fiber alteration, necrosis, interstitial oedema, were observed in any of the brain regions examined., nor alterations of the microvascular and capillary bed (i.e., basal membrane dilation or rupture, hemorrage, endothelial thickening or wall fibrosis, thrombi or occlusions, necrosis or vacuolation of endothelial cells).

Appendix 5

Discussion

The present study documents that chronic, extended-access cocaine SA in the rat produces neuroimaging alterations that closely mimic hallmark imaging findings in human cocaine addicts. Specifically, we observed significantly reduced bCBV, a marker of resting brain function, in regions that play a key contribution in higher cognitive functions and inhibitory control (fronto-cortical areas), craving and anticipation (fronto-hippocampal areas) and reward (mesolimbic areas). Moreover, cocaine SA was associated with reduced striatal reactivity to dopaminergic stimulation, and the presence of putative functional alterations in the inhibitory interplay between reticular thalamus and the activation of fronto-cortical areas. Our results provide neuroimaging evidence of multiple alterations in rat brain function following chronic and voluntary cocaine-intake that serve as plausible neuro-biological substrate for the behavioural expression of compulsive drug-intake in laboratory animals.

Chronic cocaine abuse is often modelled in behavioural paradigms where rodents are trained to voluntarily self-administer the drug. Several experimental parameters are known to exert a significant influence on the pattern of drug intake, thus allowing a better reproduction of key clinical features of cocaine addiction (*reviewed in 15*). Here we implemented a prolonged, extended-access cocaine SA protocol with repeated binge-abstinence periods (*40-42*) to mimic the characteristics of high-dose, chronic cocaine abuse in humans. Prolonged SA is instrumental in inducing behavioural patterns of drug intake that mimic key clinical features of cocaine-addiction such as compulsive drug-use despite the presence of environmental adversities (*12*), and high propensity to relapse to drug seeking (*43*). The chronic nature of the protocol employed (covering ≈ 10% of the average adult life-span of a rat) (*44*) permits to mimic patient populations with a significant history (> 6 months) of cocaine addiction like those typically enrolled in human neuroimaging studies, thus maximising the translational relevance of our findings.

Moreover, the use of an extended-access to cocaine (i.e. ≥ 6 hours) allows to model specific neuro-behavioural features of addiction, such as persistent alterations in cognitive functions (*18*), increased motivation for cocaine (*14*), and escalation in drug intake (*13*). Repeated periods of forced abstinence were introduced to reduce the acute toxic effects of the drug and to ensure sustained motivation to self-administer high doses of cocaine (*15*). Although the total cocaine intake achieved with the present protocol is higher than that observed with short-access paradigms, the values attained are sufficiently distant from the limit of acute toxicity (*45, 46*), which explains the lack of lethality observed in this study.

Compared to unlimited access protocols, where drug intake exhibits high and low numbers of infusions on alternating days (*41*), the extended-access protocol used here ensured sustained SA of high doses of cocaine. In contrast to what reported by other groups (*13, 46, 47*), we did not observe unequivocal evidence of dose escalation (either in the first hour or over the whole session), although a trend towards an increased cocaine intake was apparent after linear regression analysis of mean cocaine intake over consecutive sessions (Supplementary Figure 3). Several experimental parameters may account for this discrepancy, especially differences in ceiling of cocaine intake across different rat strains (*discussed in 48, and 49*).

A ten-day washout period was introduced prior to the imaging study to rule out acute carry-over effects of the drug and minimise the potential interference of acute abstinence symptoms on measures of brain function. Most of the neurochemical and behavioural alterations that can be related to acute withdrawal have an almost immediate onset, peak between 6 and 72 h after termination of drug access and generally cease within 2–7 days from the last cocaine session. (*50-54*). It is therefore unlikely that the imaging findings contain major contributions from transient neuro-biological phenomena related to acute cocaine abstinence.

MRI measures of bCBV allow high resolution mapping of resting brain function that tightly correlate with regional energy metabolism and cerebral blood flow (*19, 55, 56*). Our data showed the presence of reduced bCBV in the cingulated gyrus, pre-frontal and orbito-frontal cortex, thalamus and hippocampus of cocaine SA subjects. These results are in excellent agreement with clinical neuroimaging research of cocaine addiction, where reduced frontal and striatal perfusion have been consistently observed (*2-4, 57, 58*), a feature that is found to correlate with the cognitive impairments, compulsion and loss of inhibitory control over drug taking which may lead to relapse (*2, 5, 59*). Importantly, cognitive deficits have been observed in rats allowed extended (but not limited) access to cocaine (*18*), a phenomenon that involved working memory and sustained attention tasks (two prefrontal-cortex-dependent tasks) as well as object recognition measures (a hippocampus dependent task). The involvement of hippocampal systems is also consistent with the role played by this brain structure in contextual conditioning and memory, two functions that are altered by cocaine use and are believed to play a role in cue-elicited craving (*reviewed in 60*). Likewise, the reduced bCBV in ventral striatum and nucleus accumbens was not unexpected, given the established interconnection between fronto-cortical activity and ventro-striatal DA cell firing and release (*59*). In keeping with this, recent PET imaging studies showed lower levels of endogenous DA in cocaine addicts relative to comparison subjects (*61*) and primate research revealed reduced glucose utilisation in the striatal areas upon chronic cocaine use, a feature that increased cocaine exposure (*62*). The observation of focal bCBV reductions in the reticular thalamic and raphe nuclei discloses a plausible contribution of focal sub-cortical networks to the long-lasting neuro-adaptations produced chronic cocaine addiction. The thalamic effect correlates well with human neuroimaging studies showing altered GABAergic neurotransmission in the thalamus of abstinent cocaine abusers (*63*) and recent electrophysiological evidence of a state of protracted over-inhibition of reticular thalamic areas following binge

administration of cocaine (*64*). Interestingly, as serotonin is known to exert a direct excitatory action on GABAergic neurons in the thalamic reticular nucleus (*65*), the reduced activity of this nucleus and that observed in regions of the raphe may be functionally interrelated and part of a single defective circuit.

In attempt to identify a fMRI correlate of the decreased striatal dopaminergic responsivity observed in human PET studies (*6, 7, 66*), we also mapped the functional response elicited by the DA-releaser amphetamine using a phMRI protocol (*22, 67*). Several phMRI studies have provided compelling evidence that the striatal haemodynamic response produced by amphetamine reflect primarily dopaminergic effects (*reviewed in 68*). For example, amphetamine has been shown to elicit BOLD or rCBV increases in DA-rich ventro-striatal areas that are linearly-correlated to synaptic DA concentrations (*37, 69-72*). Morevoer, amphetamine-induced rCBV responses are abolished in the DA denervated areas (*73, 74*), an effect that can be later restored after fetal or stem cell transplantation (*73, 75*). Thus, the sum of these data indicates that amphetamine-induced rCBV responses can be reliably used as a marker of striatal DA neurotransmission. Within this framework, the presence of an attenuated striatal rCBV response to amphetamine in the cocaine SA group points towards a reduced-responsivity of ventro-striatal dopaminergic function analogous to what observed in PET studies in humans (*16*). This finding provides for the first time a plausible preclinical neuroimaging correlate of one of the most replicated clinical manifestation of cocaine addiction, which is believed to play a key contribution to the anhedonia and amotivation reported by drug-addicted subjects during protracted withdrawal (*8*). This result documents a potentially important correspondence between clinical and preclinical neuro-adaptational changes induced by cocaine on DA systems, an aspect that does not appear to be adequately modelled by traditional cocaine exposure paradigms, where “sensitised” (i.e. increased) dopaminergic responses are typically observed (*reviewed by 16*). As similarly attenuated striatal responses were not observed in rodent neuroimaging studies using short-term (5-days) drug administration protocols (*76, 77, Gozzi A. unpublished results*), our data suggest that, for this characteristic to be modelled in rodents, prolonged and extended access to high doses of cocaine may be required.

Correlation analysis between resting and amphetamine-evoked (rCBV) responses revealed an inverse relationship between bCBV in reticular thalamic areas and amphetamine-induced frontal activation in control subjects, but not in cocaine group. The presence of an inverse relationship between tonic reticular thalamic activity and evoked frontal function is consistent with the functional connectivity of these regions (*78*). The reticular thalamic nucleus is extremely rich in GABAergic neurons (*78*), and its inhibition can enhance fronto-cortical dopaminergic neurotransmission (*79*). As prefrontal projections to the thalamic reticular nucleus have been suggested to play a unique circuit for attentional mechanisms (*80*) the loss of correlation between basal and evoked function in cocaine SA subjects may be indicative of an altered inhibitory interplay between these structures which may underlie some of the attentional deficits observed in rats allowed extended access to cocaine (*18*). A role for thalamo-frontal dysfunctions in cocaine addiction is supported by recent neuroimaging studies showing altered thalamo-cortical connectivity in cocaine abusers under resting conditions (*11*) and when performing a cognitive task (*81*). However, as correlation measurements do not reflect causal association, further research is warranted to elucidate the exact nature of this finding. Importantly, no appreciable microscopic lesions in the vascular, neurocellular and interstitial compartments of cocaine SA brains were observed. This result is important, as it permits to rule out a potential contribution of abnormal cerebrovascular processes on the haemodynamic measures of brain function performed (i.e. bCBV and rCBV).

In summary, we provide evidence of altered brain function in rats that underwent prolonged and extended access cocaine self-administration. Consistent with clinical neuroimaging findings, cocaine-exposed animals revealed reduced basal brain function in fronto-cortical and thalamic areas, and attenuated responsivity in striatal regions upon challenge with the DA releaser amphetamine, an effect that was significantly correlated with the total cocaine intake. The consistency of these findings with neuroimaging measures in cocaine-addicted patients supports the use of prolonged and extended-access SA paradigms in the rat to investigate the neuroadaptations underlying cocaine-addiction.

Disclosure / Conflict of interest

All the authors are employees of GlaxoSmithKline. The authors declare that, except for income received from their primary employer, no financial support or compensation has been received from any individual or corporate entity over the past three years for research or professional service and there are no personal financial holdings that could be perceived as constituting a potential conflict of interest.

Acknowledgments

The authors would like to thank Valerio Crestan and Giuliano Turrini for their excellent technical support to the phMRI measures, and Pamela Rodegher from Histolab Verona, Italy for the histological preparations.

Appendix 5

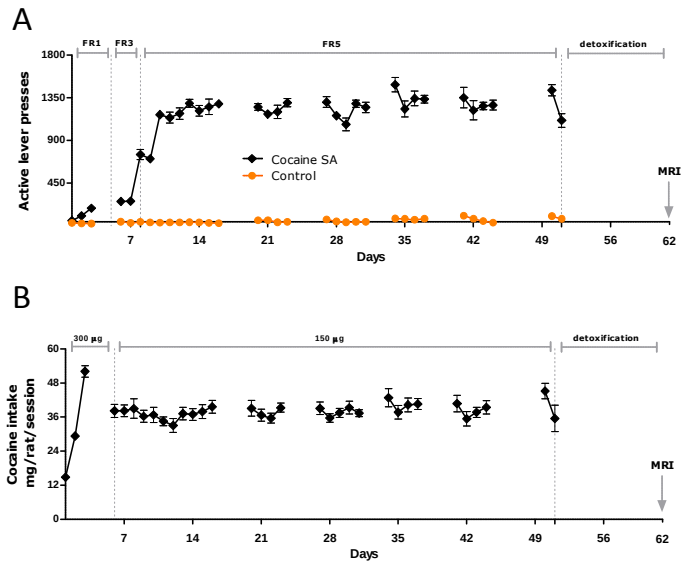

Figure 1

A: Number of active lever presses recorded in the cocaine SA group (N=19) and control (saline SA, N=14) within the 12 h SA sessions. FR: fixed-ratio; **B**; Average cocaine intake (mg/rat/session) over the course of the experiment. The dose of cocaine administered per single injection is reported on the top line (150 µg, session 1-3, 300 µg all remaining sessions)

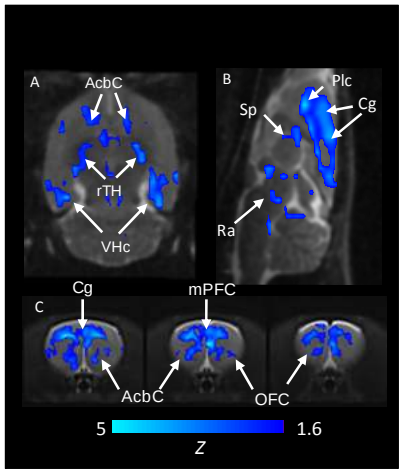

Figure 2

Anatomical distribution of the regions exhibiting significantly lower bCBV in rats chronically self-administering cocaine (cocaine SA; N=20) vs. control subjects (vehicle SA; N=14; Z> 1.6, cluster correction p=.001) in representative horizontal (A), saggital (B), and coronal slices (C). [mPFC: medial pre-frontal cortex; Plc: pre-limbic cortex; Cg: cingulate cortex; Sp; septum; AcbC: core of the nucleus accumbens; Ra: raphe nucleus: rTh; reticular thalamic nucleus; VHc; ventral hippocampus; OFC: orbito-frontal cortex]

Appendix 5

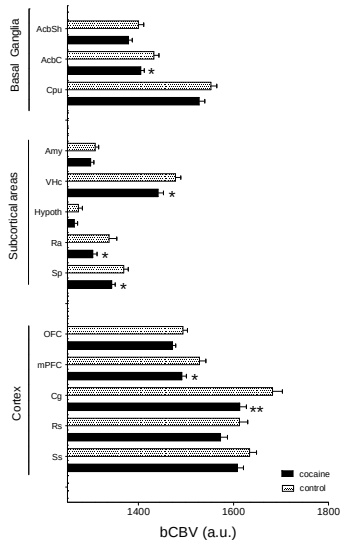

Figure 3

Mean bCBV in representative 3D anatomical volumes (*VOIs, 31*) for cocaine SA (N=20) and control subjects (saline SA; N=14). [Amy: amygdala, mPFC: medial pre-frontal cortex; Cg: cingulate cortex; Sp; septum; AcbC: core of the nucleus accumbens; AcbSh: shell of the nucleus accumbens; Cpu; caudate putamen; Ra: raphe nucleus: rTh; reticular thalamic nucleus; VHc; ventral hippocampus; Hypoth: hypothalamus; OFC: orbito-frontal cortex; Rs: retrosplenial cortex; SS; somatosensory cortex; *p<0.05; **p>0.01; one-way ANOVA, followd by Fisher LSD test]

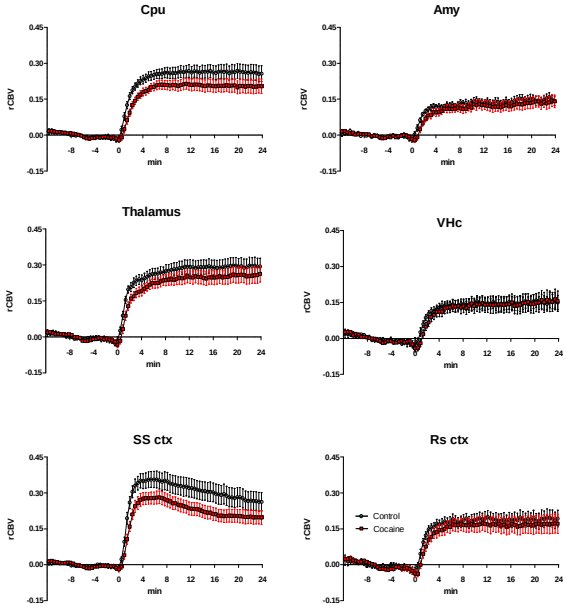

Figure 4

Temporal-profile of amphetamine-induced rCBV changes in representative VOIs of for cocaine SA (N=20) and control subjects (saline SA, N=14). Data are plotted as mean±SEM within each group. [Amy: amygdala; Cpu: caudate putamen; Thal; thalamus; VHc: ventral hippocampus; Rs: retrosplenial cortex; SS; somatosensory cortex]

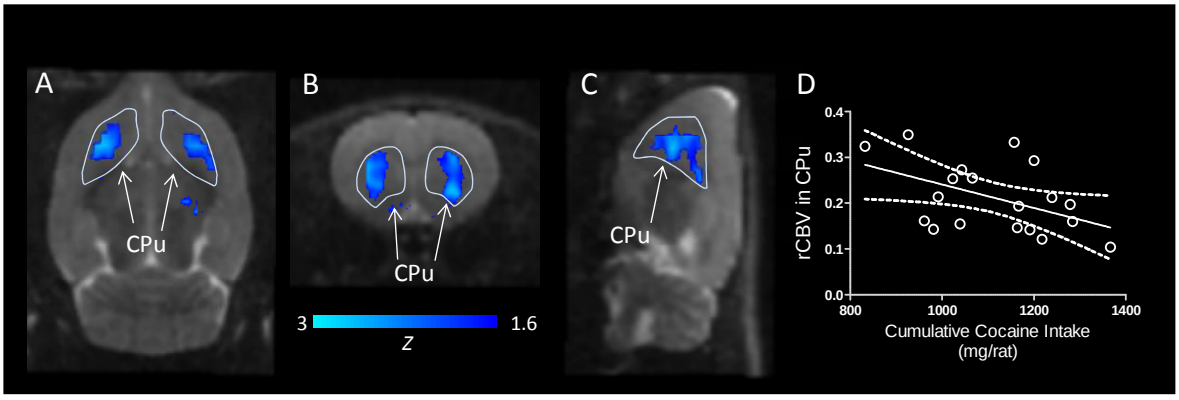

Figure 5

Ortogonal view (**A**: horizontal, **B**: coronal, **C**: saggital) of the subcortical brain regions exhibiting an attenuated rCBV response to D-ampheatmine in rats chronically self-administering cocaine (cocaine SA; N=20) vs. control subjects (vehicle SA; N=14);(Z>1.6; cluster correction p=05). Cpu: caudate putamen. **D**: correlation rCBV response to d-amphetamine in the striatum and cumulative cocaine intake over the 52 days of self-administration (p=0.03, dashed lines represent 95% confidence interval).

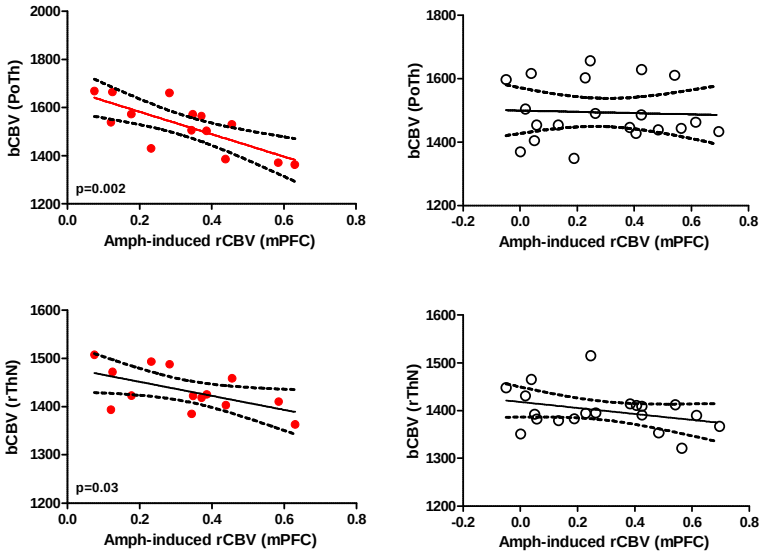

Figure 6

Correlation between bCBV in the postero-ventral thalamus (PoTh; top) and reticular thalamic nucleus (rThN; bottom) and D-amphetamine-induced rCBV response in the medial pre-frontal cortex in control subjects (**A**; saline SA; N=14) and rats chronically self-administering cocaine (**B**; cocaine SA; N=20). Dashed lines represent 95% confidence interval. The cocaine SA group did not exhibit statistically signifcant correlation (P>0.19).

Reference List

1. G. F. Koob, P. P. Sanna, F. E. Bloom, *Neuron* **21**, 467 (1998).
2. T. L. Strickland *et al.*, *J Neuropsychiatry Clin Neurosci* **5**, 419 (1993).
3. E. D. London, K. R. Bonson, M. Ernst, S. Grant, *Crit Rev. Neurobiol.* **13**, 227 (1999).
4. N. D. Volkow *et al.*, *Synapse* **12**, 86 (1992).
5. P. W. Kalivas, *Current Opinion in Pharmacology* **4**, 23 (2004).
6. N. D. Volkow *et al.*, *Synapse* **14**, 169 (1993).
7. D. Martinez *et al.*, *Neuropsychopharmacology* **29**, 1190 (2004).
8. N. D. Volkow *et al.*, *Nature* **386**, 830 (1997).
9. N. D. Volkow, J. S. Fowler, G. J. Wang, J. M. Swanson, F. Telang, *Arch Neurol* **64**, 1575 (2007).
10. D. Tomasi *et al.*, *PLoS ONE* **5**, e10815 (2010).
11. H. Gu *et al.*, *NeuroImage* **In Press, Corrected Proof**, (2010).
12. L. J. M. J. Vanderschuren, B. J. Everitt, *Science* **305**, 1017 (2004).
13. S. H. Ahmed, G. F. Koob, *Science* **282**, 298 (1998).
14. N. E. Paterson, A. Markou, *NeuroReport* **14**, (2003).
15. D. C. S. Roberts, D. Morgan, Y. Liu, *Progress in Neuro-Psychopharmacology and Biological Psychiatry* **31**, 1614 (2007).
16. R. Narendran, D. Martinez, *Synapse* **62**, 851 (2008).
17. F. H. Gawin, E. H. Ellinwood, *New England Journal of Medicine* **318**, 1173 (1988).
18. L. A. Briand *et al.*, *Neuropsychopharmacology* **33**, 2969 (2008).
19. I. Gaisler-Salomon, S. A. Schobel, S. A. Small, S. Rayport, *Schizophr Bull* **35**, 1037 (2009).
20. S. A. Small, M. K. Chawla, M. Buonocore, P. R. Rapp, C. A. Barnes, *Proceedings of the National Academy of Sciences of the United States of America* **101**, 7181 (2004).
21. A. Gozzi, V. Crestan, G. Turrini, M. Clemens, A. Bifone. Antagonism at serotonin 5HT2a receptros modulates functional activity of fonto-hippocampal circuit. Psychopharmacology in press. 2010.

Ref Type: Generic

22. A. Schwarz *et al.*, *Synapse* **54**, 1 (2004).
23. M. Moretti *et al.*, *Mol Pharmacol* **78**, 287 (2010).
24. J. B. Mandeville *et al.*, *Magn Reson Med* **39**, 615 (1998).
25. A. J. Schwarz, T. Reese, A. Gozzi, A. Bifone, *Magn Reson Imaging* **21**, 1191 (2003).
26. A. Gozzi *et al.*, *PLoS ONE* **In press**, (2011).
27. F. Micheli *et al.*, *J Med. Chem.* **50**, 5076 (2007).
28. A. Gozzi *et al.*, *Magnetic Resonance Imaging,* **25**, 826 (2007).
29. G. Zaharchuk *et al.*, *Stroke* **30**, 2197 (1999).
30. K. J. Worsley, A. C. Evans, S. Marrett, P. Neelin, *J Cereb. Blood Flow Metab* **12**, 900 (1992).
31. A. J. Schwarz *et al.*, *NeuroImage* **32**, 538 (2006).
32. Y.-C. I. Chen *et al.*, *J. Magn. Reson. Imaging* **14**, 517 (2001).
33. S. M. Smith *et al.*, *NeuroImage* **23 Suppl 1**, S208 (2004).
34. A. J. Schwarz, B. Whitcher, A. Gozzi, T. Reese, A. Bifone, *J. Neurosci. Methods* **159**, 346 (2006).
35. A. Gozzi *et al.*, *Neuropsychopharmacology* **33**, 1690 (2008).
36. A. J. Schwarz, A. Gozzi, T. Reese, A. Bifone, *Magn Reson. Med.* **57**, 704 (2007).
37. A. J. Schwarz, A. Gozzi, T. Reese, A. Bifone, *NeuroImage* **34**, 1627 (2007).
38. R. Barroso-Moguel, M. Mendez-Armenta, J. Villeda-Hernandez, C. Nava-Ruiz, A. Santamaria, *Progress in Neuro-Psychopharmacology and Biological Psychiatry* **26**, 59 (2002).
39. C. L. Scholtz, *Histochemical Journal* **9**, 759 (1977).
40. L. H. Parsons, G. F. Koob, F. Weiss, *J Pharmacol Exp Ther* **274**, 1182 (1995).
41. J. M. Wilson *et al.*, *Journal of Neuroscience* **14**, 2966 (1994).
42. J. M. Wilson, S. J. Kish, *Journal of Neuroscience* **16**, 3507 (1996).
43. V. Deroche-Gamonet, D. Belin, P. V. Piazza, *Science* **305**, 1014 (2004).

44. P. M. Sharp, M. C. La Regina, *The laboratory rat* (CRC Press, 1998), pp. 1-240.
45. J. R. Mantsch, V. Yuferov, A. M. Mathieu-Kia, A. Ho, M. J. Kreek, *Psychopharmacology* **175**, 26 (2004).
46. S. Wee, S. E. Specio, G. F. Koob, *J Pharmacol Exp Ther* **320**, 1134 (2007).
47. C. R. Ferrario *et al.*, *Biol Psychiatry* **58**, 751 (2005).
48. L. A. Knackstedt, P. W. Kalivas, *J Pharmacol Exp Ther* **322**, 1103 (2007).
49. T. Kippin, R. Fuchs, R. See, *Psychopharmacology* **187**, 60 (2006).
50. M. H. Baumann, R. B. Rothman, *Biological Psychiatry* **44**, 578 (1998).
51. G. Harris, G. Aston-Jones, *Psychopharmacology* **113**, 131 (1993).
52. D. H. Malin *et al.*, *Pharmacology Biochemistry and Behavior* **66**, 323 (2000).
53. N. H. Mutschler, K. A. Miczek, *Psychopharmacology* **136**, 402 (1998).
54. A. Markou, G. F. Koob, *Neuropsychopharmacology* **7**, 213 (1992).
55. F. Hyder *et al.*, *NMR Biomed* **14**, 413 (2001).
56. R. G. Gonzalez *et al.*, *AJNR Am J Neuroradiol* **16**, 1763 (1995).
57. S. S. Tumeh, J. S. Nagel, R. J. English, M. Moore, B. L. Holman, *Radiology* **176**, 821 (1990).
58. N. D. Volkow, N. Mullani, K. L. Gould, S. Adler, K. Krajewski, *The British Journal of Psychiatry* **152**, 641 (1988).
59. P. W. Kalivas, N. Volkow, J. Seamans, *Neuron* **45**, 647 (2005).
60. G. F. Koob, N. D. Volkow, *Neuropsychopharmacology* **35**, 217 (2009).
61. D. Martinez *et al.*, *American Journal of Psychiatry* **166**, 1170 (2009).
62. L. J. Porrino, H. R. Smith, M. A. Nader, T. J. R. Beveridge, *Progress in Neuro-Psychopharmacology and Biological Psychiatry* **31**, 1593 (2007).
63. N. D. Volkow *et al.*, *American Journal of Psychiatry* **155**, 200 (1998).
64. F. J. Urbano, V. n. Bisagno, S. I. Wikinski, O. D. Uchitel, R. R. Llinβs, *Biological Psychiatry* **66**, 769 (2009).
65. D. A. McCormick, Z. Wang, *J Physiol* **442**, 235 (1991).
66. N. D. Volkow *et al.*, *American Journal of Psychiatry* **147**, 719 (1990).
67. A. Bifone, A. Gozzi, in *Current Topics in Behavioral Neurosciences*, J. Hagan, Ed. (Springer, 2010), p. In print.
68. B. Knutson, S. Gibbs, *Psychopharmacology* **191**, 813 (2007).
69. A. L. Dixon *et al.*, *Neuropharmacology* **48**, 236 (2005).
70. J. Ren, H. Xu, J. K. Choi, B. G. Jenkins, Y. I. Chen, *Synapse* **63**, 764 (2009).
71. J. K. Choi, Y. I. Chen, E. Hamel, B. G. Jenkins, *NeuroImage* **30**, 700 (2006).
72. M. A. Preece *et al.*, *Synapse* **61**, 925 (2007).
73. Y.-C. I. Chen *et al.*, *NeuroReport* **10**, 2881 (1999).
74. Y. C. Chen *et al.*, *Magn Reson. Med.* **38**, 389 (1997).
75. L. M. Bjorklund *et al.*, *Proceedings of the National Academy of Sciences of the United States of America* **99**, 2344 (2002).
76. M. Febo *et al.*, *Neuropsychopharmacology* **30**, 936 (2005).
77. T. Reese *et al.*, *Proc. of Twelfth ISMRM Scientific Meeting and Exhibition* 228 (2004).
78. G. Paxinos, *The Rat Nervous System* (Elsevier, London, 2008), pp. 761-1193.
79. M. W. Jones, I. C. Kilpatrick, O. T. Phillipson, *Experimental Brain Research* **69**, 623 (1988).
80. B. Zikopoulos, H. Barbas, *Journal of Neuroscience* **26**, 7348 (2006).
81. D. Tomasi *et al.*, *Psychiatry Research: Neuroimaging* **155**, 189 (2007).

Appendix 6

Neuron
Article

A Neural Switch for Active and Passive Fear

Alessandro Gozzi,[1,6,7] Apar Jain,[2,6] Aldo Giovanelli,[3,4] Cristina Bertollini,[3] Valerio Crestan,[1] Adam J. Schwarz,[1] Theodoros Tsetsenis,[2] Davide Ragozzino,[3,5] Cornelius T. Gross,[2,*] and Angelo Bifone[1,7]
[1]Neurosciences CEDD, GlaxoSmithKline Medicines Research Centre, via Fleming 4, 37135 Verona, Italy
[2]Mouse Biology Unit, EMBL, via Ramarini 32, 00015 Monterotondo, Italy
[3]Pasteur Institute–Fondation Cenci Bolognetti and Department of Human Physiology and Pharmacology, Center of Excellence BEMM, University of Rome–La Sapienza, Piazzale Aldo Moro 5, 00185 Roma, Italy
[4]Department of Experimental Medicine, University of L'Aquila, Via Vetoio Coppito 2, 67100 L'Aquila, Italy
[5]Neuromed, Via Atinese 18, 86077 Pozzilli, Italy
[6]These authors contributed equally to this work
[7]Present address: Center for Nanotechnology Innovation, Italian Institute of Technology, IIT@NEST, Pisa, Italy
*Correspondence: gross@embl.it
DOI 10.1016/j.neuron.2010.07.008

SUMMARY

The central nucleus of the amygdala (CeA) serves as a major output of this structure and plays a critical role in the expression of conditioned fear. By combining cell- and tissue-specific pharmacogenetic inhibition with functional magnetic resonance imaging (fMRI), we identified circuits downstream of CeA that control fear expression in mice. Selective inhibition of a subset of neurons in CeA led to decreased conditioned freezing behavior and increased cortical arousal as visualized by fMRI. Correlation analysis of fMRI signals identified functional connectivity between CeA, cholinergic forebrain nuclei, and activated cortical structures, and cortical arousal was blocked by cholinergic antagonists. Importantly, inhibition of these neurons switched behavioral responses to the fear stimulus from passive to active responses. Our findings identify a neural circuit in CeA that biases fear responses toward either passive or active coping strategies.

INTRODUCTION

Research over the past decades has consistently pointed to the amygdala as a key component of the brain's emotional network. Numerous studies in rodents, primates, and humans have demonstrated the involvement of this structure in mediating the emotional, behavioral, and physiological responses associated with fear and anxiety particularly in response to conditioned aversive cues (Aggleton, 1992; Davis and Whalen, 2001; LeDoux, 2000). The amygdala is a highly heterogeneous cluster of forebrain nuclei that can be subdivided into cortical and striatal divisions (Swanson and Petrovich, 1998). The central nucleus (CeA) is located within the striatal division and serves as a major output of the amygdala for the control of mid- and hind-brain circuits involved in physiological and behavioral defensive responses (Amaral et al., 1992). The CeA can be further subdivided into medial and lateral subnuclei whose neurons express different neuromodulatory receptors (Huber et al., 2005; Tribollet et al., 1988; Veinante and Freund-Mercier, 1997) and appear to differentially project to downstream targets (Jolkkonen et al., 2002). However, it remains unknown how aversive signals are processed within CeA and how this nucleus differentially engages diverse downstream targets to support stimulus-appropriate fear responses.

Using a pharmacogenetic inhibition strategy (Luo et al., 2008) in transgenic mice, we were recently able to show that neural activity in a subset of neurons in CeA is necessary for freezing behavior in response to a conditioned aversive stimulus (Tsetsenis et al., 2007). These neurons, which we called type I cells (Tsetsenis et al., 2007) and which are likely to be similar to type B neurons described in rats (Schiess et al., 1999; Sah et al., 2003; Lopez De Armentia and Sah, 2004), are distinguished from the majority of remaining neurons (called type II, Tsetsenis et al., 2007) by the presence of a prominent depolarizing after-potential. Selective pharmacological suppression of neural activity in type I CeA neurons was achieved by expressing the $G\alpha_i$-coupled serotonin 1A receptor (Htr1a) under the control of a tissue-specific promoter in transgenic mice that are missing the endogenous receptor (the resulting mice are called *Htr1a*^{CeA}). Systemic treatment of *Htr1a*^{CeA} mice with a selective agonist of Htr1a, 8-hydroxy-2-(di-n-propylamino) tetralin (8-OH-DPAT), led to the opening of G protein coupled inward rectifying potassium (GIRK) channels, membrane hyperpolarization, and suppression of neural firing (Tsetsenis et al., 2007). A suppression of conditioned freezing behavior following inhibition of CeA neurons is consistent with the proposed role of CeA as an output circuit that promotes autonomic and behavioral responses to conditioned fear (Wilensky et al., 2006). Here, we combine pharmacogenetic inhibition of neural activity in CeA with functional magnetic resonance imaging (fMRI) to map in vivo neural activity in circuits downstream of CeA that are involved in conditioned fear responding. This approach identified ventral forebrain cholinergic neurons as a critical downstream target of CeA and demonstrated that type I cells within CeA actively suppress cholinergic-mediated cortical arousal and exploratory behavior at the same time as promoting freezing responses and thus serve as a switch between active and passive fear.

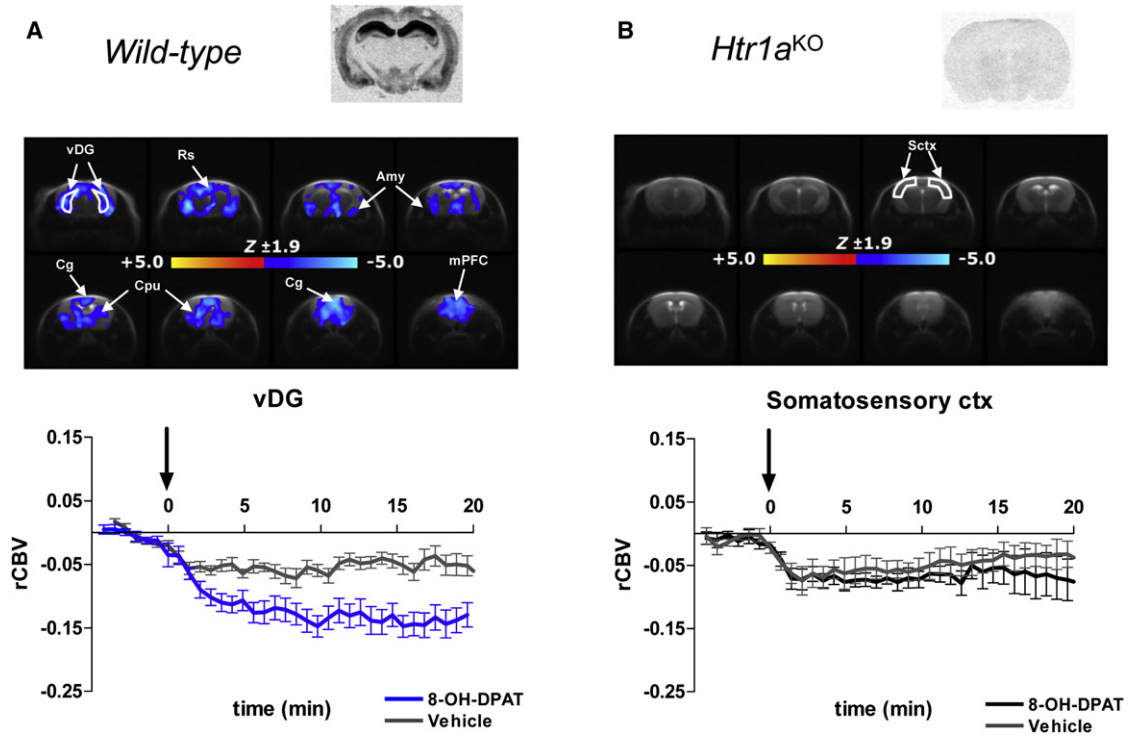

Figure 1. Pharmacological Activation of Htr1a Leads to Widespread Inhibition of Neural Activity in Wild-Type Mice

Anatomical distribution of the rCBV changes produced by administration of the Htr1a agonist, 8-OH-DPAT (0.5 mg/kg i.a.) in (A) wild-type (n = 14) and (B) Htr1a knockout (*Htr1a*^{KO}, n = 8) mice. Blue indicates significantly *reduced* rCBV compared with vehicle baseline (Z > 1.96, cluster correction, p = 0.01). For each mouse line the rCBV time course following vehicle or 8-OH-DPAT injection in a representative brain region is shown below each map (vDG, ventral dentate gyrus; Rs, retrosplenial cortex; Amy, amygdala; Cg, cingulate cortex; Cpu, caudate putamen; mPFC, medial prefrontal cortex; Sctx, somatosensory cortex). A significant decrease in rCBV was observed following 8-OH-DPAT treatment in wild-type, but not *Htr1a*^{KO} mice, demonstrating the feasibility of using rCBV to map Htr1a-dependent inhibition of neural activity. Htr1a receptor distribution (^{125}I-MPPI autoradiography) in a representative brain slice for each strain is shown for reference.

RESULTS

fMRI Mapping of Neural Activity Following Cell-Type-Specific Inhibition

To determine the feasibility of using fMRI to map neural activity changes following cell type-specific neural inhibition using the Htr1a-based system (Tsetsenis et al., 2007), wild-type mice were placed in the MR scanner and fMRI signal changes induced by systemic administration of the Htr1a agonist 8-OH-DPAT (0.5 mg/kg i.a.) were examined. For all studies, we used relative cerebral blood volume (rCBV) as a surrogate for the underlying changes in neural activity (Sheth et al., 2004). This measure has gained acceptance as the measure of choice in small animal fMRI studies where sensitivity is a significant technical challenge (Chen et al., 2001; Jenkins et al., 2003). Consistent with the efficient coupling of Htr1a to inhibitory GIRK channels (Luscher et al., 1997), systemic treatment with 8-OH-DPAT led to a significant and widespread decrease in rCBV in all structures where Htr1a is expressed (Figure 1A), including striatum, amygdala, ventral hippocampus, and prefrontal, cingulate, insular, and rhinal cortices (Z > 1.96, cluster corrected at p = 0.05). The time profile of the effect was similar in all regions examined, with a sustained negative response that lasted throughout the time-window examined (Figure S1). As seen previously (Gozzi et al., 2007; Schwarz et al., 2006), vehicle injection produced a small decrease in rCBV that probably reflected dilution of the blood-pool contrast agent.

Importantly, the agonist-induced decrease in rCBV was absent in Htr1a knockout mice confirming the selectivity of 8-OH-DPAT for Htr1a at this dose in vivo (Figure 1B). As expected, time profiles of rCBV following vehicle or 8-OH-DPAT administration in knockout mice (*Htr1a*^{KO}) showed substantial overlap in all regions examined (Figure S1). Similarly, image-based analysis did not highlight significant agonist-induced activation or deactivation (Z > 1.96, cluster correction p = 0.05). These data indicate that neural inhibition associated with activation of Htr1a can be mapped in vivo using pharmacological fMRI.

Suppression of Type I CeA Neurons Leads to Widespread Cortical Activation

Next, we examined rCBV changes following agonist-induced inhibition of type I neurons in CeA using *Htr1a*^{CeA} mice (*Htr1a*^{KO}/*Htr1a*^{KO};*Nrip2-Htr1a*/+; Tsetsenis et al., 2007). Unexpectedly, a significantly increased rCBV signal was seen in several forebrain areas, including cerebral cortex, thalamus, ventral hippocampus, amygdala, caudate putamen, and septum (Figure 2). Time course analyses of the rCBV response to

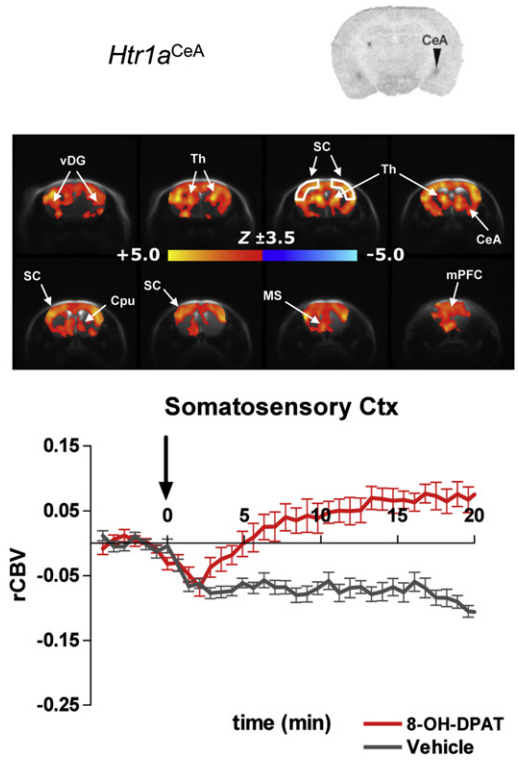

Figure 2. Cortical Arousal Following Suppression of Type I CeA Cells

Neural activity as measured by rCBV using fMRI in *Htr1a*^{CeA} mice treated with the Htr1a agonist, 8-OH-DPAT (0.5 mg/kg i.a., n = 9). Yellow/orange indicates significantly *increased* rCBV compared with vehicle baseline ($Z > 3.5$; cluster correction $p = 0.01$). Bottom panel shows rCBV time course following vehicle or 8-OH-DPAT injection in the somatosensory cortex. Significant increases in rCBV were detected following agonist treatment in several regions, including cerebral cortex, thalamus, ventral hippocampus, amygdala, caudate putamen, and septum. Htr1a receptor distribution (^{125}I-MPPI autoradiography) in a representative brain slice of *Htr1a*^{CeA} is reported for reference (vDG, ventral dentate gyrus; Th, thalamus; Cpu, caudate putamen; mPFC, medial prefrontal cortex; SC, somatosensory cortex; MS, medial septum).

8-OH-DPAT in representative regions of interest (ROIs) revealed a sustained activation that lasted throughout the time-window examined (Figure S2). Again, no agonist-induced activation was seen in knockout littermates (*Htr1a*^{KO}; Figure 1B; Figure S1).

In order to map neural circuits that mediate cortical activation in *Htr1a*^{CeA} mice following agonist treatment, we applied correlation analysis to the regional fMRI responses. This approach aims to elucidate relationships between signals elicited by agonist challenge in spatially distinct brain regions and complements the univariate approach applied to generate rCBV maps (Figures 1 and 2). These correlations can be interpreted as reflecting functional connectivity between the regions involved (Schwarz et al., 2007a) and can be used to resolve specific brain circuits engaged by pharmacological agents (Schwarz et al., 2007b). Correlation analysis revealed brain regions whose agonist-induced rCBV responses significantly correlated with a seed region located in CeA (Figure 3A). A significant pattern of correlated activity was identified linking CeA with cholinergic nuclei in the ventral forebrain, including substantia innominata (SI), diagonal band (DB), and nucleus basalis of Meynert (NBM) in 8-OH-DPAT-treated *Htr1a*^{CeA} mice (Figure 3A). A similar analysis of bottom-up connectivity from the cortical regions most strongly activated by 8-OH-DPAT in the same group showed significant connectivity between cortex and the same cholinergic nuclei (SI, DB, and NBM; Figure 3B). This connectivity is consistent with anatomical and functional studies demonstrating cholinergic innervation of cortex by these structures in rodents (Mesulam et al., 1983). When considered together with the findings of our univariate analysis (Figure 2), these results suggest that suppression of neural activity in type I CeA neurons leads to a disinhibition of selected ventral forebrain cholinergic nuclei and a consequent arousal of cortical circuits.

To test the hypothesis of a functional involvement of cholinergic circuits in the observed cortical arousal, we performed fMRI mapping in response to 8-OH-DPAT in *Htr1a*^{CeA} mice pretreated with atropine, an antagonist of muscarinic acetylcholine receptors. Atropine-sulfate (0.3 mg/kg, i.p.) significantly attenuated 8-OH-DPAT induced activation in all brain regions examined (Figures 3C and S3). Importantly, atropine-methylnitrate (0.3 mg/kg, i.p.), an atropine salt with poor blood-brain barrier penetration (Boccia et al., 2003), did not significantly block cortical arousal (Figures 3D, S2, and S3) arguing against a role of peripheral cholinergic receptors in mediating the effect. Moreover, atropine sulfate did not attenuate the rCBV response to 8-OH-DPAT in wild-type mice (Figure S3). These findings support a role for central cholinergic disinhibition in the cortical arousal seen after silencing of type I CeA neurons and are consistent with our functional connectivity mapping analysis.

Switch from Passive to Active Conditioned Behavior

Next, we examined the behavioral correlates of cortical arousal following suppression of type I CeA neuron activity. As previously reported (Tsetsenis et al., 2007), *Htr1a*^{CeA} mice treated with 8-OH-DPAT (0.2 mg/kg, s.c.) showed a significant reduction of freezing behavior during the tone when compared with vehicle-treated *Htr1a*^{CeA} mice (Figure 4A) and no change in freezing to the tone was seen in agonist-treated *Htr1a*^{KO} control littermates (ANOVA – genotype × treatment effect for freezing to the tone: $F[1, 100] = 4.51$, $p = 0.0362$, n = 19-30; Figure 4B). However, agonist-treated *Htr1a*^{CeA} mice also showed a significant increase in several exploratory and risk assessment behaviors, including digging, *exploration*, and rearing (Figure 4C). When summed as total active behavior (cumulative digging, *exploration*, and rearing), agonist-treated *Htr1a*^{CeA}, but not *Htr1a*^{KO} mice showed a dramatic shift from passive to active conditioned behavior during the tone (ANOVA – genotype × treatment effect on active behavior during tone: $F[1,100] = 4.475$, $p = 0.0369$, n = 19-30; Figures 4A–4D). Notably, agonist treatment produced only a small, nonsignificant increase in active behaviors in *Htr1a*^{CeA} mice during the prestimulus period and a similar trend was seen in *Htr1a*^{KO} mice (data not shown). These data argue for a shift in the quality of responses to the conditioned aversive stimulus following inhibition of type I CeA neurons. To determine whether active and passive behaviors were mutually exclusive expressions of fear, we examined within-animal correlations of active and passive behavior during exposure to the conditioned stimulus. An inverse correlation

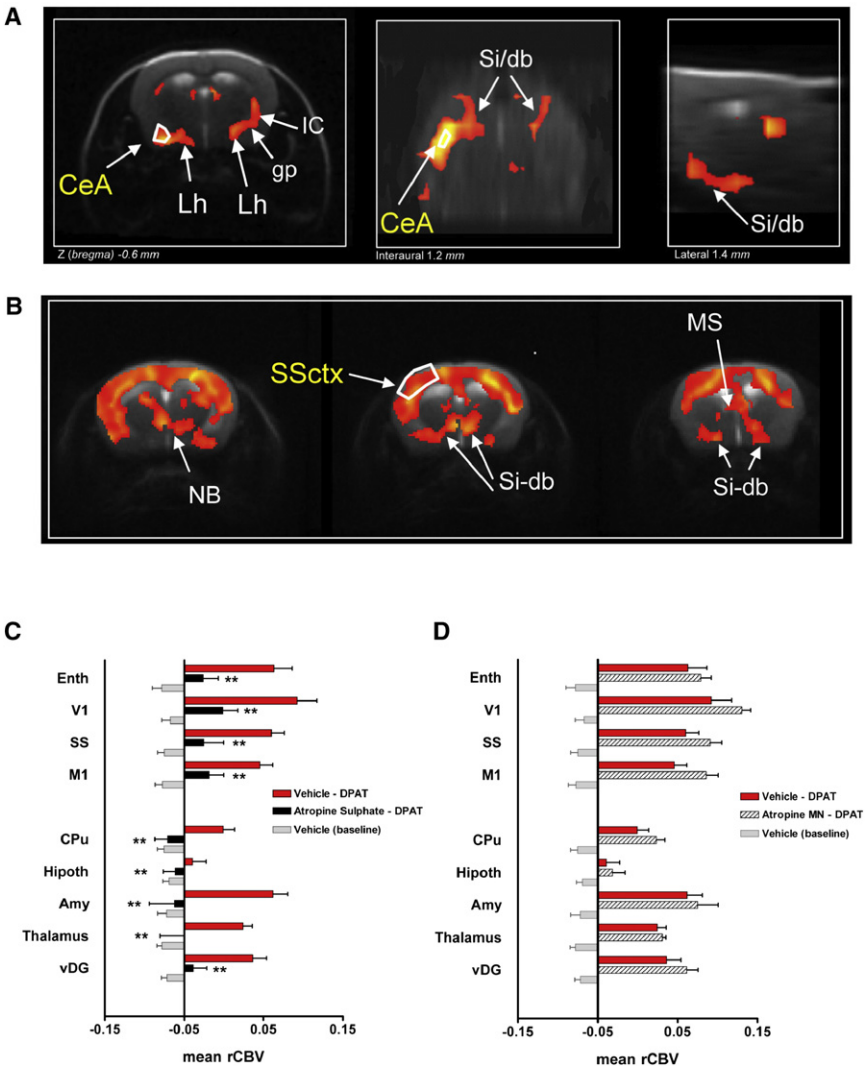

Figure 3. Atropine Blocks Cortical Arousal Following Inhibition of Type I CeA Cells

Maps of 8-OH-DPAT-induced rCBV response that significantly correlated with rCBV signal in (A) CeA and (B) somatosensory cortex (SSctx) in *Htr1a*^{CeA} mice ($Z > 1.6$, cluster correction $p = 0.01$, $n = 9$). The three images in (A) refer to three perpendicular sections located at Z_{bregma} −0.6 mm, interaural 1.2 mm, and lateral 1.4 mm, respectively. Significantly correlated rCBV signal was detected between CeA, Si, and db and between SSctx, Si, db, MS, and NB, suggesting a functional connectivity network linking CeA, ventral forebrain cholinergic nuclei, and neocortex. Pretreatment with (C) atropine sulfate ($n = 5$), but not (D) a non-brain penetrant salt of atropine (atropine methyl-nitrite, $n = 5$) blocked the rCBV signal increases seen after 8-OH-DPAT (0.5 mg/kg i.a) treatment of *Htr1a*^{CeA} mice ($n = 9$; $^{**}p < 0.01$ versus vehicle-pretreated subjects, one-way ANOVA followed by Fisher's LSD test; CeA, central nucleus of the amygdala; LH, lateral hypothalamus; gp, external globus pallidus; IC, internal capsule; Si, substantia innominata; db, nucleus of the diagonal band of Broca; MS, medial septum; NB, nucleus basalis of Meynert; SS, somatosensory cortex; M1, motor cortex; Hipoth, hypothalamus; Amy, amygdala; CPu, caudate putamen; V1, visual cortex; Enth, entorhinal cortex).

emerged between freezing and active behavior ($r^2 = 0.35$; Figure 4I), suggesting that expression of these responses was codependent.

One interpretation of our findings is that suppression of type I CeA neurons induced cortical arousal during behavioral testing, and this cortical activity directly contributed to a shift in behavioral responses to the conditioned stimulus. First, we tested whether inhibition of type I cells was associated with cortical arousal in awake behaving mice by performing c-Fos immunohistochemistry following treatment of *Htr1a*^{CeA} and *Htr1a*^{KO} littermates with 8-OH-DPAT (0.2 mg/kg, s.c.). The number of c-Fos-positive cells in the anterior cingulate area (a region showing prominent rCBV increases following agonist treatment; Figure 2) was significantly greater in agonist-treated *Htr1a*^{CeA} than *Htr1a*^{KO} mice (Figure 5). These findings confirmed increased cortical neuron activity following suppression of type I CeA neurons in behaving mice. Second, we examined whether pretreatment with atropine was able to interfere with behavioral responses to the fear stimulus. While atropine had no significant effect on freezing and/or active behaviors during the tone in agonist-treated *Htr1a*^{KO} mice suggesting normal fear recall in the presence of atropine (Figures 4F and 4H). In *Htr1a*^{CeA} mice, however, atropine pretreatment significantly reversed the suppression of freezing behavior and showed a trend for a reversal of the induction of active behaviors following 8-OH-DPAT treatment (Figures 4E and 4G). These data suggest that cholinergic neurotransmission directly contributes to the switch between passive and active behavioral responses. Notably, however, the low dose of atropine (0.1 mg/kg) had a significant and selective effect on freezing, while leaving active behaviors unaltered (Figures 4E and 4G). This dissociation reveals that active and passive behaviors are differentially dependent on cholinergic neurotransmission.

Activation of Oxytocin-Responsive Neurons in Lateral CeA

Given the dissociation between oxytocin and vasopressin receptor-expressing GABAergic projection neurons in lateral and medial CeA, respectively (Veinante and Freund-Mercier, 1997) and the exclusive enervation of SI/NBM by lateral, but not medial CeA projections (Jolkkonen et al., 2002), we considered whether type I cells might selectively inhibit oxytocin receptor-expressing cells in the lateral CeA. Whole-cell recordings in lateral CeA neurons in slices from *Htr1a*^{CeA} and *Htr1a*^{KO} littermates confirmed the presence of depolarizing

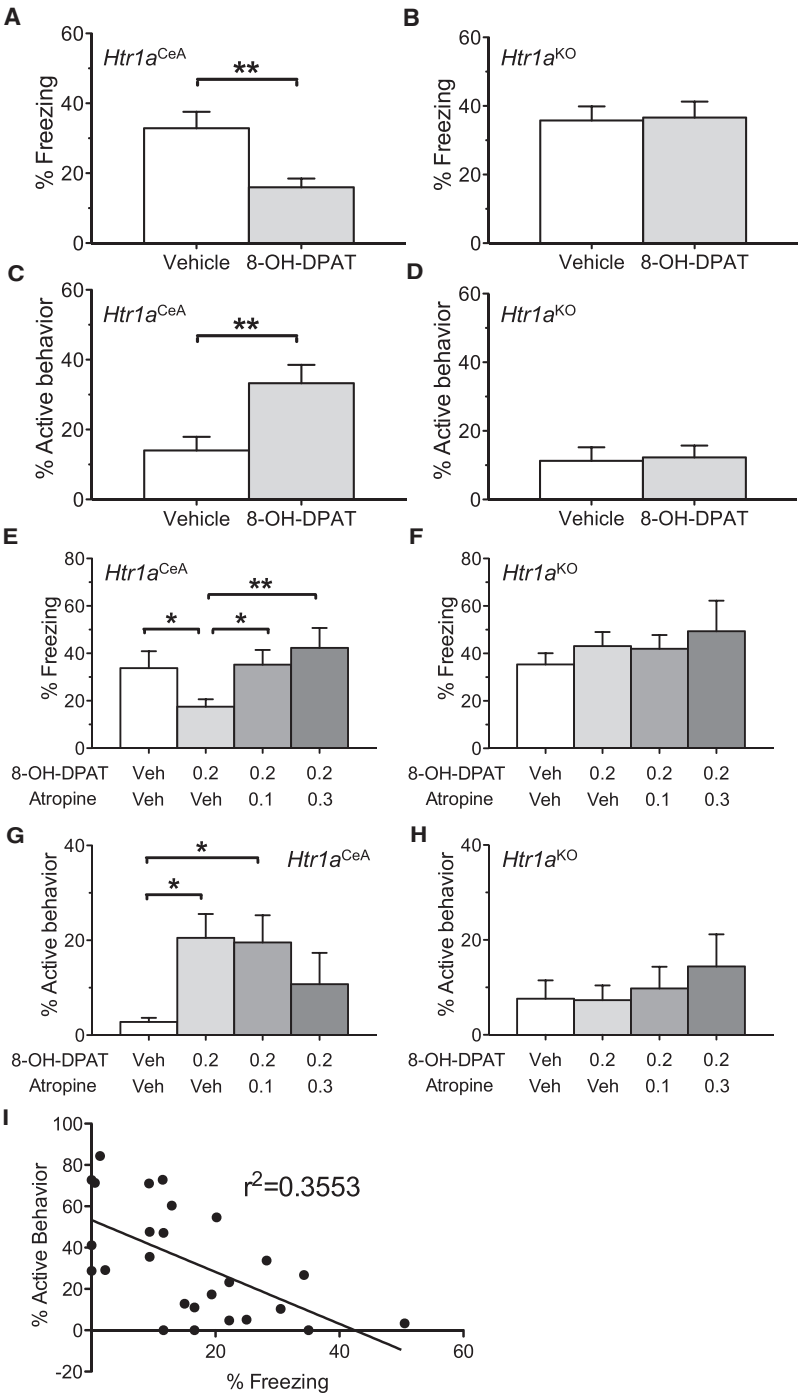

Figure 4. Switch from Passive to Active Fear Responses Following Inhibition of Type I CeA Cells

Behavioral analysis of *Htr1a*^{CeA} and *Htr1a*^{KO} mice pretreated with either vehicle (saline, s.c.) or the Htr1a agonist, 8-OH-DPAT (0.2 mg/kg, s.c.) during exposure to a tone (3 min) previously associated with footshock revealed a reduction in duration of freezing and increase in duration of active exploratory/risk assessment behavior in (A and C) *Htr1a*^{CeA} (vehicle: n = 19, agonist: n = 26), but not (B and D) *Htr1a*^{KO} mice (vehicle: n = 29, agonist: n = 30). Active behavior was scored as cumulative digging, exploration, and rearing. Atropine pretreatment (0.1 and 0.3 mg/kg, i.p.) caused a significant reversal of the inhibition of freezing seen following 8-OH-DPAT-treatment in (E) *Htr1a*^{CeA} (vehicle: n = 10, 8-OH-DPAT: n = 17, low atropine: n = 19, high atropine: N = 9), but not (F) *Htr1a*^{KO} mice (vehicle: n = 20, 8-OH-DPAT: n = 20, low atropine: n = 17, high atropine: n = 7), while showing a trend for a reversal of the increase in active behavior seen following 8-OH-DPAT-treatment at the higher dose in (G) *Htr1a*^{CeA}, but not (H) *Htr1a*^{KO} mice. (I) Plot of active behavior against freezing in individual *Htr1a*^{CeA} mice treated with 8-OH-DPAT (n = 26) revealed a negative correlation (r^2 = 0.355, p = 0.0013) between active and passive fear responses (*p < 0.05, **p < 0.01).

after-potential (DAP) positive, type I (Figure 6A) and DAP-negative, type II (Figure 6F) neurons in this subnucleus (Tsetsenis et al., 2007). Application of 8-OH-DPAT (50 μM, 1–3 min) caused inhibition of cell firing in type I neurons of *Htr1a*^{CeA} (Figures 6B and 6C), but not *Htr1a*^{KO} (3.51 ± 0.88 Hz to 3.05 ± 0.99 Hz; n = 7, p = 0.13) mice, consistent with our previous observations (Tsetsenis et al., 2007). Application of the oxytocin receptor agonist [Thr^4, Gly^7]-oxytocin (TGOT, 0.2 μM, 1–3 min) had no effect on firing of type I cells (Figures 6D–6E), but significantly increased firing of type II cells (Figures 6I–6J) consistent with the selective expression of oxytocin receptor on this class of cells. Importantly, type II cells also showed excitatory responses to 8-OH-DPAT (Figures 6G and 6H), while the Htr1a agonist had no significant effect on firing of this class of neuron in slices from *Htr1a*^{KO} controls (1.07 ± 0.19 to 1.00 ± 0.22 Hz; n = 3, p = 0.3). Oxytocin receptor-expressing cells in lateral CeA are known to inhibit vasopressin receptor-expressing cells in medial CeA (Huber et al., 2005), and recordings from the medial subnucleus in our preparations confirmed inhibitory effects of TGOT (data not shown). Together, these data are consistent with type I CeA neurons being local inhibitory neurons that tonically suppress firing of oxytocin receptor-expressing type II projection neurons in lateral CeA.

DISCUSSION

We have used pharmacological fMRI to map circuits downstream of the amygdala that are involved in the expression of conditioned fear responses. Our findings point to ventral forebrain cholinergic nuclei as a critical downstream target of CeA that promote cortical arousal and facilitate active responses at the expense of passive responses to a conditioned aversive stimulus. Several conclusions can be drawn from our study in light of previous anatomical and functional studies. First, anterograde tracing studies demonstrate that projections from amygdala to ventral forebrain cholinergic

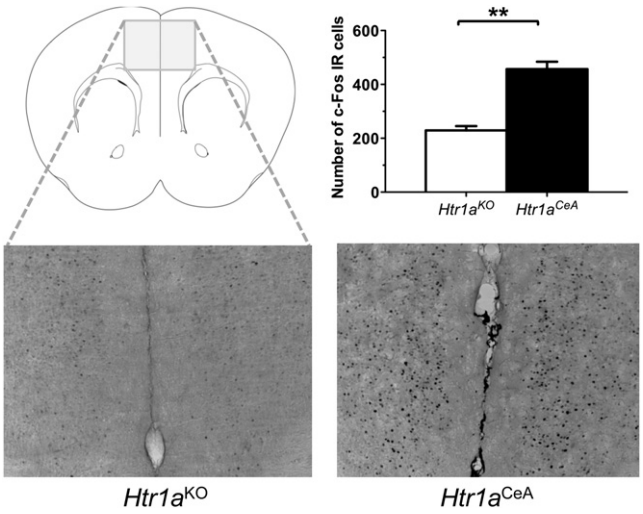

Figure 5. Increased Cortical c-Fos Immunoreactivity Following Inhibition of Type I CeA Cells

Quantification of c-Fos immunoreactivity in sections from brains of mice 90 min after treatment with 8-OH-DPAT (0.2 mg/kg, s.c.). A significantly greater increase in the number of c-Fos IR-positive nuclei was seen in the anterior cingulate area (ACA) of *Htr1a*^{CeA} (n = 4) versus *Htr1a*^{KO} (n = 3) mice (**p < 0.001).

nuclei such as SI, DB, and NBM originate exclusively from the lateral and/or capsular subnuclei of CeA (Jolkkonen et al., 2002). Because these connections make symmetric synapses onto neurons in the vicinity of cholinergic cell bodies in these target nuclei, they are likely to be GABAergic projection neurons that regulate activity of cholinergic neurons via inhibition of local GABAergic interneurons (Jolkkonen et al., 2002). An excitatory role for CeA on cortical activity is confirmed by electrophysiological studies that demonstrate a shift from large irregular slow activity (synchronous) to low voltage fast (asynchronous) cortical activity following electrical stimulation of CeA, an effect that is blocked by the cholinergic antagonist scopolamine (Dringenberg and Vanderwolf, 1997). Our electrophysiological studies demonstrate that type II cells are likely to be identical to the GABAergic, oxytocin receptor-expressing projection neurons previously described in the lateral CeA (Huber et al., 2005). Firing of these cells was consistently increased by bath application of the Htr1a agonist in *Htr1a*^{CeA} mice (Figures 6G and 6H), consistent with a direct inhibitory connection between type I and type II cells in lateral CeA. Thus, we speculate that type II neurons in lateral CeA are equal to the previously described CeA-SI/NBM projecting neurons (Jolkkonen et al., 2002) and are responsible for mediating the cortical arousal seen in our fMRI (Figure 2) and c-Fos (Figure 5) mapping studies.

Second, previous work has shown that oxytocin receptor-expressing cells in lateral CeA also project to and directly inhibit vasopressin receptor-expressing cells in medial CeA (Huber et al., 2005; data not shown). Efferents from the medial CeA project to hypothalamic and brainstem circuits that control freezing and autonomic fear responses and are thought to be responsible for conditioned freezing and autonomic responses to painful stimuli (Ehrlich et al., 2009). Thus, it is possible that disinhibition of type II cells by Htr1a agonist treatment in *Htr1a*^{CeA} mice suppresses conditioned freezing in part by directly inhibiting medial CeA projection neurons.

Third, our experiments showing that atropine blocked the switch from freezing to active behavior suggest that ventral forebrain cholinergic circuits are critical for modulating the quality of fear responses. Whether this switch is a direct consequence of increased cortical arousal or is also in part due to increased inhibition of medial CeA outputs that have been proposed to be responsible for behavioral immobility is not completely clear from our results. Our observation that atropine was able to completely reverse the effects of 8-OH-DPAT at least on freezing suggest that cholinergic mechanisms are necessary (but not necessarily sufficient) to switch away from passive fear (Figure 4E). The apparent reduced efficacy of atropine in reversing active behaviors induced by the Htr1a agonist (Figure 4G) suggests either that these are less sensitive to atropine or that other circuits are involved.

Thus, our data suggest a model in which the activity of lateral CeA projection neurons determines CeA outputs, switching behavioral responses from freezing to risk assessment and exploration (Figure 7). Under normal conditions (switch ON), lateral CeA projection neurons are tonically inhibited by type I neurons and medial CeA projection neurons are free to respond to inputs and promote freezing. When type I neurons are silenced (switch OFF) type II, oxytocin receptor-expressing lateral CeA projection neurons are disinhibited, leading to increased lateral CeA outputs to ventral forebrain and inhibition of medial CeA outputs. CeA efferents to the ventral forebrain (NBM/SI) lead to a disinhibition of cholinergic neurons and increased cortical arousal. Blockade of cholinergic neurotransmission is able to reverse the behavioral effects of the switch, suggesting that CeA-ventral forebrain outputs play a critical role in the switch. Such a circuitry is consistent with the suppression and facilitation of fear responses reported after intra-CeA administration of oxytocin and vasopressin receptor agonists, respectively (Roozendaal et al., 1992) and is in agreement with existing models of CeA function (Viviani and Stoop, 2008;Walker and Davis, 2008; Ehrlich et al., 2009).

One possible confound in the interpretation of our fMRI results is the possibility that low levels of expression of Htr1a outside type I CeA neurons may have contributed to the signal observed. Several lines of evidence suggest that such ectopic activation, if present, is minimal and does not mediate the rCBV and behavioral effects seen following 8-OH-DPAT treatment. First, similar experiments in a line of mice expressing Htr1a under the same promoter but showing expression selectively in dentate gyrus granule cells of the hippocampus (*Htr1a*^{DG}; Tsetsenis et al., 2007) did not show any increase in cortical rCBV signal (Figure S4) despite the fact that this line shows low levels of Htr1a expression in CeA (Tsetsenis et al., 2007). Thus, low levels of Htr1a do not appear to cause membrane hyperpolarization sufficient to alter neuronal firing, and this conclusion is confirmed by electrophysiological studies in slices taken from these mice (Tsetsenis et al., 2007). Second, the ability of centrally delivered atropine to suppress rCBV signal activation following 8-OH-DPAT treatment argues against the effect being mediated by activation of Htr1a within a local cortical circuit. Another possible

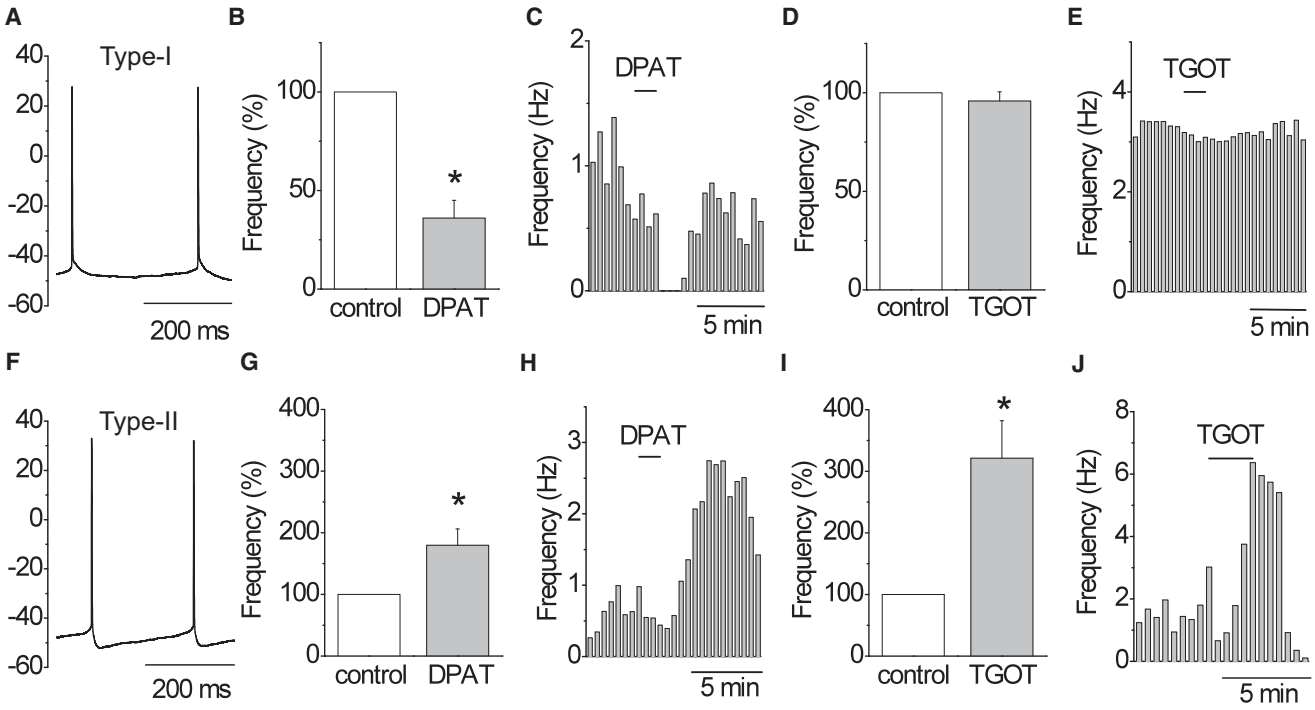

Figure 6. Type I CeA Cells Tonically Suppress Firing of Oxytocin-Responsive Neurons in Lateral CeA

Distinct firing signatures distinguished two major cell types in lateral CeA: (A) DAP^{+} type I and (F) DAP^{-} type II neurons. Whole-cell recordings in lateral CeA neurons of slices taken from *Htr1a*^{CeA} mice demonstrated that bath application of 8-OH-DPAT (DPAT, 50 μM, 1–3 min) induced a significant decrease in spontaneous firing of type I cells (B and C, n = 7) and increase in firing of type II cells (G and H, n = 9). Type II cells (I–J, n = 7), but not type I cells (D and E, n = 5) showed increased firing following application of the oxytocin receptor agonist, [Thr^{4}, Gly^{7}]-oxytocin (TGOT, 0.2 μM, 1–3 min). (B, D, G, and I) Relative mean firing frequency expressed as percentage of control value before drug delivery. (C, E, H, and J) Time course of the firing frequency of a representative cell. No significant changes in neuronal firing following 8-OH-DPAT administration were seen in slices taken from *Htr1a*^{KO} control mice (type I cells: 3.51 ± 0.88 to 3.05 ± 0.99 Hz, n = 7, p = 0.13).

confound derives from or use of a Htr1a knockout background for our studies. While these mice do show significant behavioral and physiological differences these are unlikely to have affected our conclusions given the combination of pharmacological (8-OH-DPAT versus vehicle) and genetic (*Htr1a*^{CeA} versus *Htr1a*^{KO}) controls.

An important question raised by our findings is whether type I CeA neurons are selectively involved in phasic, conditioned fear responses (Walker and Davis, 2008), or whether they also actively modulate tonic, unconditioned behavior. The fact that we detected cortical arousal following agonist treatment in both unstimulated, anaesthetized and awake, freely moving animals suggests that type I CeA neurons are tonically active in the absence of any conditioned stimulus. However, active behaviors, although in some cases present before stimulus presentation, were significantly enhanced only during the tone

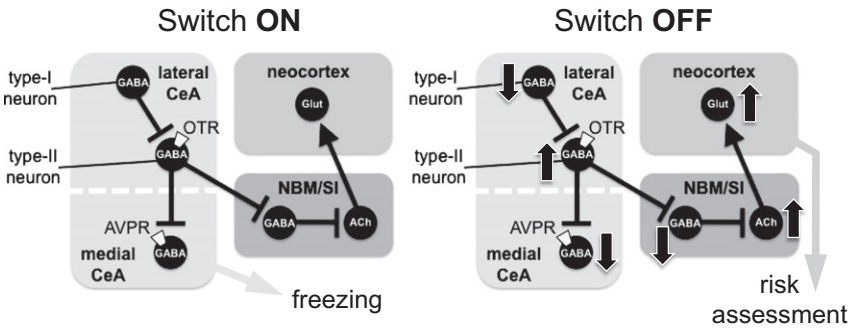

Figure 7. Proposed Circuit by which CeA Influences Active and Passive Fear Responses

Under standard conditions (Switch ON) type I cells are responsible for tonically inhibiting type II oxytocin receptor-expressing neurons in lateral CeA that project to nucleus basalis of Meynert and substantia innominata (NBM/SI). When type I cells are inhibited (Switch OFF), oxytocin receptor-expressing GABAergic projection neurons in lateral CeA are disinhibited. Increased firing of lateral CeA projection neurons leads to inhibition of ventral forebrain interneurons that maintain suppression of firing of cholinergic neurons responsible for promoting neocortical arousal. Blocking cholinergic neocortical activation (e.g., with the muscarinic antagonist atropine) leads to a reversal of the switch from passive to active behavior. Oxytocin receptor-expressing lateral CeA neurons also directly inhibit vasopressin receptor-expressing medial CeA neurons that project to hypothalamic and brainstem structures to promote freezing and parasympathetic responses to aversive conditioned stimuli (OTR, oxytocin receptor; AVPR, arginine/vasopressin receptor; arrows highlighted in white indicate relative changes in neuronal firing).

(data not shown) suggesting that relief of tonic inhibition in CeA was not sufficient to moderate behaviors in the absence of appropriate upstream inputs. Thus, we conclude that CeA disinhibition permits the expression of exploratory and risk assessment behaviors in the presence of a fear stimulus, but that this disinhibition is not sufficient to modulate unconditioned fear responses that may converge at a lower level in the fear circuitry.

Another question of importance is whether the switch from passive to active behavior we see reflects a change in the quality of the fear response or rather a change in its intensity. Although our observed behavioral switch is clearly one of quality, rather than quantity, it is possible that it acts to regulate the activity of a single downstream circuit. Lesions of the dorsal premamillary nucleus, for example, can transform fear in the presence of a predator from freezing to cautious exploration, and, contextual fear of the predator from cautious to relaxed exploration (Cezario et al., 2008), for example. Thus, the CeA switch may be acting on a downstream rheostat-like circuit that dials between freezing/risk assessment/nonfear in a way that is consistent with the defensive distance hypothesis. Alternatively, the CeA switch could be acting independently to suppress passive and promote active behaviors. Our observation that low doses of atropine (0.1 mg/kg) selectively reverses the effects of 8-OH-DPAT on freezing in *Htr1a*^{CeA} mice, while leaving active behaviors unaffected (Figures 4G and 4H), suggests that separate circuits may be involved in these two coping strategies. A related question involves the degree to which variation in CeA switch efficacy might explain individual variation in fear behavior. It is possible, for example, that different set points of tonic activity of type I CeA cells could predispose animals to a more passive or active fear coping style. Future experiments aimed at examining the role of defensive distance or intensity as well as interindividual variability in modulating the CeA switch may help in address these hypotheses.

In summary, we have applied fMRI and correlation analysis to map circuits downstream of CeA that are involved in modulating conditioned fear. Our findings demonstrate that CeA outputs to ventral forebrain cholinergic neurons driving cortical arousal are under tonic inhibition by type I neurons in CeA and that modulation of their activity offers the animal a route to shift its conditioned fear responses from passive to active behaviors. These findings demonstrate that CeA circuits are involved in determining both the magnitude and quality of conditioned fear responses and is consistent with studies arguing in favor of a more complex role for the amygdala in modulating fear coping behavior (Walker and Davis, 2008;Wilensky et al., 2006).

EXPERIMENTAL PROCEDURES

Animals

All in vivo studies were conducted in accordance with the laws of the Italian Ministry of Health (DL 116, 1992). Protocols were reviewed and approved by a local animal care committee in accordance with the guidelines of the Principles of Laboratory Animal Care (NIH publication 86-23, revised 1985). fMRI experiments were performed in adult (>10 weeks) male mice. The transgenic lines used have been previously described (Tsetsenis et al., 2007). The strains were maintained on a mixed C57BL/6J;CBA/J;129S6/SvEvTac background. Littermates were used for all control experiments. Experiments on the effect of atropine sulfate on the inhibitory action of 8-OH-DPAT in wild-type mice were performed in C57BL/6J male mice (Charles River Italia, Como, Italy). Animals used in fMRI studies were singly housed with food and water provided ad libitum and under controlled temperature (20°C–22°C), humidity (45%–65%), and lighting (12 hr light/dark, lights on at 06:00 hr). Animals used in behavioral studies were housed as previously described (Tsetsenis et al., 2007).

Animal Anesthesia and Physiological Monitoring

Mice were anaesthetized with 4% isoflurane in a 1:1 oxygen/nitrogen mixture (0.9 l/min + 0.9 l/min) within an induction chamber connected to a vaporizer (Burtons Medical Equipment, UK). The animal was then placed supine on an interactive heating pad (Harvard Apparatus, UK) and gaseous anesthesia continuously delivered through a face mask. Mice were subsequently tracheotomized and artificially ventilated (see below). The left femoral artery was cannulated for compound administration, continuous blood pressure monitoring, infusion of paralyzing agent (pancuronium bromide, 0.5 mg/kg/hr, Sigma-Aldrich, Italy), and blood sampling for measurement of arterial blood gases. *Htr1a*^{CeA} and wild-type animals were also fitted with an intraperitoneal cannula to allow administration of anticholinergic drugs. Arterial blood gases p_aCO_2 and p_aO_2 were measured terminally and the values used retrospectively to exclude subjects that presented parameters outside the physiological range (20–50 mmHg for p_aCO_2, > 80 mmHg for p_aO_2). Mean weight and p_aCO_2 levels recorded are reported in Supplemental Information (Table S1). No statistically significant difference in postacquisition p_aCO_2 values between any of the groups was observed (one-way ANOVA followed by Fisher's LSD and Hochberg's correction for multiple comparisons with $\alpha = 0.05$).

Tracheostomy

Prior to surgical incision, each mouse received a subcutaneous infiltration of 0.05% tetracaine solution at each surgical site (neck and femoral area) at volume of 0.02 ml/point (0.04 ml/mouse). Tetracaine was chosen due to its negligible degree of brain penetration (Ferrari et al., 2010). The neck and femoral area were shaved with an electrical shaver and the skin disinfected. Rolled gauze was placed under the neck in order to extend it and facilitate the subsequent exposure of trachea for surgery incision. A midline skin incision was made along the length of the neck and, after separating the two halves of the sternohyoid muscle, the trachea exposed. The incision covered the sublaryngeal region, and a G23 cannula (Vygon, France), shortened to 0.7 cm, was inserted into the trachea. The cannula was then secured with silk suture thread (3-0 Ethicon, Johnson-Johnson, Belgium) passed through the holes of its plastic "butterfly." The cannula was then connected to a ventilation pump (Inspira ASV, Harvard Apparatus) and anesthetic gas delivery switched from the mask to the pump. Ventilation parameters were 70 bpm and tidal volume (Vt) in the range of 5.3–5.9 ml/kg. Starting Vt was chosen on the basis of measurements performed on a separate group of wild-type mice (n = 10).

Femoral Artery Cannulation

Femoral artery cannulation was performed at an IF level of 3%. We chose to cannulate the femoral artery instead of the femoral vein as customary in rat surgery due to the former's higher elasticity and resistance. This procedure allowed for quicker surgery and higher throughput compared to vein cannulation. The left leg of the animal was extended and taped on the surgical mat. A skin incision of roughly one centimeter was made above the femoral area. The left femoral artery was isolated and cannulated with a polyethylene catheter (PE10, OD 0.61 mm, ID 0.28 mm) filled with heparinized physiologic solution (25 UI/ml) containing 0.0375 mg/ml of pancuronium bromide that was continuously infused (rate 6.7 ml/kg/h) throughout the experiment to ensure constant neuromuscular blockade. This catheter was connected to a blood-pressure transducer (Biopac Systems) through a flow/flush device (CRITIFLO TA4004, Becton Dickinson). In order to allow for compound administration, a homemade Plexiglas Y-piece was placed in between the femoral catheter and the MABP transducer. The PE10 catheter was connected to the Y piece through a 2 cm PVC40 junction (OD 0.90 mm, ID 0.50 mm) inserted into a piece of Silicone tubing (Fr 3). The two-way system allowed simultaneous recording of MABP and infusion of paralyzing agent plus the injection of compounds (upon clamping of the opposite way to prevent the delivery of compound in the wrong line). After surgery (25–35 min in duration) mice

were placed into a customized stereotactic holder (Bruker, Germany) and anesthesia lowered to 1.2%.

rCBV Measurement

MRI data were acquired using a Bruker Avance 4.7 Tesla system, a 72 mm birdcage resonator for radiofrequency pulse transmit, and a Bruker curved "Mouse Brain" quadrature receive coil. The MR acquisition for each subject comprised T2-weighted anatomical images using the RARE sequence (Hennig et al., 1986; TR_{eff} = 5597 ms, TE_{eff} = 76 ms, RARE factor 8, FOV 40 mm, 256 × 256 matrix, 24 contiguous 0.75 mm slices) followed by a time series acquisition with the same spatial coverage and similar parameters (TR_{eff} = 5436 ms, TE_{eff} = 112 ms, RARE factor 32, 128 × 128 matrix, 24 contiguous 0.75 mm slices), but lower in-plane spatial resolution (312 μm^2) giving a functional pixel volume of ~0.07 mm^3. Two successive scans were averaged for a resulting time resolution of 42 s.

Total MRI time series acquisition time was 70 min (100 repetitions) for all groups. Following five reference images, 3.75 μl/g of the blood pool contrast agent Endorem (Guerbet, France) was injected so that subsequent signal changes would reflect alterations in relative cerebral blood volume (rCBV; Mandeville et al., 1998). The dose of Endorem was selected to ensure a mean signal decrease of ~60% necessary to optimize the contrast-to-noise ratio of the rCBV measurement as described (Mandeville et al., 1998). Each subject received an intra-arterial injection of vehicle (saline, 5 μl/g) followed by a challenge with 8-hydroxy-2-(di-n-propylamino) tetralin (8-OH-DPAT, Sigma, Milano) 25 min later. Vehicle injection was performed 15 min after administration of contrast agent. *Htr1a*^{CeA} and wild-type littermates mice received anticholinergic agents (0.3 mg/kg, i.p.) or saline vehicle between intra-arterial vehicle and 8-OH-DPAT injections (14 min apart). The MRI time series were acquired over a period of 25 min following the administration of the 8-OH-DPAT challenge. The dose of 8-OH-DPAT and atropine were chosen based on previous in vivo studies (Tsetsenis et al., 2007; Gasbarri et al., 1997; Boccia et al., 2003; Baratti et al., 1979). Atropine sulfate is a nonselective acetylcholine muscarinic receptor antagonist; atropine methyl-nitrate is a non-brain-penetrant salt form of atropine. All compounds were injected at 1 ml/min. Compound injection was followed by administration of 0.2 ml of saline to flush the intra-arterial line.

fMRI Data Analysis

rCBV time series data for each experiment were analyzed within the framework of the general linear model (GLM) to obtain Z statistic maps (Worsley et al., 1992). Signal intensity changes in the time series were then converted into fractional rCBV changes on a pixel-wise basis using the transform (Mandeville et al., 1998) rCBV(t) = ln(S(t)/B(t))/ln(B(t)/SPRE), where S(t) is the measured signal, B(t) the estimated background signal in the absence of transient functional stimuli, and SPRE the signal intensity prior to administration of the contrast agent. B(t) was set equal to the mean signal intensity B_0 during the 8.4 min (12 time points) period prior to compound injection. For each time series, a rCBV time series surrounding the vehicle and 8-OH-DPAT injection points were calculated independently using identical parameters, covering 8.4 min (12 time points) prechallenge baseline and 22.4 min (32 time points) postchallenge window, normalized to a common injection time point. In contrast to what we observed in the rat (Schwarz et al., 2003) the slow rate of blood-pool contrast agent elimination from mouse blood resulted in negligible signal drifts over the time-window examined, which did not require the application of detrending corrections. The T_2-weighted anatomical images from each subject were coregistered by rigid body alignment to a brain template using FLIRT, Version 5.63, part of FSL (FMRIB's Software Library, www.fmrib.ox.ac.uk/fsl) and applying the resulting transformation matrix to the accompanying rCBV time series.

Two separate anatomical templates were created in order to account for the presence of slight but significant differences in the size of the brain of the transgenic lines (KO, CeA, and DG) with respect to wild-types, with the latter showing a reduced dorsoventral and horizontal extension. Average brain templates were created by coregistering and overlaying all the anatomical scans to a representative subjects using FSL/FLIRT (affine transformation, 6 degrees of freedom). Non-brain tissue was removed from the template using FSL/BET (brain extraction tool) followed by manual removal of residual signal from spurious subcutaneous fat in posterior slices. The template thus obtained (template 1) was then used to mask individual anatomical images. The final template was created through a second iteration of the coregistration process using individual masked anatomicals and masked template 1 (affine, 7 degrees of freedom, FSL/FLIRT). The resulting transformation matrix was applied to the accompanying rCBV time series. The use of the paralyzing agent ensured that no motion-related effects were present in the time series. Data from all animals were checked for motion following acquisition by subtraction of image frames at beginning and end of the time series, and at intermediate points (e.g., before and after injection) revealing no motion artifacts in all the subjects examined.

Data were analyzed as previously described (Schwarz et al., 2006, 2007b). In brief, subjects were coregistered by rigid body alignment to a mouse brain template using FLIRT, Version 5.63, part of FSL (www.fmrib.ox.ac.uk/fsl). The template was created by coregistering and overlaying all the anatomical scans onto a representative subject using FSL/FLIRT. Signal time course analysis in pericranial ROIs of individual animals did not highlight significant motion artifacts in any of the subjects imaged. Signal intensity changes were converted into fractional rCBV changes (Mandeville et al., 1998). rCBV time series before and after intra-arterial injections were calculated with 8 and 28 pre- and postchallenge time points, respectively. Ten and 18 time points pre- and postadministration were used for intra-peritoneal administration. Activation/deactivation maps were analyzed using FEAT Version 5.63, part of FSL, with 0.8 mm spatial smoothing and model functions identified by Wavelet Cluster Analysis (Schwarz et al., 2006). Two separate regressors were identified for wild-type and *Htr1a*^{CeA} subjects (Reg 1 and Reg 2, Figure S5). Image analysis of *Htr1a*^{DG} and *Htr1a*^{KO} was performed using Reg 1 as no plausible regressor describing 8-OH-DPAT was found. Group comparisons were carried out using FLAME (FMRIB's Local Analysis of Mixed Effects). Z (Gaussianised T/F) statistic images were thresholded using clusters determined by Z > 1.96 (unless otherwise described) and a corrected cluster significance threshold of p = 0.01 (Friston et al., 1994; Worsley et al., 1992). rCBV time series for 8-OH-DPAT, vehicle, or atropine injections (Figures S1–S4) were extracted bilaterally for specific regions of interest (ROIs) anatomically defined based on a mouse stereotactic atlas (Paxinos and Franklin, 2003). The effect of atropine pretreatment on the agonist response was assessed using average rCBV over an 8–20 min postinjection time window and one-way ANOVA followed by Fisher LSD. Results are quoted and displayed as mean ± SEM unless otherwise indicated.

Unsmoothed rCBV time series for 8-OH-DPAT and vehicle injection in each subject were extracted for specific regions of interest (ROIs) based on correspondence between the anatomical images and stereotactic atlas of the mouse brain (Paxinos and Franklin, 2003) using custom in-house software written in IDL (Research Systems, Boulder, CO). rCBV time course data were shown as group mean ± standard error (SEM). Regions examined (and their approximate rostrocaudal position from z_{bregma}) were amygdala (−1.58 mm), caudate putamen (+0.74 mm), ventral dentate gyrus (−4.24 mm), dorsal dentate gyrus (−1.34 mm), posterior dentate gyrus (−3.16 mm), thalamus (−1.82 mm), hypothalamus (−1.82 mm), motor cortex (+0.62 mm), somatosensory cortex (+0.02 mm), prefrontal cortex (+1.54 mm), and cingulate cortex (+0.74 mm). All ROIs were drawn bilaterally. Maps of correlated responses across subjects (Figure 3) were calculated within a General Linear Model framework at the higher level using FSL with FLAME as previously described (Schwarz et al., 2007b). Two reference (seed) regions, left CeA (z_{bregma} −0.6 mm) and left somatosensory cortex (z_{bregma} −0.9 mm), were selected a priori. Maps were thresholded using clusters determined by Z > 1.6 and a corrected cluster significance threshold of p = 0.01. Mean arterial blood pressure data were rebinned in 10 sample subdivisions and plotted using 40 s bins (Figure S6).

Arterial blood pressure time courses were recorded using an intra-arterial transducer and a 50 Hz sampling frequency (AcqKnowledge 3.1, Biopac Systems, Goleta). Mean arterial blood pressure (MABP) was calculated by temporally smoothing raw blood pressure traces using a moving average of 300 samples (6 s). MABP data were then rebinned in 10 subdivisions. Average MABP response over a 0–20 min postinjection time window was used as a summary measurement for statistical comparison between groups. Statistical comparison of MABP and arterial blood gases (p_aCO_2 and p_aO_2) was performed using one-way ANOVA followed by Fisher's LSD (least significant

difference) test using Statistica 8.0 (Statsoft, Tulsa, OK). To simplify data presentation, MABP time course data were plotted using 40 s bins.

The composition of the experimental groups and treatments is summarized as follows: Group 1 – *Htr1a*^{KO}, vehicle/8-OH-DPAT, n = 8; Group 2 – *Htr1a*^{CeA}, vehicle/vehicle/8-OH-DPAT, n = 9; Group 3 – *Htr1a*^{CeA}, vehicle/atropine-sulfate/8-OH-DPAT, n = 5; Group 4 – *Htr1a*^{CeA}, vehicle/atropine-methyl-nitrate/8-OHDPAT, n = 5; Group 5 – *Htr1a*^{DG}, vehicle/8-OH-DPAT, n = 6; Group 6 – wild-type, vehicle/8-OH-DPAT, n = 14; Group 7 – wild-type vehicle/vehicle/8-OH-DPAT, n = 8; Group 8 – wild-type, vehicle/atropine-sulfate/8-OH-DPAT, n = 8.

Immunohistochemistry

Undisturbed littermates were injected with 8-OH-DPAT (one mouse/genotype/cage) and returned to their home cage for 90 min before trans-cardial perfusion with saline and paraformaldehyde under anesthesia. Brains were removed, postfixed overnight, and rapidly frozen before cryosectioning (40 μm). Anti-c-Fos (Calbiochem) immunohistochemistry was carried out on free-floating coronal brain sections using the ABC detection system (Vector Labs). Immunostaining was quantified manually from microscope images of matched sections (two sections/animal; averaging between hemispheres) with the aid of Image J software.

Behavioral Testing

Fear conditioning was carried out as previously described (Tsetsenis et al., 2007). In brief, mice were exposed on day 1 to a partially conditioned tone and a perfectly conditioned light stimulus (20 s stimulus coterminating with 0.5 mA, 1 s footshock, 3× tone-light-shock, 2× tone interspersed; tone: 3000 Hz, 85 dB), and tested for freezing during the tone delivered in a novel cage on day 2 (3 min baseline period followed by 6 min tone presentation). Behavioral data were extracted by manual scoring of video recordings from the 3 min baseline and first 3 min of the tone presentation with the aid of Observer software (Noldus, Wageningen, Netherlands). Digging was scored when the animal was close to the edge of the cage and was using his paws to dig and pull up the plastic flooring. Exploration was scored when the animal made pronounced whole-body movements that extended across the cage. Rearing included both wall and center rearing. All behaviors were recorded as total duration of the activity. All scoring was performed blind to genotype and treatment.

Electrophysiological Recordings

Mice (P21-P55 littermates) were deeply anesthetized with halothane and decapitated, and whole brains were rapidly removed and immersed for 10 min in oxygenated (95% O_2, 5% CO_2 [pH 7.4]) ice-cold ACSF containing 125 mM NaCl, 2.5 mM KCl, 1.25 mM NaH_2PO_4, 1.0 mM $MgCl_2$, 2.0 mM $CaCl_2$, 10 mM glucose, and 26 mM $NaHCO_3$. Horizontal (250 μm) slices were cut at 4°C with a vibratome, placed in a chamber containing oxygenated ACSF, and allowed to recover for 2 hr at room temperature. Individual slices were then transferred to the submerged slice-recording chamber and maintained at 32°C and constantly superfused with oxygenated ACSF. Central amygdala regions were identified using the hippocampus CA2 and lateral amygdala regions as references. Recording electrode resistance was 8–12 MΩ when filled with an intracellular solution of 140 mM K-gluconate, 4 mM $MgCl_2$, 0.5 mM EGTA, 10 mM HEPES, 2 mM MgATP, and 0.5 mM NaGTP (pH 7.3, 280 mOsm). Whole-cell recordings were made using an amplifier (Multiclamp 700B, Axon Instruments) and signals filtered and digitized at 10 kHz with an A/D converter (Digidata 1322A, Axon Instruments) and stored using pClamp 9 software (Axon Instruments). Spontaneous firing was recorded in current-clamp configuration with neurons held near the spiking threshold (−55 ± 5mV) by depolarizing current injection. In some experiments spontaneous frequency was enhanced by lowering ACSF Ca^{2+} concentration to 0.5 mM. Baseline activity was monitored for at least 4 min and stable baseline spiking frequency obtained before applying agonists. Drugs were freshly prepared from stock solutions and applied to the slice by a gravity-driven perfusion system (flow rate = 2 ml/min, one exchange every 3 min). Washout of agonists with ACSF reestablished spiking to initial levels within 10–15 min. Spontaneous spiking activity was analyzed by Mini Analysis Program (Synaptosoft, Decatur, GA) with detection parameters adjusted for each data file to obtain correct values of peak amplitude and frequency both in simple events and complex bursts. Mean spike frequency time course was obtained by averaging the interevent interval in 10 s bins. Effects of drugs application were quantified by averaging spike frequency at baseline and the effect plateau (1–2 min each).

Statistical Testing

Statistical testing of behavioral data was carried out using ANOVA and Fisher LSD post-hoc testing in cases of significance, except for the atropine study in which we tested the a priori hypothesis that atropine would reverse the behavioral effects of 8-OH-DPAT and used t tests. c-Fos and electrophysiological data were analyzed by t test. Correlation was assessed by Pearson's regression testing. Statistical testing of imaging data is described above or in the figure legends.

SUPPLEMENTAL INFORMATION

Supplemental Information includes six figures and one table and can be found online at doi:10.1016/j.neuron.2010.07.008.

ACKNOWLEDGMENTS

We thank Graham Sheridan for help with scoring behavior, Rosa Chiara Paolicelli, Viviana Triaca, and Emerald Perlas for help and advice in immunostaining experiment, Francesca Zonfrillo and Roberto Voci for mouse husbandry, and Stefania Rizzo for genotyping. This work was supported in part by funds from EMBL (C.T.G., T.T.) and the EC FP7 DEVANX Collaborative Grant (C.T.G., A.J.). A. Gozzi and A.B. are employees and shareholders of GlaxoSmithKline. A. Gozzi designed, carried out, and analyzed the fMRI experiments; A.J. designed, carried out, and analyzed the behavioral and immunohistochemical experiments and oversaw production of mice for fMRI studies; A. Giovanelli and D.R. designed, A. Giovanelli and C.B. carried out, and A. Giovanelli and D.R. analyzed the electrophysiological experiments; V.C. performed animal surgery and preparation; A.S. developed the functional connectivity frame work; T.T. oversaw production of mice for fMRI studies and performed behavioral experiments; A.B. and C.T.G. conceived the experiments with critical input from A. Gozzi and A.J. and oversaw the experimental work and analysis; C.T.G. and A. Gozzi wrote the manuscript with help from A.B.

Accepted: June 17, 2010
Published: August 25, 2010

REFERENCES

Aggleton, J.P. (1992). The Amygdala (New York: Wiley-Liss).

Amaral, D., Price, J., Pitkanen, A., and Carmichael, T. (1992). Anatomical organization of the primate amygdaloid complex. In The Amygdala: Neurobiological Aspects of Emotion, Memory, and Mental Dysfuncton, J.P. Aggleton, ed. (New York: Wiley-Liss), pp. 1–66.

Baratti, C.M., Huygens, P., Mino, J., Merlo, A., and Gardella, J. (1979). Memory facilitation with posttrial injection of oxotremorine and physostigmine in mice. Psychopharmacology (Berl.) *64*, 85–88.

Boccia, M.M., Blake, M.G., Acosta, G.B., and Baratti, C.M. (2003). Atropine, an anticholinergic drug, impairs memory retrieval of a high consolidated avoidance response in mice. Neurosci. Lett. *345*, 97–100.

Cezario, A.F., Ribeiro-Barbosa, E.R., Baldo, M.V.C., and Canteras, N.S. (2008). Hypothalamic sites responding to predator threats—the role of the dorsal premammillary nucleus in unconditioned and conditioned antipredatory defensive behavior. Eur. J. Neurosci. *28*, 1003–1015.

Chen, Y.-C.I., Mandeville, J.B., Nguyen, T.V., Talele, A., Cavagna, F., and Jenkins, B.G. (2001). Improved mapping of pharmacologically induced neuronal activation using the IRON technique with superparamagnetic blood pool agents. J. Magn. Reson. Imaging *14*, 517–524.

Davis, M., and Whalen, P.J. (2001). The amygdala: vigilance and emotion. Mol. Psychiatry *6*, 13–34.

Dringenberg, H.C., and Vanderwolf, C.H. (1997). Neocortical activation: modulation by multiple pathways acting on central cholinergic and serotonergic systems. Exp. Brain Res. *116*, 160–174.

Ehrlich, I., Humeau, Y., Grenier, F., Ciocchi, S., Herry, C., and Lüthi, A. (2009). Amygdala inhibitory circuits and the control of fear memory. Neuron *62*, 757–771.

Ferrari, L., Crestan, V., Sabattini, G., Vinco, F., Fontana, S., and Gozzi, A. (2010). Brain penetration of local anaesthetics in the rat: implications for experimental neuroscience. J. Neurosci. Methods *186*, 143–149.

Friston, K.J., Jezzard, P., and Turner, R. (1994). Analysis of functional MRI time-series. Hum. Brain Mapp. *1*, 153–171.

Gasbarri, A., Sulli, A., Pacitti, C., Puglisi-Allegra, S., Cabib, S., Castellano, C., Introini-Collison, I., and McGaugh, J.L. (1997). Strain-dependent effects of D2 dopaminergic and muscarinic-cholinergic agonists and antagonists on memory consolidation processes in mice. Behav. Brain Res. *86*, 97–104.

Gozzi, A., Ceolin, L., Schwarz, A., Reese, T., Bertani, S., and Bifone, A. (2007). A multimodality investigation of cerebral haemodynamics and autoregulation in phMRI. Magn. Reson. Imaging *25*, 826–833.

Hennig, J., Nauerth, A., and Friedburg, H. (1986). RARE imaging: a fast imaging method for clinical MR. Magn. Reson. Med. *3*, 823–833.

Huber, D., Veinante, P., and Stoop, R. (2005). Vasopressin and oxytocin excite distinct neuronal populations in the central amygdala. Science *308*, 245–248.

Jenkins, B.G., Chen, Y.-C.I., and Mandeville, J.B. (2003). Pharmacological magnetic resonance imaging (phMRI). In Biomedical Imaging in Experimental Neuroscience, N. van Bruggen and T. Roberts, eds. (New York: CRC Press), pp. 155–209.

Jolkkonen, E., Miettinen, R., Pikkarainen, M., and Pitkänen, A. (2002). Projections from the amygdaloid complex to the magnocellular cholinergic basal forebrain in rat. Neuroscience *111*, 133–149.

LeDoux, J.E. (2000). Emotion circuits in the brain. Annu. Rev. Neurosci. *23*, 155–184.

Lopez De Armentia, M., and Sah, P. (2004). Firing properties and connectivity of neurons in the rat lateral central nucleus of the amygdala. J. Neurophysiol. *92*, 1285–1294.

Luo, L., Callaway, E.M., and Svoboda, K. (2008). Genetic dissection of neural circuits. Neuron *57*, 634–660.

Luscher, C., Jan, L.Y., Stoffel, M., Malenka, R.C., and Nicoll, R.A. (1997). G protein-coupled inwardly rectifying K+ channels (GIRKs) mediate postsynaptic but not presynaptic transmitter actions in hippocampal neurons. Neuron *19*, 687–695.

Mandeville, J.B., Marota, J.J.A., Kosofsky, B.E., Keltner, J.R., Weissleder, R., Rosen, B., and Weisskoff, R. (1998). Dynamic functional imaging of relative cerebral blood volume during rat forepaw stimulation. Magn. Reson. Med. *39*, 615–624.

Mesulam, M.M., Mufson, E.J., Wainer, B.H., and Levey, A.I. (1983). Central cholinergic pathways in the rat: an overview based on an alternative nomenclature (Ch1-Ch6). Neuroscience *10*, 1185–1201.

Paxinos, G., and Franklin, K. (2003). The Mouse Brain in Stereotaxic Coordinates (Sydney: Academic Press).

Roozendaal, B., Schoorlemmer, G.H., Wiersma, A., Sluyter, S., Driscoll, P., Koolhaas, J.M., and Bohus, B. (1992). Opposite effects of central amygdaloid vasopressin and oxytocin on the regulation of conditioned stress responses in male rats. Ann. N.Y. Acad. Sci. *652*, 460–461.

Sah, P., Faber, E.S.L., Lopez De Armentia, M., and Power, J. (2003). The amygdaloid complex: anatomy and physiology. Physiol. Rev. *83*, 803–834.

Schiess, M.C., Callahan, P.M., and Zheng, H. (1999). Characterization of the electrophysiological and morphological properties of rat central amygdala neurons in vitro. J. Neurosci. Res. *58*, 663–673.

Schwarz, A.J., Reese, T., Gozzi, A., and Bifone, A. (2003). Functional MRI using intravascular contrast agents: detrending of the relative cerebrovascular (rCBV) time course. Magn. Reson. Imaging *21*, 1191–1200.

Schwarz, A.J., Whitcher, B., Gozzi, A., Reese, T., and Bifone, A. (2006). Study-level wavelet cluster analysis and data-driven signal models in pharmacological MRI. J. Neurosci. Methods *159*, 346–360.

Schwarz, A.J., Gozzi, A., Reese, T., and Bifone, A. (2007a). Functional connectivity in the pharmacologically activated brain: resolving networks of correlated responses to d-amphetamine. Magn. Reson. Med. *57*, 704–713.

Schwarz, A.J., Gozzi, A., Reese, T., and Bifone, A. (2007b). In vivo mapping of functional connectivity in neurotransmitter systems using pharmacological MRI. Neuroimage *34*, 1627–1636.

Sheth, S.A., Nemoto, M., Guiou, M., Walker, M., Pouratian, N., Hageman, N., and Toga, A.W. (2004). Columnar specificity of microvascular oxygenation and volume responses: implications for functional brain mapping. J. Neurosci. *24*, 634–641.

Swanson, L.W., and Petrovich, G.D. (1998). What is the amygdala? Trends Neurosci. *21*, 323–331.

Tribollet, E., Barberis, C., Jard, S., Dubois-Dauphin, M., and Dreifuss, J.J. (1988). Localization and pharmacological characterization of high affinity binding sites for vasopressin and oxytocin in the rat brain by light microscopic autoradiography. Brain Res. *442*, 105–118.

Tsetsenis, T., Ma, X.H., Lo Iacono, L., Beck, S.G., and Gross, C. (2007). Suppression of conditioning to ambiguous cues by pharmacogenetic inhibition of the dentate gyrus. Nat. Neurosci. *10*, 896–902.

Veinante, P., and Freund-Mercier, M.J. (1997). Distribution of oxytocin- and vasopressin-binding sites in the rat extended amygdala: a histoautoradiographic study. J. Comp. Neurol. *383*, 305–325.

Viviani, D., and Stoop, R. (2008). Opposite effects of oxytocin and vasopressin on the emotional expression of the fear response. Prog. Brain Res. *170*, 207–218.

Walker, D.L., and Davis, M. (2008). Role of the extended amygdala in short-duration versus sustained fear: a tribute to Dr. Lennart Heimer. Brain Struct. Funct. *213*, 29–42.

Wilensky, A.E., Schafe, G.E., Kristensen, M.P., and LeDoux, J.E. (2006). Rethinking the fear circuit: the central nucleus of the amygdala is required for the acquisition, consolidation, and expression of Pavlovian fear conditioning. J. Neurosci. *26*, 12387–12396.

Worsley, K.J., Evans, A.C., Marrett, S., and Neelin, P. (1992). A three-dimensional statistical analysis for CBF activation studies in human brain. J. Cereb. Blood Flow Metab. *12*, 900–918.

Appendix 7

NeuroImage 47 (2009) 302–311

Contents lists available at ScienceDirect

NeuroImage

journal homepage: www.elsevier.com/locate/ynimg

Community structure in networks of functional connectivity: Resolving functional organization in the rat brain with pharmacological MRI

Adam J. Schwarz [1], Alessandro Gozzi, Angelo Bifone *

Neurosciences Centre of Excellence in Drug Discovery, GlaxoSmithKline S.p.A., Via Fleming 4, 37135 Verona, Italy

ARTICLE INFO

Article history:
Received 24 January 2009
Revised 10 March 2009
Accepted 22 March 2009
Available online 2 April 2009

Keywords:
Functional connectivity
Complex network
phMRI
Pharmacological MRI
fMRI
Rat
Brain
Amphetamine
Fluoxetine
Nicotine
Modularity
Community structure

ABSTRACT

In the study of functional connectivity, fMRI data can be represented mathematically as a network of nodes and links, where image voxels represent the nodes and the connections between them reflect a degree of correlation or similarity in their response. Here we show that, within this framework, functional imaging data can be partitioned into 'communities' of tightly interconnected voxels corresponding to maximum modularity within the overall network. We evaluated this approach systematically in application to networks constructed from pharmacological MRI (phMRI) of the rat brain in response to acute challenge with three different compounds with distinct mechanisms of action (*d*-amphetamine, fluoxetine, and nicotine) as well as vehicle (physiological saline). This approach resulted in bilaterally symmetric sub-networks corresponding to meaningful anatomical and functional connectivity pathways consistent with the purported mechanism of action of each drug. Interestingly, common features across all three networks revealed two groups of tightly coupled brain structures that responded as functional units independent of the specific neurotransmitter systems stimulated by the drug challenge, including a network involving the prefrontal cortex and sub-cortical regions extending from the striatum to the amygdala. This finding suggests that each of these networks includes general underlying features of the functional organization of the rat brain.

Introduction

Functional connectivity analyses of neuroimaging data aim to elucidate relationships between signals originating in spatially distinct brain regions, an approach that complements the more established univariate approaches in which the responses in each brain region are analyzed independently (influence of local smoothness notwithstanding). A number of recent studies have shown that functional imaging data sets from individuals or groups of subjects can be resolved into several distinct 'sub-networks', each of which comprises a set of distributed brain regions in which signal changes are correlated (Cordes et al., 2001; Fransson, 2005; Beckmann et al., 2005; De Luca et al., 2006; Damoiseaux et al., 2006; Schwarz et al., 2007a). These correlations are interpreted as reflecting a functional connectivity between the brain regions involved. In keeping with the concept that brain function involves interplay between segregation and integration, such networks have been identified in a number of experimental settings, including task-free ('resting state') fMRI data in humans (Cordes et al., 2001; Fransson, 2005; Beckmann et al., 2005; De Luca et al., 2006; Damoiseaux et al., 2006) and in response to pharmacological challenge in experimental animal models (Schwarz et al., 2007a).

This emphasis on interaction *between* different brain structures in the study of functional connectivity is a good conceptual match for considering the data as a graph, or complex network (Strogatz, 2001), of nodes and links. In this representation, image voxels or parcellated brain regions represent the nodes and a measure of similarity in their responses defines the links between them (Eguiluz et al., 2005; Salvador et al., 2005; Achard et al., 2006; Achard and Bullmore, 2007). Global statistical properties of the network can then be used to infer properties such as 'small world' behavior (Watts and Strogatz, 1998; Achard et al., 2006) which have deep implications for the behavior of the system as a whole.

However, in addition to evaluating global properties, working with a complex network representation of the data also allows the identification of different 'sub-networks' within the overall data set. Such a *network partitioning* essentially addresses the same problem as cluster analysis or independent component analysis (ICA) techniques—that is, to sensibly group brain regions into sets, for each of which the members have similar profiles. In the context of a complex network, partitioning algorithms seek a division of a network into groups of nodes whose within-group links are denser than links between

* Corresponding author.
E-mail address: angelo.2.bifone@gsk.com (A. Bifone).
[1] Present address: Translational Imaging Group, Exploratory and Program Medicine, Lilly Research Laboratories, Eli Lilly and Company, Indianapolis, Indiana 46285, USA.

1053-8119/$ – see front matter
doi:10.1016/j.neuroimage.2009.03.064

groups. The presence of this feature is commonly referred to as 'community structure,' from its origins in the study of social networks, but has recently seen application to complex networks more generally and a number of algorithms have been developed (Zhou, 2003; Clauset et al., 2004; Newman and Girvan, 2004; Vragovic and Louis, 2006; Newman, 2006a,b; Raghavan et al., 2007; Ruan and Zhang, 2008). In the case of complex networks derived from brain imaging data, network partitioning has the potential to reveal system-level functional structure of the brain. Moreover, the use of community structure algorithms based on the maximization of a network-theoretic quantity known as *modularity* provides a quantification of the emergent modularity within the network (Clauset et al., 2004; Newman, 2006b). That is, the optimum value of the modularity parameter for a given network reflects the degree of segregation between the different component sub-networks. Applications of community structure approaches based on maximum modularity to the partition of brain functional connectivity networks have been demonstrated in rodents (Schwarz et al., 2008) and, more recently, in humans (Meunier et al., 2009).

In the present paper we describe the partitioning of complex networks derived from the response of the rat brain to acute pharmacological challenge ("pharmacological MRI; phMRI"). Under these conditions, widespread networks of functional connections have been demonstrated (Schwarz et al., 2007a,b,c). However, it is unclear to what extent these patterns reflect interregional correlations induced by the drug challenge itself, or the intrinsic organization of the brain, perhaps determined by the structure of the underlying neuronal substrate. To this end, we investigated the community structure of functional connectivity networks under different pharmacological stimuli, thus probing the effects arising from the engagement of different neurotransmitter systems. Specifically, we compared the emergent community structure under different conditions to discriminate between connectivity patterns that are stimulus-specific and those independent of the particular neurotransmitter system(s) engaged by the drug, which may thus correspond to general features of the rat brain functional architecture.

We work within a formal network representation of the data with nodes defined at the voxel level, and the links reflecting signal correlations between pairs of nodes. While intra-subject temporal correlations are often used to infer functional connectivity from fMRI time series, this approach can be problematic in phMRI, due to the relatively slow and widespread signal changes typically induced by a pharmacological challenge (Schwarz et al., 2007b). However, across-subject correlations in response amplitude have been used for many years with imaging techniques that do not afford high-temporal resolution, e.g., in 2DG autoradiography (Soncrant et al., 1986) and FDG-PET (Horwitz et al., 1998). By extending this approach to the analysis of phMRI data, we have recently demonstrated functional connectivity along specific neurotransmitter pathways in the rat brain under pharmacological stimulation (Schwarz et al., 2007a,b). Here, we construct and characterize whole-brain functional networks derived from inter-subject correlations in the response amplitude following drug administration. We employ a community structure algorithm based on the maximization of modularity to extract 'sub-networks' of tightly interconnected nodes and investigate differences and common features in the connectivity as the pharmacological stimulus is varied. Moreover, in order to identify the central structural features of these sub-networks, we specify a criterion to discriminate between 'core' and 'peripheral' nodes, i.e. between those that are much more densely connected to nodes within their assigned group than to those outside it, and nodes that are more loosely integrated within the assigned community.

This substantially extends recent work on complex network analyses of phMRI data (Schwarz et al., 2008) in two ways: (a) by providing a comparative partitioning across networks derived from different pharmacological challenges, thus allowing identification of common functional structures that are stimulus-independent; and (b) by specification of a criterion to improve the identification of the core structure of each sub-network.

Methods

MRI data acquisition

All experiments were carried out in accordance with Italian regulations governing animal welfare and protection. Protocols were also reviewed and consented to by a local animal care committee, in accordance with the guidelines of the Principles of Laboratory Animal Care (NIH publication 86–23, revised 1985). The data described in this paper originate from three studies, for which acquisition details were substantially similar and which have been published previously (Gozzi et al., 2006, 2008; Schwarz et al., 2007b). In short, phMRI data sensitive to changes in relative cerebral blood volume (rCBV) were acquired from male Sprague–Dawley rats on a Bruker 4.7T system under 0.8% halothane maintenance anesthesia, neuromuscular blockade and artificial ventilation with blood gas values maintained within physiological range ($30<pCO_2<50$; $pO_2>100$). Images were sensitized to rCBV changes by injection of the blood pool contrast agent Endorem (2.67 ml/kg). Anatomical reference images were acquired using a RARE sequence with RARE factor 32, matrix 256×256, FOV 40 mm, 16 contiguous 1 mm coronal slices, $TR_{eff}=5500$ ms, $TE_{eff}=76$ ms. This was followed by a time series acquisition using the same sequence, but with reduced matrix size (128×128), $TR_{eff}=2700$ ms and $TE_{eff}=100$ ms. Acquisition time per image volume was 20 s, with 4 successive excitations averaged and 64 time points per subject. In the first study, the animals were challenged with either *d*-amphetamine (1 mg/kg i.v., $N=17$) or vehicle (saline, $N=7$) respectively (Schwarz et al., 2007a,b). In the second, animals were challenged with fluoxetine (10 mg/kg i.p., $N=7$) (Schwarz et al., 2007b). In the third, animals were challenged with nicotine (1 mg/kg i.v., $N=9$) (Gozzi et al., 2006). All drug challenges were infused over 1 min following 30 min equilibration after contrast agent administration. Subsequent signal changes were tracked for approximately 20 min after the challenge, to capture the initial rCBV changes following infusion. In all cases, the drug-induced changes in peripheral arterial blood pressure were within the autoregulatory range associated with halothane anesthesia ($60<BP<120$ mm Hg) (Zaharchuk et al., 1999; Gozzi et al., 2007), within which abrupt pharmacological manipulation of blood pressure can be homeostatically compensated without producing significant alterations of CBV.

In total, complex networks were constructed as detailed below from four subject cohorts: the *d*-amphetamine and vehicle groups in the first study as well as from the fluoxetine and nicotine arms in the second and third.

PhMRI analysis details

Following spatial and temporal pre-processing (Schwarz et al., 2003, 2006, 2007b), image based time series analysis of the response in individual subjects was carried out within a general linear model framework (Schwarz et al., 2007b,d) in order to calculate 3D maps of the post-injection response amplitude in each subject. The response maps for the subjects in each study were then stacked together so that each voxel had an associated vector of response amplitudes across subjects. The inter-subject correlations analyzed here leverage the differential anatomical profiles of phMRI response between subjects (Fig. 1(a)).

Creation of network representations

The individual subject response amplitude maps calculated at the dimensions of the standard template brain (Schwarz et al., 2006) were

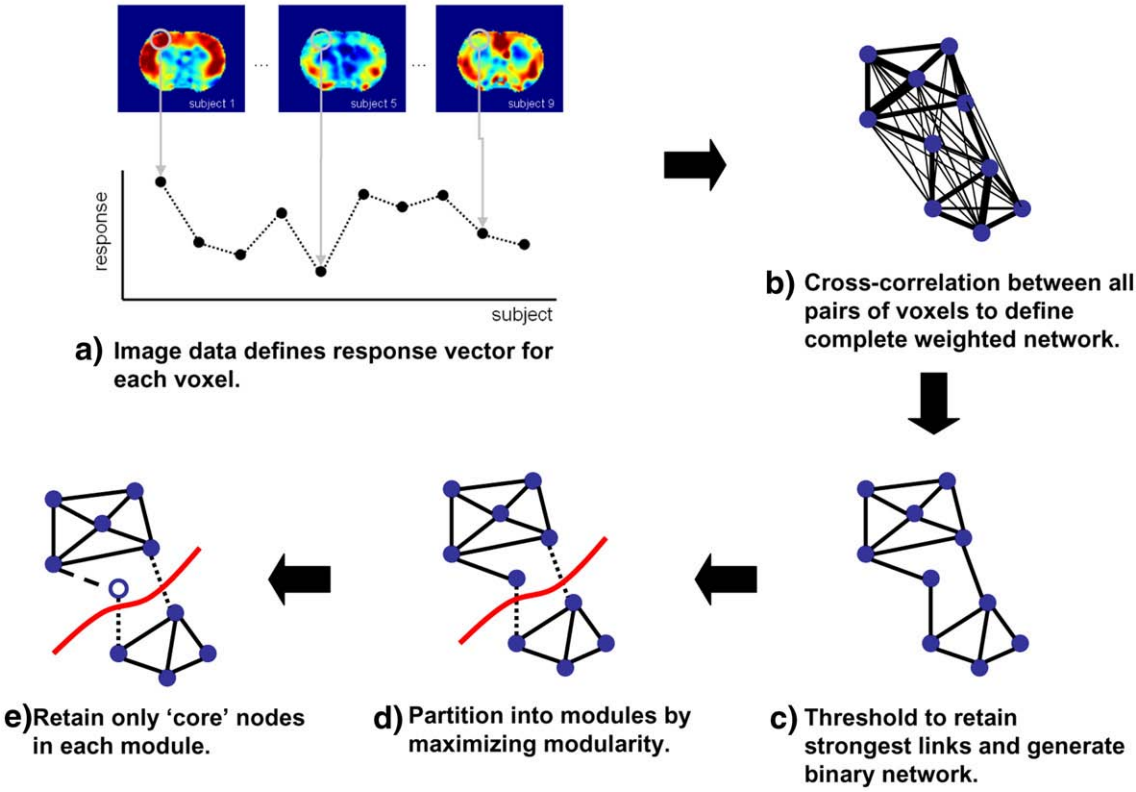

Fig. 1. Schematic overview of network creation and analysis. (a) The phMRI signal amplitude defines a response vector for each brain region or voxel. (b) Considering each voxel as a node, correlations between these vectors are used to determine link strengths in a complete, weighted network representation of the data. (c) The network is binarized by retaining only links of weight greater than a certain threshold. (d) The application of a community structure algorithm partitions the full network into 'communities' of densely interconnected nodes. (e) The use of a null model enables the selection of 'core' nodes, preferentially connected to other nodes within the same community.

rebinned in-plane by a factor of two. This was performed so that subsequent adjacency matrices remained within the memory limits of the IDL software used for much of the processing and also provided voxel volumes closer to the actual acquisition resolution (as part of the spatial normalization process, the time series' were rebinned to the template resolution; voxel size $1.94\times1.94\times8$ mm^3). For each study, a binary brain mask (Schwarz et al., 2006), covering only slices for which complete data were present for all subjects in the cohort, was used to define brain parenchyma voxels for further analysis.

A fully weighted, complete network was created for each study by considering each voxel as a node and defining the strength of the edge between each pair of voxels based on the linear correlation between the response vectors associated with each (Fig. 1(b)). Specifically, the weight of each edge w_{ij} was defined as the absolute value of the Pearson correlation coefficient r_{ij} between the inter-subject response amplitudes in each voxel, converted to lie under an approximately normal distribution by applying Fisher's r-to-z transformation:

$$w_{ij} = |z_{ij}|,$$
$$z_{ij} = \frac{1}{2}\log\left(\frac{1+r_{ij}}{1-r_{ij}}\right) \quad (1)$$

where $i, j \in \{1,\ldots, N_{\text{nodes}}\}$ specify the pair of nodes connected by each edge. These networks are undirected—each edge simply conveys the strength of a connection without regard to a causal direction. Each of the four weighted networks was then converted into a binary one by retaining only the edges with the highest weights (i.e., representing the strongest connections) (Fig. 1(c)). This step was performed in order to make networks of this size tractable for further analysis—the implementation of the community structure algorithm employed for network partitioning (see below) was only compatible with binary networks. Although extension of complex network theory to weighted networks is of considerable current interest, properties of binary networks are well established and previous fMRI complex network studies (Eguiluz et al., 2005; Achard et al., 2006) have also employed a binarization step. We applied a threshold determined as that which retained the strongest 2% of the $N_{\text{nodes}}\times(N_{\text{nodes}}-1)/2$ edges in the fully weighted network. This value was empirically determined as one that allows a diversity of node connectivities, while retaining a connected network (Schwarz et al., 2008; see also Discussion).

The resulting binary networks can be represented mathematically by an adjacency matrix A, whose elements a_{ij} describe the connectivity:

$$a_{ij} = \begin{cases} 1, \text{if nodes } i \text{ and } j \text{ are connected} \\ 0, \text{ otherwise.} \end{cases} \quad (2)$$

The numbers of nodes remaining in each network were 9898 (amphetamine), 11459 (fluoxetine), 11607 (nicotine) and 9917 (vehicle).

Network partitioning—community structure decomposition

To explore the 'community structure' within the phMRI networks (Fig. 1(d)) we applied a recent algorithm that seeks a network partition maximizing a cost function known as the *modularity*, $Q \in [-1, 1]$, defined for a binary network as

$$Q = \frac{1}{4m}\sum_{i,j}\left(A_{ij} - \frac{k_i k_j}{2m}\right)\delta_{ij}^{\text{group}}, \quad (3)$$

where $m = \frac{1}{2}\sum_{i,j} A_{ij}$ is the total number of edges in the network, $k_i = \Sigma_j A_{ij}$ is the degree of node i and $\delta_{ij}^{\text{group}}$ equals 1 if nodes i and j are in the same community and 0 otherwise. For a given partition of the network, Q measures the difference between the fraction of the edges

connecting nodes within communities and the same fraction in the case of a randomly connected network with the same partition. The closer the value of Q is to its theoretical maximum 1, the stronger the community structure, i.e. the more modular the network. Algorithms seeking a network partition that maximizes modularity yield an estimate of the number of communities into which the network should be optimally split, the composition of each community and an associated value of Q.

In this study we used the 'Fast Community' algorithm (http://www.cs.unm.edu/~aaron/research/fastmodularity.htm), which has only a linear dependence of computation time on network size. (The community structure of the networks evaluated in this study were resolved in ~3 min each on an IBM Intellistation Z pro dual-core workstation, a process that involved two runs of the algorithm—one to determine the step at which the maximum value of Q was reached, and a second to repeat and save the resulting partition corresponding to that step). Since this algorithm assigns every node to a community, very small clusters of loosely connected nodes may be identified as communities. In order to avoid this potential confound, we applied a cut-off of $N=100$ (approx 1% of the total number of nodes) as the minimum size for a community to be carried forward for further analysis. A cut-off for small clusters is justified theoretically by the intrinsic "resolution limit" of approaches based on maximum modularity (Fortunato and Barthelemy, 2007) (see also Discussion). Nevertheless, all communities whose size was below this threshold were inspected to assess the number of edges and the distribution of nodes with respect to the anatomical reference images in order to ensure that no meaningful communities were unduly discarded. Inspection of the communities below the cut-off showed a few clusters comprising very few nodes (in most cases fewer than 10), whose distribution was scattered and not considered meaningful within the aims of this study.

Core vs. peripheral nodes

Since the community structure algorithm *per se* assigns every node to a community, it is useful to have some basis for disregarding nodes that may be as strongly connected to nodes in other communities as to those in their own (or more so, if the node has been erroneously assigned by the algorithm). A measure of how 'internal' each node is to its community can be provided by the difference between the number of connections to other nodes in the same community (k_{in}) and those to nodes outside its community (k_{out}) (Radicchi et al., 2004). As we were primarily interested in identifying nodes with high connectivity to other nodes assigned to the same community, we defined the nodewise measure Δk as:

$$\Delta k = \frac{k_{in} - k_{out}}{N_c} \times 100 \quad (4)$$

where N_c is the number of nodes in the community and the maximum value is scaled to 100 (cf. Guimera et al., 2005; Guimera and Nunes Amaral, 2005 and see also Discussion). 'Core' nodes, with $k_{in} \gg k_{out}$ would therefore be associated with high values of Δk, whereas 'peripheral' nodes may have $k_{in} \sim k_{out}$ and hence $\Delta k \sim 0$. This concept provides the basis of a simple thresholding procedure to retain only the core nodes in each community. We generated five instances of a random network of a similar size (10^4 nodes) to the phMRI networks. In each case, weighted adjacency matrices were created with link weights randomly distributed under a zero-mean, unit standard deviation normal distribution. Then, the 2% of the links with the greatest weight magnitude were retained to form a binary network (i.e., as per the phMRI networks described above). We then applied the community structure algorithm to these random networks to derive a histogram of Δk capturing the distribution of the intra- vs. inter-community link counts. The algorithm determined a similar number of communities for the random networks as for the phMRI networks, but with qualitatively different Δk distributions (values tightly clustered around zero). Histograms were very similar for each of the five random networks and could be accurately modeled by a Gaussian distribution. Accordingly, a histogram of Δk from all communities combined was fit with a Gaussian function to determine the mean ($\mu = -0.164$) and standard deviation ($\sigma = 0.268$) of Δk for the random network case. From these values, a threshold corresponding to $p=0.05$ (Bonferroni-corrected; $\mu + 4.4\sigma$) was determined as $\Delta k = 1.02$. For each community, nodes with $\Delta k > 1.02$ were mapped at their voxel locations on anatomical template in a color map proportional to Δk, whereas nodes with $\Delta k < 1.02$ were considered not significantly "within" the community under this random-network model (Fig. 1(e)).

Network modularity null model

The theoretical value for the modularity of a random network is zero. However, finite random networks can present finite, positive values of the parameter Q due to statistical fluctuations (Guimera et al., 2004). Hence, the values of maximum modularity obtained for the real functional connectivity networks under investigation must be interpreted in comparison with an appropriate null model. To this end, we used the maximum modularity values for the five random networks described above as a comparator.

Results

Modularity and binarization threshold for phMRI networks

The community structure approach based on maximum modularity partitioned each network into three communities. The maximum modularity values, Q_{max}, are summarized in Table 1. Of the four phMRI networks, the values of Q_{max} were higher for the three networks constructed from response to the psychoactive compounds (0.31–0.38) than that for the vehicle network (0.29). However, all four had Q_{max} significantly greater than values found with equivalent random networks (~0.05).

In the same table, the binarization thresholds applied to retain 2% of the links in each network are also reported. The value z of the threshold reflects the average strength of the correlations for each treatment group. The lowest threshold was applied to the vehicle network, reflecting substantially weaker inter-voxel correlations. Application of a higher threshold would have yielded fewer links (less than 0.1% or 0.5%, at $z=3.85$ and $z=3.45$), with many disconnected nodes, consistent with an overall more loosely connected network for the vehicle control group.

Distribution of Δk

The distribution of Δk for the random networks yielded a bimodal distribution, with most values clustered about $\Delta k = 0$ and the remainder under a second peak at $\Delta k \sim -11$. The portion of the

Table 1
Binarization threshold (z), and maximum modularity (Q_{max}) found using the FastCommunity algorithm for each of the four phMRI networks and the random networks.

Drug	z-threshold	Q_{max}
Amphetamine	3.45	0.31
Fluoxetine	3.45	0.38
Nicotine	3.85	0.37
Vehicle	3.05	0.29
Random[a]	2.33 ± 2.9e-4	0.051 ± 0.00017

[a] Mean ± standard deviation of $N=5$ instances of random network.

histogram at $\Delta k \sim 0$ was well described by a Gaussian function which was fit to the data in order to establish a positive cut-off value of Δk, for which larger values could be interpreted as unlikely under the null scenario of random connections (Fig. 2(a)). A one-sided probability of $p_{corr} < 0.05$ under this null distribution was used to derive a cut-off value of $\Delta k > 1.02$ to define the 'core' nodes in each community.

Applying this threshold to the phMRI networks removed nodes with $\Delta k < 1.02$ that were not sufficiently 'internal' to the community, or were mis-assigned ($\Delta k < 0$) (Fig. 2(b)). In two of the three communities in each of the three active challenge phMRI networks, these removed nodes corresponded mainly to voxels around the edges (spatially) of node clusters containing anatomically reasonable distributions of core nodes. Additionally, one of the three communities in each active-challenge phMRI network comprised almost exclusively below-threshold nodes, with few surviving the thresholding process (Fig. 2(b)).

Anatomical distribution of voxel communities

In all three active-challenge phMRI networks, the two communities with voxels predominantly surviving the random model thresholding corresponded to anatomically plausible, symmetrical distributions of voxels (Figs. 3(a–c)). In each case, one community was dominated by voxels in the cortex—particularly sensorimotor regions—while the other identified connectivity structure that included more sub-cortical and limbic areas.

In the amphetamine network, the second community comprised voxels primarily in sub-cortical regions and prefrontal cortices (Fig. 3(a))—a pattern that strongly resembled the 'mesolimbic dopamine' signature previously obtained from a cluster analysis of the same data (Schwarz et al., 2007a). (This community also provided a most dramatic illustration of the utility of the thresholding method to retain core nodes—see Supplementary data).

In the fluoxetine network, the second community presented a different anatomical distribution, involving the prefrontal and anterior cingulate cortices, ventral cortical regions (e.g., Piriform cortex), the amygdala and more extensive involvement of the striatum, thalamus and hippocampus (Fig. 3(b)).

In the nicotine network, the sensorimotor cortical regions were grouped together with voxels in the thalamus, hypothalamus, hippocampus and inferior colliculi (Fig. 3(c)).The second community included voxels in cingulate, prefrontal and orbitofrontal cortices, extending back to the striatum, amygdala, piriform cortex, entorhinal cortex and visual/parietal cortices.

In contrast to the three networks derived from active drug challenge, the community structure in the vehicle (saline) network

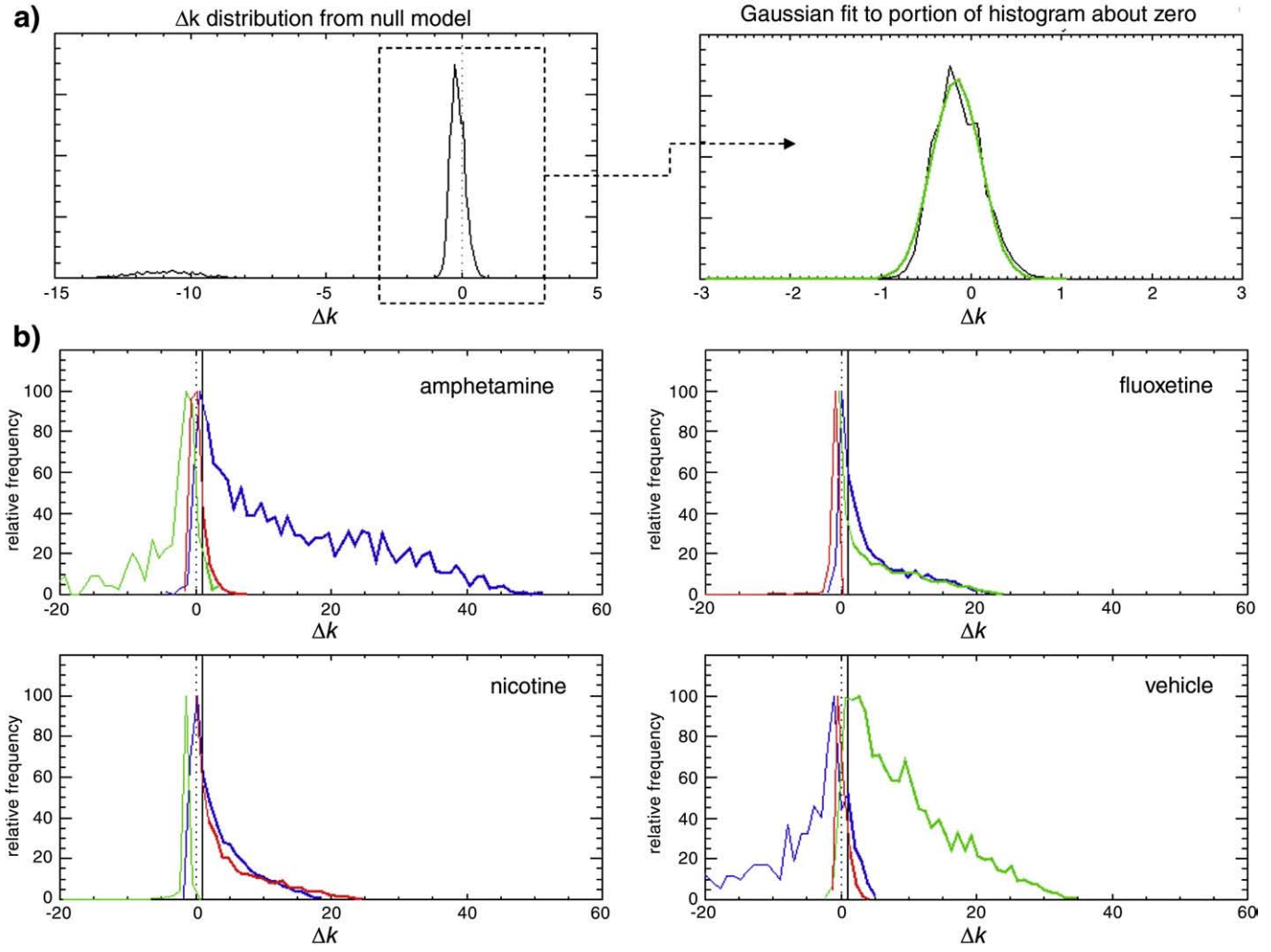

Fig. 2. (a) Distribution of Δk following partitioning of the null model networks. The peak centered close to zero was well described by a Gaussian distribution. Since we are interested in identifying nodes with positive Δk values greater than expected in the null scenario, we selected a threshold value corresponding to a one-sided $p < 0.05$ under this null distribution (Bonferroni-corrected for multiple comparisons by the number of nodes in the network)—namely $\Delta k = 1.02$. (b) Histograms of Δk for each community in each of the four networks. Portions of the histogram corresponding to $\Delta k > 1.02$ are shown in bold to the right of the solid vertical line and represent core nodes retained after the thresholding procedure. $\Delta k = 0$ is shown as a vertical dotted line. Histograms of the different communities are shown in different colors for clarity.

Appendix 7

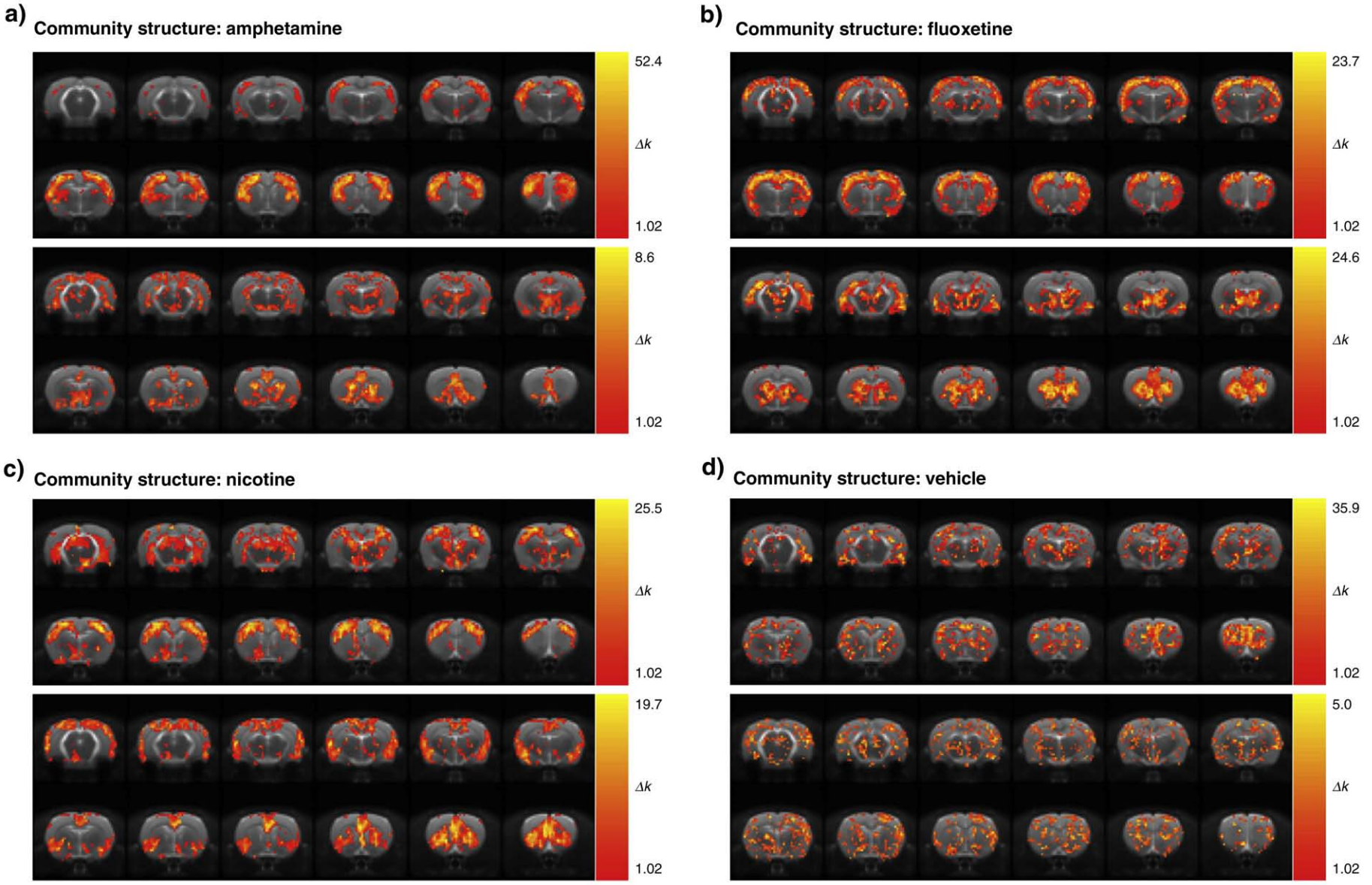

Fig. 3. Community structure as a function of pharmacological challenge. Maps of the voxels in each of the two major communities resolved by the maximum-modularity partitioning of the four networks are shown for (a) d-amphetamine, (b) fluoxetine, (c) nicotine and (d) saline. For each community, the 'core' nodes surviving the null model thresholding are mapped at their corresponding voxel locations. The color assigned to each voxel reflects the Δk statistic at that node.

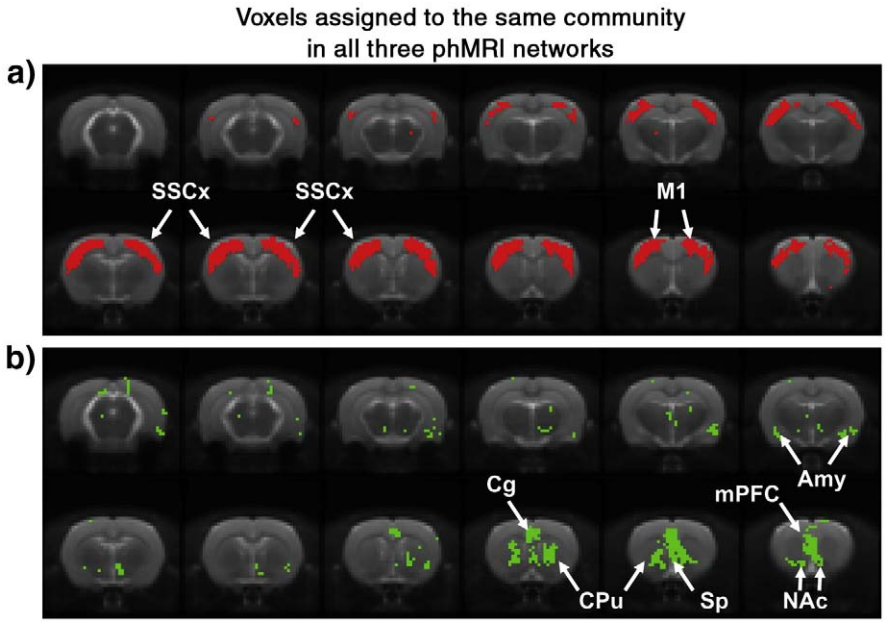

Fig. 4. Voxels assigned to the same community in all three drug-challenge phMRI networks. (a) A set of cortical voxels comprising motor (M1), somatosensory (SSCx) and parietal cortices. (b) A set of voxels in regions including cingulate (Cg) and medial prefrontal (mPFC) cortices, parts of the caudate putamen (CPu) and accumbens (NAc), septum/BNST (Sp), hypothalamus and amygdale (Amy).

resulted in more scattered, less symmetric anatomical distributions of voxels (Fig. 3(d)). The main anatomical features present were a concentration of voxels with higher Δk values in the mPFC and ventral hippocampal regions in the first community.

Common connectivity features across the drug-challenge networks

While there were some interesting differences between the communities identified for each drug, common connectivity features independent of the drug challenge were apparent in the three phMRI maps. The voxels that were commonly assigned to each community across all three drug challenge networks are shown in Fig. 4. Motor and somatosensory cortical regions were consistently grouped together (Fig. 4(a)). Another connectivity signature common across all drug challenges comprised voxels in cingulate and medial prefrontal cortices, parts of the caudate putamen and accumbens, hypothalamus and amygdala (Fig. 4(b)). The functional division identified between sensorimotor and cingulate/prefrontal cortices is consistent with neuroanatomical boundaries (Paxinos and Watson, 1998).

Discussion

We have shown that phMRI data, represented mathematically as a network of nodes with links determined by correlation strength, can be partitioned into meaningful 'communities' of closely interconnected voxels by means of a widely-used community structure algorithm. When mapped back into the anatomical space of the rat brain, these communities presented anatomically reasonable, bilateral patterns for all three drugs investigated.

The correlations in response amplitude used to determine the connections between nodes can be considered to represent a functional coupling between the different brain regions in response to the pharmacological challenge administered. This interpretation is consistent with the brain structures identified as being functionally connected in the different communities. In the *d*-amphetamine network, the communities identified strongly resembled the 'fronto-cortical' and 'mesolimbic dopamine' distributions found by applying a *k*-means clustering algorithm to the same data set (Schwarz et al., 2007a). The mesolimbic dopamine system in particular is a critical brain system underlying response to rewarding stimuli and implicated in psychiatric conditions including drug addiction, depression and schizophrenia (Hyman and Malenka, 2001; Laruelle et al., 2003; Nestler and Carlezon, 2006) and was delineated by the present method as a set of functionally connected brain structures including the dopaminergic midbrain (ventral tegmental area), striatum and prefrontal/cingulate cortices. The identification of such functional structure opens the possibility of detecting modulation of this brain system in disease models or by pharmacological treatment (Schwarz et al., 2007c). In the fluoxetine network, the second community was highly reminiscent of the sub-cortical 'network' identified in a prior seed-region analysis (Schwarz et al., 2007b). In the nicotine network, the second community closely resembled the univariate activation map but with increased involvement of the parietal and visual cortices. In contrast, the univariate activation maps in the amphetamine and fluoxetine data sets more closely resembled the predominantly cortical regions assigned to the first community.

These data show that each of three distinct drug challenges induces coupled responses in particular communities of connected brain regions, including structures not identified in a standard univariate group comparison with vehicle. Interestingly, a group of voxels involving the prefrontal/cingulate cortices and parts of the caudate putamen, accumbens, septum/BNST and amygdala were grouped together in all three pharmacological challenge networks, as were a group of voxels in the sensorimotor cortex. This suggests that the response to pharmacological stimulus involves tightly coupled responses in these regions independent of the specific drug employed, and is consistent with evidence showing strong intrinsic connectivity between neurons in these brain structures; in particular, a group of structures extending from the central nucleus of the amygdala rostral through the bed nucleus of the stria terminalis to the nucleus accumbens has been proposed as a functional unit known as the extended amygdala and underlying the reinforcing properties of drugs of abuse (Koob, 2003). Consistent with this, the present data identified pixels in these regions along with parts of the caudate putamen, prefrontal and cingulate cortices as a functional unit independent of the three challenge drugs. Moreover, the finding of this grouping of brain structures across all three compound networks

suggests that these regions respond as a functional unit more generally than just in a drug dependence setting. Finally, while most functional connectivity studies with human structural or functional data have resolved mostly cortical networks, the present results demonstrate key features within the organization of the limbic system and its interface to the prefrontal cortex.

Since the community structure algorithm assigns every node to a community, an important aspect of the present study was the use of a random network model to provide a well-defined "null" distribution of Δk and hence a basis for deciding whether a node is really 'within' its assigned community (having many more connections to nodes within the same community than to those in others). In other words, the thresholding procedure provided a means of retaining only core nodes and eliminating peripheral nodes that are not strongly within the community to which they were assigned by the algorithm. The model applied in this study was derived from simple random networks but there is scope for the development of more sophisticated null scenarios. In a conceptually different approach to thresholding nodes based on the Δk statistic, core nodes can also be identified as those whose community assignment is stable upon multiple network partitions with noise added to the edge weights (Gfeller et al., 2005). Moreover, while in the present study we sought a core/peripheral node distinction, a more general consideration of the role of nodes based on their topological characteristics is possible. For example, a measure of within-community degree and a 'participation coefficient' capturing the extent to which a node is linked outside its community were used together to define a range of node roles, including 'connectors' which possess many links to more than one community and are thus critical for communication between communities (Guimera et al., 2005; Guimera and Nunes Amaral, 2005).[2] The identification of 'hubs' or nodes with connector properties from human structural and resting state functional connectivity networks has also been recently reported (Hagmann et al., 2008). Whereas our emphasis in the present study was on the segregation of the functional connectivity networks into functional units, nodes (and hence neuroanatomical regions) with connector-like roles are likely to be critical to the integration of these separate functional units (Hagmann et al., 2008; Buckner et al., 2009). These aspects remain to be elucidated for the rat brain.

Community structure algorithms provide an attractive means of partitioning functional connectivity data represented as networks. The algorithm employed in the present study enabled the large ($\sim 10^4$ node) networks, created from a voxel-level representation of the imaging data, to be partitioned in a reasonable computation time. However, an issue with many algorithms based on the maximization of modularity is what is referred to as a "resolution limit" (Fortunato and Barthelemy, 2007)—small communities tend not to be detected as the algorithm identifies structure on a scale similar to that of the parent network. This may be the case in the present data, where all four phMRI networks were partitioned into three communities, each with membership on the order of thousands. Despite the compelling anatomical distributions of the functional structures identified, the present results may not therefore represent globally optimal partitions of the networks including structure on all network size scales. However, the *d*-amphetamine data set was also partitioned using a *k*-means clustering approach (Schwarz et al., 2007a), which showed a similar subdivision in terms of number and size of clusters of nodes as those found in the present study. Moreover, pharmacological stimuli activate widespread neurotransmitter networks (e.g., dopaminergic for *d*-amphetamine or serotonergic for fluoxetine) which project extensively in the brain, and are unlikely to result in small and localized sub-networks of correlated activity. Nevertheless, a potential bias towards large communities should be borne in mind when interpreting the present results. The development of community structure algorithms that do not suffer from this limitation is an active area of current research in the field of complex networks (Rosvall and Bergstrom, 2007, 2008; Ruan and Zhang, 2008; Arenas et al., 2008).

The correlations between the responses in all pairs of voxels generate variable link weights in a weighted, complete network (i.e., all possible connections exist). However, in large networks such as those investigated in the present study (ca. 10^4 nodes), a conversion of the fully-weighted network into a binary one is often necessary for reasons of computational tractability. We thresholded each network so as to retain the strongest 2% of the edges in a binarized version. The resulting network topology represents a middle ground between two undesirable extremes. As more edges are retained, node connections become increasingly dense and, since weight values are ignored, dynamic range in the link weights and hence topological distinction is lost. Alternatively, as fewer edges are retained, the network becomes disconnected and topological information also becomes suppressed. To assess the impact of the choice of binarization threshold on the resulting communities, we also ran the algorithm on versions of the networks created using different thresholds. For thresholds such that the retained fraction of links was in the range ~1%–10%, the main features of the communities were stable and independent of the precise choice of threshold. For fractions lower and higher than this, the communities began to split and merge respectively, consistent with the loss of information associated with the two extreme cases outlined above.

The images were smoothed before conversion into the network representation, introducing a local correlation between responses in neighboring voxels. However, a key reason for smoothing is to compensate in part for residual differences in image alignment between different subjects when performing group-level, voxelwise operations. In the present data, the networks are derived from inter-subject correlations and so this point is critical. To assess the effect of smoothing, we also performed the analyses on networks derived from unsmoothed image data. The anatomical structures identified in each community were highly consistent between networks constructed from the smoothed and unsmoothed data, while the maps were much cleaner in the smoothed case (see Supplementary data).

In addition to comparing networks derived from the response to three active compounds at active doses, we explicitly considered a network constructed from a vehicle group throughout. This provides a valuable comparator in the interpretation of results from the other three networks beyond parameters derived from the random networks. Explicit comparison with a vehicle group is standard practice in order to differentiate the effects of the pharmaceutical compound from those due to the solvent in which it is dissolved. Ideally a benign vehicle, such as physiological saline in the present study, is used and expected to elicit minimal central response *per se*. This is reflected in the overall weaker correlations, as reflected by the lower binarization threshold that retained 2% of the nodes. Nevertheless, in addition to capturing physiological 'baseline' variation in the time courses, the injection of a vehicle bolus may conceivably give rise to weak functional effect. In the present study, an intravenous injection volume of 1 ml/kg was used, along with a 0.3 ml/kg flush, yielding a total injection volume of 1.3 ml/kg, injected over 1 min. For a 300 g rat, assuming a blood volume of 18.77 ml this equates to ~7% of the total blood volume. When using blood pool contrast agents, this results in a slight dilution of the agent which can manifest as a small signal change post-injection. The injection may also give rise to an autonomic response related to the sensation of the injection. The network analysis of the vehicle data showed weaker neuroanatomical features than in the other three networks, but nevertheless a substantially larger value

[2] Interestingly, in the context of an emphasis on connections between communities, nodes with many or all of their links within the same community were designated 'peripheral' in (Guimera et al., 2005; Guimera and Nunes Amaral, 2005), in contrast to the terminology employed in the present study.

of the maximum modularity coefficient compared to a random network, and some anatomical dependence, suggesting correlated responses in the mPFC and ventral hippocampus.

The networks examined in the present study were derived from inter-subject correlations in the haemodynamic response amplitude following acute drug administration. Complex networks can also be generated from intra-subject temporal correlations, for example those examined in studies of baseline or 'resting state' functional connectivity (Raichle and Snyder, 2007) or from task-evoked responses (Eguiluz et al., 2005). Several recent studies have demonstrated correlations in resting-state low-frequency fMRI signal fluctuations in anaesthetized rodents (Kannurpatti et al., 2003; Lu et al., 2007; Pawela et al., 2008; Zhao et al., 2008; Kannurpatti et al., 2008). Interestingly, bilateral patterns of connectivity were observed applying seed-region correlation analysis under various anaesthetic regimens, including urethane (Kannurpatti et al., 2003), medetomidine (Pawela et al., 2008; Zhao et al., 2008), isoflurane (Kannurpatti et al., 2008) and alpha-chloralose (Lu et al., 2007). Functional connectivity derived from temporal correlations is conceptually different from the connectivity whose structure was explored here. While the former relies on spontaneous fluctuations, whose origin is still the subject of active investigation, our approach exploits the inter-subject variability in the response to a pharmacological challenge and reflects correlated responses to specific stimuli. The approach of community structure partitioning is easily applicable to all these scenarios and the modular structure identified within such functional connectivity networks may reveal important aspects of brain function not resolved by global network analyses (Achard and Bullmore, 2007).

In conclusion, we have shown that functional imaging data, represented as a network of nodes and links, can be partitioned into communities of tightly interconnected voxels using a network-theoretic algorithm to determine a solution corresponding to maximum modularity within the overall network. The specification and characterization of null comparator networks provided a means to retain only the core nodes representing true functional structure within each community. Investigating the functional structure of the rat brain in response to pharmacological challenge with three different psychoactive compounds revealed bilaterally symmetric patterns of functional connectivity underlying the engagement of different neurotransmitter systems *in vivo*. Moreover, common features across all three networks revealed two groups of brain structures that responded as functional units independent of the drug challenge, including a network involving the prefrontal cortex and sub-cortical regions extending from the striatum to the amygdala. This finding indicates that the engagement of these functional units does not depend on the specific neurotransmitter system or pattern of activation elicited by the drug, but reflects general features of the functional organization of the rat brain.

Appendix A. Supplementary data

Supplementary data associated with this article can be found, in the online version, at doi:10.1016/j.neuroimage.2009.03.064.

References

Achard, S., Bullmore, E., 2007. Efficiency and cost of economical brain functional networks. PLoS. Comput. Biol. 3, e17.
Achard, S., Salvador, R., Whitcher, B., Suckling, J., Bullmore, E., 2006. A resilient, low-frequency, small-world human brain functional network with highly connected association cortical hubs. J. Neurosci. 26, 63–72.
Arenas, A., Duch, J., Fernandez, A., Gomez, S., 2008. Size reduction of complex networks preserving modularity. New J. Physics 9, 176–191.
Beckmann, C.F., DeLuca, M., Devlin, J.T., Smith, S.M., 2005. Investigations into resting-state connectivity using independent component analysis. Philos. Trans. R. Soc. Lond B Biol. Sci. 360, 1001–1013.
Buckner, R.L., Sepulcre, J., Talukdar, T., Krienen, F.M., Liu, H., Hedden, T., ndrews-Hanna, J.R., Sperling, R.A., Johnson, K.A., 2009. Cortical hubs revealed by intrinsic functional connectivity: mapping, assessment of stability, and relation to Alzheimer's disease. J. Neurosci. 29, 1860–1873.
Clauset, A., Newman, M.E., Moore, C., 2004. Finding community structure in very large networks. Phys. Rev. E. Stat. Nonlin. Soft. Matter Phys. 70, 066111.
Cordes, D., Haughton, V.M., Arfanakis, K., Carew, J.D., Turski, P.A., Moritz, C.H., Quigley, M.A., Meyerand, M.E., 2001. Frequencies contributing to functional connectivity in the cerebral cortex in "resting-state" data. AJNR Am. J. Neuroradiol. 22, 1326–1333.
Damoiseaux, J.S., Rombouts, S.A., Barkhof, F., Scheltens, P., Stam, C.J., Smith, S.M., Beckmann, C.F., 2006. Consistent resting-state networks across healthy subjects. Proc. Natl. Acad. Sci. U. S. A. 103, 13848–13853.
De Luca, M., Beckmann, C.F., De, S.N., Matthews, P.M., Smith, S.M., 2006. fMRI resting state networks define distinct modes of long-distance interactions in the human brain. Neuroimage 29, 1359–1367.
Eguiluz, V.M., Chialvo, D.R., Cecchi, G.A., Baliki, M., Apkarian, A.V., 2005. Scale-free brain functional networks. Phys. Rev. Lett. 94, 018102.
Fortunato, S., Barthelemy, M., 2007. Resolution limit in community detection. Proc. Natl. Acad. Sci. U. S. A. 104, 36–41.
Fransson, P., 2005. Spontaneous low-frequency BOLD signal fluctuations: an fMRI investigation of the resting-state default mode of brain function hypothesis. Hum. Brain Mapp. 26, 15–29.
Gfeller, D., Chappelier, J.C., De Los, R.P., 2005. Finding instabilities in the community structure of complex networks. Phys. Rev. E. Stat. Nonlin. Soft. Matter Phys. 72, 056135.
Gozzi, A., Schwarz, A., Reese, T., Bertani, S., Crestan, V., Bifone, A., 2006. Region-specific effects of nicotine on brain activity: a pharmacological MRI study in the drug-naive rat. Neuropsychopharmacology 31, 1690–1703.
Gozzi, A., Ceolin, L., Schwarz, A., Reese, T., Bertani, S., Crestan, V., Bifone, A., 2007. A multimodality investigation of cerebral hemodynamics and autoregulation in pharmacological MRI. Magn Reson. Imaging 25, 826–833.
Gozzi, A., Large, C.H., Schwarz, A., Bertani, S., Crestan, V., Bifone, A., 2008. Differential effects of antipsychotic and glutamatergic agents on the phMRI response to phencyclidine. Neuropsychopharmacology 33, 1690–1703.
Guimera, R., Nunes Amaral, L.A., 2005. Functional cartography of complex metabolic networks. Nature 433, 895–900.
Guimera, R., Sales-Pardo, M., Amaral, L.A., 2004. Modularity from fluctuations in random graphs and complex networks. Phys. Rev. E. Stat. Nonlin. Soft. Matter Phys. 70, 025101.
Guimera, R., Mossa, S., Turtschi, A., Amaral, L.A., 2005. The worldwide air transportation network: anomalous centrality, community structure, and cities' global roles. Proc. Natl. Acad. Sci. U. S. A. 102, 7794–7799.
Hagmann, P., Cammoun, L., Gigandet, X., Meuli, R., Honey, C.J., Wedeen, V.J., Sporns, O., 2008. Mapping the structural core of human cerebral cortex. PLoS. Biol. 6, e159.
Horwitz, B., Rumsey, J.M., Donohue, B.C., 1998. Functional connectivity of the angular gyrus in normal reading and dyslexia. Proc. Natl. Acad. Sci. U. S. A. 95, 8939–8944.
Hyman, S.E., Malenka, R.C., 2001. Addiction and the brain: the neurobiology of compulsion and its persistence. Nat. Rev. Neurosci. 2, 695–703.
Kannurpatti, S.S., Biswal, B.B., Hudetz, A.G., 2003. MAP reversibly modulates resting state fMRI low-frequency fluctuations in anesthetized rats. Proc. ISMRM 11, 1856 Ref Type: Abstract.
Kannurpatti, S.S., Biswal, B.B., Kim, Y.R., Rosen, B.R., 2008. Spatio-temporal characteristics of low-frequency BOLD signal fluctuations in isoflurane-anesthetized rat brain. Neuroimage 40, 1738–1747.
Koob, G.F., 2003. Neuroadaptive mechanisms of addiction: studies on the extended amygdala. Eur. Neuropsychopharmacol. 13, 442–452.
Laruelle, M., Kegeles, L.S., bi-Dargham, A., 2003. Glutamate, dopamine, and schizophrenia: from pathophysiology to treatment. Ann. N. Y. Acad. Sci. 1003, 138–158.
Lu, H., Zuo, Y., Gu, H., Waltz, J.A., Zhan, W., Scholl, C.A., Rea, W., Yang, Y., Stein, E.A., 2007. Synchronized delta oscillations correlate with the resting-state functional MRI signal. Proc. Natl. Acad. Sci. U. S. A. 104, 18265–18269.
Meunier, D., Achard, S., Morcom, A., Bullmore, E., 2009. Age-related changes in modular organization of human brain functional networks. Neuroimage 44, 715–723.
Nestler, E.J., Carlezon Jr., W.A., 2006. The mesolimbic dopamine reward circuit in depression. Biol. Psychiatry 59, 1151–1159.
Newman, M.E., 2006a. Finding community structure in networks using the eigenvectors of matrices. Phys. Rev. E. Stat. Nonlin. Soft. Matter Phys. 74, 036104.
Newman, M.E., 2006b. Modularity and community structure in networks. Proc. Natl. Acad. Sci. U. S. A. 103, 8577–8582.
Newman, M.E., Girvan, M., 2004. Finding and evaluating community structure in networks. Phys. Rev. E. Stat. Nonlin. Soft. Matter Phys. 69, 026113.
Pawela, C.P., Biswal, B.B., Cho, Y.R., Kao, D.S., Li, R., Jones, S.R., Schulte, M.L., Matloub, H.S., Hudetz, A.G., Hyde, J.S., 2008. Resting-state functional connectivity of the rat brain. Magn. Reson. Med. 59, 1021–1029.
Paxinos, G., Watson, C., 1998. The Rat Brain in Stereotaxic Coordinates. Academic Press, San Diego.
Radicchi, F., Castellano, C., Cecconi, F., Loreto, V., Parisi, D., 2004. Defining and identifying communities in networks. Proc. Natl. Acad. Sci. U. S. A. 101, 2658–2663.
Raghavan, U.N., Albert, R., Kumara, S., 2007. Near linear time algorithm to detect community structures in large-scale networks. Phys. Rev. E. Stat. Nonlin. Soft. Matter Phys. 76, 036106.
Raichle, M.E., Snyder, A.Z., 2007. A default mode of brain function: a brief history of an evolving idea. Neuroimage 37, 1083–1090.
Rosvall, M., Bergstrom, C.T., 2007. An information-theoretic framework for resolving community structure in complex networks. Proc. Natl. Acad. Sci. U. S. A. 104, 7327–7331.
Rosvall, M., Bergstrom, C.T., 2008. Maps of random walks on complex networks reveal community structure. Proc. Natl. Acad. Sci. U. S. A. 105, 1118–1123.

Ruan, J., Zhang, W., 2008. Identifying network communities with a high resolution. Phys. Rev. E. Stat. Nonlin. Soft. Matter Phys. 77, 016104.
Salvador, R., Suckling, J., Schwarzbauer, C., Bullmore, E., 2005. Undirected graphs of frequency-dependent functional connectivity in whole brain networks. Philos. Trans. R. Soc. Lond B Biol. Sci. 360, 937–946.
Schwarz, A.J., Reese, T., Gozzi, A., Bifone, A., 2003. Functional MRI using intravascular contrast agents: detrending of the relative cerebrovascular (rCBV) time course. Magn. Reson. Imaging 21, 1191–1200.
Schwarz, A.J., Danckaert, A., Reese, T., Gozzi, A., Paxinos, G., Watson, C., Merlo-Pich, E.V., Bifone, A., 2006. A stereotaxic MRI template set for the rat brain with tissue class distribution maps and co-registered anatomical atlas: application to pharmacological MRI. Neuroimage 32, 538–550.
Schwarz, A.J., Gozzi, A., Reese, T., Bifone, A., 2007a. Functional connectivity in the pharmacologically activated brain: resolving networks of correlated responses to d-amphetamine. Magn. Reson. Med. 57, 704–713.
Schwarz, A.J., Gozzi, A., Reese, T., Bifone, A., 2007b. In vivo mapping of functional connectivity in neurotransmitter systems using pharmacological MRI. Neuroimage 34, 1627–1636.
Schwarz, A.J., Gozzi, A., Reese, T., Heidbreder, C.A., Bifone, A., 2007c. Pharmacological modulation of functional connectivity: the correlation structure underlying the phMRI response to d-amphetamine modified by selective dopamine D3 receptor antagonist SB277011A. Magn. Reson. Imaging 25, 811–820.
Schwarz, A.J., Whitcher, B., Gozzi, A., Reese, T., Bifone, A., 2007d. Study-level wavelet cluster analysis and data-driven signal models in pharmacological MRI. J. Neurosci. Methods 159, 346–360.
Schwarz, A.J., Gozzi, A., Bifone, A., 2008. Community structure and modularity in networks of correlated brain activity. Magn. Reson. Imaging 26, 914–920.
Soncrant, T.T., Horwitz, B., Holloway, H.W., Rapoport, S.I., 1986. The pattern of functional coupling of brain regions in the awake rat. Brain Res. 369, 1–11.
Strogatz, S.H., 2001. Exploring complex networks. Nature 410, 268–276.
Vragovic, I., Louis, E., 2006. Network community structure and loop coefficient method. Phys. Rev. E. Stat. Nonlin. Soft. Matter Phys. 74, 016105.
Watts, D.J., Strogatz, S.H., 1998. Collective dynamics of 'small-world' networks. Nature 393, 440–442.
Zaharchuk, G., Mandeville, J.B., Bogdanov Jr., A.A., Weissleder, R., Rosen, B.R., Marota, J.J., 1999. Cerebrovascular dynamics of autoregulation and hypoperfusion. An MRI study of CBF and changes in total and microvascular cerebral blood volume during hemorrhagic hypotension. Stroke 30, 2197–2204.
Zhao, F., Zhao, T., Zhou, L., Wu, Q., Hu, X., 2008. BOLD study of stimulation-induced neural activity and resting-state connectivity in medetomidine-sedated rat. Neuroimage 39, 248–260.
Zhou, H., 2003. Distance, dissimilarity index, and network community structure. Phys. Rev. E. Stat. Nonlin. Soft. Matter Phys. 67, 061901.

5 - References

1. Achard S, Bullmore E (2007). Efficiency and cost of economical brain functional networks. *PLoS Comput Biol* **3**: e17.
2. Achard S, Salvador R, Whitcher B, Suckling J, Bullmore E (2006). A resilient, low-frequency, small-world human brain functional network with highly connected association cortical hubs. *J Neurosci* **26**: 63-72.
3. Aggleton JP (1992): *The Amygdala*. Wiley-Liss. 300 pp.
4. Ahmed SH, Koob GF (1998). Transition from Moderate to Excessive Drug Intake: Change in Hedonic Set Point. *Science* **282**: 298-300.
5. Anand A, Charney DS, Oren DA, Berman RM, Hu XS, Cappiello A*, et al.* (2000). Attenuation of the neuropsychiatric effects of ketamine with lamotrigine: support for hyperglutamatergic effects of N-methyl-D-aspartate receptor antagonists. *Arch Gen Psychiatry* **57**: 270-276.
6. Attwell D, Laughlin SB (2001). An Energy Budget for Signaling in the Grey Matter of the Brain. *J Cereb Blood Flow Metab* **21**: 1133-1145.
7. Bandettini PA, Wong EC, Hinks RS, Tikofsky RS, Hyde JS (1992). Time course EPI of human brain function during task activation. *Magn Reson Med* **25**: 390-397.
8. Beckmann CF, DeLuca M, Devlin JT, Smith SM (2005). Investigations into resting-state connectivity using independent component analysis. *Philos Trans R Soc Lond B Biol Sci* **360**: 1001-1013.
9. Beckmann CF, Smith SM (2004). Probabilistic independent component analysis for functional magnetic resonance imaging. *IEEE Trans Med Imaging* **23**: 137-152.
10. Belliveau JW, Kennedy DN, McKinstry RC, Buchbinder RM, Weisskoff R, Cohen MS*, et al.* (1991). Functional mapping of the human visual cortex by magnetic resonance imaging. *Science* **254**: 716-719.
11. Bifone A, Gozzi A (2010): Functional and pharmacological MRI in understanding brain fucntion. In: Hagan J (ed). *Current Topics in Behavioral Neurosciences*. Springer. p In print.
12. Bifone A, Gozzi A, Schwarz AJ (2010). Functional connectivity in the rat brain: a complex network approach. *Magn Reson Imag* **28**: 1200-1209.
13. Boujraf S, Summers P, Belahsen F, Prussmann K, Kollias S (2009). Ultrafast bold fMRI using single-shot spin-echo echo planar imaging. *J Med Phys* **34**: 37-42.
14. Boxerman JL, Hamberg LM, Rosen BR, Weisskoff RM (1995). MR contrast due to intravascular magnetic susceptibility perturbations. *Magn Reson Med* **34**: 555-566.
15. Briand LA, Flagel SB, Garcia-Fuster MJ, Watson SJ, Akil H, Sarter M*, et al.* (2008). Persistent Alterations in Cognitive Function and Prefrontal Dopamine D2 Receptors Following Extended, but Not Limited, Access to Self-Administered Cocaine. *Neuropsychopharmacology* **33**: 2969-2980.
16. Bullmore E, Sporns O (2009). Complex brain networks: graph theoretical analysis of structural and functional systems. *Nat Rev Neurosci* **10**: 186-198.
17. Caine SB, Lintz R, Koob GF (1993): Intravenous drug self-administration techniques in animals. In. American College of Neuropsychopharmacology. pp 117-143.
18. Carlsson A, Waters N, Carlsson ML (1999). Neurotransmitter interactions in schizophrenia--therapeutic implications. *Biological Psychiatry* **46**: 1388-1395.
19. Cavazzuti M, Porro CA, Biral GP, Benassi C, Barbieri GC (1987). Ketamine effects on local cerebral blood flow and metabolism in the rat. *J Cereb Blood Flow Metab* **7**: 806-811.
20. Chen Y-CI, Mandeville JB, Nguyen TV, Talele A, Cavagna F, Jenkins BG (2001). Improved Mapping of Pharmacologically Induced Neuronal Activation Using the IRON Technique with Superparamagnetic Blood Pool Agents. *J Magn Reson Imaging* **14**: 517-524.
21. Clinton SM, Meador-Woodruff JH (2004). Thalamic dysfunction in schizophrenia: neurochemical, neuropathological, and in vivo imaging abnormalities. *Schizophrenia Research* **69**: 237-253.
22. Davis M, Whalen PJ (2001). The amygdala: vigilance and emotion. *Mol Psychiatry* **6**: 13-34.
23. Deakin JFW, Lees J, McKie S, Hallak JEC, Williams SR, Dursun SM (2008). Glutamate and the Neural Basis of the Subjective Effects of Ketamine: A Pharmaco-Magnetic Resonance Imaging Study. *Arch Gen Psychiatry* **65**: 154-164.

24. Dirnagl U, Niwa K, Lindauer U, Villringer A (1994). Coupling of cerebral blood flow to neuronal activation: role of adenosine and nitric oxide. *American Journal of Physiology - Heart and Circulatory Physiology* **267**: H296-H301.
25. Disbrow EA, Slutsky DA, Roberts TPL, Krubitzer LA (2000). Functional MRI at 1.5 tesla: A comparison of the blood oxygenation level-dependent signal and electrophysiology. *Proceedings of the National Academy of Sciences of the United States of America* **97**: 9718-9723.
26. Duncan GE, Leipzig JN, Mailman RB, Lieberman JA (1998a). Differential effects of clozapine and haloperidol on ketamine-induced brain metabolic activation. *Brain Res* **812**: 65-75.
27. Duncan GE, Moy SS, Knapp DJ, Mueller RA, Breese GR (1998b). Metabolic mapping of the rat brain after subanesthetic doses of ketamine: potential relevance to schizophrenia. *Brain Res* **787**: 181-190.
28. Duncan GE, Zorn S, Lieberman JA (1999). Mechanisms of typical and atypical antipsychotic drug action in relation to dopamine and NMDA receptor hypofunction hypotheses of schizophrenia. *Mol Psychiatry* **4**: 418-428.
29. Duong TQ, Yacoub E, Adriany G, Hu X, Ugurbil K, Vaughan JT*, et al.* (2002). High-resolution, spin-echo BOLD, and CBF fMRI at 4 and 7 T. *Magn Reson Med* **48**: 589-593.
30. Edvinsson L, Krause DN (2002): *Cerebral Blood Flow and Metabolism*. Lippincott Williams & Wilkins: Philadelphia.
31. Eguiluz VM, Chialvo DR, Cecchi GA, Baliki M, Apkarian AV (2005). Scale-free brain functional networks. *Phys Rev Lett* **94**: 018102.
32. Ekstrom A (2010). How and when the fMRI BOLD signal relates to underlying neural activity: The danger in dissociation. *Brain Research Reviews* **62**: 233-244.
33. Farber NB (2003). The NMDA receptor hypofunction model of psychosis. *Ann N Y Acad Sci* **1003**: 119-130.
34. Flecknell P (1987): *Laboratory Animal Anesthesia*. Academic Press: Cambridge.
35. Friston K, Ashburner J, Kiebel S, Nichols T, Penny W (2007): *Statistical Parametric Mapping: The Analysis of Functional Brain Images*. Academic Press.
36. Friston KJ (1996): Statistical Parametric Mapping and Other Analyses of Functional Imaging Data. In: Toga AW, Mazziotta JC (eds). *Brain Mapping: The Methods*. Academic Press: San Diego. pp 363-386.
37. Friston KJ (1997): Analyzing brain images: Principles and overview. In: Frackowiak RSJ, Friston KJ, Frith C, Dolan R, Mazziotta JC (eds). *Human Brain Function*. Academic Press. pp 25-41.
38. Friston KJ, Frith CD, Liddle PF, Frackowiak RS (1993). Functional connectivity: the principal-component analysis of large (PET) data sets. *JCBFM* **13**: 5-14.
39. Friston KJ, Jezzard P, Turner R (1994). Analysis of functional MRI time-series. *Human Brain Mapping* **1**: 153-171.
40. Gadian DG (2004): *NMR and its Application to Living Systems*. Oxford University Press: Oxford.
41. Gaisler-Salomon I, Schobel SA, Small SA, Rayport S (2009). How High-Resolution Basal-State Functional Imaging Can Guide the Development of New Pharmacotherapies for Schizophrenia. *Schizophr Bull* **35**: 1037-1044.
42. Gawin FH, Ellinwood EH (1988). Cocaine and Other Stimulants. *New England Journal of Medicine* **318**: 1173-1182.
43. Gozzi A, Ceolin L, Schwarz A, Reese T, Bertani S, Bifone A (2006). A multimodality investigation of cerebral haemodynamics and autoregulation in phMRI. *Book of abstracts: 14th Annual Meeting of the International Society of Magnetic Resonance in Medicine* **P-2138**: 307.
44. Gozzi A, Crestan V, Turrini G, Clemens M, Bifone A (2010a). Antagonism at serotonin 5-HT2A receptors modulates functional activity of fonto-hippocampal circuit. *Psychopharmacology* **209**: 37-50.
45. Gozzi A, Herdon H, Schwarz A, Bertani S, Crestan V, Turrini G*, et al.* (2008a). Pharmacological stimulation of NMDA receptors via co-agonist site suppresses fMRI response to phencyclidine in the rat. *Psychopharmacology* **201**: 273-284.
46. Gozzi A, Large C, Schwarz A, Bertani S, Crestan V, Bifone A (2008b). Differential Effects of Antipsychotic and Glutamatergic Agents on the phMRI Response to Phencyclidine. *Neuropsychopharmacology* **33**: 1690-1703.
47. Gozzi A, Apar J, Giovanelli A, Bertollini C, Crestan V, Schwarz AJ*, et al.* (2010b). A neural switch for active and passive fear. *Neuron* **67**: 656-66.

48. Gozzi A, Schwarz AJ, Reese T, Crestan V, Bifone A (2008c). Drug-anaesthetic interaction in phMRI: the case of the pyschotomimetic agent phencyclidine. *Magn Reson Imag* **26**: 999-1006.
49. Greene R (2001). Circuit analysis of NMDAR hypofunction in the hippocampus, in vitro, and psychosis of schizophrenia. *Hippocampus* **11**: 569-577.
50. Greicius MD, Krasnow B, Reiss AL, Menon V (2003). Functional connectivity in the resting brain: a network analysis of the default mode hypothesis. *Proc Natl Acad Sci U S A* **100**: 253-258.
51. Gu H, Salmeron BJ, Ross TJ, Geng X, Zhan W, Stein EA*, et al.* (2010). Mesocorticolimbic circuits are impaired in chronic cocaine users as demonstrated by resting-state functional connectivity. *NeuroImage* **In Press, Corrected Proof**.
52. Hahn EL (1950). Spin Echoes. *Phys Rev* **80**: 580.
53. Hennig J (1988). Multiecho imaging sequences with low refocusing flip angles. *Journal of Magnetic Resonance (1969)* **78**: 397-407.
54. Hennig J, Nauerth A, Friedburg H (1986). RARE imaging: a fast imaging method for clinical MR. *Magn Reson Med* **3**: 823-833.
55. Homayoun H, Jackson ME, Moghaddam B (2005). Activation of Metabotropic Glutamate 2/3 Receptors Reverses the Effects of NMDA Receptor Hypofunction on Prefrontal Cortex Unit Activity in Awake Rats. *J Neurophysiol* **93**: 1989-2001.
56. Horwitz B, Duara R, Rapoport SI (1984). Intercorrelations of glucose metabolic rates between brain regions: application to healthy males in a state of reduced sensory input. *J Cereb Blood Flow Metab* **4**: 484-499.
57. Hudetz AG (1997). Blood flow in the cerebral capillary network: a review emphasizing observations with intravital microscopy. *Microcirculation* **4**: 233-252.
58. Huettel S, Song AW, McCarthy G (2004): *Functional Magnetic Resonance Imaging*. Sinauer: Sunderland.
59. Iadecola C, Yang G, Ebner TJ, Chen G (1997). Local and Propagated Vascular Responses Evoked by Focal Synaptic Activity in Cerebellar Cortex. *J Neurophysiol* **78**: 651-659.
60. Jenkins BG, Chen Y-CI, Mandeville JB (2003): Pharmacological Magnetic Resonance Imaging (phMRI). In: van Bruggen N, Roberts T (eds). *Biomedical Imaging in Experimental Neuroscience*. CRC Press: New York. pp 155-209.
61. Jenkins BG, Sanchez-Pernaute R, Brownell AL, Chen YC, Isacson O (2004). Mapping dopamine function in primates using pharmacologic magnetic resonance imaging. *J Neurosci* **24**: 9553-9560.
62. Kalivas PW, Volkow N, Seamans J (2005). Unmanageable Motivation in Addiction: A Pathology in Prefrontal-Accumbens Glutamate Transmission. *Neuron* **45**: 647-650.
63. Kalivas PW (2004). Glutamate systems in cocaine addiction. *Current Opinion in Pharmacology* **4**: 23-29.
64. Kim SG, Ugurbil K (2003). High-resolution functional magnetic resonance imaging of the animal brain. *Methods* **30**: 28-41.
65. Kinon BJ, Zhang L, Williams JE, Osuntokun OO, Millen BA, Kollack-Walker S (2010). LY2140023 monohydrate: an agonist at the mglu2/3 receptor for the Treatment of Schizophrenia. *Schizophrenia Research* **117**: 379.
66. Kircher TT, Thienel R (2005). Functional brain imaging of symptoms and cognition in schizophrenia. *Prog Brain Res* **150**: 299-308.
67. Knutson B, Gibbs S (2007). Linking nucleus accumbens dopamine and blood oxygenation. *Psychopharmacology* **191**: 813-822.
68. Koob GF, Sanna PP, Bloom FE (1998). Neuroscience of addiction. *Neuron* **21**: 467-476.
69. Krimer LS, Muly EC, III, Williams GV, Goldman-Rakic PS (1998). Dopaminergic regulation of cerebral cortical microcirculation. *Nat Neurosci* **1**: 286-289.
70. Kristiansen LV, Huerta I, Beneyto M, Meador-Woodruff JH (2007). NMDA receptors and schizophrenia. *Curr Opin Pharmacol* **7**: 48-55.
71. Krystal JH, Karper LP, Seibyl JP, Freeman GK, Delaney R, Bremner JD*, et al.* (1994). Subanesthetic effects of the noncompetitive NMDA antagonist, ketamine, in humans. Psychotomimetic, perceptual, cognitive, and neuroendocrine responses. *Arch Gen Psychiatry* **51**: 199-214.

72. Kwong KK, Belliveau JW, Chesler DA, Goldberg IE, Weisskoff R, Poncelet BP*, et al.* (1992). Dynamic magnetic resonance imaging of human brain activity during primary sensory stimulation. *Proc Nat Acad Sci USA* **89**: 5675-5679.
73. Kyrtatos PG, Lehtolainen P, Junemann-Ramirez M, Garcia-Prieto A, Price AN, Martin JF*, et al.* (2009). Magnetic Tagging Increases Delivery of Circulating Progenitors in Vascular Injury. *J Am Coll Cardiol Intv* **2**: 794-802.
74. Langsjo JW, Kaisti KK, Aalto S, Hinkka S, Aantaa R, Oikonen V*, et al.* (2003). Effects of subanesthetic doses of ketamine on regional cerebral blood flow, oxygen consumption, and blood volume in humans. *Anesthesiology* **99**: 614-623.
75. Large CH (2007). Do NMDA receptor antagonist models of schizophrenia predict the clinical efficacy of antipsychotic drugs? *J Psychopharmacol* **21**: 283-301.
76. LeDoux JE (2000). Emotion circuits in the brain. *Annu Rev Neurosci* **23**: 155-184.
77. Lee JH, Durand R, Gradinaru V, Zhang F, Goshen I, Kim DS*, et al.* (2010). Global and local fMRI signals driven by neurons defined optogenetically by type and wiring. *Nature* **465**: 788-792.
78. Lee SP, Silva AC, Kim SG (2002). Comparison of diffusion-weighted high-resolution CBF and spin-echo BOLD fMRI at 9.4 T. *Magn Reson Med* **47**: 736-741.
79. Leslie RA, James MF (2000). Pharmacological magnetic resonance imaging: a new application for functional MRI. *Trends Pharmacol Sci* **21**: 314-318.
80. Li SJ, Li Z, Wu G, Zhang MJ, Franczak M, Antuono PG (2002). Alzheimer Disease: evaluation of a functional MR imaging index as a marker. *Radiology* **225**: 253-259.
81. Liddle PF, Lane CJ, Ngan E (2000). Immediate effects of risperidone on cortico--striato--thalamic loops and the hippocampus. *The British Journal of Psychiatry* **177**: 402-407.
82. Logothetis NK, Pauls J, Augath M, Trinath T, Oeltermann A (2001). Neurophysiological investigation of the basis of the fMRI signal. *Nature* **412**: 150-157.
83. London ED, Bonson KR, Ernst M, Grant S (1999). Brain imaging studies of cocaine abuse: implications for medication development. *Crit Rev Neurobiol* **13**: 227-242.
84. Lowe MJ, Phillips MD, Lurito JT, Mattson D, Dzemidzic M, Mathews VP (2002). Multiple sclerosis: low-frequency temporal blood oxygen level-dependent fluctuations indicate reduced functional connectivity initial results. *Radiology* **224**: 184-192.
85. Lu H, van Zijl PCM (2005). Experimental measurement of extravascular parenchymal BOLD effects and tissue oxygen extraction fractions using multi-echo VASO fMRI at 1.5 and 3.0 T. *Magn Reson Med* **53**: 808-816.
86. Luo L, Callaway EM, Svoboda K (2008). Genetic Dissection of Neural Circuits. *Neuron* **57**: 634-660.
87. Luria A (1973): *The working brain*. New York: Basic Books.
88. Malonek D, Grinvald A (1996). Interactions between electrical activity and cortical microcirculation revealed by imaging spectroscopy: implications for functional brain mapping. *Science* **272**: 551-554.
89. Mandeville JB, Marota JJA, Kosofsky BE, Keltner JR, Weissleder R, Rosen B*, et al.* (1998). Dynamic functional imaging of relative cerebral blood volume during rat forepaw stimulation. *Magn Reson Med* **39**: 615-624.
90. Mandeville JB, Jenkins BG, Chen YC, Choi JK, Kim YR, Belen D*, et al.* (2004). Exogenous contrast agent improves sensitivity of gradient-echo functional magnetic resonance imaging at 9.4 T. *Magn Reson Med* **52**: 1272-1281.
91. Mandeville JB, Marota JJA (1999). Vascular filters of functional MRI: Spatial localization using BOLD and CBV contrast. *Magn Reson Med* **42**: 591-598.
92. Mangia S, Giove F, Tkac I, Logothetis NK, Henry PG, Olman CA*, et al.* (2009). Metabolic and hemodynamic events after changes in neuronal activity: current hypotheses, theoretical predictions and in vivo NMR experimental findings. *J Cereb Blood Flow Metab* **29**: 441-463.
93. McKeown MJ, Makeig S, Brown GG, Jung TP, Kindermann SS, Bell AJ*, et al.* (1998). Analysis of fMRI data by blind separation into independent spatial components. *Hum Brain Mapp* **6**: 160-188.
94. McRobbie D, Moore E, Graves MJ, Prince M (2007): *MRI: from Picture to Proton*. Cambridge University Press: Cambridge.
95. Medoff DR, Holcomb HH, Lahti AC, Tamminga CA (2001). Probing the human hippocampus using rCBF: contrasts in schizophrenia. *Hippocampus* **11**: 543-550.
96. Meltzer HY (1996). Pre-clinical pharmacology of atypical antipsychotic drugs: a selective review. *Br J Psychiatry Suppl*: 23-31.

97. Menon RS, Ogawa S, Hu X, Strupp JP, Anderson P, U¦ºurbil K (1995). BOLD Based Functional MRI at 4 Tesla Includes a Capillary Bed Contribution: Echo-Planar Imaging Correlates with Previous Optical Imaging Using Intrinsic Signals. *Magn Reson Med* **33**: 453-459.
98. Meunier D, Achard S, Morcom A, Bullmore E (2009). Age-related changes in modular organization of human brain functional networks. *Neuroimage* **44**: 715-723.
99. Mitelman SA, Shihabuddin L, Brickman AM, Hazlett EA, Buchsbaum MS (2005). Volume of the cingulate and outcome in schizophrenia. *Schizophrenia Research* **72**: 91-108.
100. Miyamoto S, Leipzig JN, Lieberman JA, Duncan GE (2000). Effects of ketamine, MK-801, and amphetamine on regional brain 2-deoxyglucose uptake in freely moving mice. *Neuropsychopharmacology* **22**: 400-412.
101. Morris BJ, Cochran SM, Pratt JA (2005). PCP: from pharmacology to modelling schizophrenia. *Curr Opin Pharmacol* **5**: 101-106.
102. Nakki R, Sharp FR, Sagar SM, Honkaniemi J (1996). Effects of phencyclidine on immediate early gene expression in the brain. *J Neurosci Res* **45**: 13-27.
103. Narendran R, Martinez D (2008). Cocaine abuse and sensitization of striatal dopamine transmission: A critical review of the preclinical and clinical imaging literature. *Synapse* **62**: 851-869.
104. Newman ME (2006). Modularity and community structure in networks. *Proc Natl Acad Sci U S A* **103**: 8577-8582.
105. Newman ME, Girvan M (2004). Finding and evaluating community structure in networks. *Phys Rev E Stat Nonlin Soft Matter Phys* **69**: 026113.
106. Ngai AC, Ko KR, Morii S, Winn HR (1988). Effect of sciatic nerve stimulation on pial arterioles in rats. *American Journal of Physiology - Heart and Circulatory Physiology* **254**: H133-H139.
107. Ngai AC, Meno JR, Winn HR (1995). Simultaneous measurements of pial arteriolar diameter and laser-Doppler flow during somatosensory stimulation. *J Cereb Blood Flow Metab* **15**: 124-127.
108. Ngan ETC, Lane CJ, Ruth TJ, Liddle PF (2002). Immediate and delayed effects of risperidone on cerebral metabolism in neuroleptic naive schizophrenic patients: correlations with symptom change. *J Neurol Neurosurg Psychiatry* **72**: 106-110.
109. Norris DG, Zysset S, Mildner T, Wiggins CJ (2002). An Investigation of the Value of Spin-Echo-Based fMRI Using a Stroop Color-Word Matching Task and EPI at 3 T. *NeuroImage* **15**: 719-726.
110. Ogawa S, Lee TM, Kay AR, Tank DW (1990a). Brain magnetic resonance imaging with contrast dependent on blood oxygenation. *Proc Nat Acad Sci USA* **87**: 9868-9872.
111. Ogawa S, Menon RS, Tank DW, Kim SG, Merkle H, Ellermann JM*, et al.* (1993). Functional brain mapping by blood oxygenation level-dependent contrast magnetic resonance imaging. A comparison of signal characteristics with a biophysical model. *Biophys J* **64**: 803-812.
112. Ogawa S, Tank DW, Menon R, Ellermann JM, Kim SG, Merkle H*, et al.* (1992). Intrinsic signal changes accompanying sensory stimulation: functional brain mapping with magnetic resonance imaging. *Proceedings of the National Academy of Sciences of the United States of America* **89**: 5951-5955.
113. Ogawa S, Lee TM (1990). Magnetic resonance imaging of blood vessels at high fields: In vivo and in vitro measurements and image simulation. *Magn Reson Med* **16**: 9-18.
114. Ogawa S, Lee TM, Nayak AS, Glynn P (1990b). Oxygenation-sensitive contrast in magnetic resonance image of rodent brain at high magnetic fields. *Magn Reson Med* **14**: 68-78.
115. Oja JME, Gillen J, Kauppinen RA, Kraut M, van Zijl PCM (1999). Venous blood effects in spin-echo fMRI of human brain. *Magn Reson Med* **42**: 617-626.
116. Parellada E, Catafau AM, Bernardo M, Lomena F, Gonzalez-Monclus E, Setoain J (1994). Prefrontal dysfunction in young acute neuroleptic-naive schizophrenic patients: a resting and activation SPECT study. *Psychiatry Res* **55**: 131-139.
117. Paterson NE, Markou A (2003). Increased motivation for self-administered cocaine after escalated cocaine intake. *NeuroReport* **14**.
118. Patil ST, Zhang L, Martenyi F, Lowe SL, Jackson KA, Andreev BV*, et al.* (2007). Activation of mGlu2/3 receptors as a new approach to treat schizophrenia: a randomized Phase 2 clinical trial. *Nat Med* **13**: 1102-1107.
119. Paulson OB, Newman EA (1987). Does the release of potassium from astrocyte endfeet regulate cerebral blood flow? *Science* **237**: 896-898.

120. Pawela CP, Biswal BB, Cho YR, Kao DS, Li R, Jones SR*, et al.* (2008). Resting-state functional connectivity of the rat brain. *Magn Reson Med* **59**: 1021-1029.
121. Pawela CP, Biswal BB, Hudetz AG, Schulte ML, Li R, Jones SR*, et al.* (2009). A protocol for use of medetomidine anesthesia in rats for extended studies using task-induced BOLD contrast and resting-state functional connectivity. *Neuroimage* **46**: 1137-1147.
122. Paxinos G (2008): *The Rat Nervous System*. Elsevier: London. 1193 pp.
123. Paxinos G, Watson C (2005): *The Rat Brain in Stereotaxic Coordinates (5th edn.)*. Elsevier.
124. Poser BA, van ME, Norris DG (2010). Exploring the post-stimulus undershoot with spin-echo fMRI: Implications for models of neurovascular response. *Hum Brain Mapp*.
125. Poser B, Norris D (2007). Fast spin echo sequences for BOLD functional MRI. *Magnetic Resonance Materials in Physics, Biology and Medicine* **20**: 11-17.
126. Posner MI, Petersen SE, Fox PT, Raichle ME (1988). Localization of cognitive operations in the human brain. *Science* **240**: 1627-1631.
127. Ramnani N, Behrens TE, Penny W, Matthews PM (2004). New approaches for exploring anatomical and functional connectivity in the human brain. *Biol Psychiatry* **56**: 613-619.
128. Roberts DCS, Morgan D, Liu Y (2007). How to make a rat addicted to cocaine. *Progress in Neuro-Psychopharmacology and Biological Psychiatry* **31**: 1614-1624.
129. Rogers BP, Morgan VL, Newton AT, Gore JC (2007). Assessing functional connectivity in the human brain by fMRI. *Magn Reson Imag* **25**: 1347-1357.
130. Salvador R, Suckling J, Schwarzbauer C, Bullmore E (2005). Undirected graphs of frequency-dependent functional connectivity in whole brain networks. *Philos Trans R Soc Lond B Biol Sci* **360**: 937-946.
131. Schwarz AJ, Danckaert A, Reese T, Gozzi A, Paxinos G, Watson C*, et al.* (2006a). A stereotaxic MRI template set for the rat brain with tissue class distribution maps and co-registered anatomical atlas: application to pharmacological MRI. *NeuroImage* **32**: 538-550.
132. Schwarz AJ, Gozzi A, Bifone A (2008). Community structure and modularity in networks of correlated brain activity. *Magn Reson Imaging* **26**: 914-920.
133. Schwarz AJ, Gozzi A, Bifone A (2009). Community structure in networks of functional connectivity: resolving functional organization in the rat brain with pharmacological MRI. *Neuroimage* **47**: 302-311.
134. Schwarz AJ, Gozzi A, Reese T, Bifone A (2007a). Functional connectivity in the pharmacologically activated brain: resolving networks of correlated responses to d-amphetamine. *Magn Reson Med* **57**: 704-713.
135. Schwarz AJ, Reese T, Gozzi A, Bifone A (2003). Functional MRI using intravascular contrast agents: detrending of the relative cerebrovascular (rCBV) time course. *Magn Reson Imaging* **21**: 1191-1200.
136. Schwarz AJ, Whitcher B, Gozzi A, Reese T, Bifone A (2006b). Study-level wavelet cluster analysis and data-driven signal models in pharmacological MRI. *J Neurosci Methods* **159**: 346-360.
137. Schwarz AJ, Gozzi A, Reese T, Bifone A (2007b). In vivo mapping of functional connectivity in neurotransmitter systems using pharmacological MRI. *NeuroImage* **34**: 1627-1636.
138. Schwarz AJ, Gozzi A, Reese T, Heidbreder CA, Bifone A (2007c). Pharmacological modulation of functional connectivity: the correlation structure underlying the phMRI response to d-amphetamine modified by selective dopamine D3receptor antagonist SB277011A. *Magn Reson Imag* **25**: 811-820.
139. Sheth SA, Nemoto M, Guiou M, Walker M, Pouratian N, Hageman N*, et al.* (2004). Columnar Specificity of Microvascular Oxygenation and Volume Responses: Implications for Functional Brain Mapping. *Journal of Neuroscience* **24**: 634-641.
140. Silbersweig DA, Stern E, Frith C, Cahill C, Holmes A, Grootoonk S*, et al.* (1995). A functional neuroanatomy of hallucinations in schizophrenia. *Nature* **378**: 176-179.
141. Smith SM, Jenkinson M, Woolrich MW, Beckmann CF, Behrens TE, Johansen-Berg H*, et al.* (2004a). Advances in functional and structural MR image analysis and implementation as FSL. *NeuroImage* **23 Suppl 1**: S208-S219.
142. Smith SM, Jenkinson M, Woolrich MW, Beckmann CF, Behrens TEJ, Johansen-Berg H*, et al.* (2004b). Advances in functional and structural MR image analysis and implementation as FSL. *NeuroImage* **23**: S208-S219.
143. Soncrant TT, Horwitz B, Holloway HW, Rapoport SI (1986). The pattern of functional coupling of brain regions in the awake rat. *BRAIN RES* **369**: 1-11.

144. Soyka M, Koch W, M+Âller H, R++ther T, Tatsch K (2005). Hypermetabolic pattern in frontal cortex and other brain regions in unmedicated schizophrenia patients. *European Archives of Psychiatry and Clinical Neuroscience* **255**: 308-312.
145. Steward CA, Marsden CA, Prior MJ, Morris PG, Shah YB (2005). Methodological considerations in rat brain BOLD contrast pharmacological MRI. *Psychopharmacology (Berl)* **180**: 687-704.
146. Strickland TL, Mena I, Villanueva-Meyer J, Miller BL, Cummings J, Mehringer CM*, et al.* (1993). Cerebral perfusion and neuropsychological consequences of chronic cocaine use. *J Neuropsychiatry Clin Neurosci* **5**: 419-427.
147. Strogatz SH (2001). Exploring complex networks. *Nature* **410**: 268-276.
148. Thompson R, Correia M, Cusack R (2010). Vascular contributions to pattern analysis: Comparing gradient and spin echo fMRI at 3T. *NeuroImage*.
149. Thulborn KR, Waterton JC, Matthews PM, Radda GK (1982). Oxygenation dependence of the transverse relaxation time of water protons in whole blood at high field. *Biochimica et Biophysica Acta (BBA) - General Subjects* **714**: 265-270.
150. Tomasi D, Volkow ND, Wang R, Carrillo JH, Maloney T, Alia-Klein N*, et al.* (2010). Disrupted Functional Connectivity with Dopaminergic Midbrain in Cocaine Abusers. *PLoS ONE* **5**: e10815.
151. Tsetsenis T, Ma XH, Lo Iacono L, Beck SG, Gross C (2007). Suppression of conditioning to ambiguous cues by pharmacogenetic inhibition of the dentate gyrus. *Nat Neurosci* **10**: 896-902.
152. Tucker KA, Potenza MN, Beauvais JE, Browndyke JN, Gottschalk PC, Kosten TR (2004). Perfusion abnormalities and decision making in cocaine dependence. *Biological Psychiatry* **56**: 527-530.
153. Tumeh SS, Nagel JS, English RJ, Moore M, Holman BL (1990). Cerebral abnormalities in cocaine abusers: demonstration by SPECT perfusion brain scintigraphy. Work in progress. *Radiology* **176**: 821-824.
154. Uludag K (2010). To dip or not to dip: Reconciling optical imaging and fMRI data. *PNAS* **107**: E23.
155. Uylings HB, Groenewegen HJ, Kolb B (2003). Do rats have a prefrontal cortex? *Behav Brain Res* **146**: 3-17.
156. Vanderschuren LJMJ, Everitt BJ (2004). Drug Seeking Becomes Compulsive After Prolonged Cocaine Self-Administration. *Science* **305**: 1017-1019.
157. Volkow ND, Hitzemann RJ, Wang GJ, Fowler JS, Wolf AP, Dewey SL*, et al.* (1992). Long-term frontal brain metabolic changes in cocaine abusers. *Synapse* **12**: 86.
158. Volkow ND, Mullani N, Gould KL, Adler S, Krajewski K (1988). Cerebral blood flow in chronic cocaine users: a study with positron emission tomography. *The British Journal of Psychiatry* **152**: 641-648.
159. Volkow ND, Wang GJ, Fowler JS, Logan J, Gatley SJ, Hitzemann R*, et al.* (1997). Decreased striatal dopaminergic responsiveness in detoxified cocaine-dependent subjects. *Nature* **386**: 830-833.
160. Volkow ND, Fowler JS, Wang GJ, Swanson JM, Telang F (2007). Dopamine in Drug Abuse and Addiction: Results of Imaging Studies and Treatment Implications. *Arch Neurol* **64**: 1575-1579.
161. Wang YX, Hussain SM, Krestin GP (2001). Superparamagnetic iron oxide contrast agents: physicochemical characteristics and applications in MR imaging. *Eur Radiol* **11**: 2319-2331.
162. Weisskoff RM, Zuo CS, Boxerman JL, Rosen BR (1994). Microscopic susceptibility variation and transverse relaxation: theory and experiment. *Magn Reson Med* **31**: 601-610.
163. Worsley KJ, Evans AC, Marrett S, Neelin P (1992). A three-dimensional statistical analysis for CBF activation studies in human brain. *J Cereb Blood Flow Metab* **12**: 900-918.
164. Yang G, Zhang Y, Ross ME, Iadecola C (2003). Attenuation of activity-induced increases in cerebellar blood flow in mice lacking neuronal nitric oxide synthase. *American Journal of Physiology - Heart and Circulatory Physiology* **285**: H298-H304.
165. Zaharchuk G, Mandeville JB, Bogdanov AA, Jr., Weissleder R, Rosen BR, Marota JJ (1999). Cerebrovascular dynamics of autoregulation and hypoperfusion. An MRI study of CBF and changes in total and microvascular cerebral blood volume during hemorrhagic hypotension. *Stroke* **30**: 2197-2204.
166. Zhao F, Zhao T, Zhou L, Wu Q, Hu X (2008). BOLD study of stimulation-induced neural activity and resting-state connectivity in medetomidine-sedated rat. *Neuroimage* **39**: 248-260.

167. Zhou Y, Shu N, Liu Y, Song M, Hao Y, Liu H*, et al.* (2008). Altered resting-state functional connectivity and anatomical connectivity of hippocampus in schizophrenia. *Schizophrenia Research* **100**: 120-132.
168. Zikopoulos B, Barbas H (2006). Prefrontal Projections to the Thalamic Reticular Nucleus form a Unique Circuit for Attentional Mechanisms. *Journal of Neuroscience* **26**: 7348-7361.

6 - Publication List

Published Manuscripts

[1] **Gozzi A,** A Schwarz, V Crestan, Angelo Bifone**;** Drug-anaesthetic interaction in phMRI: the case of the pyschotomimetic agent phencyclidine, Magnetic Resonance Imaging, 2008, 26(7); 999-1006

[2] **Gozzi A**, Large CH, Schwarz AJ, Crestan V, Bifone A. Differential effects of antipsychotic and glutamatergic agents on the phMRI response to phencyclidine", (2008), Neuropsychopharmacology, 2008, 33(7); 1690-703

[3] **Gozzi A**, Herdon H, Schwarz AJ, Crestan V, Bifone A, Pharmacological stimulation of NMDA receptors via co-agonist site suppresses fMRI response to phencyclidine in the rat. Psychopharmacology, 2008, 201(2):273-84

[4] Schwarz,AJ, **Gozzi A**, Bifone A. Community structure and modularity in networks of correlated brain activity, Magnetic Resonance Imaging , 2008; 26(7); 914-920

[5] Schwarz AJ, **Gozzi A**, Bifone A Community structure in networks of functional connectivity: Resolving functional organization in the rat brain with pharmacological MRI, NeuroImage, 2009, 47(1); 302-311

[6] Ferrari L, Crestan V, Sabattini G, Vinco F, Fontana S, **Gozzi A** Brain penetration of local anaesthetics in the rat: implications for experimental neuroscience; J Neurosci Methods. 2009, 186(2):143-9.

[7] **Gozzi A**, Crestan V, Turrini G, Clemens M, Bifone A; Antagonism at Serotonin 5-Ht_{2A} Receptors Modulates Functional Activity Of Fronto-Hippocampal Circuit, Psychopharmacology 2010;209(1):37-50

[8] **Gozzi A**, Jain A, Crestan V, Schwarz A, Tsetsenis T, Sheridan G, Gross C, Bifone A; A neural switch for active and passive fear; Neuron, 2010, 67:655-666

[9] **Gozzi A** *et al.* Functional Magnetic Resonance Imaging reveals different substrates for the effects of OX1 and OX2 receptor antagonists, 2011, PLOS One, In press,

[10] **Gozzi A**. Bifone A. Imaging del Cervello: stato dell'arte preclinico. Quarterly Journal of Nuclear medicine and Molecolar Imaging, 2010, In press

Review articles

[11] Bifone A**, Gozzi A,** Schwarz A; Functional connectivity in the rat brain: a complex network approach; Magnetic Resonance Imaging, 2010, 28,1200-1209

Book chapters

[12] Bifone A, **Gozzi A**; Functional and pharmacological MRI in understanding brain function, In "Neuropharmacological research models", Edited by J. Hagan; In press.

Manuscripts submitted

[13] **Gozzi A** Turrini G, Dacome L, Tessari M, Agosta F, Lepore S, Corsi C, Lanzoni A, Bifone A; Altered basal and reactive brain function after chronic cocaine self-administration: a magnetic resonance imaging study in the rat, Submitted to J. Neuroscience

Oral Presentations – Invited Seminars

[14] **Gozzi A.** Functional MEMRI without compromising the integrity of the BBB: application to pharmacological studies. Annual Meeting of the ISMRM, May 2008, Toronto

[15] **Gozzi A**. et al;, Linking genes to brain function: expression of serotonin 5-HT1A receptors in specific neuronal populations produces divergent phMRI response to the selective agonist 8-OH-DPAT Annual Meeting of the ISMRM, May 2008, Toronto

[16] Schwarz A, **Gozzi A**, Bifone A. Partitioning functional connectivity networks using "community structure" algorithms. Annual Meeting of the ISMRM, May 2008, Toronto

[17] **Gozzi A**. Pharmacological MRI: a new window on system-level pharmacology. Italian MRI user's meeting, June 2008, Milan

[18] **Gozzi A**. Applicazione dell'imaging farmacologico alla farmacologia del sistema nervoso central, University of Verona, Faculty of Medicine, September 2008, Verona

[19] **Gozzi A** Orexin, dopamine, and the reward system: insights from neuroimaging and behavioural studies. GSK Scinovation, September 2008, Verona

[20] **Gozzi A** Imaging drug action in the brain with phMRI, Istituto Farmacologico Mario Negri, November 2008, Milano

[21] **Gozzi A.** Multimodality imaging for the study of pharmacological parameters in the brain**;** 4^th DIMI Workshop, "Molecular Imaging in Drug Discovery and Preclinical development", June 22-23, 2009, Milan

[22] **Gozzi A**, Jain A, Crestan V, Schwarz A, Tsetsenis T, Sheridan G, Gross C, Bifone A; Mapping the circuit of fear with pharmacogenetic silencing and fMRI, 18th Annual Meeting of the International Society of Magnetic Resonance in Medicine, May 2010, Stockholm

[23] **Gozzi A.** Probing brain function with pharmacological MRI: application to psychiatric drug research; International college of neuro-psychopharmacology (CINP), June 2010, Hong-Kong

[24] **Gozzi A.** Modulation of the glutamatergic system: form rat to human, British Association for Pyshcopharmacology Summer meeting, Harrogate July 2010, (Abstract appeared on J of Pysch, Vol 24 S3)

[25] **Gozzi A**. Imaging del Cervello: stato dell'arte preclinico. XXI° Corso nazionale di aggiornamento in medicina nucleare ed imaging molecolare, Associazione Nazionale Medicina Nucleare e Imaging Molecolare, Sorrento, Nov 2010

Conference Proceedings (peer-reviewed)

[26] **Gozzi A**, Schwarz A, Crestan V, Bifone A. Functional MEMRI without compromising the integrity of the BBB: application to pharmacological studies. Proc. Of 16th Annual Meeting of the ISMRM May 2008, Toronto

[27] **A Gozzi**, G. Turrini, V. Crestan, D. Amantini, M. Corsi, A. Bifone; Differential Modulation of Cortical and Subcortical Circuits by Selective Orexin-1 and Orexin-2 Receptor Antagonists, Annual Meeting of the International Society of Neuroscience (SFN) Chicago, October 2009

[28] **Gozzi A**, Jain A, Crestan V, Schwarz A, Tsetsenis T, Sheridan G, Gross C, Bifone A; A neural switch for active and passive fear; Annual Meeting of the International Society of Neuroscience (SFN) Chicago, October 2009

[29] **Gozzi A** Turrini G, Dacome L, Tessari M, Agosta F, Lepore S, Corsi C, Lanzoni A, Bifone A; White matter microstructural alterations induced by chronic cocaine self-administration: a Diffusion

Tensor Imaging study in the rat. 18th Annual Meeting of the International Society of Magnetic Resonance in Medicine (ISMRM), May 2010, Stockholm

[30] Bifone A, Schwarz AJ, **Gozzi A**. Stimulus-independent functional connectivity in the rat brain. 18th Annual Meeting of the International Society of Magnetic Resonance in Medicine (ISMRM), May 2010, Stockholm

Additional Conference Proceedings

[31] Ferrari L., Turrini G., **Gozzi A**; Non-invasive continuous monitoring of blood pressure and pCO_2 for longitudinal fMRI studies in the rat; FELASA-Scandinavian Symposium; 14-17 June 2010, Helsinki

[32] E. Merlo Pich, **Gozzi A**., M. Corsi, A. Bifone. Role of Orexin Receptors in the Amygdala: Evidence from Preclinical Pharmaco-fMRI and Behavioural Explorations; ISBRA, Paris, September 2010.

[33] E. Merlo Pich, **Gozzi A.**, A. Bifone, Piccoli, M. Massagrande, P. Martinelli, D Amantini, D. Montanari, S. Zamuner, P. Bettica, R. Di Fabio, M. Corsi, E. Ratti; Central orexin peptidergic system as target for novel treatments of insomnia, anxiety and drug addiction: recent findings from the GSK Discovery Performance Unit. Congresso della Societa' Italiana di Chimica Medicinale, Camerino, Aprile 2010.